University of California Santa Cruz

Ultrafast Spin Dynamics of Next-Generation Nanomagnetic Technologies

A dissertation submitted in partial satisfaction
of the requirements for the degree of

DOCTOR OF PHILOSOPHY

in

Electrical Engineering

by

Mike R. Jaris

December 2019

The dissertation of Mike Jaris is approved by

_____
Professor Holger Schmidt, Chair

_____
Professor Nobuhiko Kobayashi

_____
Professor Michael Isaacson

_____
Quentin Williams
Vice Provost and Dean of Graduate Studies

TABLE OF CONTENTS

Chapter 1: Introduction **17**
1.1 Magnetic Recording 17
1.1.1 State-of-the-Art 17
1.1.2 Nanomagnetic Devices 19
1.1.3 Potential Role of All Optical Switching 20
1.2 Spintronic Devices 20
1.2.1 Spin Transfer-Torque Magnetic-Random Access Memory 20
1.2.2 Spin Torque Nano-Oscillators 23
1.2.3 Neuromorphic Computing 25
1.3 Magneto-Elastic Devices 25
1.3.1 SAW-Assisted Switching 27
1.3.2 SAW-Driven Nano-Oscillators 29
1.4 Outline 31
Chapter 2: Magnetization Dynamics **33**
2.1 Dynamics of a Single Spin 33
2.2 Free Energies of Magnetic Systems 36
2.2.1 Exchange Energy 37
2.2.2 Zeeman Energy 39
2.2.3 Stray Field Energy 39
2.2.4 Magnetic Anisotropy Energy 43
2.2.5 Surface Anisotropy Energy 45
2.2.6 Magnetostriction 48
2.3 Ferromagnetic Resonance 50
2.3.1 Derivation of Kittel Formula with Damping 50
2.4 Intrinsic and Extrinsic Damping 56
2.4.1 Intrinsic Sources of Damping 56
2.4.1.1 Phonon-Magnon Damping 56
2.4.1.2 Itinerant Electron Mechanisms 57
2.4.2 Extrinsic Sources of Damping 60
2.4.2.1 Inhomogeneous Broadening 61

2.4.2.2 Two Magnon Scattering 63
Chapter 3: Measurement Methods 68
3.1 Magneto-Optic Effects 68
3.1.1 Wave Equation 69
3.1.2 Lorentz Model 74
3.1.3 Dielectric Tensor 79
3.1.3.1 MOKE Enhancement 87
3.1.3.2 2x2 Transfer Matrix Formalism 91
3.1.3.3 4x4 Yeh Formalism 95
3.2 Stroboscopic Measurements 100
3.2.1 Ultrafast Demagnetization 102
3.2.2 Three-Temperature Model 107
3.3 Detection 109
3.3.1 Crossed Polarizer 110
3.3.2 Balanced Photodiode 115
3.4 TR-MOKE Setup 118
3.4.1 WITec TR-MOKE Setup 119
3.4.2 Electromagnet TR-MOKE Setup 121
3.4.3 Tuning the Pump Beam 123
3.5 Time Domain Analysis 125
3.5.1 Background Subtraction 125
3.5.2 Damping Analysis 126
Chapter 4: Magnetization Dynamics and Damping Behavior of Co/Ni Multilayers with a Graded Ta Capping Layer 129
4.1 Introduction 129
4.2 Applications of Co/Ni 129
4.2.1 Dyzaloshinskii–Moriya interaction 130
4.2.2 Novel Co/Ni-Based Spintronic Memory Architecture 131
4.3 Samples and Experimental Details 133
4.3.1 Interface Roughness Measurements via Glancing X-Ray Reflectivity 134
4.4 Results and Discussion 135

4.5 Conclusion 141

Chapter 5: Dual-Purpose Dielectric Coating for SAW Suppression and Cavity Enhancement 142

5.1 Introduction 142

5.1.1 SAW Excitation in Nanopatterned Arrays 143

5.1.2 Coupling Between SAWs and Magnetization Dynamics 144

5.2 Samples and Experimental Details 146

5.3 Suppression of SAWs 153

5.4 Damping Behavior of STT-MRAM Devices 156

5.5 Conclusion 159

Chapter 6: Magneto-elastic Excitation of Single Nanomagnets for Optical Measurement of the Intrinsic Gilbert Damping 160

6.1 Introduction 161

6.2 Samples and Experimental Details 164

6.3 Results and Discussion 169

6.4 Conclusion 172

Chapter 7: SAW-Driven Spin Dynamics of Single Nanomagnets with Varying Size and Shape 174

7.1 Introduction 174

7.2 Samples and Experimental Details 174

7.3 Magneto-Mechanical Simulations of Nonlocal SAW Design 175

7.4 Role of Nanomagnet Size and Shape on SAW Driven Spin Dynamics 177

7.4.1 Selective Excitation and Damping Behavior of Orthogonally Oriented Elliptical Nanomagnets 177

7.4.2 Size-Dependent Damping of Cylindrical Nanomagnets 184

7.5 Conclusion 190

Chapter 8: SAW-Assisted, Helicity-Dependent All-Optical Switching of FeTb Thin Films 191

8.1 Introduction 191

8.2 AOS Setup at UCSC 193

8.3 Experimental Results 195

8.3.1 HD-AOS of FeTb Films 195

8.3.2 SAW-Assisted HD-AOS Experiments 197

8.4 Conclusion 203
References 204

Table of Figures

Fig. 1.1. (a) Illustration of a HAMR HDD device with the near-field laser device attached to the read/write head. Currently, this technology stores information in a magnetic domain that encompasses multiple grains, as shown by the red outline in (b) the SEM image of a granular magnetic film. For comparison, in (c) an SEM image of a nanopatterned surface shows that in this case each bit corresponds to a nanocylinder. Taken from [2]. 3

Fig. 1.2. (a) Illustration of a full STT-MRAM cell, which includes an access transistor that is used to address the device. In (b,c), the resistance of the device is plotted as both a function of (b) an externally applied magnetic field and (c) the electrical current density through the device in the absence of an external magnetic field. Taken from [3]. 5

Fig. 1.3. (a) Top-down microscope image of the surface of a 3-terminal STNO utilizing the spin Hall effect to excite the STNO into an auto-oscillatory state, and in (b) a schematic illustration of the circuit. (c) The spectra response of the device is shown for various currents, which shows that the strength of the oscillation increases with the SHE current. Lastly, in (d) the spectra from (c) are used to plot the frequency response of the device which shows the dynamic range of the STNO, and in (e) the corresponding output power is plotted. Taken from [4]. 9

Fig. 1.4. (a) Illustration of the sample layout, where the nanomagnets are placed between a pair of interdigitated transducers (IDTs) on a piezoelectric substrate, and (b), the magnetic state of the nanomagnets after being subjected to SAWs, studied using magnetic-force microscopy (MFM), which shows the uniform state (pre-AW) and the vortex state (post-AW). In (c), the results of the micromagnetic calculation show excellent agreement between theory and experiment and reproduces the transition to the vortex state after being subjected to an elastic force. Taken from [5]. 14

Fig. 2.1. Illustration of a spin precessing about an externally applied field H_{ext} as described by Eq. (2.1.5). 21

Fig. 2.2. Fields of a bar magnet. (a) B-field (b) H-field and (c) magnetization. Taken from [9]. 28

Fig. 2.3. Diagrams of ellipsoids of revolution for which the Eq. (2.2.24) can be analytically determined. Taken from [13]. 31

Fig. 2.4. The face-centered cubic and hexagonal close packed crystal structures and their relevant inter-atomic distances *a* and *c*. Taken from [15] 32

Fig. 2.5. Illustration of the three major contributions to the interfacial anisotropy of an Fe–MgO interface: (a) hybridization of the atomic orbitals of the magnetic layer and the barrier, (b) elastic stress due to the lattice distortion and (c) crystal symmetry breaking due to the interface. Circles show position of the atoms for Fe, O, Mg for largest (blue), medium (red) and smallest

(green) spheres, respectively. (a) Ellipses show hybridized Fe–O orbitals; (b) dotted circles correspond to initially undistorted Fe atom positions; (c) dotted circles represent the initial positions of Mg and O atoms before their removal to create vacuum|Fe interface. Taken from [19].....35

Fig. 2.6. Spherical coordinate system used to describe the magnetization. 41

Fig. 2.7. Damping parameter ($\lambda = \alpha\gamma Ms$) of Co, Fe and Ni films measured as a function of temperature exhibits low-T and high-T increases in damping. Taken from [27]. 49

Fig. 2.8. Illustration of local resonance distribution due to spatial variation of magnetic properties adapted from ref. [33]. 53

Fig. 2.9. (a) Kittel frequency of a sample in an applied field canted 30° from surface normal with an anisotropy field $H_K = 2kOe$ and a gyromagnetic ratio γ=2x10^7 [Hz/Oe]. (b) Histogram of spatially varying anisotropy field centered around 2kOe considered in the simulation. (c) Resonance curves at an applied field of 2.5kOe superimposed upon one another for each of the anisotropy fields considered. (d) Comparison between the ensemble resonance (black) and the intrinsic resonance (red) show appreciable broadening due to IHB. (e) Resonance curves of the same sample in an applied field of 10kOe. (f) The ensemble and intrinsic behavior are once again compared and are nearly identical.....55

Fig. 2.10. Spin-wave dispersion plots for magnetic fields applied at different angles θ_H.There are no modes degenerate with the fundamental mode in the out-of-plane configuration, while there are several such modes in the in-plane configuration. Taken from [33].....56

Fig. 2.11. (a) Effective damping parameter measured on a 30nm thick Ni film with an applied field canted 30° from the surface normal. (b) Estimated TMS contribution after fitting the data using Eq. (2.4.14) to obtain $\xi \sim 60$ nm and h'~46 Oe. (c,d) spin wave manifolds of the Ni film for two exemplary cases, H_{app} = 1 kOe (c) and 6 kOe (d).....60

Fig. 3.1. Electric and magnetic fields of light described by Eq. (3.1.11).....64

Fig. 3.2. Electron bound to a nucleus by a "spring-like" force that gives rise to the oscillatory behavior of the electron. 68

Fig. 3.3. Example of light striking dielectric surface used to derive Snell's law.....75

Fig. 3.4. Illustration of obliquely incident ray showing how the *s* and *p* components are defined. 82

Fig. 3.5. Illustration of Gaussian intensity distribution of tightly focused laser beam probing a cylindrical nanomagnet. Because the beam waist is larger than the nanomagnet, the reflected signal will be a mixture of light reflected from the substrate and the magnet. Taken from [45].

.....85

Fig. 3.6. (a) Normalized effective Kerr signal for Ni nanomagnets on bare Si substrate for $w0 = 1\ \mu m$ and $w0 = 200\ nm$, corresponding to the blue and black lines, respectively. The red line was plotted using $Rsub = 0.5\%$ and $w0 = 1\ \mu m$ to show the efficacy of ARC. (b) Effective Kerr signals as a function of various R_{sub} at a fixed spot size of $w0 = 500\ nm$. 86

Fig. 3.7. (a) Interfaces between two dielectrics illustrating reference planes at interface for both ports. (b) Illustration of the relationships input-output relationships between the scattering and transfer matrices. Taken from [47]. 89

Fig. 37.8. Example of multilayer structure described by cascaded network of individual T matrices. Taken from [47].....90

Fig. 3.9. Illustration of the incident and reflected fields for a nonmagnetic medium. Taken from [48].....92

Fig. 3.10. The four eigenmodes of the electromagnetic wave in a magnetic medium. According ot the notations used in Eq. (3.1.102), waves going from medium 1 to 2 are denoted by E_i and those going from 2 to 1 are E_r. Taken from [48].....95

Fig. 3.11. Remnant magneto-optic contrast measured by Beaurepaire et al. for a nickel thin film after absorbing a 60 fs laser pulse. Taken from [51]. 100

Fig. 3.12. (a) Change in the exchange splitting in Ni (measured using TR-ARPES) for an absorbed fluence below (0 .21 mJ/cm^2, grey) and above (1.7 mJ/cm^2) the critical fluence F_c; the solid lines are fits to Eq. (3.2.1). (b) Magnetization dynamics measured using TR-MOKE over a range of fluences, the highest fluence is sufficient to fully suppress the sample magnetization. The solid lines are fits to Eq. (3.2.1) using the same parameters from the TR-ARPES data with auxiliary calculations to account for the depth-average effects in the MOKE measurement. The inset shows the extracted amplitudes of Ai in Eq. (3.2.1) as a function of laser fluence, where the brackets denote the depth-averaging. Taken from [56].....101

Fig. 3.13. Illustration of the subsystems behavior which shows that the electron system directly absorbs the optical power, while the spin and lattice systems suck heat from the electron system after absorption. (b) Simulated time-evolution of the electron, spin and lattice temperatures using Eqs. (3.2.2-4) for a 30 nm thick Ni film excited by a 150 fs laser pulse with a fluence of 1.75 mJ/cm^2. Note that within roughly 5 ps all three of the temperature equilibrate.....106

Fig. 3.14. Example of a crossed-polarizer setup used to measure the MOKE of magnetic films. 110

Fig. 3.15. A typical photodetector circuit used to measure the current of a photodiode which is modelled as an ideal source (i_{PD}) in the schematic above. The noisy contributions are modelled

as discrete circuit elements for the sake of demonstration.....112

Fig. 3.16. Schematic of the WiTec TR-MOKE setup outlined in this section.....118

Fig. 3.17. (a) Illustration of the two-lens system that focus the pump beams into the MO in order to change the beam profiles. Knife edge measurements (100X MO) of the (a) collimated probe beam (w_0 ~ 500 nm) and (c) the focused pump beam which shows a shift in the focal plane for different lens separations. (d) Summary of the pump beam size at the focal point of the probe as a function of the lens separation. 126

Fig. 4.1. (a) Schematic stack structure of the prototype mCell device and (b) a diagram illustrating how the mCell utilizes CIDWM to toggle the magnetoresistance of the device between high and low states. The color-coded images are micromagnetic simulations of the spin-hall effect switching. Taken from [73].....134

Fig. 4.2. (a) Multilayer sequence with illustration of the measurement geometry; M and H_{app} are the magnetization and applied field vectors with polar angles θ and θ_H relative to the surface normal, respectively. (b) Cross-sectional transmission electron microscope image of the sample; (c) X-ray reflectivity measurements (open symbols) and simulations (lines) for three different Ta thicknesses. 137

Fig. 4.3. (a) Resonance frequencies extracted from TR-MOKE DFT spectra (dots) and fit to eq. (1) for 0.3 nm Ta layer. (b) Summarized results of Kittel fitting procedure (eg. shown in (a)) for multiple Ta thicknesses. Taken from [80]. 139

Fig. 4.4. (a) TR-MOKE data (circles) for each Ta thickness after omitting initial demagnetization and subtracting bi-exponential background, lines are the results of a least squares fitting to a damped sinusoid (line) (Data has been offset and normalized for visualization). (b) Minimum αeff measured at a bias field angle θ_H = 85° for each of the Ta thicknesses studied.....140

Fig. 4.5. (a) Effective Lorentzian linewidth of the Kittel resonance extracted from TR-MOKE measurements of 1.1 nm Ta cap (dots) and the best fit of $\Delta\omega eff$ using Eq. (4.3.7) (red line), for comparison, the intrinsic linewidth (dashed black line) using $\alpha G = 0.035$ is plotted to demonstrate the magnitude of IHB; (b) $\Delta\omega eff$ from (a) converted to α_{eff}. Taken from [80]. 143

Fig. 4.6. (a) Local anisotropy field distribution as a function of Ta capping layer thickness determined via fitting data to Eq. (4.3.7) as shown in Fig. 4.5 (a). (b) $\Delta H_{K,eff}$ data from (a) normalized by corresponding $H_{K,eff}$ for each Ta thickness reveals a nearly constant ratio for the full range of Ta thicknesses. Taken from [80]. 144

Fig. 5.1. Schematic illustration of a conventional interdigital transducer used to generate SAWs. Taken from ref. [90]. 147

Fig. 5.2. The sample used in this study is an array of 30 nm thick elliptical Ni nanomagnets, with major and minor axes of 140 and 80 nm, respectively, arranged on a pitch of p = 212 nm. The field-dependent DFT of the normalized (a) nonmagnetic signal, (b) the TR-MOKE signal, (c) simulated magnetization dynamics, and (d,e) non-normalized versions of (b,c), respectively. Taken from ref. [93].....150

Fig. 5.3. (a) SEM image of the MTJ nanomagnet array revealing slight variations in the shape between devices. Normalized DFT spectra of the TR-MOKE signal taken on the uncoated MTJ array for (b) conventional pump-pulse setup, and (c) two time-delayed pump pulses set to annihilate SAWs. In both cases, no magnetic signal can be observed in the spectra due to the large reflectivity of the TiN surface.....152

Fig. 5.4. The reflectivity of the SiN/TiN series as a function of the dielectric layer thickness (blue dots) and the calculated response (red line) using an estimated TiN index of $n2 = 2.83 - 3.68i$. Per Eq. (5.2.6), the ideal dielectric index for perfect antireflection is n_1 = 3.2 (dashed black line). 155

Fig. 5.5. MOKE hysteresis loops of each (a) CoFeB stack without SiN coating and (b) after being coated. The improved signal-to-noise characteristics and Kerr rotation can be seen in the data. (c) The CE factor for each sample using the average Kerr rotation of the entire set (red line) and for each individual sample (blue line), and (d) the corresponding I_{ME} factor; inset: reflectivity of SiN/MTJ stack compared to SiN/TiN. 156

Fig. 5.6. The field-dependent normalized TR-MOKE spectra taken at $\theta H = 75o$ of the (a) unpatterned MTJ film and (b) the MTJ nanomagnet array coated with 65 nm of SiN; the dashed lines are the Kittel frequencies (Eq. 2.3.20) corresponding to the H_K values specified in the figures. The higher H_K value of the array is responsible for the slightly higher frequency. In (c), the effective damping of both samples are shown, revealing a large discrepancy in α_{eff} between the film and nanomagnets (the dashed lines here are only a guide to the eye).....158

Fig. 5.7. The field-dependent TR-MOKE spectra taken at $\theta H = 30o$ for (a) an unpatterned Ni film, (b) the nanomagnet array without coating, and (c) the array coated with 65 nm of SiN. In (d) the time evolution of the lock-in reflectivity is shown, as well as the corresponding DFT in (e) which we use to identify the SAW frequencies, which are accurately predicted by Eq. (5.1.2).....160

Fig. 5.8. (a) Micromagnetic simulation of magneto-elastic field created by SAWs with and without a dielectric coating; (b) the discrete Fourier transform ($Happ = 5\ kOe \mid \theta H = 30o$). The coated response is offset for clarity; insets: FEM geometries used for modelling. In (c), the effective damping of the unpatterned film, uncoated and coated arrays are plotted to demonstrate the obscuring of the intrinsic damping behavior (uncoated) and the restoration of

the intrinsic response.....161

Fig. 5.9. In (a), the normalized time evolution ($Happ = 5kOe, \theta H = 80o$) of a single device (top, $\alpha = 0.005$) is shown adjacent to the normalized ensemble signal, which is the sum of all 20 elements with slightly different shapes used as inputs for the micromagnetic simulation (Fig. 5.3 (c)). A large reduction in the apparent lifetime of the signal occurs due to dynamic dephasing of the ensemble response. Using Eq. (5.4.2), we estimated the FWHM of the spread in the nanomagnet anisotropy fields caused by shape fluctuations ($\Delta HK, shape \approx 150$ Oe). The experimentally observed, field-dependent ($\theta H = 80o$) damping of the film and coated MTJ array are shown in (b) and were also fitted using Eq. (5.4.2) to determine $\Delta HK, film$ and $\Delta HK, array$. 164

Fig. 6.1. The field-dependent, absolute Fourier spectra of TR-MOKE measurements of (a) Nickel and (b) Cobalt nanomagnet arrays comprised of 160x160x30 nm^3 squares with pitches of 330 and 250 nm, respectively. The cropped plots on the right of (a,b) are the nonmagnetic channels recorded by the sum channel signal which are used to determine the SAW frequencies. The results of fitting Eqs. (6.1.1) and (6.1.2) are shown in (c) for the Ni sample and (d) for the Co sample. For (c), the double resonance in the spectra is caused by the pronounced edge mode being strongly excited in addition to the center mode. In (e) the effective damping of both arrays was determined via Eq. (6.1.3) and plotted for 3 resonances, while the lines correspond to the well-known intrinsic Gilbert damping of Ni (solid) and Co (dashed). Taken from ref. [102]. 168

Fig. 6.2. To verify that the pinning width (and αeff) are independent of the strength of the magneto-elastic effect, the field-dependent response was modeled for B_i spanning four orders of magnitude, the result shown in (a) verifies that this method is independent of the magneto-elastic coefficient. In (b), the damping specified in the simulation was varied to test the validity of Eq. (6.1.3) and yielded a direct measurement of the input in each case. Taken from ref. [102]. 170

Fig. 6.3. (a) SEM image of the two-material array, the dashes show the dimensions of the pump (blue) and probe (red) beams used in this study. In (b) the field-dependent Fourier spectra of the magnetic and nonmagnetic spectra show the well-defined SAWs frequencies determined by Eq. (5.1.1), and just as before the magnetic signal is enhanced when the spin-wave frequency is in the vicinity of f_{SAW}. The magnetic spectra in the 16.2 GHz bin from (b) is fitted in (c) using the Lorentzian-like functions defined in sec. 6.1 using a singular damping parameter for both functions to improve the accuracy. This procedure was carried out for each of the crossover points which is summarized in (d) alongside the effective damping measured on an unpatterned film with conventional TR-MOKE, as well as the damping estimated from a purely Ni array with identical dimensions. 173

Fig. 6.4. SEM image of (a) a single nanomagnet placed between identical sets of Al bars which are used to generate the SAWs, and (b) a zoomed in version of (a). In (c), the optical geometry of the experiment is illustrated.....175

Fig. 6.5. TR-MOKE time traces of the optically (OPT) excited (a) Ni film and (b) isolated nanomagnet (NM), and (c), (d) the corresponding field-dependent Fourier spectra of the film and NM, respectively, measured with a fixed field angle θH = 30°. (e) TR-MOKE trace of the MEL driven nanomagnet (H_{app} = 3.7 kOe), and (f) nonmagnetic signal of the acoustically modulated nanostructure. The illustrations in panels (a), (b) and (e), (f) indicate the pump-probe configurations used and the applied field geometry, respectively. The field-dependent Fourier spectra of the acoustically driven NM shown in (g) reveals strong MEL enhancement when the magnetic and nonmagnetic modes are degenerate. SAWs are identified by monitoring the transient reflectivity, shown in (h), and therefore do not depend on the applied field. Taken from ref. [101].....177

Fig. 6.6. Field dependence of the normalized complex Fourier spectra (imaginary Fourier component – circles, real Fourier component – squares) of the MEL driven dynamics at (a)-(d) four distinct SAW frequencies, and (e)-(h) four distinct applied field geometries using a single sample (pitch = 400 nm). (i) Pinning width determined by fitting both the real and imaginary Fourier spectra from Figs. 4(a-d) plotted against f_{SAW} including the fit to Eq. (3) (red dashed line) used to estimate the damping, and (j) summary of ΔH_p from Figs. 4(a),(e)-(h) plotted against θ_H. The data exhibits no significant variation of the pinning width as a function of the applied field angle, which supports the interpretation that the relationship between α and ΔH_p for the nanomagnet is not complicated by extrinsic mechanisms. Taken from ref. [101]. 179

Fig. 6.7. Field dependence of the effective damping of the Ni film and single nanomagnet (NM) measured using conventional TR-MOKE (closed black circles and open pink squares, respectively). For comparison, the damping measured using the MEL approach is included (blue triangles). The effective damping of the film was fit using Eq. (2.x.x) to estimate the intrinsic damping (0.03) (red line), and the dashed red line is a guide to the eye indicating the intrinsic α. Taken from ref [101]. 180

Fig. 7.1. (a) The displacement ($u_z(t)$) at each node in the *xz* plane at the center of the nanomagnet 2 ns after the pump triggers the SAWs; (inset) mesh of the simulated elastic response of a 200x30 nm Ni nanocylinder deformed by SAWs (enhanced by a factor of 1000 for visualization). In (b), the lock-in reflectivity signal and corresponding DFT of a D = 200 nm between Al bars (p = 400 nm) shows a realistic SAW, and in (c) the simulated response exhibits qualitatively similar behavior. 187

Fig. 7.2. (a) SEM image of the easy-axis ellipse embedded between the Al bars where the dashed line illustrates the FWHM of the probe beam, (b) the TR-MOKE spectra of the SAW driven dynamics, and (c) the time evolution of the Kerr signal on resonance (H_{res} = 2.8 kOe). The same data for the hard-axis ellipse is shown in (d-f), where the resonance in for this sample occurs at H_{res} ~ 3.2 kOe due to the shape anisotropy. The dashed lines in the colormaps (b,e) show the spin wave characteristics of each device measured using conventional TR-MOKE which relies on ultrafast demagnetization to excite the magnetic precession. Taken from [105]. 188

Fig. 7.3. (a) SEM image of the two adjacent, orthogonal ellipses embedded in the bars with the the probe profile (dashed line) overlaid just as before, and (b) the field-dependent spectra of the ensemble response showing that the resonance of both devices can be detected simultaneously. Taken from [105]. 190

Fig. 7.4. (a,b) Field-dependent spectra of the magneto-elastic simulations of the easy- and hard-axis ellipses, respectively, and in (c,d) the corresponding linewidth analyses of the simulated resonances show enhanced damping for both samples. In (e,f), the experimental linewidths of the data shown in Fig. 7.2 show nearly identical behavior as the simulations. Taken from [105]. 191

Fig. 7.5. (a,b) Fourier amplitude of the ensemble resonance frequency component (7.8 GHz) for the hard- (H_{app} = 3.2 kOe) and easy-axis (H_{app} = 2.8 kOe) samples, respectively, excited by a small field-like pulse. The same data is plotted in (c,d) for MEL excited nanomagnets where the mode is now at the center of the sample where H_{MEL} is largest. Taken from ref. [105]...194

Fig. 7.6. (a) SEM image of the 200 to 700 nm nanomagnets embedded in the Al wire grid. In (b,c) the dynamic Kerr signals of the D = 200 (H_{res} = 3.1 kOe) and D = 700 nm (H_{res} ~ 2.6 kOe) samples shows the large difference in the precession amplitudes as well as the opposite scaling behavior of $\Delta\theta k$ with λSAW. Similar measurements were performed for each sample and the amplitudes are summarized in (d) for the three wavelengths. The dashed lines are exponential fits to the data using the following function $\Delta\theta K \propto Aexp - DB + C$ for the samples that satisfy ($D < 1.5\ \lambda SAW$). 196

Fig. 7.7. (a) The field-dependent TR-MOKE spectra of the D = 600 nm, p = 412 nm sample, and (b) the corresponding Fourier components used to analyze the damping behavior. The damping for diameters ranging between 150 to 730 nm are summarized in (c), which reveals a critical point near $D = \lambda SAW$ where the damping jumps substantially. Finally, in (d) the effective damping of a D = 200 nm sample driven by various SAWs is (within error) the exact same for all three measurements. 198

Fig. 7.8. (a) The maximum precession amplitudes of m_z taken from micromagnetic calculations of SAW driven ($\lambda SAW = 400\ nm$) spin dynamics for various nanomagnet diameters reveal an exponential increase with decreasing D, just as was experimentally observed. In (b), the time evolution of m_z is shown for the D = 200 and 500 nm nanomagnets, respectively, to show the distinct behavior of each sample at H_{res}. In (c) and (d), the difference between f_{SAW} and the local resonance frequency (f_{res}) of each cell in the simulation is plotted as a histogram to show that the resonance frequencies in the small sample are more tightly distributed; inset: spatial distributions of $fres - fSAW$ for each sample which show that the magnetic resonance deviates most near the nodes of the standing wave which is shown by the illustration of the fundamental acoustic mode (u_z) above the mode profiles.....199

Fig. 8.1. (a) MOKE-microscope image of the GdFeCo sample after it has been demagnetized by an oscillating magnetic field where the light and dark portions of the image correspond to positive and negative magnetic moments, respectively. In (b), the sample has been illuminated

by a right-hand ($\sigma +$) pulse (top) which switches the region that had previously had a negative magnetic moment to positive while the pulse has no effect on the region that was already positively magnetized. At the bottom of the image, $\sigma -$ pulse was used and shows that the opposite is true in this case. Between the two opposite helicity CP pulses, the authors used a linearly polarized pulse which resulted in random magnetic domains with no net magnetization. Taken from ref. [108].....204

Fig. 8.2. MOKE images of the GdFeCo surface after being subjected to approximately 20 laser fluences using both LHCP and RHCP. The profiles on the right show the intensity of the pulses used to write the spots. The sample was saturated to the M^+ direction before each measurement. Taken from ref. [108].....205

Fig. 8.3. (a) The HD-AOS beam path used to test the FeTb films, and (b) the MOKE imaging path to detect the micron-scale changes in the magnetization. In (c), MOKE image of the FeTb sample surface after AOS beams with opposite helicities and various fluences were scanned across the sample surface. The size of the written domains are directly proportional to the fluence. In the regions surrounding the HD-AOS lines, the sample is demagnetized and forms randomly oriented domains that reduce the magnetostatic energy. 210

Fig. 8.4. (a) Modified AOS setup that splits the pulse into two beams that have a variable time delay that corresponds to the time required for the SAW to travel from the bars to the AOS pulse. (b) Photograph of the completed HD-AOS setup in the Sinsheimer 111c microscopy lab. 212

Fig. 8.5. Wide-field MOKE image of the FeTb film near the FIB-milled regions (dark squares). On the perimeter of the image the virgin film is demagnetized and has a large coercivity (~ 2 T) and is compatible with HD-AOS. In stark contrast, the area surrounding the bars are single domain and can be switched by an external field on the order of 1 kOe. When the ultrafast beam is scanned across the area irradiated by Ga^+ ions, a helicity-independent domain is written that can only be reversed by an external field. From left to right, two domains were written side-by-side using two beams with opposite helicities, however, once they enter the perturbed region there is no difference in the domain written by each beam.....215

Fig. 8.6. Wide-field MOKE images of the FeTb film surface when illuminated by the AOS beam (top), the SAW beam (middle), and both beams which are separated by a 1.5 ns time delay. On the left-hand side of the figure the larger beam completely encompasses the smaller one, whereas on the right-hand side the domains are completely separated only one beam is on. Note that even though the domains are separated when one beam is on, they overlap when both strike the sample, which is shown in the bottom panel. Here, the domain written by the AOS beam is nearly twice as large despite having the same fluence and spot size. In addition, the domain on the left-hand side of the time-delayed beam in both cases is demagnetized, as opposed to uniformly magnetized.....216

Fig. 8.7. SEM image of circular Al bars deposited on the FeTb film to focus the strain wave at an optimum distance from the SAW pump beam. 218

List of Abbreviations and Acronyms

3TM: 3-Temperature Model

ARC: Anti-Reflection Coating

ARPES: Angle-Resolved Photoemission Spectroscopy

BPM: Bit Patterned Media

CE: Cavity Enhancement

CIDWM: Current-Induced Domain Wall Motion

CP: Circularly Polarized

DFT: Discrete Fourier Transform

DMI: Dzyaloshinskii-Moriya Interaction

DMTJ: Dual Magnetic Tunnel Junction

FDM: Finite-Difference Method

FEM: Finite-Element Method

FFT: Fast Fourier Transform

FMR: Ferromagnetic Resonance

GMR: Giant Magnetoresistance

HAMR: Heat-Assisted Magnetic Recording

HD-AOS: Helicity-Dependent All-Optical Switching

HDD: Hard-Disk Drive

IDC: International Data Corporation

IDT: Interdigitated Transducer

IHB: Inhomogeneous Broadening

LLG: Landau-Lifshitz Gilbert (equation)

MEL: Magneto-Elastic

MTJ: Magnetic Tunnel Junction

OOMMF: Object-Oriented Micromagnetic Framework

OPL: Optical Path Length

PBC: Periodic Boundary Conditions

PMA: Perpendicular Magnetic Anisotropy

QWP: Quarter Wave Plate

RIE: Reactive Ion Etching

SAW: Surface Acoustic Wave

SHE: Spin Hall Effect

SHG: Second Harmonic Generator

SNR: Signal to Noise Ratio

STNO: Spin-Torque Nano-Oscillator

STT-MRAM: Spin Transfer-Torque Magnetic-Random Access Memory

TMR: Tunneling Magnetoresistance

TR-MOKE: Time-Resolved Magneto-Optic Kerr Effect

VNA: Vector Network Analyzer

XRD: X-Ray Diffraction

XRR: X-Ray Reflectivity

Abstract

Ultrafast Spin Dynamics of Next-Generation Nanomagnetic Technologies

Mike Jaris

Over the past 50 years, our society has experienced a technological revolution that has fundamentally changed the way our world operates. At the heart of this revolution are the computational building blocks that work together to perform mathematical operations and save the results. For many years, the size of the computing elements (e.g. transistors) has been consistently shrunk so that more devices could fit on a chip in order to increase computational power. To provide adequate data storage for the ever-increasing number of computations, the hard-disk drive (HDD) was developed in the 1980s and would forever revolutionize the landscape of memory storage. Today, HDDs still account for a vast majority of the data stored worldwide. These devices store information using the magnetization of nanoscopic domains in a granular magnetic film, however, in recent years it has become increasingly challenging to reduce the size of the domains further without fundamentally changing the HDD. Indeed, the latest iteration of this technology has incorporated lasers into the devices to leverage multiple degrees of freedom in order to achieve higher bit densities. This example highlights a common trend for all next-generation computational technologies – the strong coupling between distinct physical systems must be utilized to sustain the improvements our society has become accustomed to. In order to realize this lofty goal, the physics of nanoscale systems must be well understood to predict their behavior. As our collective understanding of this field

continues to flourish, novel effects are found that open doors to previously unimaginable technologies that may usher in a revolution of their own. Indeed, there are both technological and fundamental interests to study nanostructured devices.

In this thesis, the time-resolved magneto-optic Kerr effect (TR-MOKE) will be utilized to probe the ultrafast spin dynamics of magnetic films, multilayer heterostructures, and nanostructures. Our experimental observations of these systems are evaluated by combining various field of science and technology, including (but not limited to) condensed matter theory, signal processing, and optics. In doing so, we seek to fully explain the data and to enrich the understanding of these underexplored systems to inform the rational design of next-generation technologies. Specifically, a great deal of attention will be paid to emergent nanotechnologies that leverage the coupling between the magnetic system and either the electronic or mechanical properties of the device to tailor the performance. In this work, a novel method to restore the intrinsic magnetization dynamics and simultaneously improve the magneto-optical response of dense nanomagnet arrays will be presented. Then, our work on the spin dynamics of isolated nanomagnets resonantly excited by microwave-frequency acoustic waves will be reviewed, wherein we show for the first time that the coupling efficiency is ultimately limited by the damping of the magnetic system. In addition, the role of the nanomagnet geometry and the acoustic wavelength will be fully explored to determine critical parameters that govern the dynamic magneto-elastic resonance. Lastly, the development of an optical system to study the

interplay between ultrafast all-optical switching and surface acoustic waves will be reviewed.

Acknowledgements

Rarely in your academic career are you provided an opportunity to speak candidly, but here I am, and I plan to take full advantage of it! When I arrived in Santa Cruz in 2013, I was 22 years old and knew absolutely everything about physics and electrical engineering – I reckoned I could knock out a PhD in about 4 years, no problem.

Enter Professor Holger Schmidt, who quickly let me know that I did not know everything (I'm cringing as I write this remembering my first research presentation when I argued with him about semiconductor physics) – suffice it to say, I came to UCSC with a lot of room for growth. Holger, I can never thank you enough for the time and energy that you put into my development, and for the outstanding amount of patience that you had to have to deal with me at times. I have learned so much from you, both as a person and as a scientist, that I will carry with me the rest of my life.

Of course, a lot of other people in this group have helped me out over the years. First and foremost, thank you to the brilliant, selfless Dr. Yu Yahagi, who spent countless hours with me in the lab, often at the expense of his own progress. I learned so much from you about coding, signal processing, optics, electronics – the list goes on and on. You were always a wealth of information and never hesitated to help, I am forever in your debt and am blessed to have worked under you. To Dr. Cassidy 'Big Cass' 'Derk' Berk, my man, my magnetic brother in arms, my fellow crazed scientist who loved shooting lasers at magnets and running around in the

redwoods as much as I do. You're an amazing friend, physicist, guitarist, and, in general, a pretty damn cool dude, thank you for always being there.

To the other members who were in the trenches with me most of the time: Dr. Black, Dr. Parks, Dr. Rahman, Anik 'B-Sug' Duttaroy, and Gopikrishnan 'The Gopinator' Gopalakrishnan Meena, we all experienced the highs and lows (many, many lows) of graduate school together and managed to help keep each other sane. Thank you all for being terrific friends and co-workers over the years, I miss you all dearly and hope we never lose touch. To Dr. Tom Yuzvinsky, thank you for the numerous things you have helped me with over the past 6 years, from propane regulators to teaching me about thin film deposition to sharing insanely obscure trivia that only you would know, you're one of the brightest people I have ever met and it has been an absolute honor to know you. To the rest of the applied optics group members, both new and old, I could go on and on, but I'll never forget you all and am glad to have known each and every one of you. Last, but not least, a very special thanks to Lexa Stambaugh for the love and support she has shown me over the years. Your day is coming soon, just hang in there.

CHAPTER 1
Introduction

1.1 Magnetic Recording

1.1.1 State-of-the-Art Hard-Disk Drives

This year, magnetic data storage accounted for more than 75% of storage shipped worldwide, and the International Data Corporation (IDC) has projected it will to continue to make up over half the market past the year 2025. This may be surprising given the ubiquity of solid-state storage devices (SSDs) in personal computers, but for large-scale, long-term data storage, SSDs cannot match the efficiency and retentivity that hard-disk drives (HDDs) provide. The IDC's prediction assumes that the storage capacity of HDDs will continue to double every two years, which is an increasingly challenging endeavor because each bit is a nanoscale magnetic domain that can be randomly flipped by thermal energy with greater likelihood as the domain dimensions shrink. The stability of each domain is determined by the average amount of time between random thermal flips of the magnetization, known as the Neel relaxation time (τ_N), which is determined by the Neel-Arrhenius rate equation as follows [1]

$$\tau_N = \tau_0 e^{\frac{K_u V}{k_B T}} \tag{1.1.1}$$

Here, $\tau_0$is the attempt lifetime of the material (~1 ns), K_U is the magnetic anisotropy, V is the bit volume, and $k_B T$ is the thermal energy, where k_B is Boltzmann's constant and T is the temperature. According to this relationship, reducing V exponentially

decreases the Neel relaxation time, thus, highly anisotropic magnetic materials (higher K_U) are necessary to keep τ_N large. However, a larger magnetic anisotropy also means a stronger external field is required to flip the magnetization. Nonetheless, modern HDDs use materials with very large magnetic anisotropy, hence, the inductive coil near the surface can no longer reorient the domains using an electromagnetic field alone. Instead, a method known as heat-assisted magnetic recording (HAMR) is used to write smaller domains by incorporating a near-field laser onto the induction coil. The laser heats a nanometer size region of the magnetic material to partially demagnetize the area, thereby making the region more susceptible to the external magnetic field. While the commercial implementation of this technology is in its infancy and still has a lot of room to grow, the magnetic community is already searching for new ways to reduce sizes even further in next-generation devices.

The situation described above underscores a more general trend in modern computer technology – conventional methods of downscaling have reached fundamental limitations, and new solutions (e.g. HAMR, Fig. 1.1) are necessary to sustain the computational growth we have become accustomed to. Indeed, as computational building blocks such as transistors and magnetic storage rapidly approach atomic length scales, the interplay between various degrees of freedom (e.g. thermal, mechanical, magnetic, etc.) must be well-understood to facilitate further miniaturization. As our understanding of nanoscale systems continues to flourish, we find that the coupling between physical processes can be used to enhance the operation characteristics of devices.

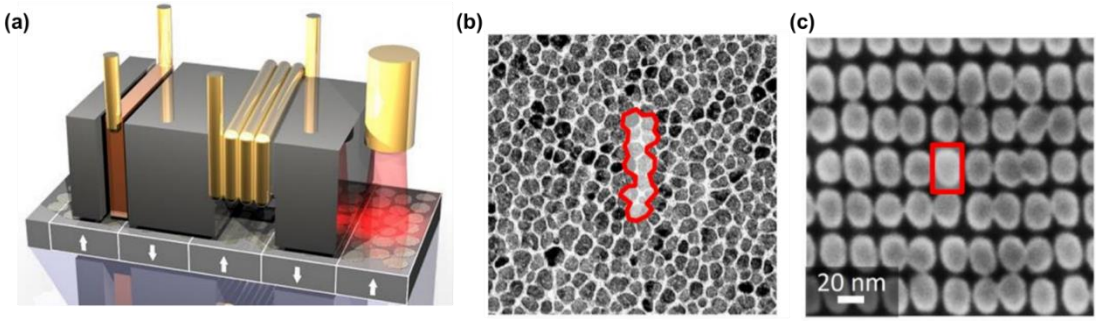

Fig. 1.1. (a) Illustration of a HAMR HDD device with the near-field laser device attached to the read/write head. Currently, this technology stores information in a magnetic domain that encompasses multiple grains, as shown by the red outline in (b) the SEM image of a granular magnetic film. For comparison, in (c) an SEM image of a nanopatterned surface shows that in this case each bit corresponds to a nanocylinder. Taken from **[2]**.

1.1.2 Nanomagnetic Devices

For many years, bit patterned media (BPM) has been identified as the leading candidate to supplant HAMR. In BPM, each bit is a lithographically defined magnetic nanostructure arranged in a periodic array (Fig. 1.1 (c)). One advantage of laterally confining the magnetic material is the emergence of an effect known as magnetic shape anisotropy, which can be utilized to increase K_U in Eq. (1.1.1) via the device geometry. Nanopatterning of the surface also leads to changes in the thermal, mechanical and electronic properties of the devices that can be exploited to further improve performance. For example, it is highly anticipated that BPM will work well with HAMR, because the heat in the nanomagnet cannot diffuse laterally, in stark contrast with the granular media currently used in HDDs, which means less optical power will be required to demagnetize the bit as well as a smaller chance of unintentionally switching a nearby device. Moreover, the confinement also leads to discretization of

the electron and phonon systems that can be used to further optimize the efficiency of the laser heating.

1.1.3 Potential Role of All-Optical Switching

Because BPM is already on the precipice of widespread commercial implementation, it is already time to look ahead at the *next* generation of magnetic storage technologies. Indeed, one notable approach that was recently discovered, known as helicity-dependent all-optical switching (HD-AOS), utilizes circularly polarized pulses of light to directly control the magnetization. As we have just seen in the preceding sections, commercially available HDD systems have already integrated lasers into the system, thus, it is not hard to imagine that HD-AOS may be readily implemented to further improve the operating characteristics. In addition, the details regarding the microscopic processes that underpin HD-AOS are still the subject of intense debate, hence, there is widespread optimism that this technique will enrich our understanding of magnetic systems to better inform the rational design of devices.

1.2 Spintronic Devices

1.2.1 Spin Transfer-Torque Magnetic-Random Access Memory

Magnetic nanostructures have also received a lot of interest for their potential role in a variety of applications, including next-generation logic devices [3], ultra-tunable microwave generation and detection [2], and magnetic biosensing [4]. For each of these applications, the connection between the sample geometry and magnetization is utilized to improve the operation characteristics of the device. Take, for instance,

spin transfer-torque magnetic random-access memory (STT-MRAM), which is a novel memory technology that utilizes electron tunneling in two-terminal structures to control the magnetic state of a ferromagnetic layer via an applied potential bias (Fig. 1.2). Unlike HDDs which read and write data by scanning the inductive coil

across the magnetic surface, STT-MRAM devices can be directly addressed via an electrical bias and, therefore, do not need any moving parts and have much faster response times. Additionally, since the energy required to switch the magnetization in these devices is directly related to the current density, exponentially less power is required to flip the magnetic moment as the dimensions of the nanostructure are scaled down.

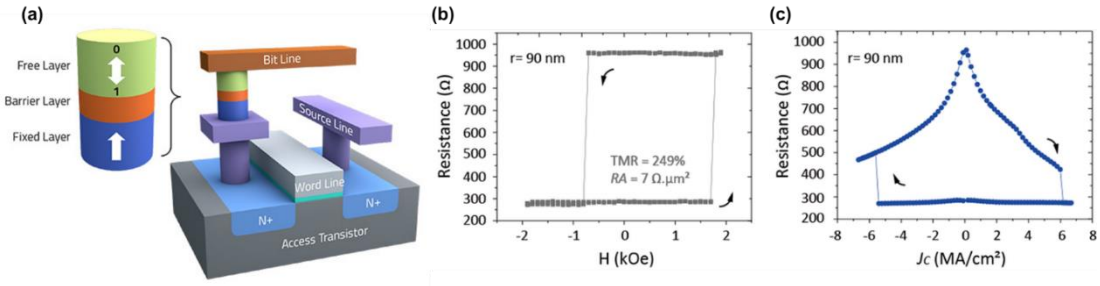

Fig. 1.2. (a) Illustration of a full STT-MRAM cell, which includes an access transistor that is used to address the device. In (b,c), the resistance of the device is plotted as both a function of (b) an externally applied magnetic field and (c) the electrical current density through the device in the absence of an external magnetic field. Taken from **[5]**.

At the heart of an STT-MRAM device is the *magnetic tunneling junction* (MTJ), which denotes a pair of ultrathin ferromagnetic layers (~1-2 nm) separated by an equally thin insulating barrier. As current passes through the device, one of the layers (fixed layer) polarizes the spins along the direction of its magnetization. Because

the layers are separated by an insulating layer the electrons must tunnel from one layer to the other, and the probability of the event is directly determined by the number of available states on the other side of the barrier. Therefore, the conductivity of the device depends on the configuration of the two ferromagnetic layers – when they are parallel there are more states for spin-polarized electrons which in turn leads to higher conductivity than when the layers are antiparallel. When the device is electrically biased and in an antiparallel state, however, each electron exerts a torque on the magnetization of the second layer. If the current density reaches a critical threshold (J_{c0}) then the torque provided by the electrons will be enough to switch the magnetization of the second layer. One interesting property of STT-MRAM is the fact that J_{C0} can be directly related to a dynamic magnetic parameter known as the *Gilbert damping* (α). While a great deal of this thesis is dedicated to the origins and estimation of α in real devices, here, it is important to note the direct connection between the magnetic system and the operation characteristics.

Despite the favorable scaling properties and operation characteristics of STT-MRAM, the technology has struggled to overtake the incumbent technology, dynamic-random access memory (DRAM), over the past decade. In DRAM, a binary bit is stored via the charge in a nanocapacitor whose performance depends on the device size and permittivity (ϵ_r) of the material. Even though downscaling requires materials with larger ϵ_r, DRAM has continued to improve performance each year which has held off competing technologies such as STT-MRAM. In addition, after more than a decade of research and development, STT-MRAM has not been able to increase the areal bit

density in commercial chips to compete with the capacity offered by DRAM. This may seem odd at first, because MTJ devices with diameters around 10 nm have been available for over 5 years [6]. However, the limiting factor is not the cell size of the device, but the top-down fabrication (ion beam etching) that is required to create commercial-grade MTJs. When the nanomagnet arrays are too dense, the precision of the etching process suffers immensely due to shadowing effects, which in turn leads to a large spread in the performance characteristics of devices that is not tenable for commercial-grade chips. Although a method like reactive ion etching (RIE) may seem like a viable alternative, the heterogenous composition of STT-MRAM results in corrosion or delamination that prohibits the use of RIE. Recently, MTJs grown on pre-patterned conductive pillars have been demonstrated [7], which may open the door for dense STT-MRAM arrays, however, this work is still in its early stages and must be studied further to determine its plausibility.

Instead, STT-MRAM has been identified for its potential as an embedded memory device (eMRAM) to fill in the latency gaps between various memory types (SRAM, DRAM, SSDs) [8]. While eMRAM cannot compete with the speed of SRAM and DRAM, these technologies store information in a volatile manner that results in far greater power consumption. Moreover, eMRAM offers much larger areal bit densities (10-100 Gb/in^2) than SRAM which lessens the performance gap between these technologies despite the large difference in write times. Indeed, eMRAM is now found in commercially available products and is expected to become more common as further improvements are made.

1.2.2 Spin-Torque Nano-Oscillators

The MTJ is also a fundamental building block for a family of devices known as spin-torque nano-oscillators (STNOs), which are tunable microwave devices that utilize the spin transfer-torque to drive self-sustained magnetization precessions (Fig. 1.3). These devices are being extensively studied for their potential role in applications such as signal generation and modulation (e.g. telecommunications) [9], spin wave generation [10], and neuromorphic computing [11].

Although the stack structures of STNOs are very similar to STT-MRAM, these devices operate very differently and, therefore, face unique challenges. In STT-MRAM, a direct electrical bias can be applied for a small window of time to switch the magnetization without damaging the structure. However, if STNO devices are excited into an auto-oscillatory state using spin-polarized current injected into the free layer, large currents must be used to generate sizeable signals which in turn leads to dielectric breakdown of the tunneling barrier. Instead, STNOs have begun to utilize the *spin Hall effect* (SHE) in a nearby nonmagnetic metal layer (W, Ta, Pt) to generate pure spin currents that directly counteract the damping of the magnetic precession. Because the SHE is generated in a pure metal, electromigration in the nonmagnetic layer is the limiting factor that determines the damage threshold of the device, as opposed to dielectric breakdown of the MTJ. In Fig. 1.3, a STNO device that utilizes both STT and the SHE to sustain auto-oscillations is shown along with the electrical characteristics of the device. In (d,e), the frequency and corresponding output power are plotted as a function of the driving current to demonstrate the potential of these devices. As STNOs

continue to make rapid progress, it is expected that they will soon begin to see commercial implementation.

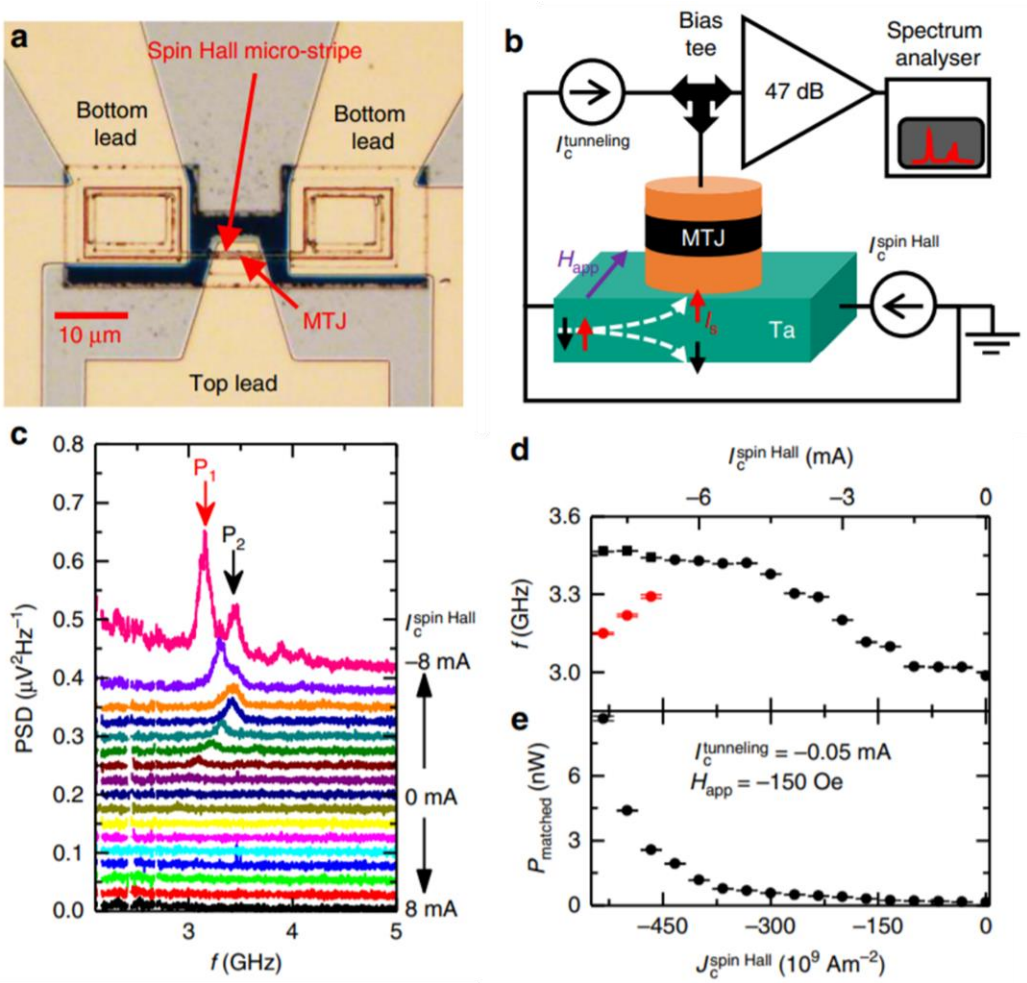

Fig. 1.3. (a) Top-down microscope image of the surface of a 3-terminal STNO utilizing the SHE to excite the STNO into an auto-oscillatory state, and in (b) a schematic illustration of the circuit. (c) The spectral response of the device is shown for various currents, which shows that the strength of the oscillation increases with the SHE current. Lastly, in (d) the spectra from (c) are used to plot the frequency response of the device which shows the dynamic range of the STNO, and in (e) the corresponding output power is plotted. Taken from **[12]**.

1.2.3 Neuromorphic Computing

As was alluded to earlier, MTJs have also been identified as potential candidates for neuromorphic computing applications, which aim to emulate the neuro-biological architectures present in nervous systems to carry out algorithms that are not well-suited for digital computation (e.g. reservoir computing, machine learning, etc.). Neuromorphic computing elements exhibit either analog or nonlinear responses, as opposed to digital devices. By taking advantage of the uniqueness of the response, these systems can perform tasks that are exceedingly complex for classical systems using a small number of devices.

One noteworthy example of neuromorphic computing using a spintronic device was reported by Torrejon et al. in 2017 [11], where the authors used a single MTJ as an oscillator to serve as a reservoir computing device. They showed that using the auto-oscillations of the device, speech recognition could be carried out with over 99.5% accuracy – which was a 15-fold improvement over the control that did not utilize the auto-oscillations of the MTJ. Of course, it is also worth mentioning that their experiment still required a conventional computer to perform a variety of tasks during the training and analysis, as well as a wave form generator and other sensitive electronic equipment to measure the response of the device. Thus, the realization of this technology still has a long way to go, nonetheless, this work demonstrates the potential of spintronic structures for neuromorphic applications.

1.3 Magneto-Elastic Devices

Up to this point, we have seen that techniques which utilize the coupling between various degrees of freedom such as STT, HAMR, and HD-AOS are of significant interest for emergent nanomagnetic technologies. An underexplored approach at the nanoscale is to utilize the strong coupling between the mechanical and magnetic systems, which stems from the fact that the magnetization of a device is linked to the elastic profile of the material via spin-orbit coupling of the electrons. When a demagnetized sample is magnetized by an external field it changes length as a result of this coupling, which is known as *magnetostriction*. Similarly, when a mechanical force is applied to the material, an elastic strain (ϵ) is generated which in turn gives rise to a field inside the sample. This process is known as *inverse magneostriction*, as well as the *Villari* or *magneto-elastic* effect (MEL). In one dimension, the elastic strain is simply defined as

$$\epsilon = \frac{\Delta L}{L} \tag{1.3.1}$$

where ΔL is the change in the length, or displacement, due to the force, and L is the length of the sample. Because the size is in the denominator of the equation, nanostructures can experience very large strains when displaced by small amounts.

In addition to the fact that large strains are accessible at the nanoscale, there are other favorable aspects of MEL nanotechnologies. For instance, one of the primary sources of magnetic anisotropy, magneto-crystalline anisotropy, is a direct result of

strong spin-orbit coupling between the spins of the electrons and the atomic nuclei. Similarly, the magnitude of the magneto-elastic field generated in response to an elastic deformation is also determined by the strength of the spin-orbit coupling. Thus, magneto-elastic approaches are well-suited for the highly anisotropic magnetic materials that are being used in next-generation devices. Indeed, this is the one of the reasons that MEL effects, which were first discovered over a century ago, have received renewed interest in recent years as nanomagnetic technologies become more prevalent.

1.3.1 SAW-Assisted Switching

One exciting method of magneto-elastically controlling nanomagnetic structures uses *surface acoustic waves* (SAWs) to dynamically modulate the elastic profile of the device. For decades, SAWs have been extensively studied and used in a number of diverse applications ranging from bio-sensing [13] to telecommunications [14]. A favorable aspect of SAWs is the fact that they can be generated with very low losses, which makes them attractive for low-power applications. In addition, the frequency of the acoustic waves is inversely proportional to the wavelength, just like light, and lies in the GHz range for SAWs with micrometer wavelengths. Because the spin dynamics in nanostructures tend to naturally oscillate at GHz frequencies as well, a dynamic resonance between the acoustic and magnetic degrees of freedom occurs that is highly attractive for some next-generation technologies.

Recently, several groups have shown that SAWs can be used to switch the magnetization of unpatterned magnetic films as well as nanomagnets. For example,

Sampath et al. [15] studied the behavior of elliptical Co nanomagnets (340x270x12 nm^3) excited by SAWs, which have two distinct, stable magnetic configurations (Fig. 1.4). In these devices the ground state of the magnetization is a uniform spin texture, with all the uncompensated spins in the sample aligned in a single direction. The next-lowest energy state is known as a vortex state, where the magnetization breaks into multiple magnetic domains that minimize their magnetostatic energy by aliging the north and south poles of each domain to form a vortex. By setting the nanomagnets into their ground state and then subjecting them to intense SAWs via interdigitated transducers on a piezoelectric substrate, they showed that the dynamic strain caused the devices to transition to the vortex-state in a highly reproducible manner. Using micromagnetic simulations, the authors went on to show that the experimentally observed behavior matched remarkably well with calculations.

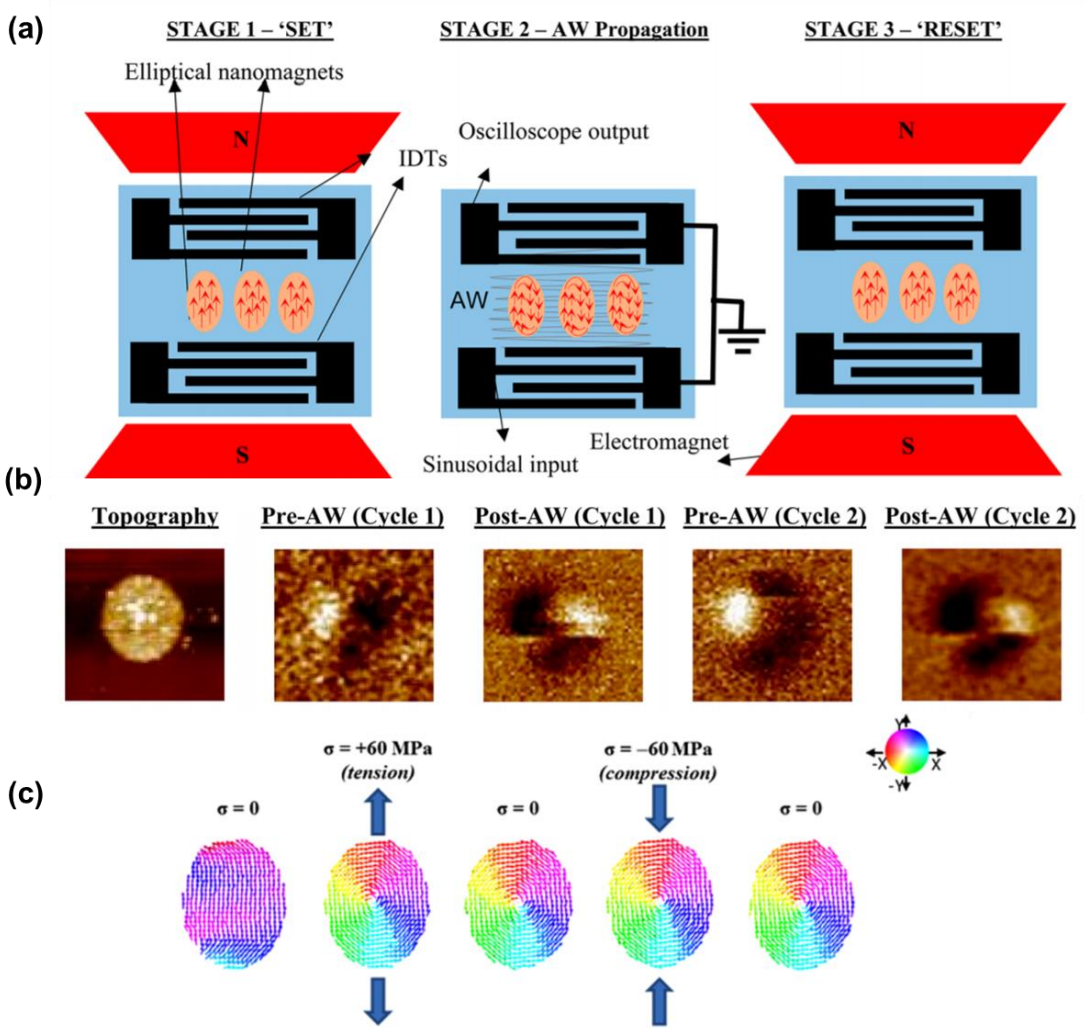

Fig. 1.4. (a) Illustration of the sample layout, where the nanomagnets are placed between a pair of interdigitated transducers (IDTs) on a piezoelectric substrate, and (b), the magnetic state of the nanomagnets after being subjected to SAWs, studied using magnetic-force microscopy (MFM), which shows the uniform state (pre-AW) and the vortex state (post-AW). In (c), the results of the micromagnetic calculation show excellent agreement between theory and experiment and reproduces the transition to the vortex state after being subjected to an elastic force. Taken from **[15]**.

They also estimated that the energy dissipation of the mechanically driven magnetization reversal was on the order of aJ (10^{-18} J), which is orders of magnitude better than competing ultralow-power storage technologies. However, it is worth noting that this analysis does not consider the energy used to generate the acoustic waves,

which is certainly much larger than aJs. In addition, in this study the devices could not be returned to their original state using the acoustic wave alone, and, therefore, relied on an external field to reset the structure. Nonetheless, this work demonstrates the potential for highly efficient magneto-elastic storage technologies. In addition to the example above, SAWs could also be used to reduce the critical current threshold for switching in STT-MRAM devices. The current threshold is defined as the amount of current required to perturb the magnetic moment of the device from equilibrium via spin transfer-torque because most of the energy is used to overcome the inertia of the system. Instead of relying solely on STT, however, a SAW could synchronously perturb the system from equilibrium, which would in turn reduce the amount of current required to switch the device. Previously, groups have used a constant (static) mechanical strain to achieve lower switching currents in MTJs [16, 17], but to the best of our knowledge, no group has reported the use of SAWs for this purpose yet.

1.3.2 SAW-Assisted Nano-Oscillators

In the previous section the dynamic coupling between the strain and magnetization that occurs when the systems are on resonance was neglected. It is well-known that resonantly coupled systems can exchange energy more effectively, which could be utilized to further optimize magneto-elastic approaches. As we have just seen in section 1.2, tunable nanoscale microwave oscillators (STNOs) are in high demand for a variety of applications. To this end, it has been proposed that the dynamic coupling between SAWs and magnetic oscillations could be utilized to further improve the performance of these devices.

Although SAWs are typically generated using a pair of IDTs on a piezoelectric substrate, they naturally occur whenever micro- or nanostructures are arranged periodically on a smooth surface. Indeed, Yahagi et al. showed that the naturally occurring SAWs in dense nanomagnet arrays strongly couple to the magnetization dynamics when the systems are on resonance resulting in a large enhancement of the precession amplitude [18]. Now, recall that the output power of the microwave signal generated by STNOs is limited by the dielectric breakdown of the tunneling barrier in the MTJ (STT) and electromigration in the SHE layer. Hence, in these systems the amplitude of the magnetic precession cannot be increased any further by supplying more current. Instead, the microwave signal amplitude can be enhanced by summing the individual response of a densely packed array of nominally identical STNOs. If we assume that the spread in the mechanical and magnetic parameters of the devices is small, then the ensemble signal will grow linearly with the number of devices. However, since SAWs are already present in this case due to the array geometry, they could serve as an additional source of energy to increase the amplitude of the magnetic oscillations which in turn would lead to a nonlinear increase in output power with respect to the number of devices! Because this approach utilizes mechanical modes that are intrinsic to the system, it does not require any additional fabrication steps and is, therefore, a highly attractive method to improve the operation characteristics of STNO arrays. Moreover, the hybridization of the mechanical and magnetic systems could be utilized as an additional means to control the spin wave dispersion, which may lead to novel device functionalities.

In some cases, the inevitable spread in magnetic parameters between nanomagnets precludes the use of STNO arrays to achieve larger signal amplitudes. Nonetheless, SAWs can still be utilized to improve the operation characteristics. Instead of relying on an array to support SAWs, IDTs can be fabricated alongside the STNO and synchronized with the device using a phase-locked loop. Although this approach does require some additional fabrication steps, unlike the previous example, the constraints on the geometry of the IDT structures are far more lenient than for a MTJ device; thus, it is unlikely that the lithography of the acoustic system will be prohibitively challenging.

1.4 Outline of Chapters

To realize the exciting nanotechnologies presented in this chapter, the physical properties of magnetic nanostructures must be well-understood because they directly determine the operation characteristics of devices. However, because the total magnetic moment of a device is proportional to the volume, many conventional approaches do not have adequate resolution and/or sensitivity to detect the dynamic behavior of nanomagnets. In addition, it is well known that as device dimensions approach atomic length scales the behavior can change dramatically due to the emergence of quantum effects (e.g. state-of-the-art transistors). Thus, researchers are constantly searching for new ways to study magnetic nanostructures to enrich our understanding of the physics that underpin the magnetic behavior to guide the rational design of these technologies.

In the following chapter, the physics that govern the dynamic behavior of magnetic bodies will be reviewed in detail, with special attention paid to the spin wave dispersion in nanomagnets, as well as the intrinsic and extrinsic (artificial) damping mechanisms that siphon energy from the magnetic system to other degrees of freedom. In chapter 3, a comprehensive review of magneto-optics and measurement techniques will be presented, including a detailed consideration of the relevant optical and electronic properties (e.g. noise, modulation, etc.) that govern key magneto-optic measurement parameters such as sensitivity and resolution. In addition, recent studies that shed light on the microscopic processes governing the ultrafast response of magnetic systems excited by a femtosecond laser pulse will be discussed. Using the theories and techniques presented in these first three chapters, the magnetization dynamics of Co/Ni superlattice structures studied in this work will be presented in chapter 4. In the following chapter, our experimental observations of the dynamic response of densely packed arrays of prototypical STT-MRAM devices will be reviewed. Here, because SAWs obscure the intrinsic spin dynamics, our novel approach to simultaneously enhance the magneto-optic response while suppressing SAWs will be demonstrated. In the chapters 6 and 7, the dynamic coupling between the mechanical and spin degrees of freedom will be utilized to explore an entirely new approach to athermally excite isolated nanostructures in order to study their dynamic magnetic properties. Because the magneto-elastic effect is directly determined by the strain, which is itself related to the sample geometry, the effect of nanomagnet size and shape, as well as the SAW wavelength, on the magneto-elastic resonance will be

reviewed. In the final chapter, our progress in developing an experimental setup to study the interplay between SAWs and all-optical switching of the magnetization will be presented.

CHAPTER 2
Magnetization Dynamics

In this chapter, the ultrafast spin dynamics of magnetic thin films and nanostructures will be discussed. Starting with a quantum description of a single spin in a magnetic field, the equation of motion for macroscopic ferromagnets will be derived. Then, the forces that determine the characteristics of the magnetization dynamics will be reviewed. Finally, the mechanisms that channel energy away from the spin system into the lattice, thereby causing the magnetic precession to dampen, as well as common experimental artifacts that obscure the true damping behavior will be explored.

2.1 Dynamics of a Single Spin

To introduce the conceptual framework of ferromagnetic resonance, we will begin by considering a single spin $\boldsymbol{s}$ in the presence of an externally applied magnetic field $\boldsymbol{H_{ext}}$. Using quantum theory, we can determine the equation of motion that governs the dynamic behavior of the spin [19, pp. 199-234]. The Schrödinger equation for the system is

$$i\hbar \frac{d|\psi\rangle}{dt} = H|\psi\rangle \tag{2.1.1}$$

where the H is the Hamiltonian that describes the interaction between $\boldsymbol{s}$ and $\boldsymbol{H_{ext}}$ and is expressed as

$$H = -g\mu_0\mu_B \boldsymbol{H_{ext}} \cdot \boldsymbol{s} \tag{2.1.2}$$

Here, μ_0 is the permeability of free space, μ_B is the Bohr magneton, and g is the spectroscopic splitting factor. The time evolution of the spin can be determined by taking the commutation between **s** and the Hamiltonian

$$i\hbar \frac{d\langle \boldsymbol{s} \rangle}{dt} = [\boldsymbol{s}, H] \tag{2.1.3}$$

which is easily solved with the help of the commutation rules for spin operators

$$[\boldsymbol{s}_i, \boldsymbol{s}_j] = i\hbar \epsilon_{ijk} \boldsymbol{s}_k \tag{2.1.4}$$

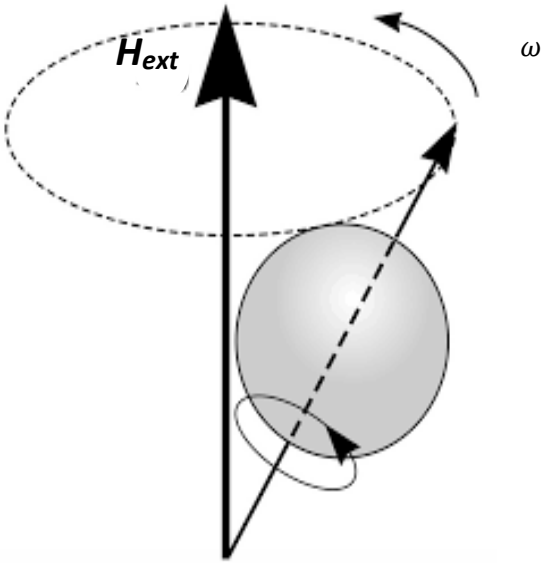

Fig. 2.1. Illustration of a spin precessing about an externally applied field H_{ext} as described by Eq. (2.1.5).

where ϵ_{ijk} is the Levi-Civita symbol, which is +1 if *ijk* = 123, 231; or 312, -1 if *ijk* = 132, 213, or 321; 0 otherwise. Deriving expressions for all 3 components leads to a general expression

$$\frac{d\langle \boldsymbol{s} \rangle}{dt} = \frac{g\mu_0\mu_B}{\hbar} (\boldsymbol{s} \times \boldsymbol{H_{ext}}) \tag{2.1.5}$$

This exercise yields an important result – a spin placed in a magnetic field will precess around the equilibrium axis determined by the external field. Furthermore, the precession frequency directly depends on the energy of the system, which in this case was determined solely by the strength of the field. Here, because the precession is *undamped* the magnetic moment will oscillate indefinitely, and the system will never relax to equilibrium. However, in a real system the spin belongs to a fermionic particle such as an electron. The electron itself will belong to a nucleus around which it orbits, and as a result there are additional forces acting on the particle. For instance, the spin is coupled to the nucleus via *spin-orbit coupling*, which allows for energy to be transferred from the spin precession to the lattice which will cause damping of the oscillation.

The equation of motion we have just derived for one spin can be generalized for the case of a homogenously magnetized body by using the following relation between **M** and $\langle \boldsymbol{s} \rangle$

$$\boldsymbol{M} = \frac{g\mu_0\mu_B}{\hbar}\langle \boldsymbol{s} \rangle \tag{2.1.6}$$

This allows us to rewrite Eq. (2.1.5) as follows

$$\frac{d\boldsymbol{M}}{dt} = -\gamma(\boldsymbol{M} \times \boldsymbol{H_{ext}}) \tag{2.1.7}$$

where the *gyromagnetic ratio* $\gamma = g\mu_B/\hbar$ has been introduced, which is approximately 28 GHz/T for a free electron. Eq. (2.1.7) is known as the Landau-Lifshitz (LL) equation [20] if $\boldsymbol{H_{ext}}$ is replaced with the effective field, $\boldsymbol{H_{eff}}$, which includes contributions to the

magnetic energy such as anisotropy fields and exchange interactions. As discussed earlier, various mechanisms will channel energy into the nearby lattice causing the precession to damp out, however, there is no term in the LL equation that accounts for this. In 1955, Gilbert added a dimensionless damping parameter, α, to the LL equation [21]

$$\frac{d\boldsymbol{M}}{dt} = -\gamma\left(\boldsymbol{M} \times \boldsymbol{H_{eff}}\right) + \frac{\alpha}{M_S}\left(\boldsymbol{M} \times \frac{d\boldsymbol{M}}{dt}\right) \tag{2.1.8}$$

This form is known as the Laundau-Lifshitz-Gilbert (LLG) equation and is widely used to describe the spin dynamics of ferromagnetic films and nanostructures. In more complicated systems (eg. exchange coupled layers, spin transfer-torque) additional terms must be included to fully describe the dynamic behavior. Because the dynamic behavior has been shown to depend on the energy of the system, in the following section the prominent sources of magnetic energy will be discussed.

2.2 Free Energies of Magnetic Systems

In order to understand the dynamic behavior of a ferromagnet an appropriate expression for the energy of the system must be derived. It is useful to begin with the Helmholtz free energy *F* of a magnetized body, which is defined as [22]

$$F(\boldsymbol{M}, T) = U - TS \tag{2.2.1}$$

where *U* is the internal energy of the system, *T* is the temperature, *S* is the entropy and $\boldsymbol{M}$ is the magnetization. Furthermore, if the system is kept at constant temperature in

the presence of an external induction field $\boldsymbol{B}$, then the change in the Helmholtz free energy, *dF*, of a reversible change of state can be expressed as

$$dF = -SdT + \boldsymbol{B} \cdot d\boldsymbol{M} \tag{2.2.2}$$

Another thermodynamic potential, the Gibbs free energy *G*, is similar to the Helmholtz energy and is defined as

$$G(\boldsymbol{H}) = F - \boldsymbol{M} \cdot \boldsymbol{B} \tag{2.2.3}$$

and a reversible change of state for this potential can be expressed as

$$dG = -SdT - \boldsymbol{M} \cdot d\boldsymbol{B} \tag{2.2.4}$$

Now, its worth discussing these potentials briefly because they are not consistently defined in the literature which can be very confusing. It must be noted that in Eqs. (2.2.2) and (2.2.4) the effects of pressure and volume on the magnetic system were assumed to be negligible. Secondly, if Eq. (2.2.2) is instead expressed as

$$dF = -SdT - \boldsymbol{M} \cdot d\boldsymbol{B} \tag{2.2.5}$$

then the differential of the Helmholtz and Gibbs free energies are identical, and it is the case that many texts alternate between these definitions of *dF*. The difference between the two forms is that Eq. (2.2.4) does not include the mutual field energy. If Eq. (2.2.2) is used to describe *dF*, then we end up with the following relations for the magnetization and magnetic flux

$$\boldsymbol{M_{eff}} = -\left(\frac{\partial G}{\partial \boldsymbol{B}}\right)_T \tag{2.2.6}$$

$$\boldsymbol{B_{eff}} = -\left(\frac{\partial F}{\partial \boldsymbol{M}}\right)_T \tag{2.2.7}$$

Finally, we have defined a relevant quantity for our experimental configuration that can be used to solve the equation of motion for our system. In these equations the subscript "eff" has been added to emphasize that $\boldsymbol{B_{eff}}$ and $\boldsymbol{M_{eff}}$ are the *effective* fields inside the sample. From these relationships we see that a change in the field will not only change $\boldsymbol{B_{eff}}$, but also $\boldsymbol{M_{eff}}$ which in turn will alter the resonance behavior of the system. These relationships will be used later to relate the magnetic energies of the sample to the dynamics.

2.2.1 Exchange Energy

At the heart of spontaneous magnetization lies the exchange interaction, which itself is a quantum mechanical effect that only occurs between two identical particles. Because fermions, such as electrons, are spin ½ particles they cannot occupy the same state simultaneously as a consequence of the Pauli principle [23]. As a simple example, consider two nearby atoms with unpaired electrons, according to the Pauli exclusion principle they cannot occupy the same orbital if their spins are parallel. Therefore, when the orbitals of these unpaired outer valence electrons overlap, the distributions of their electric charge in space are further apart if the spins are aligned, which reduces the total energy and makes this a more favorable configuration. However, there is a competing force due to the magnetic dipole-dipole interaction which itself prefers an antiparallel configuration, thus, the former is only true in cases where the exchange energy – which is the difference in energy between parallel and antiparallel electron pairs – is much

larger than the competing dipole-dipole interaction. For reference, Iron is ferromagnetic because the exchange force is approximately 1000 times stronger than the dipole-dipole force.

In ferromagnetic systems of interest such as Fe or Co, it can be assumed that the exchange interactions dominate, and the valence electrons tend to align themselves. For continuous materials with small angles between spins, the energy due to the exchange interaction can be expressed as follows [24]

$$E_{ex} = \int A_{ex} \left[(\nabla m_x)^2 + \left(\nabla m_y\right)^2 + (\nabla m_z)^2 \right] dV \tag{2.2.8}$$

where $\boldsymbol{m} \equiv \boldsymbol{M}/M_s$, and A_{ex} is the exchange stiffness constant of the material that is defined as [19]

$$A_{ex} = \frac{zJ_{ex}d^2}{12V_0} \tag{2.2.9}$$

where J_{ex} is the exchange integral of the electrons, z is the number of nearest neighbors, d is the interatomic distance, and V_0 is the volume of the unit cell. This expression is only valid when the angles between neighboring valence electron spins are small and no long-range interactions (eg. RKKY) are present. Typically, for thin films and nanostructures, A_{ex} is different than the bulk value and must be determined experimentally. One way to determine the exchange stiffness using TR-MOKE is to measure the field-dependent frequency of the first-order pseudo-standing spin wave (PSSW) because it directly depends on A_{ex} [25].

2.2.2 Zeeman Energy

Just as we saw in the previous example of a spin in a magnetic field, a magnetized body in a magnetic field experiences a torque due to the Zeeman interaction. The torque will act so as to align the magnetic moment of the sample to the field, and the energy associated with the interaction is [26]

$$E_z = -\int \boldsymbol{M} \cdot \boldsymbol{H_{ext}} dV = -M_s H_{app} \cos(\theta) \tag{2.2.10}$$

where $\theta$is the angle between the magnetization vector and the applied field.

2.2.3 Stray Field Energy

Stray field energy is also known as the self-energy, shape anisotropy energy, or most commonly as the demagnetization field energy. The demagnetization field is a consequence of Gauss's law, which states

$$\nabla \cdot \boldsymbol{B} = \nabla \cdot (\boldsymbol{H} + \boldsymbol{4\pi M}) = 0 \tag{2.2.11}$$

It follows that the stray field can be defined as the divergence of the magnetization as such [24]

$$\nabla \cdot \boldsymbol{H_d} = -4\pi \boldsymbol{\nabla} \cdot \mathbf{M} \tag{2.2.12}$$

The energy associated with the demagnetization field can then be expressed as

$$E_d = \frac{1}{2}\int_{all\ space} \boldsymbol{H_d^2} dV = -\frac{1}{2}\int_{sample} \boldsymbol{M} \cdot \boldsymbol{H_d} dV \tag{2.2.13}$$

where the factor of ½ is included to account for the self-interaction.This relationship shows us that the stray field energy is always positive because the function $\boldsymbol{H_d^2}$ is even.

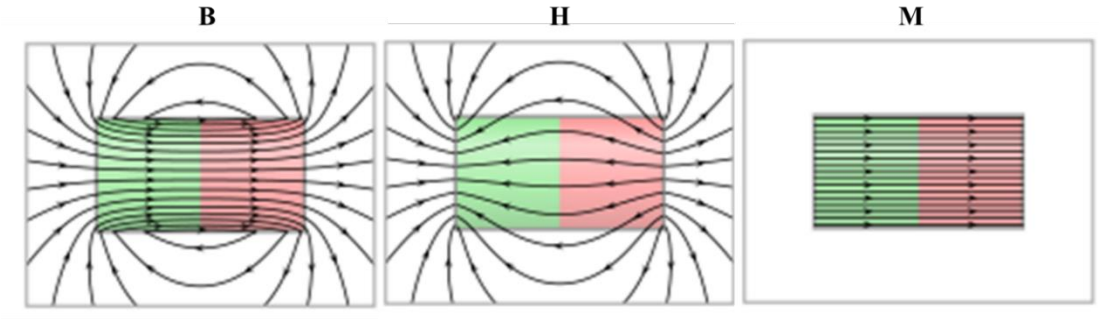

Fig. 2.2. Fields of a bar magnet. (a) B-field (b) H-field and (c) magnetization. Taken from **[27]**.

Although the above relationships were obtained with relatively little work, the integrals above are nearly impossible to solve. By introducing a scalar magnetic potential Φ_D, the demagnetization field can be rewritten as [28]

$$\boldsymbol{H_D} = -\nabla\Phi_D \tag{2.2.14}$$

Now, according to Eq. (2.2.11) we can also relate $\boldsymbol{M}$ to Φ_D as follows

$$\nabla^2\Phi_D = 4\pi\nabla\cdot\boldsymbol{M} \tag{2.2.15}$$

Because this relationship is only valid inside the sample, the following boundary conditions must follow

$$\Phi_{D,\boldsymbol{r<R}} - \Phi_{D,\boldsymbol{r>R}} = 0 \tag{2.2.16}$$

$$\frac{\partial\Phi_{D,\boldsymbol{r<R}}}{\partial n} - \frac{\partial\Phi_{D,\boldsymbol{r>R}}}{\partial n} = \boldsymbol{M}\cdot\boldsymbol{n} \tag{2.2.17}$$

where the subscript **r<R** denotes the region inside the magnetized sample and **r>R** is outside, **n** is the unit vector along the outward surface normal. Eq. (2.2.15) is a Poisson

equation with the "volumetric and surface magnetic charges" ρ and σ, respectively, which are purely mathematical constructs arising from the artificially defined point charges originating from uncompensated magnetic moments defined as follows

$$\rho = -4\pi\nabla \boldsymbol{M} \tag{2.2.18}$$

$$\sigma = \boldsymbol{n} \cdot \boldsymbol{M} \tag{2.2.19}$$

Now, Eq. (2.2.15) can be rewritten using Eq. (2.2.18)

$$\nabla^2 \Phi_D = \rho \tag{2.2.20}$$

in order to solve the partial differential equation in the same manner as an electrostatic problem of a point charge. The non-homogenous boundary value problem can be solved with the help of a Green's function *G(**r**,**r**')* with the following form [29]

$$G(\boldsymbol{r}, \boldsymbol{r}') = \frac{1}{4\pi|\boldsymbol{r} - \boldsymbol{r}'|} \tag{2.2.21}$$

The scalar magnetic potential in Eq. (2.2.14) can be calculated with the following integral

$$\Phi_D = \frac{1}{4\pi}\left(-\int_V \left(\frac{\boldsymbol{\nabla}' \boldsymbol{M}(\boldsymbol{r}')dV'}{|\boldsymbol{r} - \boldsymbol{r}'|}\right) + \int_S \left(\boldsymbol{n} \cdot \frac{\boldsymbol{M}(\boldsymbol{r}')dS'}{|\boldsymbol{r} - \boldsymbol{r}'|}\right)\right) \tag{2.2.22}$$

which leads to the following expression for the demagnetizing field

$$\boldsymbol{H_D}(\boldsymbol{r}) = -\nabla\Phi_D = \frac{1}{4\pi}\left(-\int_V \left(\frac{(\boldsymbol{r} - \boldsymbol{r}')\rho(\boldsymbol{r}')dV'}{|\boldsymbol{r} - \boldsymbol{r}'|^3}\right) + \int_S \left(\frac{(\boldsymbol{r} - \boldsymbol{r}')\sigma(\boldsymbol{r}')dS'}{|\boldsymbol{r} - \boldsymbol{r}'|^3}\right)\right) \tag{2.2.23}$$

This relationship shows that the demagnetizing field is directly determined by the geometry of the magnetized sample, hence, this term is interchangeably referred to as the *shape anisotropy*. Analytical solutions of Eq. (2.2.23) exist for ellipsoids of revolution, which include spheres, infinite thin films and rods – all of which can be mathematically expressed using elliptical functions [28]. For these shapes, the demagnetizing field of a **saturated** magnetic body can be expressed as the product of a diagonal tensor and the magnetization vector

$$\boldsymbol{H_D} = -\overleftrightarrow{N_D}\boldsymbol{M} \tag{2.2.24}$$

The analytic solutions of N_D are summarized in Table 2.1 in terms of the diagonal tensor elements N_a, N_b, and N_c, which correspond to the three major axes of the ellipsoid shown in Fig. 2.3. For all samples, the demagnetizing factors along all three directions must add up to unity: $N_a + N_b + N_c = 1$. In cases where the tensor is not diagonal, an appropriate rotation of the reference frame can diagonalize the tensor.

As an example, Eq. (2.2.24) can be plugged into Eq. (2.2.13) to directly determine the demagnetization energy for the case of a prolate spheroid [30]

$$E_D = -\frac{1}{2}((N_c(M_s cos(\theta))^2 + N_a(M_s sin(\theta))^2) \tag{2.2.25}$$

where θ is the angle between the c-axis and the magnetization. This equation shows that in this case the energy is minimized when the magnetization is aligned along the semi-major axis of the ellipse. Although magnetic nanostructures are never truly ellipsoids of revolution, it is generally the case that their shape anisotropy will act to

align the magnetization along the longest dimension. To determine the demagnetization field of shapes that do not belong to the family above, numerical techniques are required and will be discussed in more detail in section 4.4.2.2.

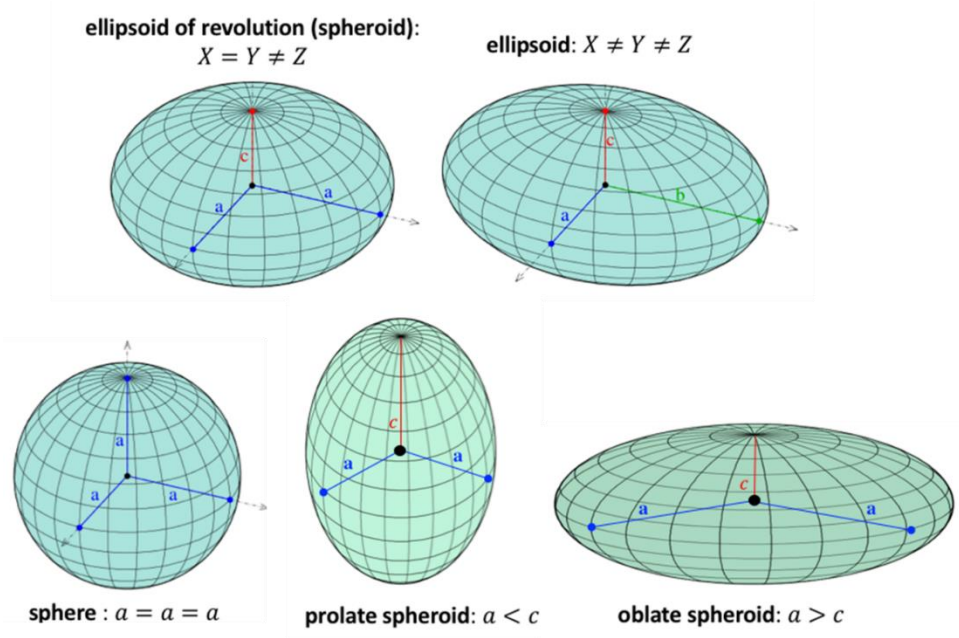

Fig. 2.3. Diagrams of ellipsoids of revolution for which the Eq. (2.2.24) can be analytically determined. Taken from **[31]**.

Shape	N_a	N_b	N_c
Sphere (a = b = c)	1/3	1/3	1/3
Prolate Spheroid (a = b, c>a)	$\frac{1}{2} - \frac{N_c}{2}$	$\frac{1}{2} - \frac{N_c}{2}$	$\frac{1}{p^2}\left(\frac{a}{p}\ln(a+p+1)\right)$
Oblate Spheroid (a=b, c<a)	$\frac{1}{2} - \frac{N_c}{2}$	$\frac{1}{2} - \frac{N_c}{2}$	$\frac{a^2}{p^2}\left(1 - p^{-1}\sin^{-1}\frac{p}{a}\right)$
Infinite Thin Film (a = b = ∞, c = 0)	0	0	1

Infinite Cylinder (a = b = 0, c = ∞)	1/2	1/2	0

Table 2.1. Explicit solutions for diagonal demagnetization tensor elements for ellipsoids of revolutions defined by $\left(\frac{x}{a}\right)^2 + \left(\frac{y}{b}\right)^2 + \left(\frac{z}{c}\right)^2 = 1$, $p = \sqrt{r^2 - 1}$.

2.2.4 Magnetic Anisotropy Energy

Another interaction that contributes to the free energy landscape is *magnetocrystalline anisotropy*, which occurs due to spin-orbit coupling between the electron and the lattice. The orientation of the electron orbitals are strongly coupled to the atoms, or lattice, and weakly coupled to the spin. As a result, when an external force (eg. an applied magnetic field) acts to align a spin in a particular direction, it is also exerts a force that acts to re-orient the orbital which has an associated energy cost [32].

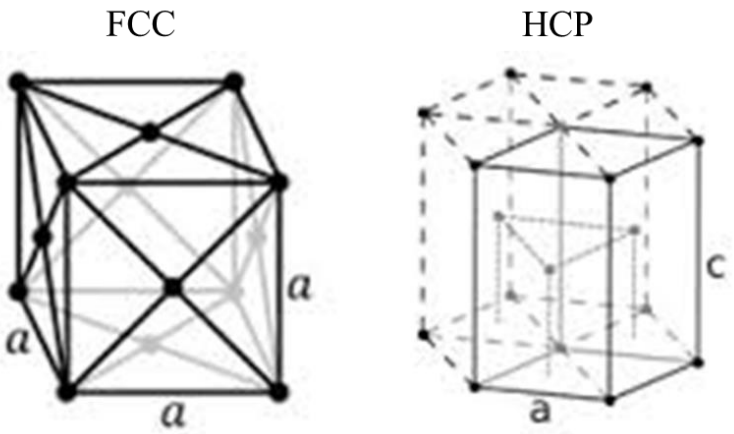

Fig. 2.4. The face-centered cubic and hexagonal close packed crystal structures and their relevant inter-atomic distances *a* and *c*. Taken from **[33]**

Because the magnetocrystalline anisotropy is a function of the atomic arrangement, each of the different crystal structures has its own distinct expression for the energy. Here, two types of crystal structures will be reviewed – hexagonal and cubic – because they are commonly encountered in magnetic 3d metals such as Co, Fe, and Ni

(interestingly, Co undergoes a phase transition from hcp to fcc at approximately 700K [34]). First, we will consider the anisotropy energy for the hexagonal close packed (hcp) system (Fig. 2.4) which exhibits what is known as *uniaxial anisotropy*, which means the energy depends on the orientation with respect to a single direction. The uniaxial energy is expressed as [32]

$$E_{uni} = K_1 \sin(\theta)^2 + K_2 \sin(\theta)^4 + K_3 \sin(\theta)^6 \ldots \quad (2.2.26)$$

where the subscript denotes the order of the anisotropy constant and θ is the angle between magnetization and the c-axis shown in Fig. 2.4. In most cases, it is more than sufficient to consider the first-order term. Thus, if the sign of K_1 is positive (eg. Co) the magnetocrystalline energy will be minimized when $\boldsymbol{M}$ is along the c-axis, and when the sign of K_1 is negative the energy is minimized when $\boldsymbol{M}$ is orthogonal to said axis. Now, we will consider the magnetocrystalline energy of cubic crystal structures, such as Fe and Ni, for which the magnetocrystalline energy can be expressed as

$$E_{cubic} = K_1(\alpha_1^2\alpha_2^2 + \alpha_2^2\alpha_3^2 + \alpha_1^2\alpha_3^2) + K_2\alpha_1^2\alpha_2^2\alpha_3^2 \ldots \quad (2.2.27)$$

where $\alpha_i = \cos(\theta_i)$ and i corresponds to the {a,b,c} crystallographic axes. If K_2 is negligible, then a positive K_1 value (eg. Fe) means the energy is minimized when the magnetization is along <100> directions, and when K_1 is negative (eg. Ni) the energy is smallest when the magnetization is along the <111> directions.

2.2.5 Surface Anisotropy

Nowadays, most information-based magnetic technologies (eg. HDD media, MTJs, etc.) utilize ultrathin magnetic layers embedded in multilayer heterostructures [35]. In these samples, the layers that are adjacent to the magnetic layer strongly affect the magnetization orientation as well, which is referred to as *interface anisotropy*. Unlike magnetocrystalline anisotropy which is an intrinsic property of the magnetic material, the characteristics of interfacial anisotropy can be "tuned" via the elemental composition of the layers surrounding the magnetic material, their thickness, and even the layer sequence [36]. The strength of interface anisotropy is inversely proportional to the magnetic film thickness, thus, it is most effectively utilized in vanishingly thin structures. A prime example of a magnetic system that utilizes this type of anisotropy is the CoFeB/MgO interface, which has been extensively studied for its role in STT-MRAM and STO applications [3]. At the interface, the Fe and O atoms hybridize and form Fe-O bonds that act as a source of uniaxial anisotropy and re-orient the magnetization along the surface normal direction. There are also anisotropic contributions from the elastic stress induced by the lattice mismatch between layers as well as the difference in the symmetry of the crystal structure at the surface. Despite the fact that CoFeB has a bcc crystal structure with in-plane magnetocrystalline anisotropy, the interfacial anisotropy is strong enough to cause the CoFeB to have an out-of-plane easy axis if the CoFeB is thin enough (typically <2nm thick, depending on the interface quality). To the first order, the energy associated with the interfacial anisotropy has the form [3]

$$E_i = -\frac{\sigma}{t}\cos(\theta)^2 \tag{2.2.28}$$

where σ is the interfacial anisotropy energy per unit area, t is the sample thickness, and θ is the angle between the magnetization vector and the surface normal.

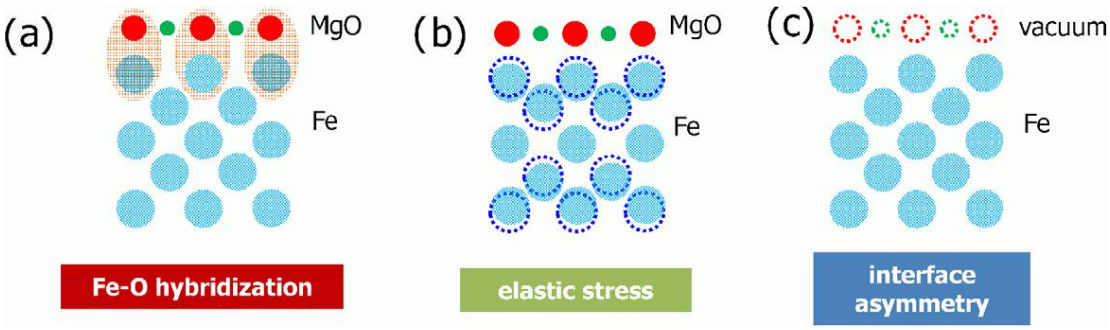

Fig. 2.5. Illustration of the three major contributions to the interfacial anisotropy of an Fe–MgO interface: (a) hybridization of the atomic orbitals of the magnetic layer and the barrier, (b) elastic stress due to the lattice distortion and (c) crystal symmetry breaking due to the interface. Circles show position of the atoms for Fe, O, Mg for largest (blue), medium (red) and smallest (green) spheres, respectively. (a) Ellipses show hybridized Fe–O orbitals; (b) dotted circles correspond to initially undistorted Fe atom positions; (c) dotted circles represent the initial positions of Mg and O atoms before their removal to create vacuum|Fe interface. Taken from **[3]**.

A very useful parameter when discussing MTJs with perpendicular magnetic anisotropy (PMA) is known as the anisotropy field, H_K, which is defined as

$$H_K = \frac{2K_u}{M_s} - 4\pi M_s \tag{2.2.29}$$

for bulk materials with uniaxial PMA K_u, where the factor $4\pi M_s$ is the demagnetization field of a thin film (in cgs units) magnetized in the out-of-plane (OOP) direction. For interfacially-induced PMA (iPMA) samples, the effective anisotropy is a sum of the interfacial and crystal fields [37]

$$K_{eff} = \frac{\sigma}{t} - K_B \tag{2.2.30}$$

where t is the film thickness and K_B is the in-plane magnetocrystalline anisotropy. If the interfacial anisotropy dominates, then $\frac{\sigma}{t} \gg K_B$ and the expression for the anisotropy field reduces to

$$H_K = \frac{2\sigma}{M_s t} - 4\pi M_s \tag{2.2.31}$$

When the anisotropy field is greater than 0 the film will have an OOP easy-axis, and when it is less than 0 it will prefer an in-plane magnetization. For OOP magnetic bits, the stability of the bit (i.e. its ability to withstand thermal fluctuations) can be defined as

$$\Delta = \frac{E_b}{k_B T} = \frac{K_u V}{k_B T} = \frac{H_k M_s V}{2 k_B T} \tag{2.2.32}$$

where E_b is the energy barrier between equilibrium magnetic states, k_B is the Boltzmann coefficient, and V is the volume of the magnetic element. For circular devices with iPMA, Eq. (2.2.31) can be used to replace H_K in Eq. (2.2.32) as follows [3]

$$\Delta = \frac{(\sigma - 2\pi M_s^2 t)\pi A R w^2}{4 k_B T} \tag{2.2.33}$$

where AR is the aspect ratio and w is the diameter. This expression of the energy barrier demonstrates the crucial role interface anisotropy plays for STT-MRAM devices.

2.2.6 Magnetostriction

In the previous sections we have seen that the crystal field can strongly influence the behavior of the magnetic system via spin-orbit coupling. However, we neglected the equal but opposite force that the lattice experiences from this interaction. By neglecting this force, we implicitly assumed that the atomic nuclei were fixed in their equilibrium positions. It turns out that when a magnetic field is applied, the atoms can move such that the orbitals re-orient themselves to reduce the overall energy of the system. When the atoms move, the macroscopic dimensions of the magnetic body change, this phenomenon is known as *magnetostriction* [38]. It turns out that even in the absence of an external field, a magnetized sample is "stretched out" relative to its demagnetized state. A reciprocal effect, known as *inverse magnetostriction*, occurs when a spontaneously magnetized body is elastically deformed by an external mechanical force that gives rise to an internal field. Inverse magnetostriction is interchangeably referred to as the *magneto-elastic (MEL)* or the *Villari* effect. The strength of the MEL effect depends on the crystal structure and the magnetic material. For cubic crystals, the magneto-elastic properties are defined by the fractional elongation along <100> and <111> directions as follows [38]

$$\left(\frac{\delta l}{l}\right)_{100} \equiv \lambda_{100} = -\frac{2}{3}\frac{B_1}{c_{11} - c_{22}} \tag{2.2.34}$$

$$\left(\frac{\delta l}{l}\right)_{111} \equiv \lambda_{111} = -\frac{1}{3}\frac{B_2}{c_{44}} \tag{2.2.35}$$

where l is the macroscopic length of the sample along the crystal axis, δl is the change in length from an ideal demagnetized state to a saturated state, B_i are the magneto-elastic constants along the principle axes, and c_i are the moduli of elasticity for a cubic system. In practice, a great deal of care must be taken to grow single-crystal ferromagnets, thus, most samples are polycrystalline and the magnetostriction constant in this case is [38]

$$\lambda_s = \frac{2}{5}\lambda_{100} + \frac{3}{5}\lambda_{111} \tag{2.2.36}$$

For polycrystalline samples, the magnetoeleastic constant is isotropic, hence $B=B_1=B_2$, and is defined as

$$B = -3\lambda_s G \tag{2.2.37}$$

where G is the shear modulus. For ultrathin samples, effects at the surface (eg. surface roughness, hybridization, etc.) are non-negligible and can strongly affect the magneto-elastic behavior. The *effective* magneto-elastic constant B_{eff} is defined in a similar manner as K_{eff} in Eq. (2.2.30) as follows [39]

$$B_{eff} = B_{bulk} + \frac{B_s}{t} \tag{2.2.38}$$

where B_{bulk} is the magneto-elastic constant defined in Eq. (2.2.37) and B_s is the contribution from the surface. The dynamic behavior of a magneto-elastic system can be very complicated, so for the sake of simplicity only the phenomenological description will be considered here. The MEL contribution to the Gibbs free energy can be written as [1]

$$E_{MEL} = \frac{B_1}{M_s^2}\sum_p M_p^2 \varepsilon_{pp} + \frac{B_2}{M_s^2}\sum_p \sum_{q\neq p} M_p M_q \varepsilon_{pq} + \cdots$$
$$\frac{A_1}{M_s^2}\sum_p \sum_q \sum_{l\neq q} \frac{\partial M_p}{\partial x_q}\frac{\partial M_p}{\partial x_l}\varepsilon_{ql} + \frac{A_2}{M_s^2}\sum_p \sum_p \left(\frac{\partial M_p}{\partial x_q}\right)^2 \varepsilon_{qq} \quad (2.2.39)$$

where M_i are the magnetization components along the axes x_i, $A_{1,2}$ are the exchange terms, and ε_{pq} are the elastic strain tensor elements defined as

$$\varepsilon_{ij} = \frac{1}{2}\left(\frac{\partial u_i}{\partial x_j} + \frac{\partial u_j}{\partial x_i}\right) \quad (2.2.40)$$

where $\boldsymbol{u}(\boldsymbol{r}) = \boldsymbol{r} - \boldsymbol{r_0}$ is the displacement vector of the point $\boldsymbol{r}$ relative to an equilibrium position $\boldsymbol{r_0}$. In most cases, the final two terms in Eq. (2.2.39) that depend on $A_{1,2}$ are negligibly small and can simply be ignored.

2.3 Ferromagnetic Resonance

In section 2.1 we derived an equation of motion (Eq. (2.1.11)) for a uniform magnetic body in an externally applied field and saw that the equation of motion for the magnetization vector depended on H_{eff}. According to Eq. (2.2.7), the effective field is determined by the partial derivative of the Helmholtz free energy with respect to the magnetization. Now, all of the sources of magnetic energy discussed in the preceding section can be used to determine analytic expressions for the ferromagnetic resonance of thin films as a function of $F(\theta, H_{ext})$.

2.3.1 Derivation of Kittel Formula with Damping

The fundamental spin wave mode of a homogenously magnetized ferromagnetic thin film is colloquially referred to as the *Kittel mode* – named after physicist Charles Kittel who first reported a general solution of the LLG equation in 1951 [40]. An important, albeit subtle, implication of the phrase "homogenously magnetized thin film" is that the spin-wave is assumed to be infinitely long, which means that all of the spins move in phase and that the wavenumber k = 0 rad/cm. In order to simplify the derivation it is easiest to work in a spherical coordinate system. The magnetization vector in Cartesian and spherical coordinates is

$$\boldsymbol{M} = \begin{bmatrix} M_x \\ M_y \\ M_z \end{bmatrix} = M_s \begin{bmatrix} sin\theta\cos\,\phi \\ sin\theta sin\phi \\ cos\theta \end{bmatrix} \tag{2.3.1}$$

where θ is the angle between the surface normal and the magnetization and ϕ is the azimuthal angle between the x-axis and the magnetization (Fig. 2.6). A complete expression for the free energy of the system which determines the effective field must be known in order to solve Eq. (2.1.12). As an example, we will assume our magnetic film has a uniaxial PMA and no elastic strain is present, for which the free energy can be expressed as

$$F = -K_z \cos(\theta)^2 - \mu_0 M_s H_{ext}(\sin(\theta)\cos(\phi) + \sin(\theta)\sin(\phi) + \cos(\theta)) + \cdots \\ \frac{1}{2}\mu_0 M_s^2 \cos(\theta)^2 \tag{2.3.2}$$

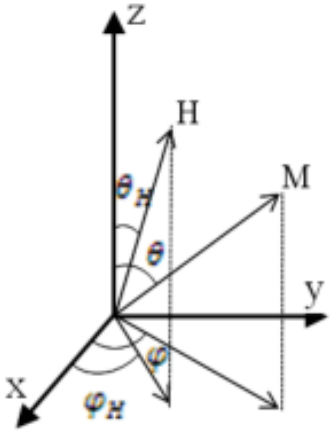

Fig. 2.6. Spherical coordinate system used to describe the magnetization.

Now, Eq. (2.2.7) can be rewritten in the following form [41]

$$\boldsymbol{H_{eff}} = -\left(\frac{\partial F}{\partial \boldsymbol{M}}\right) = -\left(\frac{\partial F}{\partial r}\widehat{\boldsymbol{e_r}} + \frac{1}{M_s}\frac{\partial F}{\partial \theta}\widehat{\boldsymbol{e_\theta}} + \frac{1}{M_s \sin(\theta)}\frac{\partial F}{\partial \phi}\widehat{\boldsymbol{e_\phi}}\right) \tag{2.3.3}$$

where $\widehat{\boldsymbol{e_\iota}}$ are the spherical unit vectors for the radial, polar and azimuthal components. If we assume that the length of the magnetization vector is fixed, which we'll see later is a good approximation, then the time-dependence of the magnetization can be expressed as

$$\frac{d\boldsymbol{M}}{dt} = M_s \frac{d\theta}{dt}\widehat{\boldsymbol{e_\theta}} + M_s \sin(\theta)\frac{d\phi}{dt}\widehat{\boldsymbol{e_\phi}} \tag{2.3.4}$$

This equation can be used to simplify Eq. (2.3.3) to a pair of coupled equations with the following form [1]

$$(1+\alpha^2)\frac{d\theta}{dt} = -\frac{\gamma}{M_s}\left(\alpha\frac{\partial F}{\partial \theta} + \frac{1}{\sin(\theta)}\frac{\partial F}{\partial \phi}\right) \tag{2.3.5}$$

$$(1+\alpha^2)\frac{d\phi}{dt} = \frac{\gamma}{M_s \sin(\theta)}\left(\frac{\partial F}{\partial \theta} + \frac{\alpha}{\sin(\theta)}\frac{\partial F}{\partial \phi}\right) \tag{2.3.6}$$

Because we are ultimately interested in solving for small deviations of **M** about its equilibrium, we assume the solutions have the following form

$$\delta\theta = \theta - \theta_0 = \delta\theta_A e^{i\omega t} \tag{2.3.7}$$

$$\delta\phi = \phi - \phi_0 = \delta\phi_A e^{i\omega t} \tag{2.3.8}$$

where $\delta\theta_A$ and $\delta\phi_A$ are the precession amplitudes, ω is the eigenfrequency, and θ_0 and ϕ_0 are the equilibrium angles of the magnetization that can be determined by the following energy minimization conditions

$$\left(\frac{\partial F}{\partial \theta}\right)_{\theta=\theta_0} = 0 \tag{2.3.9}$$

$$\left(\frac{\partial F}{\partial \phi}\right)_{\phi=\phi_0} = 0 \tag{2.3.10}$$

If we assume that the field lies in the x-z plane, then $\phi = 0$ and Eq. (2.3.9) is simply

$$\sin(2\theta_0) = \frac{2H_{ext}}{H_K}\sin(\theta_H - \theta_0) \tag{2.3.11}$$

where H_K is the anisotropy field introduced in Eq. (2.2.30) and θ_H is the polar angle of the applied magnetic field as shown in Fig. 2.6. This is a self-consistent equation that must be solved numerically (unless θ_H is 0 or 90^o). In Eqs. (2.3.7) and (2.3.8) we have

imposed a small-angle approximation for our system, which permits a Taylor expansion of the free energy

$$F = F_0 + \frac{1}{2}\left(F_{\theta\theta}\theta^2 + 2F_{\theta\phi}\theta\phi + F_{\phi\phi}\phi^2\right) \tag{2.3.12}$$

where F_0 is the free energy at equilibrium, and the partial derivatives are $F_{\theta\theta} = \frac{\partial^2 F}{\partial \theta^2}, F_{\phi\phi} = \frac{\partial^2 F}{\partial \phi^2}$, and $F_{\theta\phi} = \frac{\partial^2 F}{\partial \phi \partial \theta}$. Eqs. (2.3.7, 8, and 12) can be combined to rewrite Eqs. (2.3.5) and (2.3.6) as

$$\left(i\omega + \frac{\gamma}{M_s \sin(\theta_0)} F_{\theta\phi} + \frac{\alpha\gamma}{M_s} F_{\theta\theta}\right)\delta\theta_A + \left(\frac{\gamma}{M_s \sin(\theta_0)} F_{\phi\phi} + \frac{\alpha\gamma}{M_s} F_{\theta\phi}\right)\delta\phi_A = 0 \tag{2.3.13}$$

$$\left(\frac{\gamma}{M_s \sin(\theta_0)} F_{\theta\theta} - \frac{\alpha\gamma}{M_s \sin(\theta_0)^2} F_{\theta\phi}\right)\delta\theta_A - \cdots$$
$$\left(i\omega - \frac{\gamma}{M_s \sin(\theta_0)} F_{\theta\phi} + \frac{\alpha\gamma}{M_s \sin(\theta_0)^2} F_{\phi\phi}\right)\delta\phi_A = 0 \tag{2.3.14}$$

These two equations form a system of equations that can be expressed in matrix form as

$$\begin{pmatrix} A_{11} & A_{12} \\ A_{21} & A_{22} \end{pmatrix}\begin{pmatrix} \delta\theta_A \\ \delta\phi_A \end{pmatrix} = 0 \tag{2.3.15}$$

$$A_{11} = i\omega + \frac{\gamma}{M_s \sin(\theta_0)} F_{\theta\phi} + \frac{\alpha\gamma}{M_s} F_{\theta\theta} \tag{2.3.15.1}$$

$$A_{12} = \frac{\gamma}{M_s \sin(\theta_0)} F_{\phi\phi} + \frac{\alpha\gamma}{M_s} F_{\theta\phi} \tag{2.3.15.2}$$

$$A_{21} = \frac{\gamma}{M_s \sin(\theta_0)} F_{\theta\theta} - \frac{\alpha\gamma}{M_s \sin(\theta_0)^2} F_{\theta\phi} \tag{2.3.15.3}$$

$$A_{22} = -i\omega + \frac{\gamma}{M_s \sin(\theta_0)} F_{\theta\phi} - \frac{\alpha\gamma}{M_s \sin(\theta_0)^2} F_{\phi\phi} \tag{2.3.15.4}$$

Nontrivial solutions to Eq. (2.3.15) can be found by setting the determinant equal to 0, which yields

$$\left(i\omega + \frac{\gamma}{M_s \sin(\theta_0)} F_{\theta\phi} + \frac{\alpha\gamma}{M_s} F_{\theta\theta}\right)\left(-i\omega + \frac{\gamma}{M_s \sin(\theta_0)} F_{\theta\phi} - \frac{\alpha\gamma}{M_s \sin(\theta_0)^2} F_{\phi\phi}\right) - \left(\frac{\gamma}{M_s \sin(\theta_0)} F_{\phi\phi} + \frac{\alpha\gamma}{M_s} F_{\theta\phi}\right)\left(\frac{\gamma}{M_s \sin(\theta_0)} F_{\theta\theta} - \frac{\alpha\gamma}{M_s \sin(\theta_0)^2} F_{\theta\phi}\right) = 0 \tag{2.3.16}$$

When $\alpha \ll 1$, as is often the case, the calculus above can be simplified by dropping terms that depend on the value α^2, which yields the following quadratic equation relationship between ω and the partial derivatives of the free energy

$$\omega^2 - i\alpha\omega \frac{\gamma}{M_s \sin(\theta_0)}\left(\frac{F_{\phi\phi}}{\sin(\theta)} + \sin(\theta) F_{\theta\theta}\right) + \cdots \left(\frac{\gamma}{M_s \sin(\theta_0)}\right)^2 \left(F_{\theta\phi}^2 - F_{\phi\phi} F_{\theta\theta}\right) = 0 \tag{2.3.17}$$

This relationship is often simplified even further by setting $\alpha = 0$ to determine the real part of ω (the precession frequency) via the relation [40]

$$\omega = \frac{\gamma}{M_s \sin(\theta_0)} \sqrt{F_{\theta\theta} F_{\phi\phi} - F_{\theta\phi}^2} \tag{2.3.18}$$

The undamped approximation we've just derived is known as the Smit-Suhl formula. However, because $\alpha \neq 0$ the complete solutions for ω are actually complex. The real

and imaginary parts correspond to the precession frequency and decay rate, respectively, where the latter is [1]

$$Im(\omega) \equiv \frac{1}{\tau} = \frac{\alpha\gamma}{2M_s \sin(\theta_0)}\left(\frac{F_{\phi\phi}}{\sin(\theta)} + \sin(\theta)\, F_{\theta\theta}\right) \tag{2.3.19}$$

For the free energy of a thin film with uniaxial anisotropy (Eq. 2.3.2), the frequency and damping can be conveniently expressed as

$$\omega = \gamma\sqrt{H_1 H_2} \tag{2.3.20}$$

$$\frac{1}{\tau} = \frac{\alpha\gamma(H_1 + H_2)}{2} \tag{2.3.21}$$

where H_1 and H_2 are defined as

$$H_1 = H_{ext}\cos(\theta_H - \theta_0) + H_K \cos(2\theta_0) \tag{2.3.22}$$

$$H_2 = H_{ext}\cos(\theta_H - \theta_0) + H_K \cos(\theta_0)^2 \tag{2.3.23}$$

For two specific cases, the Kittel formula can be greatly simplified because Eq. (2.3.11) can be solved analytically. If the external field is applied in the plane of the sample ($\theta_H = \frac{\pi}{2}$), the equilibrium condition is simply

$$2\sin(\theta)\cos(\theta) = \frac{2H_{ext}}{H_k}\sin\left(\frac{\pi}{2} - \theta\right) \rightarrow \sin(\theta) = \frac{H_{ext}}{H_K} \tag{2.3.24}$$

and Eq. (2.3.20) reduces to

$$\omega = \gamma\sqrt{BH} \tag{2.3.25}$$

for samples with an in-plane easy-axis (e.g. isotropic thin films). However, for samples with large PMA the Kittel frequency is determined as

$$\omega = \begin{cases} \gamma\sqrt{H_K^2 - H_{ext}^2}\ if\ H_{ext} < H_K \\ \gamma\sqrt{H_{ext}^2 - H_{ext}H_k}\ if\ H_{ext} > H_K \end{cases} \tag{2.3.26}$$

which goes to 0 as H_{ext} approaches H_K! This special case will be considered in detail in section 4.3, with specific attention paid to the damping behavior in this case. On the other hand, if the field is applied in the out-of-plane direction instead the Kittel frequency will simply be

$$\omega = \gamma(H_{ext} + H_K) \tag{2.3.27}$$

which is always positive for PMA films because H_K is positive. However, if we consider samples with in-plane easy axis (e.g. isotropic films) which have a negative anisotropy field for this configuration, the relationship presented above is only valid when $H_{ext} > 4\pi M_s$.

2.4 Intrinsic and Extrinsic Damping

Many magnetic technologies depend critically on the Gilbert damping parameter α because it ultimately characterizes the inertial energy barrier that must be overcome to initiate movement of the magnetic moment [35]. Thus, precise

determination of α is of the utmost importance for many researchers studying ultrafast spin dynamics. As we will see, there are a variety of *extrinsic* contributions that artificially enhance the experimentally observed damping and obscure the intrinsic behavior. Neglecting these contributions leads to imprecise estimations of α, which in turn arrests the optimization of next-generation devices.

2.4.1 Intrinsic Sources of Damping

The microscopic processes that cause the magnetic moment to relax depend on the electronic structure of the material. For example, the origins of the damping in a semiconductor are vastly different than a metallic ferromagnet due to the abundance of itinerant conduction electrons the latter possesses. In recent years, however, there has been a great deal of progress in this area and in the following section the most commonly accepted models will be briefly discussed.

2.4.1.1 Phonon-Magnon Scattering

In crystalline lattices the atoms must exert forces on one another in order to keep each atom near its equilibrium position. One can imagine that the atoms are a system of balls interconnected by springs. Because all of the atoms are connected energy can propagate through the system, and it is easy to see how displacing an atom can cause mechanical waves to form. These modes are quantized and represented by quasiparticles known as *phonons*. In section 2.2.6, we saw that magneto-elastic energy is associated with the displacement of atoms from their equilibrium position. This leads

to an unavoidable source of magnetic damping in which the energy is transferred from the *magnon* system to the phonon system. A simple case was considered by Suhl – a sample with homogenous magnetization and strain – for which he derived an expression of the damping caused by magnon-phonon interactions [42]

$$\alpha_{ph} = \frac{2\gamma(1+\nu)^2 B_2^2 \eta}{M_s E^2} \tag{2.4.1}$$

where η is the phonon viscosity, B_2 is the magneto-elastic shear constant, E is the Young's modulus, and ν is the Poisson ratio. In metallic systems this is a relatively weak source of damping, for example, in Ni $\alpha_{ph} \sim 0.001$ which is 30-fold smaller than the Gilbert damping. Thus, other channels of spin relaxation must be considered to complete the picture.

2.4.1.2 Itinerant Electron Mechanisms

It is well-known that the predominant source of damping in ferromagnetic metals is the spin-orbit coupling of itinerant electrons, which links the uniformly precessing magnetization to the lattice, thereby leading to scattering of the spins. However, one fact has puzzled researchers for decades – the damping in metals is smallest at some finite temperature and increases at both lower and higher temperatures (Fig. 2.7). This temperature-dependent damping behavior is often referred to as conductivity-like and resistivity-like contributions, respectively.

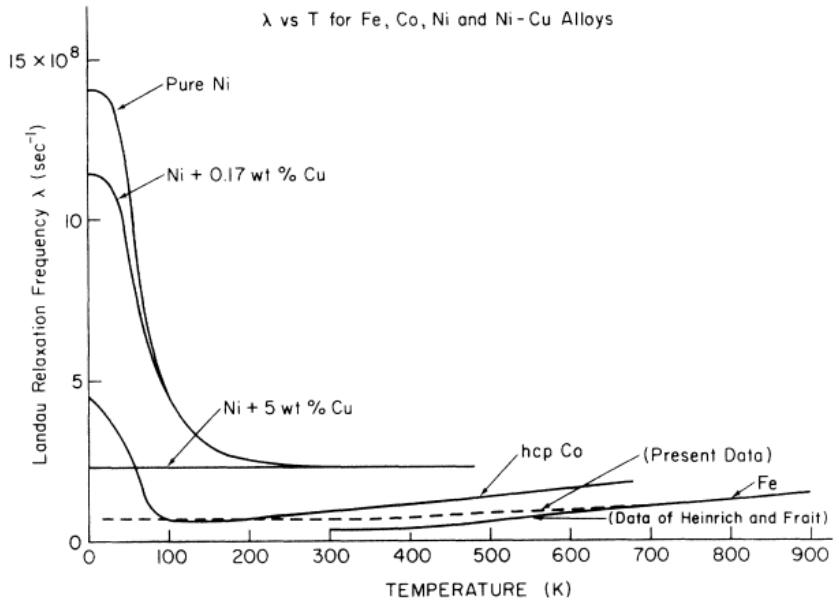

Fig. 2.7. Damping parameter ($\boldsymbol{\lambda = \alpha\gamma M_s}$) of Co, Fe and Ni films measured as a function of temperature exhibits low-T and high-T increases in damping. Taken from **[43]**.

Although the origins of magnetic damping in metallic ferromagnets are still hotly debated, the theories derived by Vladimír Kamberský are the *most* widely accepted and are known as the *breathing Fermi-surface* [44] and *torque-correlation models* [45]. Despite the fact that the former is referred to in the literature more frequently, the latter is more general and accurately predicts the damping behavior of metals at low and high temperatures alike.

Kamberský's results are focused on the changing status of the Fermi energy levels [46]. As the magnetization precesses, the energies of the electronic states are perturbed. For intraband transitions (low temperature), this results in some occupied states being pushed above the Fermi level and some unoccupied states below it. This, in turn, generates electron-hole pairs near the Fermi level that exist for a lifetime τ and

then relax through scattering into the lattice. Because the initial and final state of the electron are the same, the matrix elements do not describe a real transition but instead provide a measure of the energy of the electron-hole pairs that are annihilated by an electron-lattice event. For interband transition (high temperature), lattice scattering broadens the electron energy bands such that there is significant overlap between them at the Fermi level. The oscillating exchange field, caused by the uniform precession, induces quasielastic transitions between states (*k* is conserved). Because the majority of these transitions occur between states with different spin character, this process is essentially the decay of a uniform precession magnon into a single electron spin-flip excitation. These events occur more frequently as the overlap between bands increase, which qualitatively matches the resistivity-like behavior. The two models are identical in the conductivity-like regime, but the breathing Fermi-surface model fails to predict the resistivity-like behavior. Kamberský's torque-correlation model is expressed in terms of the damping rate λ which is related to the Gilbert damping as follows [47]

$$\lambda = \alpha\gamma M_s = \frac{g^2\mu_B^2}{\hbar}\sum_{n,m}\int \frac{dk^3}{(2\pi)^3}|\Gamma_{nm}^{-}(k)|^2 W_{nm}(k) \tag{2.4.2}$$

Here, $\Gamma_{nm}^{-}(k)$ is a matrix element that measures the transitions between states in bands *m* and *n* induced by spin-orbit torque and is determined by the following relationship

$$|\Gamma_{nm}^{-}(k)| = \langle n,k|[\sigma^{-}, H_{SO}|m,k\rangle \tag{2.4.3}$$

where H_{SO} is the spin-orbit Hamiltonian and $\sigma^- = \sigma_x - i\sigma_y$ where σ_x and σ_y are the Pauli spin matrices. These transitions describe the annihilation of a uniform precession magnon which carries no linear momentum because k=0. The term $W_{nm}(k)$ is defined as [47]

$$W_{mn}(k) = \left(\frac{1}{\pi}\right) \int \delta\omega_1 \eta(\omega_1) A_{nk}(\omega_1) A_{mk}(\omega_1) \tag{2.4.4}$$

where $\eta(\omega)$ is the negative derivative of the Fermi function with respect to energy that effectively "picks out" states near the Fermi surface. Eq. (2.4.3) describes the spectral overlap between states which is in turn used to evaluate the scattering. Unlike many competing theories, this model qualitatively predicts the conductivity and resistivity-like contributions to the damping that have puzzled researchers for decades. The conductivity-like contribution is *intraband* scattering within a single band (m=n) for which the final states are the same and resistivity-like scattering events described by Eq. (2.4.2). On the other hand, the resitivity-like contribution is *interband* scattering between two different bands ($m \neq n$).

In practice, it is very difficult to quantitatively compare Kamberský's theories to experimental results, because the models require precise knowledge of the band- and temperature-dependent electron scattering lifetimes in transition metals. Nonetheless, Gilmore et al. [47] used estimates of the scattering times and reported excellent qualitative agreement between Kamberský's torque-correlation model and the damping behavior in Co, Fe, and Ni thin films.

2.4.2 Extrinsic Sources of Damping

In the previous section, the origins of magnetic damping in metals were discussed. Such calculations are too computationally intensive even for even the simplest cases (eg. perfect crystals) and are of little use in a practical setting. Instead, the Gilbert damping of a material is determined by measuring the spin dynamics and then fitting the data with a damped precession to estimate the lifetime and frequency [48]. Per Eq. (2.3.19), the frequency and lifetime of the precession are determined by the internal energies of the system (eg. magnetocrystalline, demagnetization, and exchange energies). Because the transient magnetic response depends on many variables, a single measurement is not sufficient to determine the relevant parameters. Instead, the dynamics must be measured over a range of applied fields in order to accurately estimate the various contributions. In addition, there are a number of *extrinsic* mechanisms that artificially enhance the observed damping and make accurate determination of the Gilbert damping challenging. For applications such as STT-MRAM, precise determination of α is crucial as it directly determines critical operation characteristics of MTJs [3]. In the following, some common extrinsic mechanisms will be discussed, as well as ways in which to disentangle the intrinsic and extrinsic phenomena.

2.4.2.1 Inhomogeneous Broadening

Inhomogeneous broadening (IHB) of the ferromagnetic resonance is one of the most prominent sources of extrinsic damping in films with large iPMA. IHB is an

increase in the linewidth, or damping, of the measured resonance due to microscale variations of key magnetic parameters (eg. M_s and K_u), which determine the resonance frequency per Eq. (2.3.18). In polycrystalline films IHB can occur because the grains are oriented randomly and their crystallographic axes are not aligned, thus, the magnetocrystalline energy varies from grain-to-grain. Additional sources of magnetic inhomogeneity include – but are not limited to – variations in interfacial anisotropy (eg. surface roughness) as well as defects and dislocations in the lattice. The distribution of parameters leads to a spread in the local resonance which in turn broadens the effective resonance observed experimentally. Because the linewidth of the damping is directly determined by the frequency [48]

$$\Delta f = 4\pi\alpha f \tag{2.4.5}$$

and the simplest way to mitigate the effects of IHB is to raise f by increasing H_{app}.

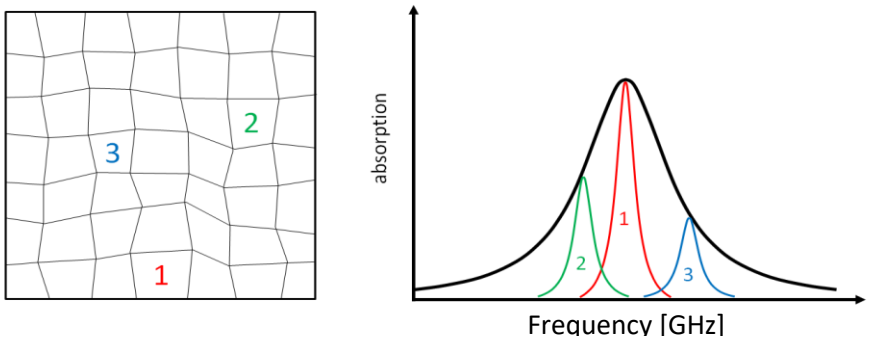

Fig. 2.8. Illustration of local resonance distribution due to spatial variation of magnetic properties adapted from ref. **[49]**.

As an example, consider a sample with a spatially varying anisotropy, caused by surface roughness, which has a distribution of resonance frequencies shown in the histogram in Fig. 2.8. When the applied field is small, the local anisotropies cause the

spread in the resonance frequencies to be quite large (Fig. 2.9 (c)). When all the individual resonances are aggregated, the result is an appreciably broadened linewidth. However, when the same sample is measured at a larger field, the total linewidth is much closer to the intrinsic value. This behavior is due to the fact that the separation between the resonance frequencies is more or less fixed, so long as the Kittel mode is monotonically increasing with the applied field. As the intrinsic linewidth gets larger, the contribution of the constant broadening becomes relatively small. This behavior leads to a simple addition to the linewidth in Eq. (2.4.4) which reads [48]

$$\Delta f(f) = 4\pi\alpha f + \Delta f_0 \tag{2.4.6}$$

where Δf_0 is represents the distribution of magnetic parameters, and the slope of Δf gives the true Gilbert damping. It should be noted that when the applied field is along the anisotropy hard axis of the sample the Kittel frequency does not increase monotonically with the applied field. As a result, the linear behavior predicted by Eq. (2.4.6) is no longer valid and a more careful approach must be taken. This will be discussed in more detail in section 5.4.2.

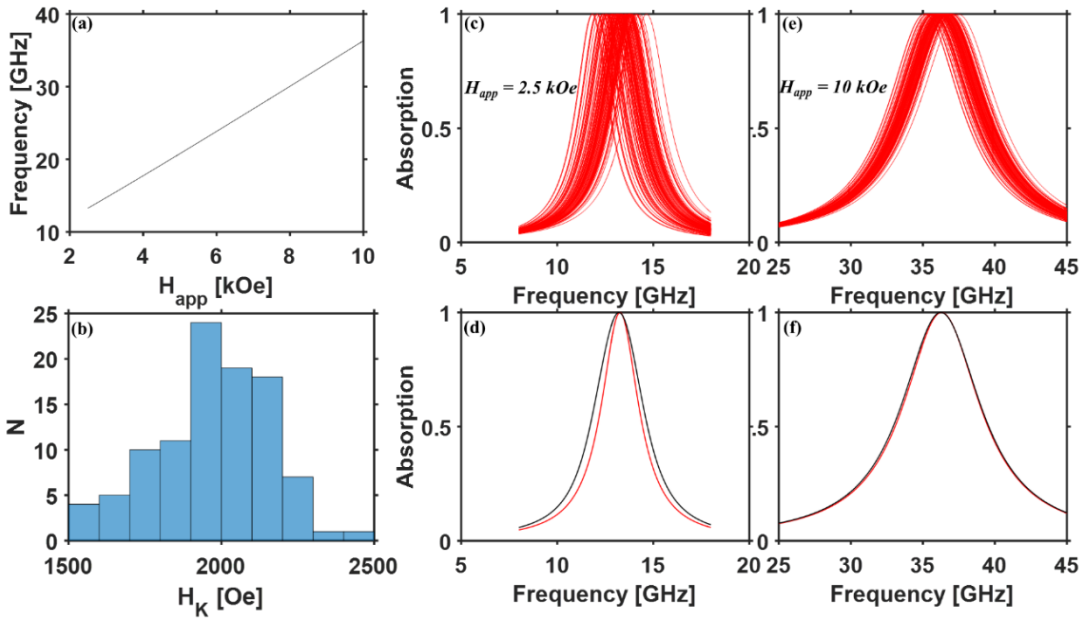

Fig. 2.9. (a) Kittel frequency of a sample in an applied field canted 30^o from surface normal with an anisotropy field $H_K = 2kOe$ and a gyromagnetic ratio $\boldsymbol{\gamma}$=2x10^7 [Hz/Oe]. (b) Histogram of spatially varying anisotropy field centered around 2kOe considered in the simulation. (c) Resonance curves at an applied field of 2.5kOe superimposed upon one another for each of the anisotropy fields considered. (d) Comparison between the ensemble resonance (black) and the intrinsic resonance (red) show appreciable broadening due to IHB. (e) Resonance curves of the same sample in an applied field of 10kOe. (f) The ensemble and intrinsic behavior are once again compared and are nearly identical.

2.4.2.2 Two-Magnon Scattering

Another source of extrinsic damping that must be considered is known as *two-magnon scattering* (TMS), which is the annihilation of a uniform precession (k=0) magnon into a finite-length spin wave ($k \neq 0$) magnon with the same frequency (Fig. 2.10) [1, 48]. Interestingly, because the energy is not transferred out of the magnetic system it is not a true damping process, but rather a spin-dephasing process; nonetheless, the apparent damping of the uniform mode will be larger than the intrinsic damping as a result. In a perfectly uniform film, all spin wave modes are independent,

decoupled normal modes of the system and scattering between states is not possible. Variations in the local field due to imperfections mediate scattering of the uniform mode into higher order spin waves. However, it should be noted that in some cases TMS can be avoided. Just as we saw with IHB when the applied field is large - with respect to the sample magnetization - the TMS contribution becomes negligible and the damping can be evaluated by the linear slope of the linewidth [48]. Secondly, when the polar angle of the magnetization is smaller than 45° there are no degenerate spin waves for the uniform precession to scatter into and TMS is not operative. Although this is easily achieved in cavity-based FMR and BLS studies by simply applying the field in the normal direction, this geometry is incompatible with polar TR-MOKE measurements because the system is only sensitive to changes in m_z. Instead, the TR-MOKE signal is largest when the magnetization is canted, and in this case the TMS contribution to the damping must be quantified to extract the intrinsic Gilbert damping of the system.

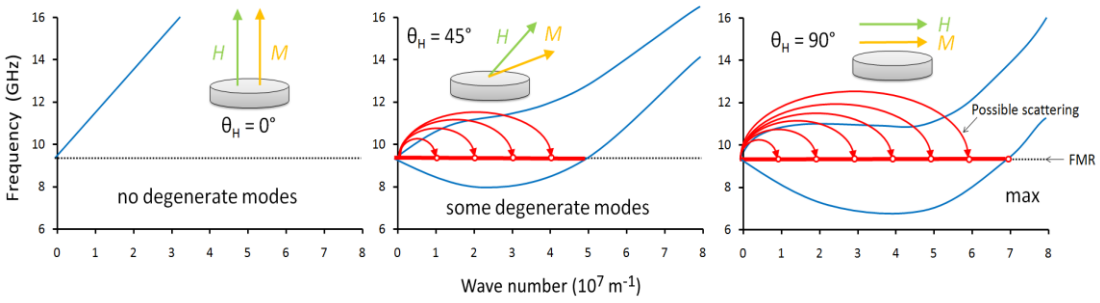

Fig. 2.10. Spin-wave dispersion plots for magnetic fields applied at different angles $\boldsymbol{\theta_H}$.There are no modes degenerate with the fundamental mode in the out-of-plane configuration, while there are several such modes in the in-plane configuration. Taken from **[49]**.

Because the TMS process intrinsically depends on the presence of a scattering site, the physical nature of the defect plays a crucial role in determining the character of the scattering process. For example, Arias and Mills [50] considered three distinct sources of inhomogeneity that enable TMS: (i) spatially inhomogeneous Zeeman energy, (ii) spatially-varying dipolar energy, and (iii) inhomogeneous interfacial anisotropy due to surface roughness. The authors derived formulas for each type of defect that required precise knowledge of the geometry and magnitude of the scatterer. As a result, for one to truly estimate the contribution of magnon scattering to the damping, the microstructural properties of the sample must be precisely known. However, authors found that scattering due to (iii) is the prominent source of TMS in ultrathin films, therefore, to a first approximation the model for this case need only be considered.

To determine an expression for the TMS contribution to the apparent damping of the uniform mode in ultrathin films, we first express the self-energy *U* of the precession as [51]

$$\mathrm{U}(0,\omega_0) = \frac{\Sigma_{\boldsymbol{k}}\gamma^2 N(0,\boldsymbol{k})}{\omega_k^2 - \omega_0^2 + i\omega_0\delta\omega_k} \tag{2.4.7}$$

where ω_k and $\delta\omega_k$ are the spin wave dispersion relation and inverse lifetime of the spin wave, respectively, and $N(0,\boldsymbol{k})$ is the scattering intensity defined as

$$N(0,\boldsymbol{k}) = \frac{\gamma^2}{3} h'(0,\boldsymbol{k})^2 (H_{XX} + H_{YY})^2 \tag{2.4.8}$$

The functions H_{XX} and H_{YY} are extensions of H_1 and H_2 described in Eqs. (2.3.22) and (2.3.23) with k-dependent terms arising from the exchange energy described by Eq. (2.2.27). The addition of the exchange energy leads to the following expressions

$$H_{XX} = H_1 + 4\pi M_s(1 - N_k)\left(\frac{k_x}{k}\right)^2 + \left(\frac{2A_{ex}}{M_s}\right)k^2 \tag{2.4.9}$$

$$H_{YY} = H_2 + 4\pi M_s N_k \sin(\theta)^2 + 4\pi M_s(1 - N_k)\cos(\theta)^2\left(\frac{k_y}{k}\right)^2 + \left(\frac{2A_{ex}}{M_s}\right)k^2 \tag{2.4.10}$$

where k_x and k_y are the x- and y-components of the wave vector, respectively, A_{ex} is the exchange stiffness constant, h' is a random magnetic field that causes scattering, and N_k is the demagnetization factor of the spin waves given by

$$N_k = \frac{1 - e^{-kd}}{kd} \tag{2.4.11}$$

In order to calculate $N(0,\boldsymbol{k})$ as a function of h', the correlation function $C(\boldsymbol{k})$ can be used as follows

$$|h'(0,\boldsymbol{k})|^2 = \langle h'^2\rangle C(\boldsymbol{k}) \tag{2.4.12}$$

where $C(\boldsymbol{k})$ is given by

$$C(\boldsymbol{k}) = \frac{2\pi\xi}{(1 + (k\xi)^2)^{\frac{3}{2}}} \tag{2.4.13}$$

Here, ξ is the correlation length of the inhomogeneous magnetic field which mediates the scattering process. The TMS contribution to the precession lifetime can now be expressed as

$$\frac{1}{\tau_{TMS}} = \frac{Im\{U(0,\omega_0\}}{\omega_0} = \frac{N_0 \Sigma_{\boldsymbol{k}} C(\boldsymbol{k})}{\omega_0} Im\left\{\frac{1}{\omega_k^2 - \omega_0^2 + i\omega_0 \delta\omega_k}\right\} \tag{2.4.14}$$

where N_0 is defined as

$$N_0(\boldsymbol{k}) = \frac{\gamma^4}{3}\left(H_{XX}(\boldsymbol{k}) + H_{YY}(\boldsymbol{k})\right)^2 \langle h'^2 \rangle \tag{2.4.15}$$

and the spin wave frequency and lifetime, ω_k and τ_k, respectively, are determined by the relations

$$\omega_k = \gamma\sqrt{H_{XX}(\boldsymbol{k}) H_{YY}(\boldsymbol{k})} \tag{2.4.16}$$

$$\delta\omega_k = \frac{1}{\tau_k} = \alpha\gamma\left(H_{XX}(\boldsymbol{k}) + H_{YY}(\boldsymbol{k})\right) \tag{2.4.17}$$

Remarkably, despite the complex derivation up to this point only 3 parameters, ξ, h', and α must be allowed to vary when fitting Eq. (2.4.14) to the experimentally observed damping. As an example, in Fig. 2.11 below, Eq. (2.4.14) is used to estimate the TMS contribution to the damping of an unpatterned, 30 nm thick Ni film measured using TR-MOKE. At small applied fields the TMS contribution is relatively large and the spin wave manifold is broad, however, at large applied fields the extrinsic contribution

becomes negligible as and effective damping is nearly identical to the intrinsic value of 0.03

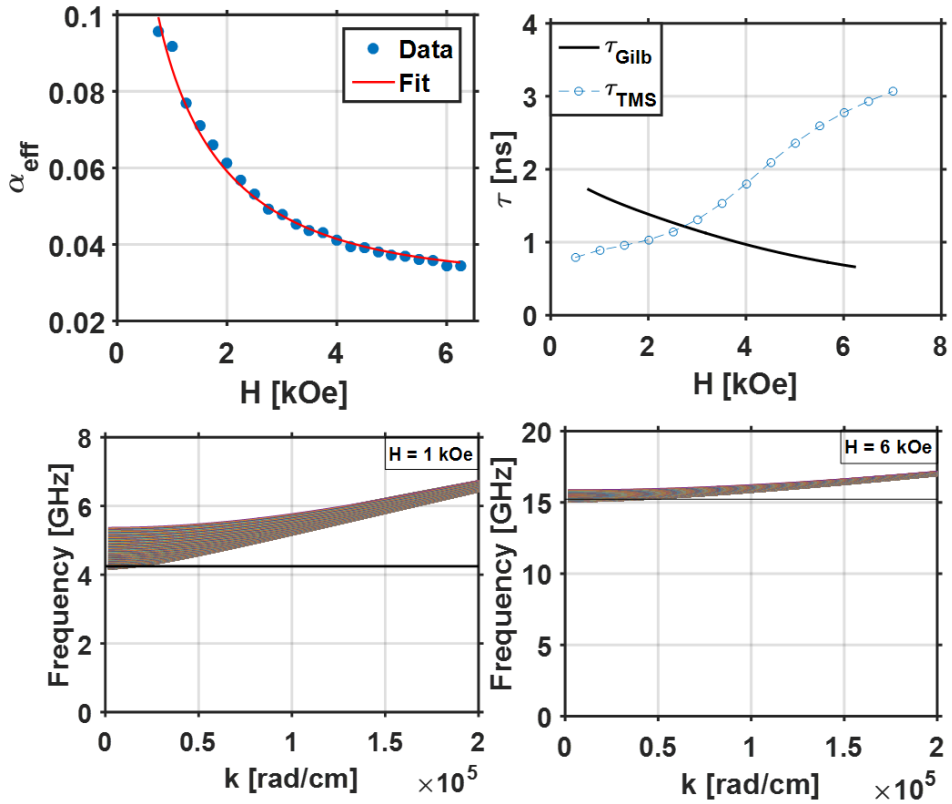

Fig. 2.11. (a) Effective damping parameter measured on a 30nm thick Ni film with an applied field canted 30° from the surface normal. (b) Estimated TMS contribution after fitting the data using Eq. (2.4.14) to obtain $\boldsymbol{\xi \sim 60}$ nm and $h' \sim 46$ Oe. (c,d) spin wave manifolds of the Ni film for two exemplary cases, $H_{app} = 1$ kOe (c) and 6 kOe (d).

CHAPTER 3
Measurement Methods

In this chapter, optical techniques used to probe the magnetization of samples will be explored. The Faraday and magneto-optic Kerr effects (MOKE) will be reviewed and the physical origin of these effects will be explored from the standpoint of the Lorentz oscillator model. This will lead to a more general discussion on the magneto-optic effects and the phenomenological dielectric tensor. Analytical descriptions of far-field MOKE measurements of nanomagnetic structures will be reviewed with emphasis on maximizing MOKE sensitivity. To this end, the transfer-matrix and Yeh formalisms will be covered and used to demonstrate the design of cavity-enhancement (CE) layers which enable the detection of magnetic structures well below the diffraction limit. With the theoretical descriptions established, the experimental methods to detect magneto-optic effects will be presented. Finally, the time-resolved (TR-MOKE) method will be introduced, including details about the setups used in the studies presented in this thesis, as well as the analysis techniques used to parse the experimental data.

3.1 Magneto-Optic Effects

Magneto-optics (MO) describes the interaction between light and magnetic fields or spontaneously magnetized bodies. In 1845, Michael Faraday discovered the first magneto-optic effect, the *Faraday effect*, in which he observed that a polarized beam of light incurs a polarization rotation when passed through a magnetic material

or a field applied along the propagation direction [52]. In fact, this discovery was the first experimental evidence of the electromagnetic nature of light and was crucial to the development of electromagnetic theory. Approximately three decades after Faraday's discovery Kerr observed a similar phenomenon – a polarized beam experiences a polarization rotation upon reflection from a magnetized body, this effect is known as the *magneto-optic Kerr effect* [53]. A similar effect, magnetic double refraction, was observed in the 19th century by Voigt while studying optical properties of vapors in the presence of strong magnetic fields [54]. A few years later, Cotton and Mouton reported the same effect in paramagnetic liquids [55]. All of these effects are based on the interaction of visible light with matter; thus, they are known as *conventional* magneto-optics. Analogous effects exist at shorter wavelengths (X-rays) and are still relatively new additions to the magneto-optic family.

3.1.1 Wave Equation

In order to understand the magneto-optic effects, one must first understand the interactions between light and matter which are described by Maxwell's equations [26]

$$\nabla \cdot \boldsymbol{D} = \rho \tag{3.1.1}$$

$$\nabla \cdot \boldsymbol{B} = 0 \tag{3.1.2}$$

$$\nabla \times \boldsymbol{E} = -\frac{\partial \boldsymbol{B}}{\partial t} \tag{3.1.3}$$

$$\nabla \times \boldsymbol{H} = \boldsymbol{j} + \frac{\partial \boldsymbol{D}}{\partial t} \tag{3.1.4}$$

where $\boldsymbol{H}$ and $\boldsymbol{B}$ are the magnetic field and induction, respectively, $\boldsymbol{E}$ and $\boldsymbol{D}$ are the electric field and displacement, respectively, ρ is the electric charge and $\boldsymbol{j}$ is the current density. The fields described above can be related to materials via the following relationships [29]

$$\boldsymbol{D} = \epsilon_0 \boldsymbol{\epsilon} \boldsymbol{E} = \epsilon_0 \boldsymbol{E} + \boldsymbol{P} \tag{3.1.5}$$

$$\boldsymbol{B} = \mu_0 \boldsymbol{\mu} \boldsymbol{H} = \mu_0 (\boldsymbol{H} + \boldsymbol{M}) \tag{3.1.6}$$

$$\boldsymbol{j} = \boldsymbol{\sigma} \boldsymbol{E} \tag{3.1.7}$$

where, $\boldsymbol{P}$ is the polarization vector, and $\boldsymbol{\epsilon}$, $\boldsymbol{\mu}$, $\boldsymbol{\sigma}$ are the permittivity-, permeability-, and conductivity-tensors, respectively.

For electrically neutral media (e.g. air) there is no charge or current, therefore, in this case electromagnetic radiation can propagate as an electromagnetic wave. Using the vector calculus property that the divergence of the curl of a vector field is 0, Eqs. (3.1.1) and (3.1.4) can be combined to derive the following

$$\nabla \cdot (\nabla \times \boldsymbol{H}) = \nabla \cdot \boldsymbol{j} + \frac{\partial}{\partial t} (\nabla \cdot \boldsymbol{D}) = \nabla \cdot \boldsymbol{j} + \frac{\partial \rho}{\partial t} = 0 \tag{3.1.8}$$

This describes the conservation of charge and leads to an important result – that only the fields of the light wave can generate currents and charge-density fluctuations.

Now, if we take the curl of the previous equaiton and make use of Eqs. (3.1.5-7) we end up with

$$\nabla \times (\nabla \times \boldsymbol{E}) = \nabla \times \left(-\frac{\partial \boldsymbol{B}}{\partial t}\right) = -\mu_0 \boldsymbol{\mu}\left(\nabla \times \frac{\partial \boldsymbol{H}}{\partial t}\right)$$
$$= -\mu_0 \boldsymbol{\mu}\frac{\partial}{\partial t}\left(\boldsymbol{j} + \frac{\partial \boldsymbol{D}}{\partial t}\right) = -\mu_0 \boldsymbol{\mu}\left(\boldsymbol{\sigma}\frac{\partial \boldsymbol{E}}{\partial t} + \epsilon_0 \boldsymbol{\epsilon}\frac{\partial^2 \boldsymbol{E}}{\partial t^2}\right) \quad (3.1.9)$$

Recalling the following property from vector calculus $\nabla \times (\nabla \times \boldsymbol{E}) = \nabla(\nabla \cdot \boldsymbol{E}) - (\nabla \cdot \nabla)\boldsymbol{E}$ and plugging it into Eq. (3.1.9), we obtain the wave equation

$$\nabla(\nabla \cdot \boldsymbol{E}) - \nabla^2 \boldsymbol{E} + \mu_0 \boldsymbol{\mu}\left(\boldsymbol{\sigma}\frac{\partial \boldsymbol{E}}{\partial t} + \epsilon_0 \boldsymbol{\epsilon}\frac{\partial^2 \boldsymbol{E}}{\partial t^2}\right) = 0 \quad (3.1.10)$$

If the medium is non-conductive ($\sigma \approx 0$), the wave equation is satisfied by a temporally- and spatially harmonic electric field

$$\boldsymbol{E} = E_0 e^{i(\boldsymbol{k}\cdot\boldsymbol{r} - \omega t)} \quad (3.1.11)$$

where $\boldsymbol{k}$ is the wavevector of the light, and $\boldsymbol{r}$ is the position vector. The E-field in the equation above is known as a *plane wave*, and per Eq. (3.1.4) the magnetic field must have a similar form and be orthogonal to the electric field and propagation direction (as shown in Fig. 3.1).

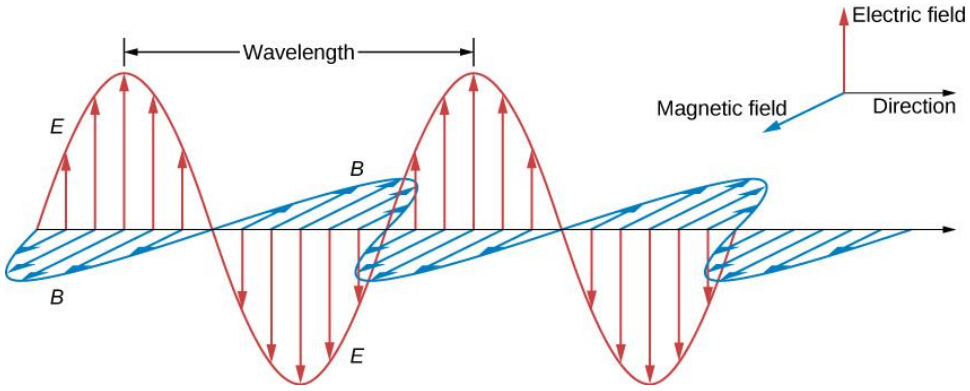

Fig. 3.1. Electric and magnetic fields of light described by Eq. (3.1.11).

The magnitude of the wave vector is determined by the refractive index and wavelength in vacuum, n and λ_0, respectively, as follows [56]

$$|\boldsymbol{k}| = nk_0 = n\frac{2\pi}{\lambda_0} \tag{3.1.12}$$

Because the wave number is directly related to the frequency and velocity of a wave by the relation $|\boldsymbol{k}| = \omega/v$, the velocity of the light in dielectric media must be

$$v = \frac{c_0}{n} \tag{3.1.13}$$

where c_0 is the speed of light in vacuum.

Since most technologically relevant magnetic materials are metals, we should also consider the solutions to Eq. (3.1.10) for media with finite conductivity. The derivation is greatly simplified by replacing the differential operator using the relation $\nabla \rightarrow i\boldsymbol{k}$ [57]. To see why this is possible, consider the divergence of the electric field defined in Eq. (3.1.11)

$$\nabla \cdot \boldsymbol{E} = \frac{\partial E_x}{\partial x} + \frac{\partial E_y}{\partial y} + \frac{\partial E_z}{\partial z} = \left(ik_x E_{x,0} + ik_y E_{y,0} + ik_z E_{z,0}\right)e^{i(\boldsymbol{k}\cdot\boldsymbol{r}-\omega t)} = i\boldsymbol{k}\cdot\boldsymbol{E} \tag{3.1.14}$$

or, similarly, the x-component of the curl

$$(\nabla \times \boldsymbol{E})_x = \frac{\partial E_z}{\partial y} - \frac{\partial E_y}{\partial z} = \left(ik_y E_{z,0} - ik_z E_{y,0}\right)e^{i(\boldsymbol{k}\cdot\boldsymbol{r}-\omega t)} = i(\boldsymbol{k}\times\boldsymbol{E})_x \tag{3.1.15}$$

which generalizes to

$$\nabla \times \boldsymbol{E} = i\boldsymbol{k}\times\boldsymbol{E} \tag{3.1.16}$$

In addition, the substitution $\frac{\partial}{\partial t} \rightarrow -i\omega$ helps to simplify the derivation even further. We can again use Eq. (3.1.11) to justify this as follows

$$\frac{\partial \boldsymbol{E}}{\partial t} = -i\omega E_0 e^{i(\boldsymbol{k}\cdot\boldsymbol{r}-\omega t)} = -i\omega \boldsymbol{E} \tag{3.1.17}$$

Now, Eq. (3.1.10) can be rewritten in the following way

$$(\boldsymbol{k}\cdot\boldsymbol{E})\boldsymbol{k} - \boldsymbol{k^2 E} + \mu_0\epsilon_0\boldsymbol{\mu}\omega^2\tilde{\boldsymbol{\epsilon}}\boldsymbol{E} = 0 \tag{3.1.18}$$

where $\boldsymbol{k}$, n, and $\tilde{\boldsymbol{\epsilon}}$ are now complex and defined as follows

$$\boldsymbol{k} = \boldsymbol{k}' + i\boldsymbol{k}'' \tag{3.1.19}$$

$$n = \frac{\boldsymbol{k}}{k_0} = \frac{\lambda_0}{2\pi}(\boldsymbol{k}' + i\boldsymbol{k}'') = n' + in'' \tag{3.1.20}$$

$$\tilde{\boldsymbol{\epsilon}} = \boldsymbol{\epsilon} + \frac{i\boldsymbol{\sigma}}{\epsilon_0\omega} \tag{3.1.21}$$

Because the atomic moments of magnetic materials cannot respond at optical frequencies, we can assume the permeability is isotropic and equal to unity. This simplification leads to the following expression for Eq. (3.1.18) [57]

$$\frac{k_i(\boldsymbol{k}\cdot\boldsymbol{E})}{k_0^2} - n^2 E_i + \sum_{j=1}^{3} \tilde{\epsilon}_{ij} E_j = 0 \tag{3.1.22}$$

For normally incident light this equation can be easily solved and the electric field of the wave propagating in lossy media can be determined as

$$\boldsymbol{E} = E_0 e^{i\left(\frac{\omega}{c_0}(n'+in'')z-\omega t\right)} = E_0 e^{i\left(\frac{\omega}{c_0}n'z-\omega t\right)} e^{\frac{-\omega}{c_0}n''z} \tag{3.1.23}$$

This equation can be decomposed into two parts – a harmonic function like Eq. (3.1.11) and an exponential decay of the field amplitude. The flux of radiant energy per unit area is known as the *irradiance* and is proportional to the square of the electric field. Using the E-field in the equation above to calculate the irradiance leads to the *Beer-Lambert law*

$$I(z) = \frac{1}{2} c_0 \tilde{\epsilon} |\boldsymbol{E}|^2 = I_0 e^{-\alpha z} \tag{3.1.24}$$

$$\alpha = \frac{2\omega n''}{c_0} \tag{3.1.25}$$

Here, I_0 is the irradiance at the surface, and α is the absorption coefficient of the material in units of m^{-1}, taking the inverse yields the *skin depth*

$$\delta = \frac{1}{\alpha} \tag{3.1.26}$$

The skin depth is the length at which the flux density drops by a factor of e^{-1}, and is typically between 5-15 nm for metals. This is a direct limitation to magneto-optic studies of magnetic heterostructures (eg. STT-MRAM), because if the layer of interest is farther from the surface than δ, there will be virtually no light reflected from that layer to be analyzed.

3.1.2 Lorentz Model

In the late 19th century, Dutch physicist Hendrik Antoon Lorentz attempted to describe the interaction between atoms and electric fields in classical terms [58]. He

proposed that electrons were bound to the nuclei by a spring-like force (Fig. 3.2) that behaves according to Hooke's law $F = kx$, where x is the displacement vector from equilibrium. Thus, an electron in the presence of an applied field would experience a coulombic force that would compress or

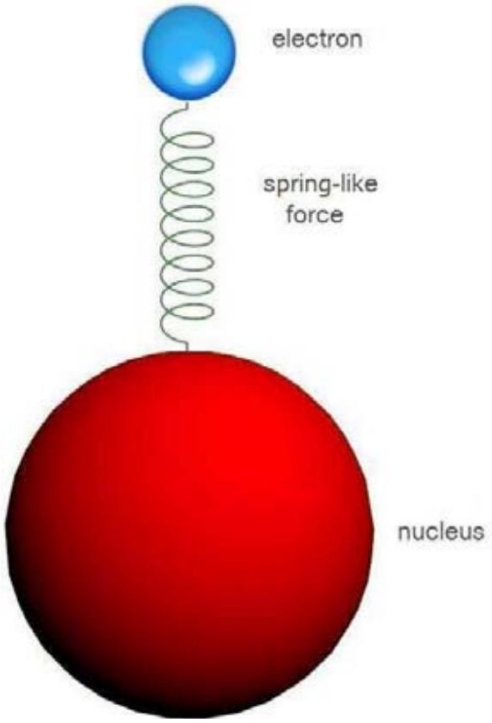

Fig. 3.2. Electron bound to a nucleus by a "spring-like" force that gives rise to the oscillatory behavior of the electron.

stretch the spring, which in turn would cause the electron to oscillate if the field is removed. If we assume position of the nucleus is fixed, which is justified because $m_N >> m_e$, then according to Newton's 2nd law ($F = m_e \frac{\partial^2 x}{\partial x^2}$) a spring-like force leads to the following equation of motion

$$\frac{\partial^2 x}{\partial x^2} = -\frac{k}{m_e} x \tag{3.1.27}$$

The non-trivial solution to this problem is an undamped oscillation about equilibrium. Systems that obey Eq. (3.1.27) are commonly referred to as *harmonic oscillators*, due to their time-dependent motion

$$x(t) = Acos(\omega_0 t) \tag{3.1.28}$$

where $\omega_0 = \sqrt{k/m}$ is the natural frequency of the system.

Because we are ultimately interested in using the Lorentz model to describe the magneto-optic phenomena, our derivation will differ slightly from Lorentz's which did not consider the case of a magnetized body. In fact, the first person to use the Lorentz oscillator model to explain gyrotropic effects was physicist George Fitzgerald in 1898 [59]. The basic idea of the Lorentz model is that the medium is composed of a uniform density of harmonic oscillators, each of which have a fundamental charge *–e*. For the purpose of simplifying our derivation, we can assume that the magnetic field is uniform along the z-direction ($\boldsymbol{B} = B_0\hat{\boldsymbol{z}}$). Now, if an electromagnetic wave is propagating along the z-direction and is linearly polarized in the x-direction, the electric field in vacuum is given by

$$\boldsymbol{E}(z,t) = \frac{1}{2}E_0 e^{i(k_0 z - \omega t)}\hat{\boldsymbol{x}} \tag{3.1.29}$$

According to the Faraday effect, we know that the polarization will incur a rotation after propagating through a magnetic field, or mathematically, the E-field will have a nonzero y-component such that

$$\boldsymbol{E}(z,t) = \frac{1}{2}\left(E_x(z)\hat{\boldsymbol{x}} + E_y(z)\hat{\boldsymbol{y}}\right)\mathrm{e}^{i(kz-\omega t)} \tag{3.1.30}$$

To arrive at this result, we must begin by considering the force each electron feels due to the electric field from the light, the magnetic field, and its attraction to the nucleus

$$\boldsymbol{F} = -e(\boldsymbol{E} + \boldsymbol{v} \times \boldsymbol{B}) - m_e\omega_0^2\boldsymbol{r} \tag{3.1.31}$$

where **r** is the displacement of the electron. Here, because the electric field must be orthogonal to $\boldsymbol{k}$, the electron oscillates in the x-y plane which means the displacement can be expressed as

$$\boldsymbol{r}(t) = x(z,t)\hat{\boldsymbol{x}} + y(z,t)\hat{\boldsymbol{y}} \tag{3.1.32}$$

For visible wavelengths, we can assume that $r \ll \lambda$ which allows us to approximate the electron as a dipole so we can evaluate the amplitude and phase of the optical field at the equilibrium position of the oscillator. Now, using the force defined in Eq (3.1.31) the equations of motion for the oscillator are

$$\frac{\partial^2 x}{\partial t^2} + \omega_0^2 x = -\frac{eE_x(z)e^{i(kz-\omega t)}}{2m_e} - \frac{eB_0}{m_e}\frac{\partial y}{\partial t} \tag{3.1.33}$$

$$\frac{\partial^2 y}{\partial t^2} + \omega_0^2 y = -\frac{eE_y(z)e^{i(kz-\omega t)}}{2m_e} + \frac{eB_0}{m_e}\frac{\partial x}{\partial t} \tag{3.1.34}$$

The derivation can be simplified by limiting the situation to small polarization rotations, which means the electric field amplitude in the x-direction is approximately unchanged, or $E_x(z) \approx E_x(0) = E_0$. This assumption also allows us to neglect the

influence of the y-component of the field on the dynamics, and Eq. (3.1.33) can be rewritten as

$$\frac{\partial^2 x}{\partial t^2} + \omega_0^2 x = -\frac{eE_0 e^{i(kz-\omega t)}}{2m_e} \tag{3.1.33b}$$

This steady-state solution to this equation can now be directly solved and used to determine Eq. (3.1.34) as follows [59]

$$x(z,t) = -\frac{eE_0 e^{i(kz-\omega t)}}{2m_e(\omega_0^2 - \omega^2)} \tag{3.1.35}$$

$$y(z,t) = -\frac{eE_y(z) e^{i(kz-\omega t)}}{2m_e(\omega_0^2 - \omega^2)} + \frac{e^2 B_0 E_0 e^{i(kz-\omega t)} i\omega}{2m_e^2(\omega_0^2 - \omega^2)^2} \tag{3.1.36}$$

Because our derivation of the wave equation leading to Eq. (3.1.10) was limited to media with no charges we were able to neglect the polarization field $\boldsymbol{P}$ defined by (3.1.5). Using the position vector of the electrons defined in Eq. (3.1.32), a concentration of *N* electrons per volume will generate the following $\boldsymbol{P}$-field

$$\boldsymbol{P}(t) = -Ne\boldsymbol{r}(t) = -Ne(x(z,t)\hat{\boldsymbol{x}} + y(z,t)\hat{\boldsymbol{y}}) \tag{3.1.37}$$

and the wave equation with this additional term is now

$$\frac{\partial^2 \boldsymbol{E}}{\partial z^2} - \frac{1}{c_0^2}\frac{\partial^2 \boldsymbol{E}}{\partial t^2} = \frac{1}{\epsilon_0 c_0^2}\frac{\partial^2 \boldsymbol{P}}{\partial t^2} \tag{3.1.38}$$

Because we have explicitly defined the polarization, we can simply plug it in to the equation above and solve for the x-component of the field

$$(n^2 - 1)E_0 = \frac{Ne^2E_0}{\epsilon_0 m_e(\omega_0^2 - \omega^2)} \tag{3.1.39}$$

A similar approach can be followed to solve for the y-component (neglecting the $\partial^2\boldsymbol{E}/\partial z^2$ terms due to the slowly-varying field approximation)

$$2in\frac{\partial E_y(z)}{\partial z} = \frac{iNe^3k_0B_0E_0}{m_e^2\epsilon_0}\frac{\omega}{(\omega_0^2 - \omega^2)^2} \tag{3.1.40}$$

Since the electromagnetic wave at the surface was purely x-polarized the initial value of the y-component was zero ($E_y(0) = 0$), and integrating to solve for E_y yields

$$E_y(dz) = \frac{Ne^3B_0E_0}{2nm_0^2c_0\epsilon_0}\frac{\omega^2}{(\omega_0^2 - \omega^2)^2}dz \tag{3.1.41}$$

We can now express the Faraday rotation angle θ that the electromagnetic wave picks up as it propagates through a magnetic field as

$$\theta_F = \frac{E_y}{E_x} = \frac{Ne^3B_0L}{2nm_e^2c\epsilon_0}\frac{\omega^2}{(\omega_0^2 - \omega^2)^2} = VLB_0 \tag{3.1.42}$$

where the small-angle approximation $\sin(\theta) \approx \theta$ was used and the *Verdet* constant V was defined as [59]

$$V = \frac{Ne^3\omega^2}{2nm_e^2c\epsilon_0(\omega_0^2 - \omega^2)^2} \tag{3.1.43}$$

It is hard to see, but this definition of V allows us to predict which materials have a large Verdet constant. We must re-examine Eq. (3.1.39), which we derived by omitting

the Lorentz force term in the equation of motion. Rearranging the terms provides a direct expression for the refractive index

$$n = \sqrt{1 + \frac{Ne^2}{\epsilon_0 m_e(\omega_0^2 - \omega^2)}} \tag{3.1.44}$$

which is actually the fundamental result of the Lorentz model. If we take the derivative of this quantity with respect to the driving frequency ω, we get (after a lot of rearranging)

$$\frac{dn}{d\omega} = \frac{Ne^2\omega}{nm_e\epsilon_0(\omega_0^2 - \omega^2)^2} \tag{3.1.45}$$

and we see that the Verdet constant is proportional to the dispersion of the material as

$$V = \frac{e}{2m_e c}\omega\frac{dn}{d\omega} \tag{3.1.46}$$

Remarkably, treating the electrons as simple harmonic oscillators not only led us to the phenomenological expression for Faraday rotation, but also provided a meaningful connection between the Verdet constant and optical properties of the material. Of course, we now know that the classical approach has severe limitations and that light-matter interactions are ultimately governed by quantum mechanics. Approximately half a century after Fitzgerald derived this result from the basis of the Lorentz model, Sommerfield showed that this effect was caused by the different refractive indices for left- and right-hand circularly polarized (LHCP and RHCP,

respectively) light propagating in magnetic fields, which can be derived from first-principles calculations. The helicity-dependent refractive indices are

$$n_{RHCP} = \sqrt{1 + \frac{Ne^2}{\epsilon_0 m_e}\left(\frac{1}{\omega_0^2 - \omega^2 + \frac{eB_0}{m_e\omega}}\right)} \approx n\sqrt{\omega - \frac{eB_0}{2m_e}} \tag{3.1.47}$$

$$n_{LHCP} = \sqrt{1 + \frac{Ne^2}{\epsilon_0 m_e}\left(\frac{1}{\omega_0^2 - \omega^2 - \frac{eB_0}{m_e\omega}}\right)} \approx n\sqrt{\omega + \frac{eB_0}{2m_e}} \tag{3.1.48}$$

where the approximation $\left(\omega^2 \pm \frac{eB_0\omega}{m_e}\right) \approx \left(\omega \pm \frac{eB_0\omega}{2}\right)^2$ was used, and the difference between the two indices can be expressed as

$$n_{LHCP} - n_{RHCP} \approx \frac{eB_0}{m_e}\frac{dn}{d\omega} \tag{3.1.49}$$

3.1.1.3 Dielectric Tensor

As discussed in section (3.1.1.1), the inability of the spin system (permeability) to respond at optical frequencies means magneto-optic phenomena must be described by the permittivity tensor, which is precisely what we have shown in the previous section by directly connecting the Faraday effect to the dispersion. In this section, the dielectric tensor and the gyrotropic terms used to explain magneto-optic effects will be reviewed.

Before we consider the dielectric tensor and show its relation to the magneto-optic effects, we must discuss the constraints imposed by Maxwell's equations that govern the interaction of light and matter. Consider light propagating in vacuum ($n_1 \approx 1$) incident upon a dielectric material with refractive index n_2. If no charges are present at the surface, Maxwell's equations necessitate that incident, reflected, and transmitted waves have identical phase at the surface which is mathematically expressed as

$$(\boldsymbol{k_i} \cdot \boldsymbol{r})_{z=0} = (\boldsymbol{k_r} \cdot \boldsymbol{r})_{z=0} = (\boldsymbol{k_i} \cdot \boldsymbol{r})_{z=0} \tag{3.1.50}$$

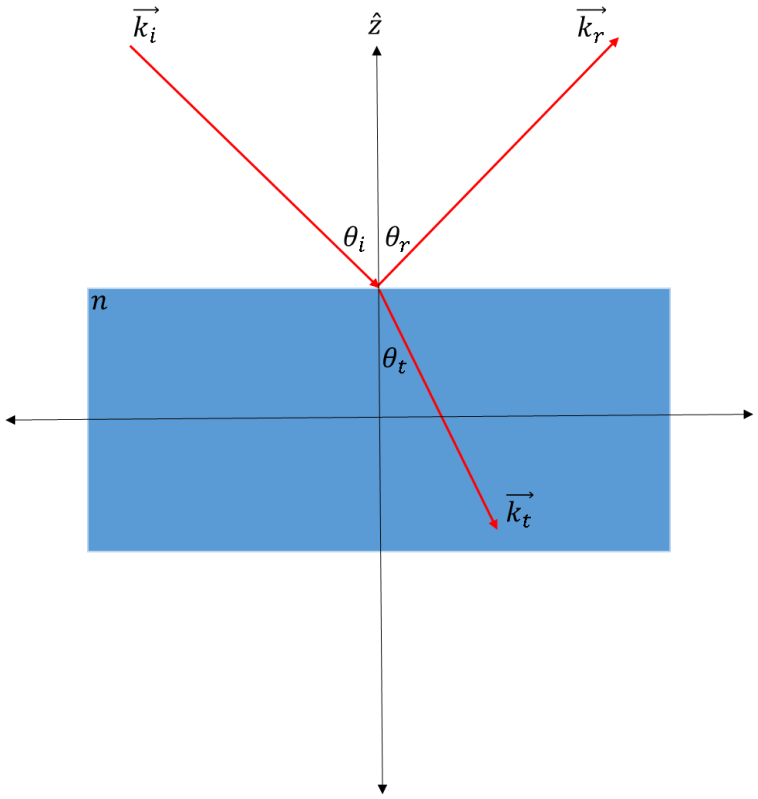

Fig. 3.3. Example of light striking dielectric surface used to derive Snell's law

Because the incident and reflected waves are in the same medium, the magnitude of the tangential component of the wavevector must be identical, thus, the angle of reflection must be identical to the angle of incidence

$$\frac{\omega}{c_0}\sin(\theta_i) = \frac{\omega}{c_0}\sin(\theta_r) \rightarrow \theta_i = \theta_r \tag{3.1.51}$$

Meanwhile, the refracted wavevector is enhanced by *n* and per Eq (3.1.50) the following must be true

$$k_{iz} = \frac{\omega}{c_0}\sin(\theta_i) = k_{tz} = \frac{n_2\omega}{c_0}\sin(\theta_t) \tag{3.1.52}$$

Cancelling out like-terms leaves us with Snell's law

$$n_1 \sin(\theta_i) = n_2 \sin(\theta_t) \tag{3.1.53}$$

Now we can move onto the permittivity, which we have already shown in Eq. (3.1.22) is a second rank tensor. First, we will consider the simplest case – a non-absorbing, nonmagnetic, isotropic material with the following dielectric properties

$$\boldsymbol{\epsilon_{iso}} = \begin{pmatrix} \epsilon_{iso} & 0 & 0 \\ 0 & \epsilon_{iso} & 0 \\ 0 & 0 & \epsilon_{iso} \end{pmatrix} \tag{3.1.54}$$

Because the tensor is diagonal, the displacement vector of light in the material is along the same direction as the incident electric field. Thus, the polarization of the light will remain constant as it interacts with the material. For samples with more complicated optical properties, the permittivity is described as the sum of several contributions as [57]

$$\tilde{\boldsymbol{\epsilon}} = \boldsymbol{\epsilon_{iso}} + \boldsymbol{\epsilon_{br}} + \boldsymbol{\epsilon_{oa}} \tag{3.1.55}$$

where the first term is given above, $\boldsymbol{\epsilon_{br}}$ is a traceless matrix that describes conventional crystal birefringence, and $\boldsymbol{\epsilon_{oa}}$ is for optical activity – such as magneto-optic effects. In general, the gyrotropic effects are relatively small and to a first approximation we only need to consider terms that linearly depend on the magnetization. Therefore, the complete dielectric tensor of a magnetic body can be expressed as

$$\tilde{\boldsymbol{\epsilon}} = \epsilon_{iso}\begin{pmatrix} 1 & -iQ_v m_z & iQ_v m_y \\ iQ_v m_z & 1 & -iQ_v m_x \\ -iQ_v m_y & iQ m_x & 1 \end{pmatrix} \tag{3.1.56}$$

where Q_V is the Voigt magneto-optical constant defined as $Q_v = i\epsilon_{xy}/\epsilon_{iso}$, which is a material-specific and wavelength-dependent parameter that describes linear magneto-optic effects. In general, Q_V is a complex quantity that is dominated by the real part, and the order of magnitude is typically around 10^{-2}.

We will now examine how the magneto-optic elements in the dielectric tensor change the light-matter interaction. To keep the algebra as simple as possible we will consider the case of normal incidence with the magnetization along the direction of propagation, which we will choose to be along the z-direction. Inserting the tensor described in Eq. (3.1.22) into the wave equation we end up with the following system of equations [57]

$$(k_0^2\epsilon_{iso} - k_z^2)E_{x,0} - k_0^2\epsilon_{iso}iQ_v E_{y,0} + 0 = 0 \tag{3.1.57}$$

$$k_0^2\epsilon_{iso}iQ_v E_{x,0} + (k_0^2\epsilon_{iso} - k_z^2)E_{y,0} + 0 = 0 \tag{3.1.58}$$

From these two equations we can determine the characteristic equation from the determinant of the coefficient matrix

$$\epsilon_{iso}\left(\left(\epsilon_{iso}-\frac{k_z^2}{k_0^2}\right)^2-Q_v^2\epsilon_{iso}^2\right)=0 \tag{3.1.59}$$

which has the approximate solution (using $\sqrt{1+x}\approx\left(1+\frac{x}{2}\right)$ for $x\ll 1$)

$$k_z\approx\pm k_0\sqrt{\epsilon_{iso}}\left(1\pm\frac{Q_v}{2}\right) \tag{3.1.60}$$

The $\pm$ corresponds to waves propagating in the forward and retrograde directions. Inserting this solution into Eq. (3.1.57) directly yields the following

$$E_{y,0}=\pm iE_{x,0} \tag{3.1.61}$$

where the $\pm$ sign now corresponds to the quantity in parentheses in Eq. (3.1.60). Because we considered the case of normal incidence, we know that inside the material $k_z=nk_0$, therefore, we can solve for *n* as

$$n_\pm=\sqrt{\epsilon_{iso}}\left(1\pm\frac{Q_v}{2}\right) \tag{3.1.62}$$

The plus and minus subscript of *n* refer to the LHCP and RHCP light, respectively, which we first saw in Eq. (3.1.47). This result confirms that for light propagating along the magnetization, there are two normal modes corresponding to opposite helicities of circularly polarized waves. If the medium is absorbing, then the helicity-dependent index becomes complex just as in Eq. (3.1.20)

$$n_{\pm} = n'_{\pm} + in''_{\pm} \tag{3.1.63}$$

Before we consider how this result can be used to describe the MOKE, it will be helpful to briefly introduce the *Jones formalism* to describe the polarization state of light. Because there cannot be an electric field component along the direction of propagation, only two dimensions need to be considered to fully describe the polarization state. If we stick with light propagating in the z-direction as we have done up to this point, the Jones vector describing the polarization is [56]

$$\boldsymbol{J} = \begin{pmatrix} E_x \\ E_y \end{pmatrix} = \begin{pmatrix} E_{x,0} e^{i\delta_x} \\ E_{y,0} e^{i\delta_y} \end{pmatrix} \tag{3.1.64}$$

where the spatiotemporal phase $e^{i(k_z z - \omega t)}$ has been omitted because it is common to both components. For example, we can describe x-polarized light using the following Jones matrix

$$\boldsymbol{J_x} = \begin{pmatrix} 1 \\ 0 \end{pmatrix} \tag{3.1.65}$$

and right-hand circularly polarized light as

$$\boldsymbol{J_R} = \frac{1}{\sqrt{2}} \begin{pmatrix} 1 \\ -i \end{pmatrix} \tag{3.1.66}$$

Now, we can replace the permittivity tensor as well. For reflected light, the Jones matrix is defined as

$$\boldsymbol{R} = \begin{pmatrix} r_{xx} & r_{xy} \\ r_{yx} & r_{yy} \end{pmatrix} \tag{3.1.67}$$

Here, the reflection coefficients r_{ii} are determined by the boundary conditions of the electric and magnetic fields at the interface [26]

$$\epsilon_1 E_{1,\perp} = \epsilon_2 E_{2,\perp} \tag{3.1.68}$$

$$E_{1,\parallel} = E_{2,\parallel} \tag{3.1.69}$$

$$B_{1,\perp} = B_{2,\perp} \tag{3.1.70}$$

$$\frac{B_{1,\parallel}}{\mu_1} = \frac{B_{2,\parallel}}{\mu_2} \tag{3.1.71}$$

where (1,2) denote two different materials, and the subscripts ($\perp$, $\parallel$) are the field components perpendicular and parallel to the plane of incidence (Fig. 3.4), respectively. The relationships above are known as the *Fresnel conditions* and are most easily solved when the light is normally incident. Because we have just shown that the two normal modes of propagation in magnetic materials are left- and right-hand circularly polarized light, solving the wave equation at the boundary (using $\boldsymbol{E} = c\boldsymbol{B}/n$) yields two polarization-dependent reflection coefficients [57]

$$r(n_+) = \frac{E_{r,+}}{E_{i,+}} = \frac{1 - n_+}{1 + n_+} \tag{3.1.72}$$

$$r(n_-) = \frac{E_{r,-}}{E_{i,-}} = \frac{1 - n_-}{1 + n_-} \tag{3.1.73}$$

The helicity-dependent reflection coefficients are used to determine the matrix elements of $\boldsymbol{R}$ as follows

$$r_{xx} = r_{yy} = \frac{1}{2}\big(r(n_+) + r(n_-)\big) = \frac{1-n}{1+n} \tag{3.1.74}$$

$$r_{xy} = -r_{yx} = \frac{i}{2}\big(r(n_+) - r(n_-)\big) = -\frac{inQ_v}{(1+n)^2} \tag{3.1.75}$$

where n is the refractive index in the demagnetized state. Putting all of this together, consider a linearly polarized beam that is normally incident onto a sample with a magnetic moment anti-parallel to the propagation direction (eg. m_z =1). If we assume the light is polarized in the x-direction, then the reflected electric field is easily determined using the Jones formalism as follows [57]

$$\begin{pmatrix} E_{x,r} \\ E_{y,r} \end{pmatrix} = \begin{pmatrix} \frac{1-n}{1+n} & -\frac{inQ_v}{(1+n)^2} \\ \frac{inQ_v}{(1+n)^2} & \frac{1-n}{1+n} \end{pmatrix} \begin{pmatrix} 1 \\ 0 \end{pmatrix} = \begin{pmatrix} \frac{1-n}{1+n} \\ \frac{inQ_v}{(1+n)^2} \end{pmatrix} \tag{3.1.76}$$

This result shows that the y-component of the reflected electric field will be entirely imaginary if n is real, which means that linearly polarized light reflected from a magnetized dielectric would become elliptic. Conversely, highly dispersive media (eg. metals) will have a relatively large real component because the imaginary term in the complex refractive index is dominant, therefore, the polarization will rotate slightly. The result in Eq. (3.1.76) can be used to define the complex *Kerr rotation* θ_K^c for the polar geometry

$$\theta_k^c = \theta_k + i\xi_k = \frac{r_{xy}}{r_{xx}} = -\frac{inQ_v}{1-n^2} \tag{3.1.77}$$

where θ_k is the *Kerr rotation* and ξ_k is the *Kerr ellipticity*. In practice, it is much easier to analyze the Kerr rotation because only a polarizer is required, whereas to measure ξ_k more complicated optical components must be incorporated to compensate the ellipticity (eg. Babinet or Brace-Kohler compensators).

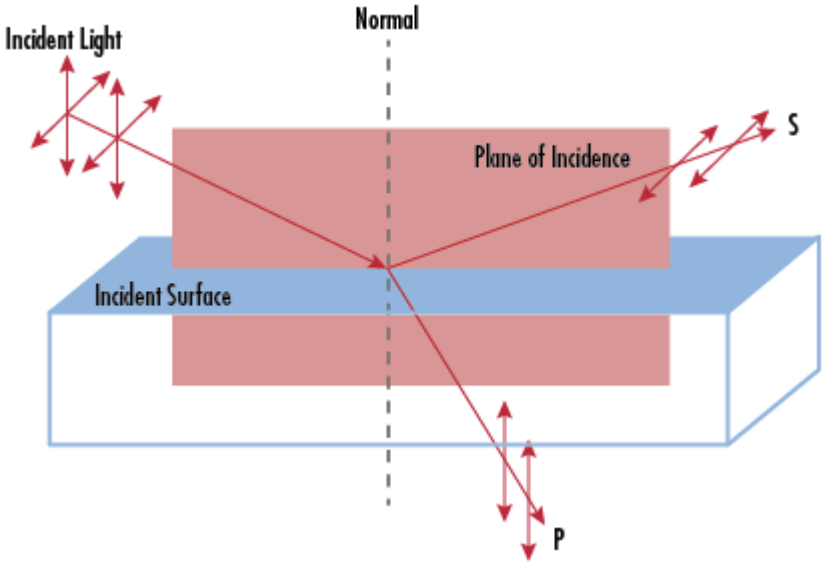

Fig. 3.4. Illustration of obliquely incident ray showing how the *s* and *p* components are defined.

For obliquely incident light (eg. Fig. 3.4), more general expressions for the reflection coefficients can be derived using the Fresnel conditions in Eqs. (3.1.68-71). Because the magnetic field is directly determined by the electric field at optical frequencies, we really only need to consider the E-field. Therefore, we define the perpendicular and parallel electric field components relative to the plane of incidence as the *s* and *p* components, respectively. In the (*s*, *p*) coordinate system the reflection matrix can then be expressed as

$$\boldsymbol{R} = \begin{pmatrix} r_{ss} & r_{ps} \\ r_{sp} & r_{pp} \end{pmatrix} \tag{3.1.78}$$

and the matrix elements, which are determined by the Fresnel relations, are [60]

$$r_{ss} = \frac{(n_1 \cos(\theta_1) - n_2 \cos(\theta_2))}{(n_1 \cos(\theta_1) + n_2 \cos(\theta_2))} \tag{3.1.79}$$

$$r_{pp} = \frac{(n_2 \cos(\theta_1) - n_1 \cos(\theta_2))}{(n_2 \cos(\theta_1) + n_1 \cos(\theta_2))} - \frac{i2n_1 n_2 \cos(\theta_1) \sin(\theta_2)\, Q_v m_x}{n_2 \cos(\theta_1) + n_1 \cos(\theta_2)} \tag{3.1.80}$$

$$r_{sp} = \frac{i n_1 n_2 \big(m_y \sin(\theta_2) + m_z \cos(\theta_2)\big) Q_v}{(n_2 \cos(\theta_1) + n_1 \cos(\theta_2))(n_1 \cos(\theta_1) + n_2 \cos(\theta_2)) \cos(\theta_2)} \tag{3.1.81}$$

$$r_{ps} = -\frac{i n_1 n_2 \cos(\theta_1) \big(m_y \sin(\theta_2) - m_z \cos(\theta_2)\big) Q_v}{(n_2 \cos(\theta_1) + n_1 \cos(\theta_2))(n_1 \cos(\theta_1) + n_2 \cos(\theta_2)) \cos(\theta_2)} \tag{3.1.82}$$

Here, m_i are the direction cosines of the magnetization, and the refractive indices n_1 and n_2 may be complex. When the light is normally incident, these equations simplify and are identical to the Fresnel coefficients in Eqs. (3.1.76).

3.1.2 MOKE Enhancement

Now that we have established a solid theoretical foundation to describe magneto-optic phenomena, we can turn our attention to the detection of nanometer-scale magnetic structures. Most nanomagnets that are of technological interest are well below the optical wavelength, thus, the size of the focused laser strongly affects the "detectability" of MOKE signals –especially in time-resolved studies where the precession angle is already very small.

The primary limitation of far-field MOKE studies is the size of the laser spot that is determined by diffraction. For a Gaussian beam, the parameter known as the

beam waist w_o defines the $1/e^2$ radius at the focal point. For a Gaussian beam focused through a microscope objective, the $1/e^2$ diameter is given by

$$2w_0 \approx \frac{1.22\lambda}{N.A.} \tag{3.1.83}$$

where *N.A.* is the numerical aperture of the objective defined as $N.A. = nsin(\theta)$. Here, n is the refractive index of the medium and θ is the aperture angle. Therefore, at best a high magnification system ($N.A. \approx 1$) can focus the laser down to a spot with a diameter that is slightly larger than the wavelength.

In Fig. 3.5 the excitation geometry of a beam tightly focused onto a nanomagnet is illustrated and clearly shows that a significant portion of the beam will be reflected from the nonmagnetic substrate. The reflected power from the nanomagnet and substrate are defined as $P_{R,mag}$ and $P_{R,sub}$, respectively, and are determined by the following integrals [61]

$$P_{R,mag} = R_{mag} \int_0^{\frac{D}{2}} 2\pi r I_0(r) dr \tag{3.1.84}$$

$$P_{R,sub} = R_{sub} \int_{\frac{D}{2}}^{\infty} 2\pi r I_0(r) dr \tag{3.1.85}$$

where $I_0(r)$ is the laser intensity distribution, R_i are the reflectivity coefficients, and D is the nanomagnet diameter.

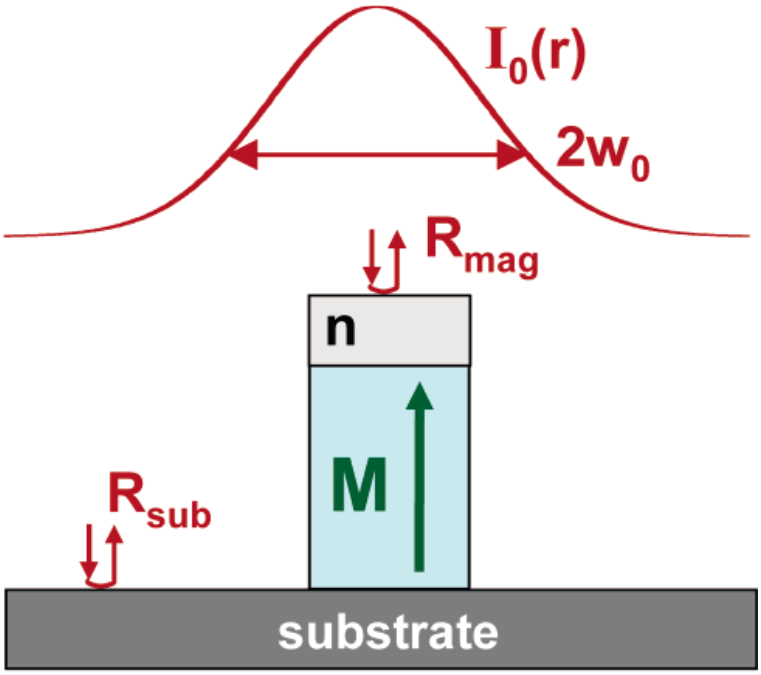

Fig. 3.5. Illustration of Gaussian intensity distribution of tightly focused laser beam probing a cylindrical nanomagnet. Because the beam waist is larger than the nanomagnet, the reflected signal will be a mixture of light reflected from the substrate and the magnet. Taken from **[61].**

Because the beam is Gaussian $I_0(r) \propto e^{-2r^2/w_0^2}$ the integration can be carried out analytically, and the effective Kerr rotation of the reflected beam is given as [61]

$$\theta_{k,eff} = \frac{\theta_k P_{R,mag}}{P_{R,mag} + P_{R,sub}} = \frac{\theta_k}{1 + \left(\frac{R_{sub}}{R_{mag}}\right)\left(e^{\frac{D^2}{2w_0^2}} - 1\right)^{-1}} \qquad (3.1.86)$$

Now, the critical role of the spot size is evident, ignoring the fraction (R_{sub}/R_{mag}) for the moment, for $D<2w_0$ the exponential term will dominate and quickly diminish $\theta_{k,eff}$. It is, therefore, crucial to minimize w_0 in MOKE studies of nanostructures to limit the effect of this term. Of course, another key element for enhancing the effective MOKE signal is to minimize R_{sub}. An ideal situation would be a substrate with a perfect

anti-reflection coating (ARC), such that R_{sub} is precisely zero. However, in practice even the best ARCs have a finite reflectance on the order of 0.1% due to imperfections such as surface roughness and impurities. To put that into perspective, in Fig. 3.6a the effective Kerr rotation (normalized to θ_k) according to Eq. (3.1.86) has been plotted for Ni nanomagnets on a bare Si substrate (R_{sub} = 33% @ $\lambda = 800nm$) probed by a beam with $w_0 = 1\ \mu m$ (blue line) and $w_0 = 200\ nm$ (black line). For comparison, an ARC substrate with R_{sub} = 0.5% was also plotted using a beam waist $w_0 = 1\ \mu m$ (red line). From these results we can clearly see that incorporating an anti-reflection substrate has a substantial effect on the MOKE signal of nanomagnetic structures. In Fig. 3.6b, the effective Kerr signal is plotted for different R_{sub} values using a fixed $w_0 = 500\ nm$, which is the experimentally measured value for the TR-MOKE setup used in this work.

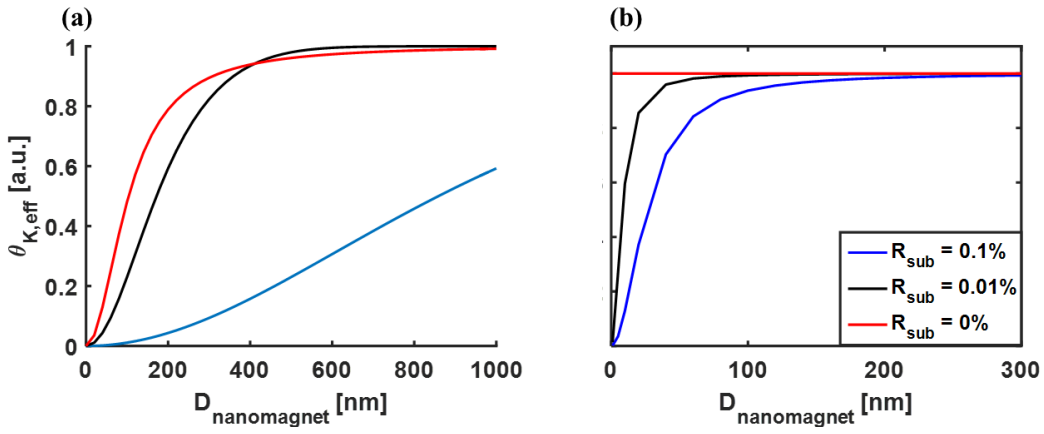

Fig. 3.6. (a) Normalized effective Kerr signal for Ni nanomagnets on bare Si substrate for $\boldsymbol{w_0 = 1\ \mu m}$ and $\boldsymbol{w_0 = 200\ nm}$, corresponding to the blue and black lines, respectively. The red line was plotted using $\boldsymbol{R_{sub} = 0.5\%}$ and $\boldsymbol{w_0 = 1\ \mu m}$ to show the efficacy of ARC. (b) Effective Kerr signals as a function of various R_{sub} at a fixed spot size of $\boldsymbol{w_0 = 500\ nm}$.

Although minimizing R_{sub} and w_0 can make it possible to detect the MOKE signals of nanomagnets only 10's of nanometers in size, there is another way to enhance the Kerr rotation known as *cavity enhancement* (CE). The basic premise of CE is to deposit an additional dielectric layer on top of the magnetic surface (Fig. 3.5), thereby creating a Fabry-Perot etalon that gives rise to multiple reflections off the magnetic surface. If the layer thickness is chosen correctly, the partial reflections add up in phase and the effective Kerr rotation is enhanced. The CE factor is defined as [62]

$$CE \equiv \frac{\theta_{k,CE}}{\theta_k} \tag{3.1.87}$$

where $\theta_{k,CE}$ is the cavity-enhanced Kerr rotation angle and θ_k is the intrinsic Kerr rotation of the sample introduced in Eq. (3.1.77). As light propagates through the dielectric layer it picks up a phase change δ given by [56]

$$\delta = \frac{2\pi nd}{\lambda} \tag{3.1.88}$$

where n is the refractive index and d is the distance light travels in the dielectric medium. For a dielectric layer with thickness L, a normally incident beam will travel a total distance $2L$. The CE effect is largest when the reflected waves constructively interfere at the surface, which occurs when the total phase change of the beam is a multiple of 2π. However, the reflection from the magnetic surface also changes the phase by an amount Δ, so the dielectric thickness is optimum when $\delta + \Delta = 2\pi$. Although this condition can be determined directly using the Fresnel coefficients, the derivation is tedious for just a single layer and gets more complicated with each

additional layer. Instead, we can make clever use of linear algebra to derive simple relationships for any arbitrary number of layers that can be rapidly evaluated with the help of computational programs such as MATLAB.

3.1.2.1 2x2 Transfer Matrix Formalism

The transfer-matrix (T-matrix) formalism can be used to simplify the analysis of any system with linearly related inputs and outputs to a simple exercise in matrix multiplication [63]. Here, we will limit ourselves to its applications in optical multilayers to determine the cavity enhancement of the polar Kerr rotation, which is the simplest case. First, the *scattering matrix* $\boldsymbol{S}$ of a dielectric interface (shown in Fig. 3.7 (a)) must be introduced, which according to the illustration in Fig. 3.7 must be defined as

$$\boldsymbol{S} = \begin{pmatrix} -r & t \\ t & r \end{pmatrix} \tag{3.1.89}$$

where *r* and *t* are the Fresnel reflection and transmission coefficients, respectively, of the interface. The reflection coefficient was defined in Eq. (3.1.75), from which we can directly determine the transmission coefficient$t = 2\sqrt{n_1 n_2}/(n_1 + n_2)$.

Now, the transfer matrix $\boldsymbol{T}$ is directly determined by $\boldsymbol{S}$ and is

$$\boldsymbol{T} = \frac{1}{t}\begin{pmatrix} 1 & -r \\ -r & 1 \end{pmatrix} \tag{3.1.90}$$

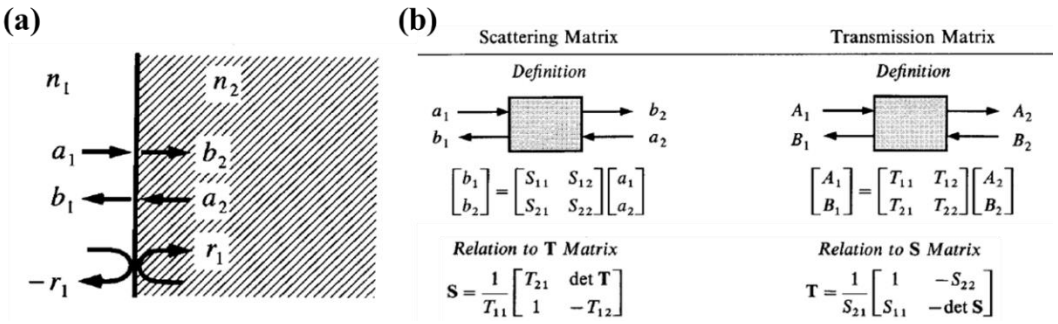

Fig. 3.7. (a) Interfaces between two dielectrics illustrating reference planes at interface for both ports. (b) Illustration of the relationships input-output relationships between the scattering and transfer matrices. Taken from **[63]**.

It should be noted that the matrices ***S*** and ***T*** presented above only defined the optical waves *at the interface*. According to Eq. (3.1.88), if the light travels a finite distance in a dielectric medium there should be a term that includes the change in phase incurred due to propagation through the layer. Assume the light in the example above travels a distance *L'* into the 2nd layer, the transfer matrix that describes this will be denoted ***T'***, and is simply

$$\boldsymbol{T'} = \begin{pmatrix} e^{i\delta} & 0 \\ 0 & e^{-i\delta} \end{pmatrix} \tag{3.1.91}$$

where $\delta = 4\pi n_2 L'/\lambda$. The incident, reflected, and transmitted waves through any number of layers can then be related by forming an appropriate matrix for each element and cascading them (as shown in Fig. 3.8) as follows

$$\begin{pmatrix} A_m \\ B_m \end{pmatrix} = \boldsymbol{T_m T_{m-1} \dots T_2 T_1} \begin{pmatrix} A_0 \\ B_0 \end{pmatrix} = \boldsymbol{T_g} \begin{pmatrix} A_0 \\ B_0 \end{pmatrix} \tag{3.1.92}$$

Now, we will see how this formalism can be used to describe the cavity enhancement of the Kerr rotation. The Fresnel coefficients in the ***S*** and ***T*** matrices

above do not account for the case of magnetic dichroism. If we replace the matrix elements with 2x2 matrices that describe the magneto-optic phenomena as follows

$$r \to \boldsymbol{r} = \frac{1}{2}\begin{pmatrix} r_+ + r_- & i(r_+ - r_-) \\ -i(r_+ - r_-) & r_+ + r_- \end{pmatrix} \tag{3.1.93}$$

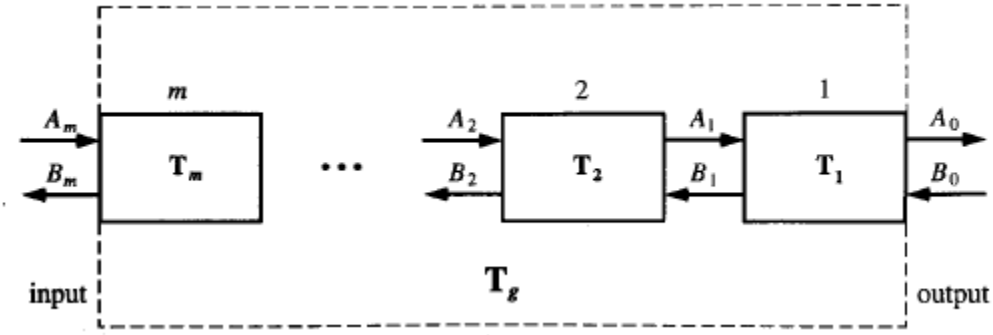

Fig. 37.8. Example of multilayer structure described by cascaded network of individual *T* matrices. Taken from **[63]**.

where the components $r_{\pm}$ are the helicity-dependent values described in Eq. (3.1.72). Because ***S*** and ***T*** are now 4x4 matrices that depend on the polarization, the inputs and outputs must also be expanded to satisfy Eq (3.1.88). For the situation sketched in Fig. 3.8, the incident and reflected inputs on the left-hand side are now [63]

$$A_m \to \boldsymbol{E_i} = \begin{pmatrix} E_{i,x} \\ E_{i,y} \end{pmatrix} \tag{3.1.94}$$

$$B_m \to \boldsymbol{E_r}\begin{pmatrix} E_{r,x} \\ E_{r,y} \end{pmatrix} \tag{3.1.95}$$

where ***E*** are the electric fields described using the Jones formalism introduced in Eq. (3.1.64). The "outputs" have been purposefully neglected because we will assume the layer described by $\boldsymbol{T_1}$ is a metal whose thickness is larger than the skin depth, therefore, no light will reach the right hand side. Omitting the propagation matrix of the thick

metal layer and replacing the matrix coefficients as we have just described, we can rewrite Eq. (3.1.92) as

$$\begin{pmatrix} \boldsymbol{E_i} \\ \boldsymbol{E_r} \end{pmatrix} = \boldsymbol{T_m T_{m-1} \dots T_2} \begin{pmatrix} \boldsymbol{E_{i,1}} \\ \boldsymbol{E_{r,1}} \end{pmatrix} = \boldsymbol{T_g} \begin{pmatrix} \boldsymbol{E_{i,1}} \\ \boldsymbol{E_{r,1}} \end{pmatrix} \tag{3.1.96}$$

To demonstrate how this can be applied to calculate the CE of the Kerr rotation, we will consider the case of a single dielectric (n_1) on a magnetic sample (n_2). The transfer matrix for this system is given by [62]

$$\boldsymbol{T} = (\boldsymbol{t_1 t_2})^{-1} \begin{pmatrix} \boldsymbol{I} e^{i\delta} + \boldsymbol{r_1 r_2} e^{-i\delta} & \boldsymbol{r_2} e^{i\delta} + \boldsymbol{r_1} e^{-i\delta} \\ \boldsymbol{r_1} e^{i\delta} + \boldsymbol{r_2} e^{-i\delta} & \boldsymbol{I} e^{-i\delta} \boldsymbol{r_1 r_2} e^{i\delta} \end{pmatrix} \tag{3.1.97}$$

and the reflected electric field is directly determined by the transfer matrix elements as

$$\boldsymbol{E_r} = (\boldsymbol{T_{21}})^{-1} \boldsymbol{T_{11}} \boldsymbol{E_i} \tag{3.1.98}$$

The enhanced Kerr rotation is simply the ratio of $\boldsymbol{E_r / E_i}$ and additional layers can be added trivially and evaluated rapidly using computational software.

3.1.2.2 4x4 Yeh Formalism

The transfer-matrix formalism presented in the section above showed that the analysis of magneto-optic response of heterostructures can be reduced to simple matrix multiplication. Because we only considered the case of normal incidence, our analysis was greatly simplified by the absence of longitudinal and transverse MOKE interactions. In this section, the general magneto-optic response for any angle of incidence and magnetization will be derived using the boundary-propagation matrix method developed by Zak et al., which is based on Yeh's 4x4 matrix formalism.

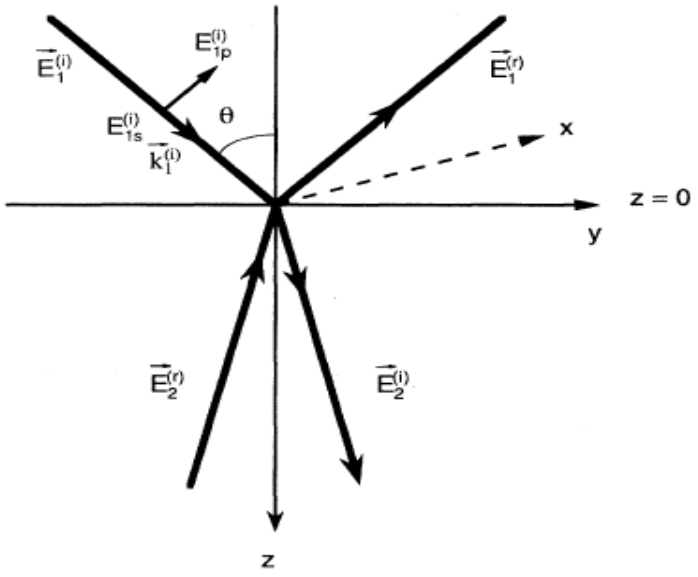

Fig. 3.9. Illustration of the incident and reflected fields for a nonmagnetic medium. Taken from **[64].**

The 4x4 matrix formalism was originally introduced by Pochi Yeh in 1979 [65] and has been extensively used to describe the propagation of plane-waves in arbitrarily anisotropic media. We can begin by assuming that the *xy* plane represents the boundary between media. Because we know the Frensel relations will determine the behavior, we denote the following vector to fully describe the electric and magnetic fields

$$\boldsymbol{F} = \begin{pmatrix} E_x \\ E_y \\ H_x \\ H_y \end{pmatrix} \tag{3.1.99}$$

Just as we saw before, the magnetic field determined by the electric field, thus, we only need to care about the E-fields. If we define the following vector

$$\boldsymbol{P} = \begin{pmatrix} E_{s,i} \\ E_{p,i} \\ E_{s,r} \\ E_{p,r} \end{pmatrix} \tag{3.1.100}$$

where (*s*,*p*) again denote the perpendicular and parallel components, and the subscripts (*i*,*r*) are for the incident and reflected fields, respectively, shown in Fig. 3.9. The vectors above are related by the boundary matrix $\boldsymbol{A}$ as $\boldsymbol{F} = \boldsymbol{AP}$. For isotropic, nonmagnetic media $\boldsymbol{A}$ is [65]

$$\boldsymbol{A} = \begin{pmatrix} 1 & 0 & 1 & 0 \\ 0 & \cos(\theta) & 0 & -\cos(\theta) \\ 0 & -n & 0 & -n \\ n\cos(\theta) & 0 & -ncos(\theta) & 0 \end{pmatrix} \tag{3.1.101}$$

where $\theta$is the angle between the propagation direction and the surface normal of the sample. Now, the boundary matching conditions between two media (1,2) are simply

$$\boldsymbol{A_1 P_1 = A_2 P_2} \tag{3.1.102}$$

Just as before, we need to also account for the phase of light as it travels through the material, for which we define the matrix $\boldsymbol{T}$ as a function of propagation depth *z* as follows

$$\boldsymbol{P_2(z) = T_2(z) P_2(z = 0)} \tag{3.1.103}$$

Using these relationships, we can describe light propagating through any multilayer system with *N* layers via

$$\boldsymbol{A_i P_i} = \prod_{\boldsymbol{m=1}}^{N} (\boldsymbol{A_m T_m A_m^{-1}}) \boldsymbol{A_f P_f} \tag{3.1.104}$$

where *i* denotes the initial (incident) medium and *f* is the final medium.

Now, we must include the gyrotropic effects to relate this result to the MOKE response of multilayer structures. The dielectric tensor in Eq. (3.1.57) can be rewritten in spherical coordinates as [64]

$$\tilde{\boldsymbol{\epsilon}} = \epsilon_{iso}\begin{pmatrix} 1 & g_z & -g_y \\ -g_z & 1 & g_x \\ g_y & -g_x & 1 \end{pmatrix} \tag{3.1.105}$$

$$g_x = icos(\theta_m)\sin(\phi_m)\,Q_v \tag{3.1.105.1.}$$

$$g_y = isin(\theta_m)\sin(\phi_m)\,Q_v \tag{3.1.105.2}$$

$$g_z = icos(\theta_m)Q_v \tag{3.1.105.3}$$

where θ_m and ϕ_m are the polar and azimuthal angles of the magnetization, respectively. Furthermore, the two refractive indices defined in Eq. (3.1.62) for normal incidence can be generalized to account for obliquely incident light in the following way

$$n_{\pm} = n\left(1 \pm \frac{1}{2}\cos(\theta + \theta_m)\,Q_v\right) \tag{3.1.106}$$

which reduces to Eq. (3.1.62) when θ=θ_m=0. As shown in Fig. 3.10, the presence of spontaneous magnetization necessitates that there are four waves propagating – two going into the medium and two going out of the medium. Each of the angles in Fig. 3.10 are explicitly determined by Snell's law, and can be related to the tangential components Ex, Ey, Hx, and Hy.

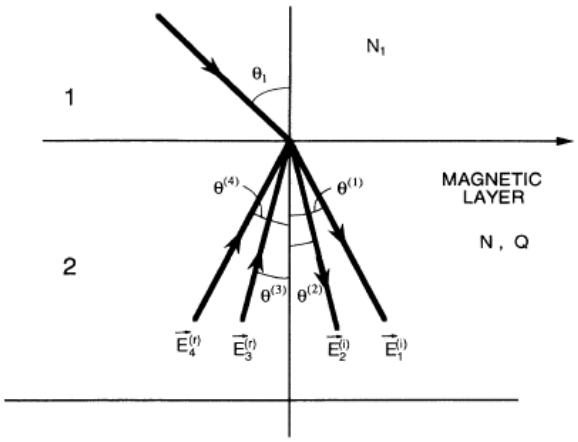

Fig. 3.10. The four eigenmodes of the electromagnetic wave in a magnetic medium. According ot the notations used in Eq. (3.1.102), waves going from medium 1 to 2 are denoted by E_i and those going from 2 to 1 are E_r. Taken from **[64].**

Accounting for the magneto-optic effects and solving for ***A*** reveals that half of the boundary matrix elements depend on the magnetization, and half remain the same as in Eq. (3.1.101). The gyrotropic elements of boundary matrix are [64]

$$A_{21} = \frac{iQ_v}{2}\tan(\theta)\,(\sin(\theta)\,g_i - 2\sin(\theta_m)\cos(\phi_m)) \tag{3.1.107}$$

$$A_{22} = \cos(\theta) + isin(\theta)Q_v \sin(\theta_m)\cos(\phi_m) \tag{3.1.108}$$

$$A_{23} = \frac{-iQ_v}{2}tan(\theta)\left(\alpha_y g_r - 2\,sin(\theta_m)\,cos(\phi_m)\right) \tag{3.1.109}$$

$$A_{31} = A_{33}\frac{g_r}{g_i} = \frac{ing_iQ_v}{2} \tag{3.1.110}$$

$$A_{42} = -A_{44}\frac{g_r}{g_i} = \frac{ing_iQ_v\,sec(\theta)}{2} \tag{3.1.111}$$

where the subscripts denote the row and column, respectively, and $g_{i,r}$ are defined as

$$g_i = \cos(\phi_m)\cos(\theta) + \sin(\theta)\sin(\theta_m)\sin(\phi_m) \tag{3.1.112}$$

$$g_r = -\cos(\phi_m)\cos(\theta) + \sin(\theta)\sin(\theta_m)\sin(\phi_m) \tag{3.1.113}$$

Lastly, the full expression for the propagation matrix $\boldsymbol{T}$ for a layer with thickness d is determined according to Eq. (3.1.104)

$$\boldsymbol{T} = \begin{pmatrix} e^{-\frac{i2\pi ndcos(\theta)}{\lambda}} & \delta_i e^{-\frac{i2\pi ndcos(\theta)}{\lambda}} & 0 & 0 \\ -\delta_i e^{-\frac{i2\pi ndcos(\theta)}{\lambda}} & e^{-\frac{i2\pi ndcos(\theta)}{\lambda}} & 0 & 0 \\ 0 & -n & e^{\frac{i2\pi ndcos(\theta)}{\lambda}} & -\delta_r e^{\frac{i2\pi ndcos(\theta)}{\lambda}} \\ 0 & 0 & \delta_r e^{\frac{i2\pi ndcos(\theta)}{\lambda}} & e^{\frac{i2\pi ndcos(\theta)}{\lambda}} \end{pmatrix} \tag{3.1.114}$$

where the terms $\delta_{i,r}$ account for the Faraday rotation and are defined as

$$\delta_i = \frac{\pi}{\lambda} ndQ_v \frac{g_i}{\cos(\theta)} \tag{3.1.115}$$

$$\delta_r = \frac{\pi}{\lambda}\, nd\, Q_v \frac{g_r}{\cos(\theta)} \tag{3.1.116}$$

If the layer is nonmagnetic ($Q_v \rightarrow 0$), we see that $\boldsymbol{T}$ is simply a diagonal matrix that accounts for the phase shift due to the dielectric medium. Furthermore, we can rewrite Eq. (3.1.102) in the following way

$$\boldsymbol{P_i} = \boldsymbol{M}\boldsymbol{P_f} \tag{3.1.113}$$

where M is determined by

$$\boldsymbol{M} = \boldsymbol{A_i^{-1}} \prod_{m=1}^{N} (\boldsymbol{A_m T_m A_m^{-1}}) \boldsymbol{A_f P_f} = \begin{pmatrix} \boldsymbol{G} & \boldsymbol{H} \\ \boldsymbol{I} & \boldsymbol{F} \end{pmatrix} \tag{3.1.114}$$

The matrix elements $\boldsymbol{G}$, $\boldsymbol{H}$, $\boldsymbol{I}$, and $\boldsymbol{F}$ are 2x2 matrices, and it can be shown that [64]

$$\boldsymbol{G^{-1}} = \begin{pmatrix} t_{ss} & t_{sp} \\ t_{ps} & t_{pp} \end{pmatrix} \tag{3.1.115}$$

$$\boldsymbol{IG^{-1}} = \begin{pmatrix} r_{ss} & r_{sp} \\ r_{ps} & r_{pp} \end{pmatrix} \tag{3.1.116}$$

where t_{ij} and r_{ij} are the Jones reflection coefficients introduced in Eq. (3.1.78).

Although this derivation was far more cumbersome than the case of strictly normal incidence, one can easily show (with the help of a computer program) that the final result is identical to Eq. (3.1.98).

3.2 Stroboscopic Measurements

In chapter 2, we saw that magnetization dynamics naturally occur at radio frequencies (MHz-GHz). In order to detect high-frequency dynamics electrically via ferromagnetic resonance (FMR), sophisticated circuits must be paired with precisely fabricated microwave cavities. For cavity based FMR approaches, SNR values as high as 90 are tenable, but the measurements are limited to only a few discrete microwave bands which are determined by the coplanar waveguide properties. Alternatively, a vector network analyzer (VNA) can be used to generate any desired frequency up to 100 GHz (for nice VNAs), but have far worse SNR (~40) values than the conventional approach [66].

Another approach to study spin dynamics utilizes a pulsed, ultrafast laser source to achieve time-resolution by tracking the magnetization via magneto-optic effects, hence the name *time-resolved magneto-optic Kerr effect* (TR-MOKE). Here, the low-

frequency limit is determined by the repetition rate of the laser, and the high-frequency limit is determined by the pulse-width (Δt_{pulse}) of the laser. Roughly speaking, at least ten data points per cycle are desirable for the purposes of regressively fitting the data; therefore, the frequency limit of an ultrafast optical approach is approximately $f_{max} \approx 1/10\Delta t_{pulse}$. Modern ultrafast laser systems offer pulse-widths down to single-femtosecond sizes, however, pulse-widths that are 100 fs wide are still capable of measuring dynamics in the Terahertz range (>300 GHz). In addition to the large range of operating frequencies, TR-MOKE setups offer very high sensitivity with a detection limit on the order of $10^6\ \mu_B$; for comparison, the detection limit of FMR systems are greater than $10^{12}\ \mu_B$ [66]. To put these numbers into perspective, a Nickel nanocylinder ($a_{lattice} \approx 3.5$ Å) with a radius of 50 nm and a height of 30 nm has roughly $10^7\ \mu_B$.

In order to achieve time-resolution, a stroboscopic approach is utilized. Although different schemes can be employed to excite the spin dynamics (photoconductive switches, ultrafast thermalization, etc.), the underlying principles are the same. The term stroboscopic denotes the fact that two pulses – a *pump* and a *probe* pulse – are generated by the same laser source and used to excite and detect the dynamics, respectively. The role of the pump is to simply perturb the magnetic equilibrium, however, it is crucial that the probe can be synchronized with the pump. Once the magnetization is misaligned from the equilibrium position, it must follow a helical trajectory back to its initial state according to the LLG equation. If the optical path length (OPL) of the probe pulse is longer than the pump's path, then it will arrive at the sample at a later time $\Delta t = \Delta OPL/c_0$, where ΔOPL is the additional length of the

probe path. Thus, the probe can measure the magnetization (via MOKE) at an exact time during the precession. If the OPL of the probe is increased even more, then the probe will record the magnetic moment at a later time in the precession. If this is done systematically, say starting with co-incident pulses and then increasing the probe's time delay by 5 ps and recording the MOKE signal, increasing the time delay by another 5 ps and recording the signal, and so forth, then the oscillation can be reconstructed by piecing together the Kerr rotation at different time delays. This assumes that the precession is deterministic (identical each time), which happens to be the case, and is why the term stroboscopic is used to describe this methodology. Each pulse only records a singular piece of the precession but doing this repetitively allows one to capture the full precession in the time-domain.

3.2.1 Ultrafast Thermal Demagnetization

In order to initiate the magnetic precession, an ultrafast pulse can quasi-instantaneously thermalize the sample which in turn reduces the total magnetic moment and changes the effective field. This behavior was first discovered in 1996 by Beaurepaire et al. while studying the laser-induced change in magneto-optic contrast of a nickel film [67]. In their seminal work, they showed that an ultrafast pulse could demagnetize the sample within a few hundred femtoseconds (Fig. 3.11). This result shocked the scientific community, as it was previously believed that the demagnetization process was governed by spin-lattice relaxations that are approximately two orders of magnitude slower than the experimentally observed behavior.

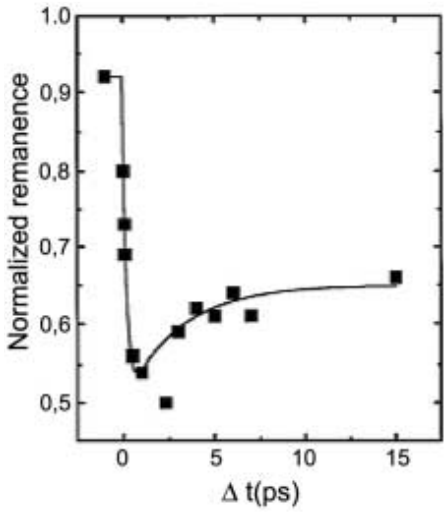

Fig. 3.11. Remnant magneto-optic contrast measured by Beaurepaire et al. for a nickel thin film after absorbing a 60 fs laser pulse. Taken from **[67]**.

Despite the fact that ultrafast demagnetization was discovered two decades ago, the microscopic processes that underpin this phenomena are still the subject of intense debate [68, 69, 70]. The convoluted nature of magneto-optical effects has stymied experimental efforts to identify the mechanisms that allow the magnetization to respond on femtosecond timescales, because the ultrafast pulse excites the sample to a highly non-equilibrium state and the ensuing optical response is the product of coupled electron, spin, and lattice degrees of freedom [71]. In other words, magneto-optic measurements within the first few picoseconds after photoexcitation are a mixture of magnetic and optical contributions with local and non-local origins that cannot be separated.

In recent years there has been a renewed interest in uncovering the microscopic origins that responsible for ultrafast demagnetization – largely due to the intrigue surrounding AOS. To address these questions, a variety of novel experiments specifically designed to investigate the non-equilibrium behavior of the spin system

during phase change. One such study was carried out by researchers at the National Institute of Science and Technology (NIST) who combined time-resolved magneto-optics and angle-resolved photo-emission spectroscopy (ARPES) measurement techniques to investigate the demagnetization process in a 400 nm thick, single-crystal Ni film [72, 73].

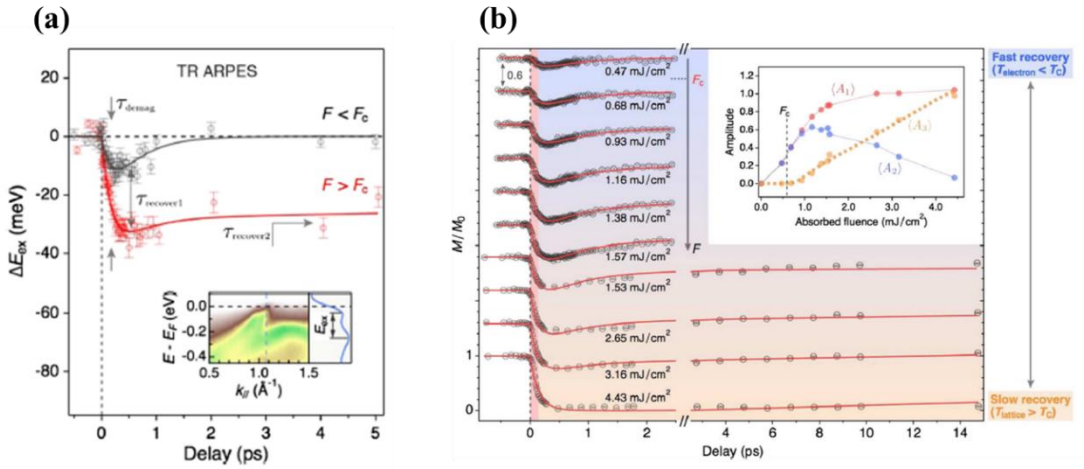

Fig. 3.12. (a) Change in the exchange splitting in Ni (measured using TR-ARPES) for an absorbed fluence below (0 .21 mJ/cm^2, grey) and above (1.7 mJ/cm^2) the critical fluence F_c; the solid lines are fits to Eq. (3.2.1). (b) Magnetization dynamics measured using TR-MOKE over a range of fluences, the highest fluence is sufficient to fully suppress the sample magnetization. The solid lines are fits to Eq. (3.2.1) using the same parameters from the TR-ARPES data with auxiliary calculations to account for the depth-average effects in the MOKE measurement. The inset shows the extracted amplitudes of $\langle \boldsymbol{A_i} \rangle$ in Eq. (3.2.1) as a function of laser fluence, where the brackets denote the depth-averaging. Taken from **[72]**.

Unlike magneto-optic measurements, the TR-ARPES technique can be used to probe the exchange splitting precisely at the surface, which provides a direct measurement of the elementary magnetization dynamics unobscured by optical effects. Using these techniques in parallel revealed that the demagnetization process depends critically on the absorbed power, which decays exponentially with depth due to the Beer-Lambert

law. Near the surface, the laser power heats the sample above the Curie temperature which causes the sample to transition to a paramagnetic phase, however, at some depth the temperature does not pass T_C and the sample stays in a ferromagnetic state. Because TR-MOKE is sensitive to the magnetization within the skin depth ($\delta \approx 10\, nm$), the response is the ensemble average of the mixed phases. The fundamental result of the study showed that the dynamic behavior of the magnetic moment after femtosecond thermalization can be described as

$$m(t,z) = 1 + a_1(z)e^{-\frac{t}{\tau_D}} - a_2(z)e^{-\frac{t}{\tau_{r,1}}} - a_3(z)e^{-\frac{t}{\tau_{r,2}}} \qquad (3.2.1)$$

where *t* is the time-delay between pump and probe pulses, $\tau_D = 176 \pm 27\, fs$ is the lifetime associated with the collapse of the exchange splitting, $\tau_{r,1}$and $\tau_{r,2}$are *fast* and *slow* recovery times, respectively, and the amplitudes *a* are fluence-dependent (depth-dependent) parameters that obey $a_1 = a_2 + a_3$. The amplitude associated with slow recovery (a_3) is zero when the fluence is below a critical value F_c, which means the re-magnetization is determined only be the fast recovery time $\tau_{r,1} = 537 \pm 173\, fs$. When the fluence is sufficiently large, i.e. heats the sample above the Curie temperature, the slow recovery ($\tau_{r,2} = 76 \pm 15\, ps$) term dominates and the sample remains in a demagnetized state far longer. From the TR-ARPES measurements, the authors were able to conclude that the fast recovery time is attributed to the damping of high-frequency magnons under the strong exchange field, for Ni H_{ex} ~ 939 T. This is the first experimental confirmation that an intense, ultrafast pulse induces a real phase transition within femtoseconds, a point which has been hotly debated since the

first measurements were reported nearly two decades ago. However, it is worth noting that in this study the low-fluence regime ($F<F_c$) could only demagnetize the sample by approximately 50%, at most. When the fluence is larger than F_c, hence, strong enough to fully demagnetize the sample, the exchange field is dissolved and the magnon damping time approaches infinity. Thus, cooling of the spin system can only be achieved via other mechanisms such as coupling to the lattice or thermal transport, which this study showed to have a much slower recovery time ($\tau_{r,2}$).

Because total quenching of the magnetization is desirable for ultra-low-power switching, the slow recovery associated with full demagnetization presents challenges for potential ultrafast information technologies. Failure to identify the microscopic origins of this behavior preclude the magnetic community from overcoming the relatively slow writing speed associated with complete demagnetization. One likely channel of relaxation is coupling to the lattice via spin-orbit coupling because the net angular momentum of the sample must be conserved, which means that the spin angular momentum must be converted into mechanical angular momentum. Indeed, this was confirmed in 1902 by Albert Einstein and Wander Johannes de Haas, and is known as the *Einstein-de Haas effect* [74]. In their experiment, the torque exerted by a ferromagnetic body during magnetization reversal was measured. However, because laser-induced demagnetization is a highly-localized process that occurs in a matter of femtoseconds, experimental confirmation of this effect on the ultrafast timescale has remained elusive. Very recently, Dornes et al. reported the direct evidence of the ultrafast Einstein-de Haas effect using time-resolved x-ray diffraction (TR-XRD) to

measure the structural dynamics of the lattice in a 15 nm thick Fe film [75]. The TR-XRD technique utilizes a femtosecond x-ray pulse (E_{photon} ~ 6.9 keV) grazing the sample surface at an angle of approximately 1°. An ultrafast laser ($t_{pulse} \approx 40\ fs, \lambda = 800\ nm, F \approx 8\ mJ/cm^2$) is synchronized with the x-ray laser and used as a pump to instigate the ultrafast demagnetization. By cleverly selecting α-iron, the researchers narrowed the potential pathways for spin-lattice dissipation down to a single, off-diagonal element in the strain tensor

$$\eta_{23} = \frac{1}{2}\left(\frac{\partial u_2}{\partial x_3} + \frac{\partial u_3}{\partial x_2}\right) = -\frac{1}{\gamma C_{3232}}\frac{dM}{dt} \tag{3.2.2}$$

where u_i is the displacement vector, x_i are the Cartesian coordinates, C_{3232} is a component of the fourth-order stiffness tensor and γ is the gyromagnetic ratio. This, in turn, meant that a change in the magnetization would launch transverse (and longitudinal) mechanical waves at Terahertz frequencies that could be detected by the TR-XRD measurement. The study showed that up to 80% of the angular momentum lost from the spin system during ultrafast demagnetization was transferred to the lattice.

It must be noted that this study only investigated the dynamics at a single pump fluence – which corresponded to an absorbed fluence of 2.7 mJ/cm^2 and a total demagnetization of approximately 10%. This fluence is far larger than the critical fluence (F_c ~ 0.59 mJ/cm^2) for *slow recovery* observed in ref. [72], which corresponded to a demagnetization of approximately 50%. Of course, the samples in these studies are different materials with vastly different thicknesses, so direct comparison between the two does not tell the whole story. Nevertheless, these discrepancies underscore the fact

that more studies are necessary in order to fully understand ultrafast demagnetization. These findings are not only relevant to our theoretical understanding of non-equilibrium spin dynamics, but are likely essential to the realization of ultra-efficient, ultrafast magnetic technologies.

3.2.2 Three-Temperature Model

Despite not knowing precisely *how* ultrafast demagnetization is possible, a model known as the *three-temperature* (3T) model is a phenomenological expression has been extensively used to describe the transfer of heat between these systems on picosecond timescales. This approach associates a temperature to the spin, electron and lattice (denoted by subscripts *s,e,l*, respectively) subsystems which transfer energy according to coupled differential rate equations describing the temperature evolution of the subsystems [76]

$$C_e \frac{\partial T_e}{\partial t} = \nabla \cdot (\kappa \nabla T_e) - G_{el}(T_e - T_l) - G_{es}(T_e - T_s) + S(t) \tag{3.2.3}$$

$$C_s \frac{\partial T_s}{\partial t} = -G_{es}(T_s - T_e) - G_{sl}(T_s - T_l) \tag{3.2.4}$$

$$C_l \frac{\partial T_l}{\partial t} = -G_{el}(T_l - T_e) - G_{sl}(T_l - T_s) \tag{3.2.5}$$

Here, κ is the thermal conductivity, *S(t)* is the heat generated by the absorption of the laser pulse, G_{ij} is the coupling between the *i* and *j* subsystems, T_i is the temperature and C_i is the heat capacity of the system. The pulse is absorbed by the electron system because the lattice and spin systems cannot respond at optical frequencies. In light of

the recent findings covered in section (3.2.1), treating the entire system with a single temperature is clearly insufficient since the TR-MOKE data

is the ensemble average over the skin-depth probed by the pulse. Therefore, care should be taken when using the 3T model to estimate the temperature of the spin subsystem. The thermal expansion caused by the pump can be determined using a simpler two-temperature (2T) model that does not include the spin system, which is accomplished by simply setting Cl, Ges and Gsl in the equations above to zero.

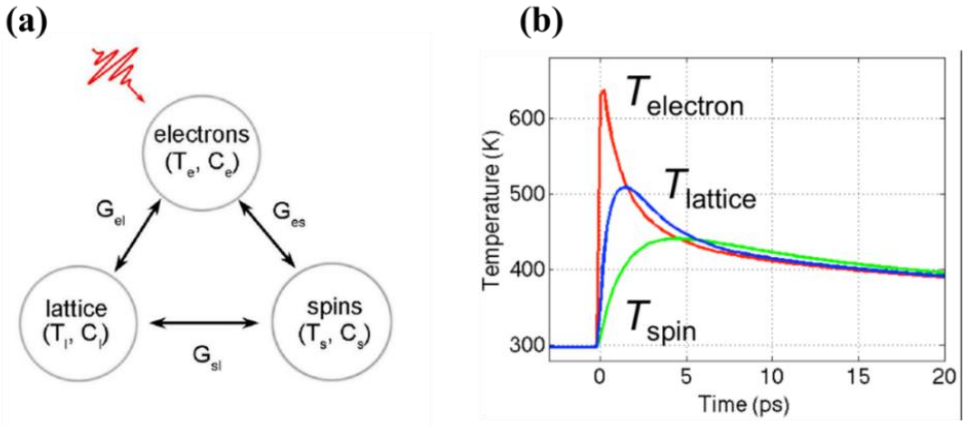

Fig. 3.13. Illustration of the subsystems behavior which shows that the electron system directly absorbs the optical power, while the spin and lattice systems suck heat from the electron system after absorption. (b) Simulated time-evolution of the electron, spin and lattice temperatures using Eqs. (3.2.2-4) for a 30 nm thick Ni film excited by a 150 fs laser pulse with a fluence of 1.75 mJ/cm^2. Note that within roughly 5 ps all three of the temperature equilibrate.

3.2.3 Thermal Anisotropy Pulse

While the processes underpinning demagnetization on the femtosecond timescale are rich, ultimately, we are concerned with the precessional dynamics that occur long after this process takes place. Here, the pump pulse is simply a way to knock the sample out of equilibrium, thereby initiating the spin dynamics. In this section, the

"anisotropy pulse" generated by the rapid thermalization of the sample will be reviewed.

Recall that the demagnetization field of the sample is directly determined by the magnetic moment. Thus, when the magnetization of the sample is reduced the stray field will also be reduced, which in turn will change the effective field and the equilibrium orientation. Because this change is the result of the temperature dependence of the magnetization, then we must consider other magnetic parameters that vary with temperature. One such parameter is the anisotropy constant, which is well-known to vary significantly with sample temperature. Therefore, the heating caused by the laser pulse will also quasi-instantaneously change the anisotropy which will also affect H_{eff} and the equilibrium position. Although other magnetic parameters may change slightly, it is well-understood that these two are primarily responsible for the thermally induced "anisotropy field pulse". As was reported in ref. [72], even when the sample is completely demagnetized the recovery time is on the order of 10's of picoseconds – at which point the effective field will be restored to its initial value causing the magnetization to precess back to its initial state.

An important aspect of the field pulse is that it must be reproducible in order to measure the magnetization dynamics stroboscopically, otherwise the lock-in averaged signals would not constructively interfere and the signal would be diminished. Because the sample is strongly biased by an external field and each pulse is approximately identical, the effective field changes by a fixed amount each time the pulse kicks the sample out of equilibrium. In typical TR-MOKE experiments, not much is known about

the magnitude of the anisotropy pulse. Of course, estimations can be carried out in a "back-of-the-envelope" manner if the temperature-dependence of the anisotropy is known and the demagnetization is quantified during the experiment. Ignoring the anisotropy, which is valid for samples such as polycrystalline Ni, the anisotropy field is purely a product of the demagnetization. If the change in magnetization is known, then the torque applied by the external field can be estimated. In practice, this is useful in determining the right order of magnitude for the field pulse used in the micromagnetic simulations of the spin dynamics. In the event that the exact pulse profile must be evaluated, a detailed report has been published outlining a procedure to back-calculate the character of the anisotropy field in ref [77].

3.3 Detection

Having extensively covered the physics governing the light-matter interactions in the presence of spontaneous magnetization, we can move on to the process of detecting these in a laboratory setting. In most cases, the polarization rotation of light induced by the MOKE is on the order of milliradians (~0.1^{o}) for a complete magnetization reversal. Now, recall that in order to derive the Kittel mode the LLG equation was linearized under the assumption of small-angle dynamics. This means that the polarization state of the probe laser in a typical TR-MOKE experiment only changes on the order of microradians – which is far too small to discern in a single-shot measurement due to detector noise limitations, temperature- and acoustic-fluctuations of optical components, and a laundry list of other extraneous happenings in a shared

laboratory. Therefore, sophisticated measurement techniques must be used to resolve the small-angle precession which will be covered in the following section.

3.3.1 Crossed Polarizer

The easiest way to measure the polarization state of a laser is to simply place a polarizer in the path and measure the power as a function of the polarizer's angle. However, even in the best-case scenario (complete magnetization reversal) the Kerr rotation is only on the order of milliradians. Therefore, one would need *at least* milliradian precision of the polarizer angle to measure such a small change. Furthermore, real polarizers are not perfect and are often defined by their *extinction ratios*, which is the ratio between the transmission factor of parallel and perpendicular polarizations, respectively, relative to the polarizer easy axis. Because they cannot completely block transversely polarized light from passing through, detecting the MOKE signal is even more challenging than precisely setting the polarizer angle. The most common optical configuration used to measure the MOKE response of materials is known as the *crossed-polarizer* setup [78], shown in Fig. 3.14 below.

In this geometry, the optical power at the detector will be determined by the difference between the polarizer angle (θ_P) and the analyzer angler (θ_A), as well as the Kerr rotation. We can assume that the angle of incidence is very small such that only the polar MOKE signal is detected. The transmitted optical power through the analyzer (P_A) in the absence of spontaneous magnetization is simply

$$P_A = P_0 R \sin(\theta_A)^2 \tag{3.3.1}$$

where P_0 is the intensity of light striking the sample and R is the sample reflectivity. Now, if the sample is magnetized the polarization of the beam rotates by an amount $\pm\theta_k$, depending on the direction of the magnetization, and the power that passes through the analyzer in this case is

$$P_{A,M^+} = P_0 R sin(\theta_A + \theta_k)^2 \tag{3.3.2}$$

$$P_{A,M^-} = P_0 R sin(\theta_A - \theta_k)^2 \tag{3.3.3}$$

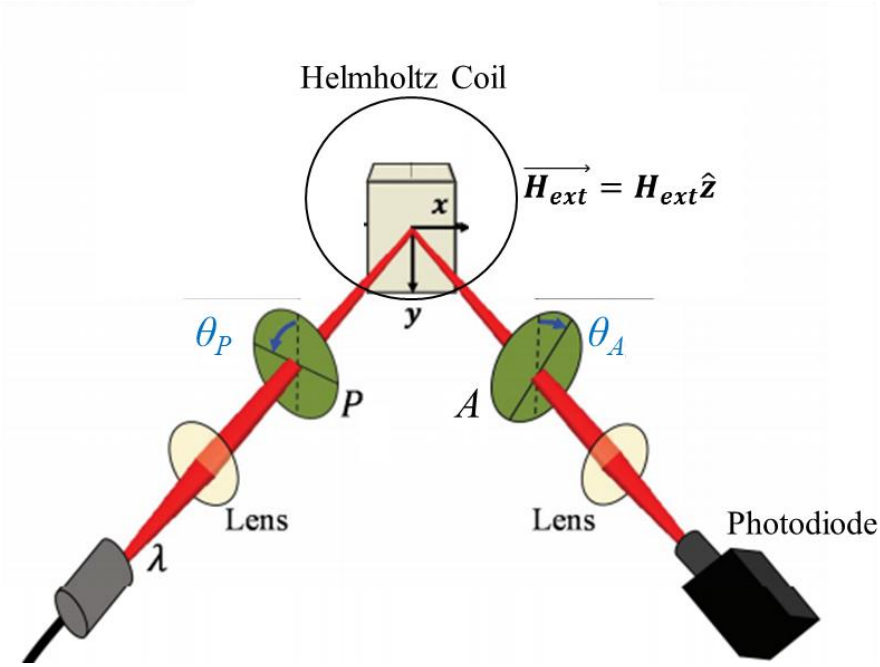

Fig. 3.14. Example of a crossed-polarizer setup used to measure the MOKE of magnetic films.

Because the signal-to-noise ratio of MOKE measurements is of the utmost importance we must consider the difference between two states, which simplifies to [79]

$$P_{A,M^+} - P_{A,M^-} = \Delta P = P_0 R \sin(2\theta_A)\sin(2\theta_k) \tag{3.3.4}$$

Then, the Kerr contrast ($\Delta P/P_A$) signal can be calculated as the ratio between the difference signal and the average power given in Eq. (3.2.6)

$$\frac{\Delta P}{P_A} = \frac{2\sin(2\theta_A)\sin(2\theta_k)}{1-\cos(2\theta_A)\cos(2\theta_k)} \approx \frac{4\theta_k}{\tan(\theta_A)} \tag{3.3.5}$$

where the final approximation is valid if and only if the Kerr rotation is small enough to permit a first-order Taylor expansion about θ_k. This equation suggests that Kerr contrast $\Delta P/P_A$ can reach arbitrarily large values as the analyzer angle approaches zero. However, we have not yet considered how the finite extinction ratio ($1/\gamma_D$) of real polarizers affect the signal. Values of γ_d are as high as 10^{-2} for relatively cheap economy sheet polarizers, and as low as 10^{-6} for high quality birefringent crystalline polarizers (eg. Glan-Thompson polarizers). The depolarization constant in this case is defined as the amount of light that passes through the analyzer (P_{min}) when it is oriented at an angle of 90^o with respect to the polarization of an incident beam (P_i)

$$\gamma_D = \frac{P_{min}}{P_i} \tag{3.3.6}$$

From this result we can rewrite the average power passing through the analyzer (Eq. 3.3.1) as

$$P_A = \frac{P_0 R}{2}(1-\cos(2\theta_A)\cos(2\theta_k)+2\gamma_D) \tag{3.3.7}$$

and the Kerr contrast in Eq. (3.3.5) becomes

$$\frac{\Delta P}{P_A} = \frac{2\sin(2\theta_A)\sin(2\theta_k)}{1-\cos(2\theta_A)\cos(2\theta_k)+2\gamma_D} \approx \frac{2\theta_k \sin(2\theta_A)}{\sin(\theta_A)^2+\gamma_D} \tag{3.3.8}$$

where we have again made use of a first-order Taylor expansion of θ_k in the approximation. The maxima of Eq. (3.3.8) can be determined by differentiating the equation with respect to θ_A and setting the derivative to zero, which yields $(\theta_A)_{max} = \sqrt{\gamma_D}$ and the Kerr contrast is then

$$\left(\frac{\Delta P}{P_A}\right)_{max} = \frac{2\theta_k}{\sqrt{\gamma_D}} \tag{3.3.9}$$

This equation shows that the sensitivity of a MOKE system is directly limited by the extinction ratio of the analyzer, therefore, it is incredibly important that one uses high-grade polarizers when measuring the dynamic magneto-optic response of nanostructures! However, this relationship only considers the *power* of the light that passes through the polarizer which must still be measured using a detector.

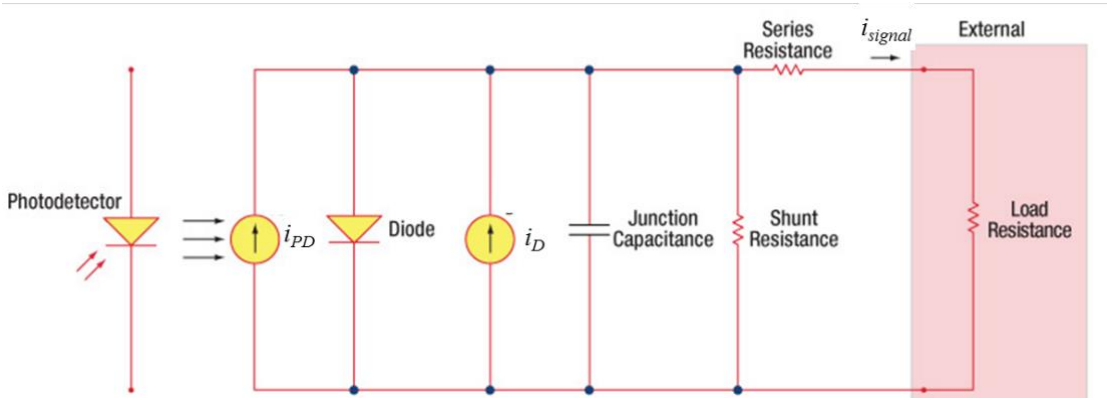

Fig. 3.15. A typical photodetector circuit used to measure the current of a photodiode which is modelled as an ideal source (i_{PD}) in the schematic above. The noisy contributions are modelled as discrete circuit elements for the sake of demonstration.

Now, we will consider the prominent sources of noise associated with the photodiode circuit (shown in Fig. 3.15). An ideal detector would only generate current upon absorption of a photon (eg. $i_{PD} = \eta P_A$), but in real devices there are various

sources of noise that generate unwanted electrical current. One undesirable contribution comes from thermally excited electrons that are swept out of the depletion region by the bias field, thereby generating a signal known as *dark current* (i_D). The dark current of a photodiode can be calculated using the following relationship [79]

$$i_D = \eta \cdot NEP \cdot B^{\frac{1}{2}} \tag{3.3.10}$$

where η is the spectral response, B is the detection bandwidth, and *NEP* stands for noise-equivalent-power which is a measure of the voltage generated by a signal with a SNR of 1. If we assume that the load resistance (R_L) dominates the equivalent resistance and that the diode has a known junction capacitance (C_j), the bandwidth is simply related to the RC time constant of the circuit as

$$B \approx \frac{1}{2\pi R_L C_j} \tag{3.3.11}$$

In addition to dark current, thermal energy can also agitate electrons inside the resistors in the photodiode circuitry which generates *Johnson noise* with a current (i_j) given by

$$i_j = \sqrt{\frac{4k_B TB}{R_{sh}}} \tag{3.3.12}$$

where R_{sh} is the shunt resistance of the photodiode. Another type of noise that is relevant for small optical power, as is the case in MOKE, is *shot noise* (i_s). This type of noise occurs due to statistical fluctuations of the photocurrent and dark current, and is determined by the following relationship

$$i_s = \sqrt{(2e(i_{PD} + i_D)B} \tag{3.3.13}$$

One last source of noise that is unavoidable in this single-detector configuration comes from power fluctuations of the laser, which generate a laser noise current (i_{Laser}) expressed as

$$i_{Laser} = f_i i_{PD} \tag{3.3.14}$$

Here, f_i is the noise fraction of the optical beam that will vary depending on the circuit parameters and is often determined experimentally (or mitigated using a superior detection scheme…). The final result of this calculus allows us to write down an expression for the signal (S) to noise (N) ratio of the MOKE setup defined as follows

$$\frac{S}{N} = \frac{\Delta i}{i_D + i_s + i_{Laser} + i_j} \tag{3.3.15}$$

Thus, the recorded Kerr signal is a convoluted response that depends on the optical and electronic components. One nice takeaway from this derivation, however, is that the SNR can be optimized by tuning the analyzer and measuring the contrast.

3.3.2 Balanced Photodiodes

While the crossed-polarizer configuration considered in the preceding section is the most common setup used to measure the MOKE response, more sophisticated schemes can improve the SNR characteristics. One limitation of the scheme is that the optimum analyzer angle corresponds to very low optical powers at the detector, which in turn makes the terms in the denominator of Eq. (3.3.15) substantial. If, however, the

analyzer is replaced with a polarizing beam splitter cube ($\gamma_D \approx 10^{-3}$) or a Wollaston prism ($\gamma_D \approx 10^{-5}$), a differential detection scheme can be employed to improve the SNR characteristics. Here, the phrase differential detection denotes a system using two photodiodes to detect the polarization state of the reflected beam. Unlike the crossed-polarizer scheme, this method does not waste any of the optical power which helps to mitigate the effects of dark current, shot and Johnson noise. If we assume that the initial beam is polarized in the x-direction in Fig. 3.13, then a polarizing splitter oriented at $\theta_A \approx 45^o$ will split the reflected beam into s and p components with essentially identical powers. Each beam is detected by its own photodiode, and the voltages are subtracted and summed by an op-amp circuit. By subtracting the two beams in this fashion, any noise due to fluctuations in the laser power are immediately eliminated. To this end, if we compare the noise density of the difference and sum channels in our setup, 0.75 and 5 $\mu V/\sqrt{Hz}$ at 1 kHz, respectively, the differential scheme cancels out a majority of the noise in each of the detectors.

In addition to the improved SNR of the measurement, there is another advantage to using a differential detection scheme. Because we are interested in the time evolution of the system after ultrafast thermalization, we must consider how the change in temperature effects other parameters – namely, the reflectivity. It is well-known that the refractive index depends on the temperature, therefore, the thermal dynamics induced by the pump laser will cause the reflectivity to vary as the electron system cools. By taking the partial derivatives of Eq. (3.3.4) with respect to the reflectivity and

Kerr rotation, we can show that the time-evolution of the difference signal will be comprised of two dynamic parts [78]

$$\Delta P(t) = \sin(\theta_A)^2\, \Delta R(t) + 2R sin(\theta_A)\Delta\theta_k(t) \qquad (3.3.16)$$

where the prefix Δ was used to represent the transient nature of the reflectance and Kerr rotation. This relationship shows that the nonmagnetic contribution will always be present in the crossed-polarizer detection scheme. However, if time-resolved measurements at opposite magnetizations are subtracted then the nonmagnetic term will cancel out (even in $\boldsymbol{M}$) and the magnetic portion will be doubled (odd in $\boldsymbol{M}$).

Now, we will consider a balanced photodiode scheme for comparison. The difference in transmitted power of the *s* and *p* components at the analyzer in this case is

$$\Delta P = R[(\cos(\theta_A)^2 - \sin(\theta_A)^2)(\theta_k^2 - 1) + 4\sin(\theta_A)\cos(\theta_A)\,\theta_K] \qquad (3.3.17)$$

By inspection we can quickly see that the setup will be nearly balanced (eg. $\Delta P = 0$) when $\theta_A \approx 45^o$, and if we again take the partial derivative to determine the dynamic response we now have

$$\Delta P(t) = 2\theta_K \Delta R(t) + 2R\Delta\theta_K(t) = 2R\theta_k\left(\frac{\Delta R(t)}{R} + \frac{\Delta\theta_k(t)}{\theta_k}\right) \qquad (3.3.18)$$

Typically, the ratio $\Delta R/R$ is on the order of 10^{-5}, and $\Delta\theta_k/\theta_k$ is between 10^{-3}-10^{-2}. Thus, changes in the reflectivity have little effect on the measured response in the balanced photodiode configuration. Furthermore, a closer inspection of Eq. (3.3.17)

reveals that truly *perfect* balance is not achieved at $\theta_A = 45^o$. If the left-hand side is set to zero and the trigonometric functions are simplified, the equation reduces to

$$0 = \cos(2\theta_A)\,(\theta_k^2 - 1) + 2\sin(2\theta_A)\,\theta_k \tag{3.3.18}$$

from which we can determine the optimal analyzer angle as follows

$$\tan(2\theta_A) = \frac{1 - \theta_k^2}{2\theta_k} \approx \frac{1}{2\theta_k} \tag{3.3.19}$$

The approximation on the right-hand side is justified because θ_k is on the order of milliradians, therefore, the leading term $(1/2\theta_k)$ is roughly 6 orders of magnitude larger. As an example, consider the case for a Ni film with a polar Kerr rotation of 0.13^o (~2.3 mrads); according to the relationship above, the analyzer angle for perfect balance is 44.8682^o. At this exact analyzer angle, the partial derivative of Eq. (3.3.18) is now

$$\Delta P(t) = 2R\Delta\theta_k(t) \tag{3.3.20}$$

where the nonmagnetic contribution to the has been completely rejected. In practice the exact value of a $\theta_k$is rarely known, and the analyzer angle is set by minimizing the D.C. value of the differential voltage between the diodes.

3.4 TR-MOKE Setup

The setup used to conduct TR-MOKE studies in this thesis will now be presented in detail. Ultrafast pulses from a Ti:sapphire laser (Coherent MIRA 900, 76 MHz repetition rate, 160 fs pulsewidth) are split into two paths, one for the probe and one for the pump (Fig. 3.16). The pump beam is immediately frequency-doubled by a

second harmonic generator (Coherent SHG), and the output is passed through a color filter to remove any residual IR light as well as a mechanical chopper operated at 1 kHz. One of the primary reasons we employ a dual-color scheme is that it allows for co-propagating pump and probe beams that can be spectrally separated in the detection path.

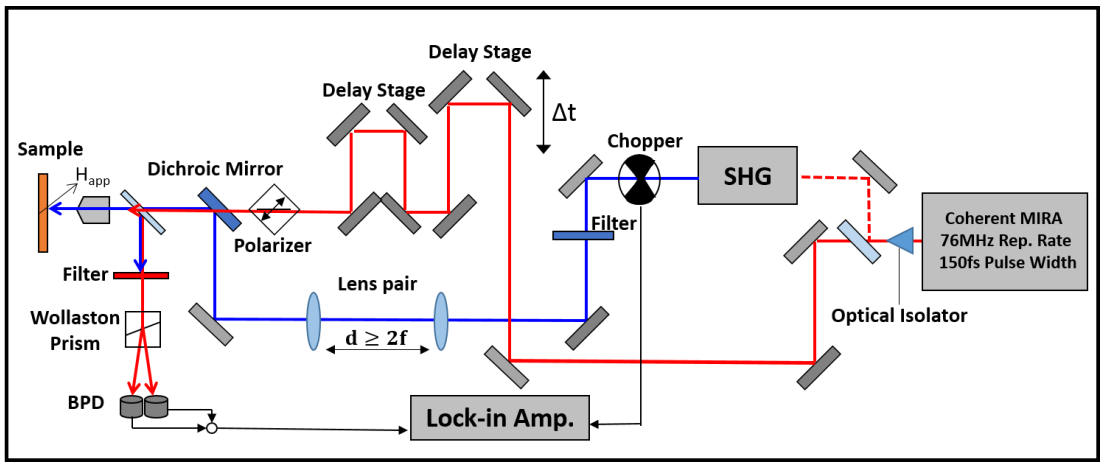

Fig. 3.16. Schematic of the WiTec TR-MOKE setup outlined in this section.

Another advantage of this approach is the use of dichroic mirrors that allow the pump to bypass the beamsplitter that directs the back-reflected probe to the detectors, which means twice as much pump power can reach the sample. The probe beam passes through a pair of optical delay stages – a Physik Instrumente M531 (20 cm) and a Newport M-IMS400PP (40 cm), which provide a total time delay between pump and probe pulses of 4 nanoseconds with approximately 20 femtosecond resolution. After the delay line, the pump and probe beams are sent to a microscope system (shown here) by default, however, an alternative path leading to an electromagnet is also available.

3.4.1 WITec TR-MOKE Setup

The default configuration that was used for most of the measurements in this thesis will be discussed. Just before the light enters the microscope system (WITec Alpha 300), it passes through a linear polarizer to ensure the beam polarization is pure because the corner-cube retroreflectors used in the delay line induce a significant amount of ellipticity. Inside the WiTec system, the beams are directed toward the sample by a R90:T10 beamsplitter cube, and then focused by a microscope objective. Because the system has an objective turret, the MO can be easily interchanged, but the default configuration is a 100X magnification objective with a numerical aperture of 0.9 that can focus the probe down to a spot size $2w_0 = 0.61\lambda/N.A.$ The experimentally measured probe beam waist at $\lambda = 800$ nm is $w_0 = 500$ nm, which is remarkably close to the theoretical value of 488 nm. After the light is reflected from the sample nearly half of the power is sent to the detection path where it passes through a Wollaston prism ($\theta_A \approx 45^o$) and then focused onto a pair of balanced photodiodes. Because the photodiode signals are subtracted directly by a dedicated circuit, the difference (magnetic) and sum channels (nonmagnetic) are sent to a pair of Stanford SR830 lock-in amplifiers referenced to the 1 kHz signal of the mechanical chopper that modulates the pump beam.

The sample is mounted on a 3-axis closed loop, piezoelectric scanner with approximately 10 nanometer resolution that is crucial for time-resolved studies of nanomagnetic devices. Beneath the sample surface, a pair of cylindrical NdFeB magnets with antiparallel magnetizations are placed side-by-side to create well-

defined, parabolic field lines. Although the magnetic field provided by the permanent magnet pair is smaller and less well defined than the field generated by the bipolar electromagnet, they do not obstruct the sample surface in any way which permits the use of high magnification systems with low working distance which is absolutely necessary to resolve nanoscale structures. To calibrate the magnetic field magnitude and angle as a function of their position, the x- and z-components of the field were measured with a Hall probe. This data was used to create an interpolated table that allows the user to specify the desired field and angle, approximately ranging between 1 to 7 kOe and 15 to 75 degrees from surface normal, respectively.

Some advantages of the WITec system are the built-in scanning functions provided by the software that accompany the microscope. One particularly useful application of this function is scanning the diffraction-limited probe beam about an anti-reflective surface with a single, isolated nanomagnet on the surface. A built-in photomultiplier tube in the WITec can synchronously record the data during the scan, and the back-reflected light intensity will be automatically plotted as a 3-dimensional colormap by the software. The exact location of the nanomagnet will be known because its reflectivity is orders of magnitude larger, and the stage can easily be positioned using the piezoelectric controller to precisely place the focused beam at the center of the nanomagnet. This setup can be adapted as a scanning MOKE microscope by placing a polarizer in the beam path. Another application of this feature is to replace the sample with a razor blade and the NdFeB magnets with a collection objective to perform knife-edge measurements of the pump and probe beams. This reduces an otherwise lengthy

and laborious process into a simple, automated scan that takes less than an hour to complete – after the experiment has been setup, of course.

However, there are also some disadvantages of the WITec system that should be discussed. First, the polarity of the NdFeB magnets is fixed, therefore, the field cannot easily be reversed. In the event they must be flipped, a calibration procedure must follow to ensure the accuracy of the applied field. In addition, the largest applied field the magnets can supply is around 7kOe, which is enough for many samples with relatively low anisotropy and saturation magnetization but is insufficient to saturate samples with large anisotropy fields (eg. CoNi or CoPt multilayers). This is also an issue if one wishes to estimate the damping from the high-field limit – especially for systems with large iPMA. In the event either of these limitations are untenable, the alternate beam path leads to a bipolar electromagnet that does not suffer from these problems.

3.4.2 Electromagnet TR-MOKE Setup

Before the pump and probe beams reach the WITec microscope stage, a pair of flip-mirrors can be erected in the respective beam paths to redirect the pulses toward a dipole electromagnet (GMW 3470) controlled by a bipolar power supply (BOP 50-8DL, 50 V, 8 A). Without cooling, the maximum operating current that can be supplied to the electromagnet is 3.5 amps ($H_{app,max}$ ~ 1.3 T), however, the induction coils are surrounded by cooling tubes that can be pumped with filtered, distilled water from a nearby source allowing for a maximum current of 5 amps ($H_{app,max}$ ~ 1.8 T). Because

the field depends on the spacing, these values correspond to a pole spacing of ~ 1 mm, for reference, a standard Si substrate is 0.5 mm thick. Depending on the max field necessary, the pole spacing can be varied by the user. This also means that the field needs to be calibrated each time the poles are moved, which can be easily done using an automated Labview script described in the following paragraph. **Please note that the screws holding the poles in place must be very tightly secured because the attractive force in this case is very large!** Suffice it to say that this was experimentally proven, and the result was the pulverization of some thin films.

To calibrate the field, the voltage of a millimeter scale Hall probe is recorded by a GPIB-connected DC multimeter. The LabVIEW program synchronously sets the current and voltage supplied to the electromagnet by the BOP-50 power supply while recording the applied field. In the standard calibration procedure, the applied voltage is kept constant while the current is reduced in increments specified by the user as either a constant current step size or a pre-defined list. At each step, the field is recorded by the Gaussmeter at a rate of 1 kHz which is the primary limiting factor of the calibration speed. At each applied field, the current, voltage and magnetic field are saved to create a database for LabVIEW programs to call during automated MOKE experiments. Because the poles of the electromagnet are magnetic, their remnant magnetization contributes to the effective field, which is relevant for situations where the polarity of the magnetization is varying (e.g. hysteresis measurements and sample demagnetization). In these situations, a separate LabVIEW program that iteratively reduces the maximum current supplied to the electromagnet during the hysteresis

measurement should be used to generate the calibration data. In situations like TR-MOKE, however, the remanence of the poles is constant during the experiment and does not need to be accounted for. Some programs also just simply saturate the field in the positive direction each time before applying the desired field, which only increases the program run-time by a factor of 2. Because the Hall probe is only 1 mm thick, it can usually be kept behind the sample to constantly monitor the applied field during experiments, and its presence is only an issue when the applied field needs to be maximized by reducing the pole spacing.

Because the magnetic field cannot be applied further than 20^o out of the plane, there are several considerations one must be aware of when using this setup. First, the sample must have an out-of-plane component in order to detect the polar MOKE signal, thus, the magnetic moment of samples with an in-plane easy-axis must be canted by an external field with an out-of-plane component. However, only a small portion of the field ($\sin(20^o) \approx 1/3$) will be normal to the sample surface even at the largest possible angle. This means that the magnetic moment of samples with large M_s values (e.g. Cobalt with an anisotropy field $-4\pi M_s \approx 12000\ emu/cc$) cannot be pulled more than 15 degrees out of the plane per Eq. (2.3.11). Lastly, when the magnetization is applied in the sample plane the extrinsic damping contributions from two magnon scattering and inhomogeneous broadening (for samples with PMA) are inevitable and are usually largest. In order to extract the intrinsic damping behavior, these effects must be estimated using the methods described in section (2.4.2). The relevant characteristics of the WITec and Electromagnet are

summarized in Table 3.1 below.

Setup	***WITec***	***Electromagnet***
Max H_{app}	~7 kOe (θ_H dependent)	$\pm$1.8 T (pole spacing < 1 mm)
True Field Resolution	<100 Oe	<1 Oe
θ_H *Range*	15^o-75^o	0^o-20^o
θ_H *Accuracy*	$\pm 5^o$	± 0
Lateral Resolution	<100 nm	5 μm*
Ideal For	*TR-MOKE of nanostructures*	*Static and Dynamic Film Characterization*

Table 3.1. Summary of the relevant magnetic and geometric parameters for the WITec and Electromagnet TR-MOKE setups discussed in this section. *The lateral resolution quoted here is based on the lens system used in the electromagnet setup (*f = 5 cm, N.A. ~ 0.25*), a lens or long working-distance objective with a higher *N.A.* would improve the resolution.

3.4.3 Tuning the Pump Beam

Although the dual-color scheme employed in this TR-MOKE setup allows for easy separation of pump and probe beams, there is one issue that must be considered. Because the pump wavelength is half that of the probe, the beam waist is also a factor of two smaller than the probe. In systems that are free of chromatic aberration (eg. microscope objectives), both beams will be focused at the same working distance. This is problematic for measurements where the spin dynamics are instigated locally by the pump pulse, because the excitation profile in this case is not uniform within the probed region. As a result, the signal will be an ensemble average of the non-uniform dynamics which will result in a weaker response than a homogneously excited sample. It is, therefore, crucial to independently control the pump and probe spot sizes at the sample,

which can be accomplished using a relatively simple scheme. By placing a pair of identical lenses (f = 15 cm) in the pump beam path the size and divergence of the beam can be modified. When the lenses are precisely 2f apart the beam is simply flipped with respect to the input but retains the same waist and divergence it had before the lens system. However, if the separation between the lenses is less than 2f and the beam was initially collimated, the beam exiting the second lens will now be diverging; if the lenses are further than 2f the output will be converging (Fig 3.17 (a)). By focusing the beam as it enters the microscope, the "effective" numerical aperture of the system is reduced which in turn causes the blue beam to be focused at a slightly further distance than a collimated beam (Fig. 3.17 (b-d)). Thus, the two lenses allow us to vary the pump beam spot size independently of the probe beam, which we can use to create a more homogeneous excitation profile or to excite a larger area, i.e. to produce stronger SAWs by exciting more elements.

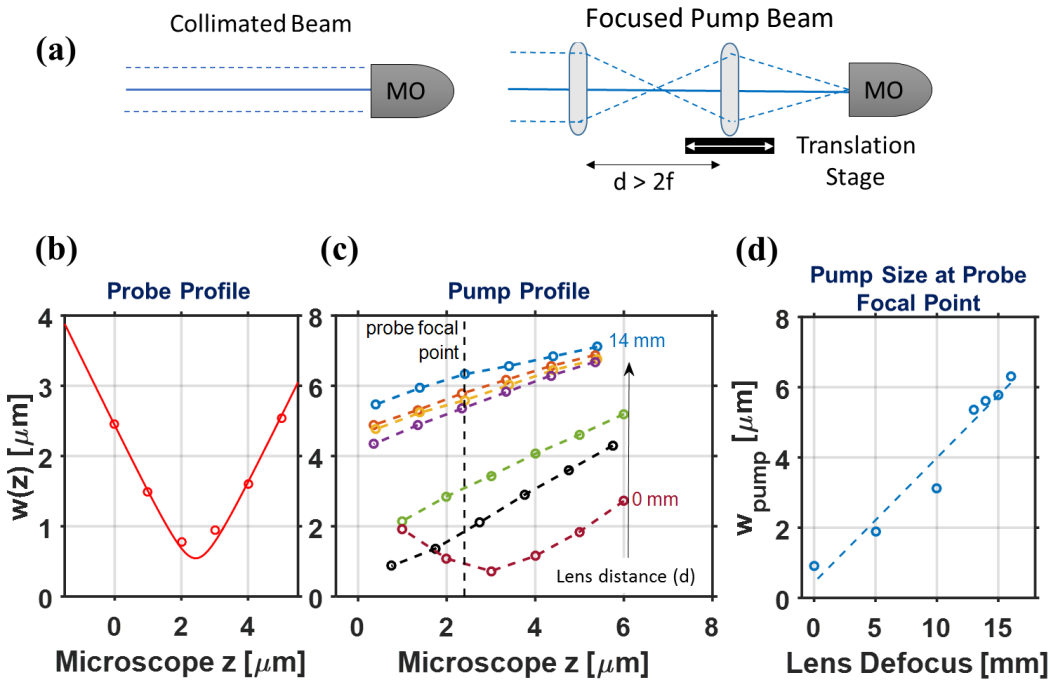

Fig. 3.17. (a) Illustration of the two-lens system that focus the pump beams into the MO in order to change the beam profiles. Knife edge measurements (100X MO) of the (a) collimated probe beam (w_0 ~ 500 nm) and (c) the focused pump beam which shows a shift in the focal plane for different lens separations. (d) Summary of the pump beam size at the focal point of the probe as a function of the lens separation.

3.5 Time Domain Analysis

In this final section on the TR-MOKE experiment, the techniques and algorithms used to analyze the time-evolution of the magnetization dynamics will be presented. In Chapter 2 we saw that the solution to the LLG equation for a thin film was an exponentially damped sinusoid with a decay determined by the Gilbert damping parameter α. However, we also know that the ultrafast laser pulse excites the sample to a highly non-equilibrium state which is unaccounted for in the derivation of the Kittel mode. A well-known, phenomenological formula that describes the TR-MOKE signal that ensues after excitation by an ultrafast laser pulse is [78]

$$\Delta\theta_k(t) = A_1 e^{-\frac{t}{\tau_1}} + A_2 e^{-\frac{t}{\tau_2}} + Asin(\omega t + \phi)e^{-\frac{t}{\tau}} \quad (3.5.1)$$

where the first two terms are related to the demagnetization and recovery processes described in Section 3.2.1 and are usually referred to as the "bi-exponential background", and the final term is the damped precession described by the Kittel equation. The bi-exponential background in the signal is due to the fact that high-energy magnons are excited by the impulsive thermalization, after which they relax and the sample returns to the ground state. In general, we are only interested in the harmonic part of the signal so the rest is simply subtracted to isolate this term so that it can be fitted and transformed into the frequency domain using an FFT algorithm for inspection.

3.5.1 Background Subtraction

The TR-MOKE signal described by Eq. (3.5.1) is generally valid for thin films, however, for heterostructures, nanopatterned arrays and single nanomagnets the vastly different thermal and acoustic properties affect the dynamics instigated by impulsive excitation. In these cases the bi-exponential term does not always sufficiently describe the background processes we wish to remove from the signal for analysis. An alternative approach, then, is to use digital filtering to isolate the magnetization dynamics by separating the low and high-frequency components in the signal. Surprisingly, bandpass and high-pass filtering caused significant distortion of the signal that adversely affected the least-squares fitting of the sinusoid. Instead, we have found that a low-pass filter can be applied to isolate the background, which is then subtracted

from the data. One such filter that we have used extensively is the Savitzky-Golay "smoothing" filter, which is a digital filter designed for the purpose of smoothing data without distorting the signal tendency. This is achieved by fitting successive subsets of adjacent data points with a low-degree polynomial by the method of linear least squares. The user defines the degree of the polynomial and the number of data points per subset, which determine the 'cutoff' frequency of the filter. In general, this filtering scheme is very robust so long as the cutoff frequency is kept as low as possible to ensure the genuine magnetization dynamics are not altered. In virtually all cases, a Savitzky-Golay filter with a polynomial degree of 4 (± 2) and a subset length of greater than half the number of data points is more than enough to remove unwanted signals.

3.5.2 Damping Analysis

In TR-MOKE experiments, the effective damping is determined by the fundamental relationship $\alpha_{eff} = 1/\omega\tau$, where ω and τ can be estimated by fitting the damped harmonic in Eq. (3.5.1) to the data. The most prominent technique for estimating model parameters is known as the *method of least-squares*, which adjusts the parameters of the model to minimize the difference, known as the residual *r*, between the data and the value predicted by the model. The residual is, therefore, defined as [80]

$$r_i = y_i - f(x_i, \beta) \tag{3.5.2}$$

where x_i is the independent variable, y_i is the dependent variable, the subscript *i* denotes the pair (x_i, y_i) where $i = 1, \ldots, N$ and *N* is the total number of data points in the set, and

the parameter β is the vector holding *m* adjustable parameters. Optimal values of the model function are determined by minimizing the sum of the squared residuals *S*

$$S = \frac{1}{N}\sum_{i=1}^{N} r_i^2 \tag{3.5.3}$$

It can be shown that the minimum value of *S* occurs when the gradient is zero

$$\frac{\partial S}{\partial \beta_j} = 2\sum_i r_i \frac{\partial r_i}{\partial \beta_j} = 0 \tag{3.5.4}$$

In nonlinear systems, the derivatives are functions of both the independent variables and the parameters and, therefore, do not have a closed solution. Thus, initial values must be provided by the user to be refined iteratively using the following approximation

$$\beta_j \approx \beta_j^{k+1} + \Delta\beta_j \tag{3.5.5}$$

where *k* is the iteration number and $\Delta\beta_j$is the vector of increments. At each iteration the model is linearized by approximation to a first-order Taylor polynomial about β^k

$$f(x_i, \beta) \approx f(x_i, \beta^k) + \sum_j \frac{\partial f(x_i, \beta^k)}{\partial \beta_j}\left(\beta_i - \beta_j^k\right) = f(x_i, \beta^k) + \sum_j J_{ij}\Delta\beta_j \tag{3.5.6}$$

Here, we have introduced the Jacobian **J**, which is a function of constants, the independent variable and the parameters – so it changes from one iteration to the next. Substituting these equations into the gradient equation above and rearranging terms we end up with the following expression

$$(\boldsymbol{J^T J})\boldsymbol{\Delta\beta} = \mathbf{J^T}\boldsymbol{\Delta y} \tag{3.5.7}$$

which directly connects the Jacobian to the confidence interval of the estimated parameters. Due to the popularity of this technique, optimized (efficient) codes are available for common software packages such as Matlab, Python, etc. Specifically, the curve-fitting toolbox functions “lsqcurvefit” and “lsqnonlin” in matlab can be used with the function “nlparci” to quickly determine the confidence of the fitted parameters.

CHAPTER 4
Magnetization Dynamics and Damping Behavior of Co/Ni Multilayers with a Graded Ta Capping Layer

4.1 Introduction

This chapter addresses the role of strong interfacial effects on the spin dynamics in ultrathin magnetic heterostructures. The sample studied in this work utilizes coupling between a ferromagnetic superlattice and heavy metal layer to support stable chiral spin textures known as *skyrmions*, which can be controlled by an applied electrical bias via the current-induced domain wall motion (CIDWM) effect. Topological spin structures have garnered a great deal of interest for their potential role in increasing magnetic data storage density, in addition to their novel physical properties which were only recently discovered. In this study, a direct connection between the anisotropy field and the effective damping was shown to obscure the intrinsic damping behavior of the system. Because the damping plays a crucial role in determining the operation characteristics of spintronic devices, precise determination of the Gilbert parameter is crucial in these systems.

4.2 Applications of Co/Ni

Since the development of the giant magnetoresistance (GMR) read-head in 1980's, interest in artificially layered magnetic systems has grown tremendously. Unlike single-crystal materials (e.g. Co, Ni, Fe), the magnetic properties of these devices can be tailored in a variety of ways, which has led to the discovery of numerous

novel effects such as tunneling magneto-resistance, spin transfer-torque, magnonic band gaps and much more.

In 1995, Gallego et al. [81] reported the first evidence of exotic properties in Co/Ni superlattices, in which they showed that these samples exhibited a superlattice transport effect that could be directly controlled by tailoring the thickness and number of Co/Ni layers in the stack. Since then, Co/Ni sequences with exceptionally large perpendicular magnetic anisotropy have been studied immensely for their potential role in STT-MRAM. In addition, it was recently reported that Co/Ni layers can be directly grown on top of ferroelectric substrates to achieve efficient strain-assisted magnetization switching [82]. Lastly, it was also recently discovered that when Co/Ni layers are grown atop a heavy metal layer such as Pt a strong the Dzyaloshinskii-Moriya interaction (DMI) occurs that allows stable skyrmions to form.

4.2.1 Dzyaloshinskii-Moriya Interaction

The DMI effect, also known as antisymmetric exchange, is an additional contribution to the total magnetic exchange interaction discussed in chapter 2. Unlike traditional exchange coupling it favors a canting of the spins, which is fundamental to the formation of skyrmions. The DMI Hamiltonian H_{DM} for two spins $\mathbf{S_i}$ and $\mathbf{S_j}$ is written as [83]

$$H_{DM} = \boldsymbol{D_{ij}} \cdot \left(\boldsymbol{S_i} \times \boldsymbol{S_j}\right) \qquad 4.2.1$$

where $\boldsymbol{D_{ij}}$ is the DMI tensor that characterizes the strength and direction of the effect. In 1958, physicist Igor Dzyaloshinskii predicted the effect due to relativistic spin lattice

and magnetic dipole interactions; two years later, Toru Moriya identified spin-orbit coupling as the microscopic mechanism responsible for this effect [84]. Experimental evidence of antisymmetric exchange in magnetic multilayers would not be reported for another four decades. However, in 2002 it was observed that the domain walls in a two monolayer-thick Fe film grown on a W(110) substrate all had the same rotational sense – a result which was inexplicable without DMI [85]. Soon after, researchers realized this effect could be used to achieve efficient CIDWM in ultrathin layers with PMA [86], which was a significant breakthrough for so-called magnetic racetrack memory. Then, in 2009 another major breakthrough occurred when researchers found that DMI led to the formation of stable chiral domains [87].

Although the DMI is being used extensively in novel spintronic architectures, many questions remain regarding the interaction between ferromagnetic layers and heavy metals (HM). Originally, it was believed that proximity-induced magnetization in the HM layer was responsible for the presence of antisymmetric exchange, however, it was later found that the strength of the effect was completely uncorrelated to the magnitude of the induced magnetic moment [88]. To this day, researchers are still working to understand the atomic interactions at the interfaces between these layers in order to fully explain the interfacial DMI.

4.2.2 Novel Co/Ni-Based Spintronic Memory Architecture

The sample studied in this chapter was developed by our collaborators at Carnegie Mellon University and used to create a novel, four-terminal spintronic memory device known as the "mCell" (Fig. 4.1).

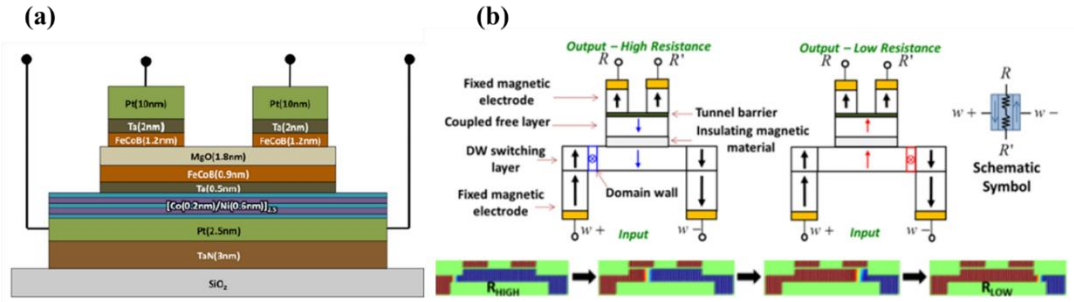

Fig. 4.1. (a) Schematic stack structure of the prototype mCell device and (b) a diagram illustrating how the mCell utilizes CIDWM to toggle the magnetoresistance of the device between high and low states. The color-coded images are micromagnetic simulations of the spin-hall effect switching. Taken from **[89]**.

To program the device, the location of a domain wall in the Co/Ni layers is controlled via CIDWM. The magnetic state of the domain wall layer is coupled to the free layer such that its magnetic state follows the current-controlled state of the bottom layer. Two magnetic tunnel junctions (*R* and *R'*) atop the free layer can probe the magnetization of the DW switching layer for read out. The switching speed of the device depends on the time it takes for the domain wall to travel from the *w+* input to the *w-* side, or vice versa, therefore, it is a function of the lateral dimensions of the device as well as the domain wall velocity. As was mentioned in the preceding section, a strong DMI is crucial in creating stable chiral domains that can be electrically controlled. Here, the antisymmetric exchange at the Ta/Co and Pt/Co interfaces acts in opposing directions which in turn lowers the domain wall velocity. The effective magnitude of the DMI can be increased by reducing the Ta thickness to weaken the

effect at the Ta/Co interface. However, the Ta serves as a seed for the stack, thus, reducing its thickness affects the properties of the active layers. To determine the optimum Ta thickness, a device with a graded Ta layer and no MTJs was fabricated to study the domain wall velocity as a function of Ta thickness. The authors found that the domain wall velocity was maximum for a Ta thickness of 0.5 nm, resulting in a peak value of 125 m/s which corresponds to switching times between 500ps to 1 ns.

During the characterization of the DW velocity in the switching layer described above, a peculiar chiral domain formation was observed. When the external magnetic field was applied along the in-plane direction, the skyrmions became distorted and formed "teardrop" shapes, as opposed to symmetric domains typically observed during these measurements. In addition, the domain wall velocity was larger when the DMI field was antiparallel to the external field – a result which had never been reported. By analyzing the free energy of the magnetic domain, the authors showed that the unique behavior was the result of a competition between the classical anisotropy field H_K and the DMI field H_{DMI}. Thus, the ability to tune the magnetic properties of the Co/Ni system ultimately led to the discovery of novel physics that have implications for both the rational design of devices utilizing CIDWM as well as our theoretical understanding of topological spin textures. It is, therefore, crucial to fully characterize the magnetic properties of this system.

4.3 Samples and Experimental Details

In the previous section the technological and academic interests surrounding the Co/Ni superlattice were reviewed. Despite the widespread intrigue, few studies have reported on the dynamic magnetic behavior in this system. Because these samples rely heavily on strong interfacial effects (e.g. interfacial DMI) to achieve the desired magnetic properties, care must be taken to ensure that unintended interactions do not inhibit the device performance. One parameter that is well-known to strongly depend on the interface interactions is the Gilbert damping parameter, which directly determines the critical current density required to switch the magnetization in STT-MRAM devices like those used in the mCell [3]. In the case of Co/Ni-based stacks, the wide variety of stack structures has resulted in a spread of reported "intrinsic" α values that vary by more than an order of magnitude [90, 91, 92]. Thus, there is strong motivation to further investigate the dynamic properties of Co/Ni systems to extract critical material parameters such as α_G, which have implications for both existing and emerging spintronic applications.

To this end, the Co/Ni multilayers used in ref. [93] with a stack configuration (Fig. 4.2 (a)) of TaN(3nm)/Pt(2.5nm)/[Co(0.2nm)/Ni(0.6nm)]x2/Co(0.2nm)/Ta(0.3-1.3nm)/TaN(6nm) were deposited by DC magnetron sputtering. TaN was used for the capping layer because it gives rise to more efficient current-driven domain wall motion than Ta alone. The base pressure was maintained at better than 3 x 10^{-7} Torr with a working pressure of 2.5mTorr Argon except for the TaN, which was prepared by reactive sputtering using an additional 0.5mTorr N2. The thickness gradient was

deposited using the wedge growth technique where the exposure time varied linearly across the surface of a 3" silicon substrate.

4.3.1 Interface Roughness Measurements via Glancing X-Ray Reflectivity

The layer thicknesses and interfacial structure were investigated using both cross-sectional transmission electron microscopy and grazing incidence X-ray reflectivity (XRR) (Fig 4.2 (b) and (c), respectively). Truly specular XRR data was recorded by Jesse Hauser using a Rigaku Smartlab diffractometer. The data was modeled using the GenX code [94], which uses a

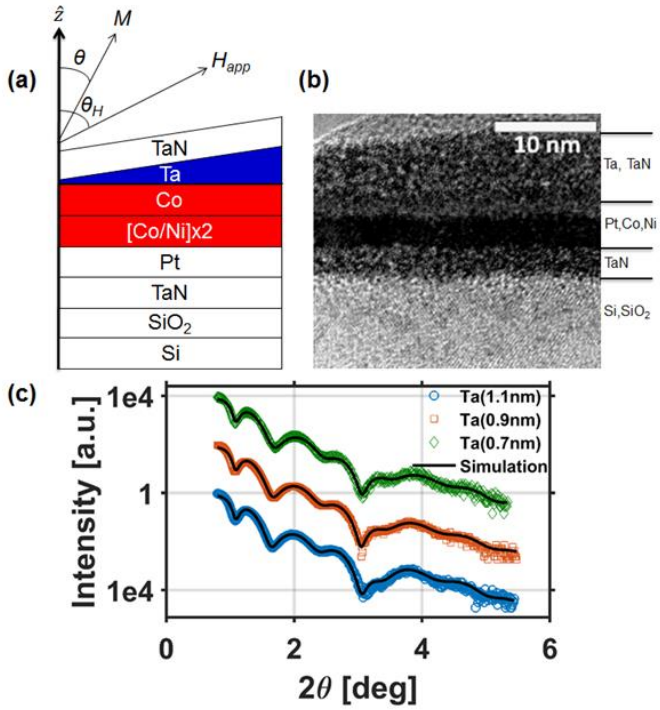

Fig. 4.2. (a) Multilayer sequence with illustration of the measurement geometry; *M* and H_{app} are the magnetization and applied field vectors with polar angles θ and θ_H relative to the surface normal, respectively. (b) Cross-sectional transmission electron microscope image of the sample; (c) X-ray reflectivity measurements (open symbols) and simulations (lines) for three different Ta thicknesses.

differential evolution algorithm with the Parratt recursive mechanism to simulate the XRR data [95]. The interface roughnesses of the Co/Ta, Ta/TaN, and TaN/air interfaces were fit to the data for each Ta thickness shown in Fig. 1(c) while all other parameters were fixed in the simulations. The fitting estimated that the Co/Ta and Ta/TaN interfaces had average rms roughnesses of 0.680 and 0.771 nm, respectively, and did not vary by more than 0.02 nm for the three Ta thicknesses measured

4.4 Results and Discussion

Magnetization dynamics of the Co/Ni sample were measured using a two-color optical pump-probe setup in both the WITec microscope as well as the electromagnet. For both cases, the pump (λ=400 nm, $1/e^2$ radius ~ 5μm, chopped at a frequency of 1 kHz) and probe pulses (λ=800 nm, $1/e^2$ radius ~ 2.5μm) were focused onto the sample at normal incidence. The field dependent dynamics were recorded for multiple applied field angles, θ_H, at 6 different locations along the Ta wedge. To analyze the data, the initial demagnetization is omitted and a bi-exponential background is subtracted to isolate a damped harmonic. A Hamming window is applied to the adjusted signal which is then converted from the time domain to the frequency domain using a discrete Fourier transform (DFT) algorithm to determine the resonance. The relaxation mode can then be related to the magnetic properties via the Kittel formula described in Section 2.3.1.

In Fig. 4.3(a) we show excellent agreement between the Kittel formula and experiment using only a single $H_{K,eff}$ value as a fitting parameter for all θ_H. The results for each Ta thickness are summarized in Fig. 2(b), showing a monotonic increase of

$H_{K,eff}$ with Ta thickness, reaching a maximum value of approximately 11.5 kOe for a 1.3nm Ta capping layer. While it is expected that the magnetic properties of the Co/Ni multi-layer saturate beyond some thickness of the Ta capping layer, the physical origin of the drop in $H_{K,eff}$ for thin Ta remains unclear. This could be related to formation of Co-N bonds at the interface or a suppression of Ta diffusion that would have otherwise reduced M_s.

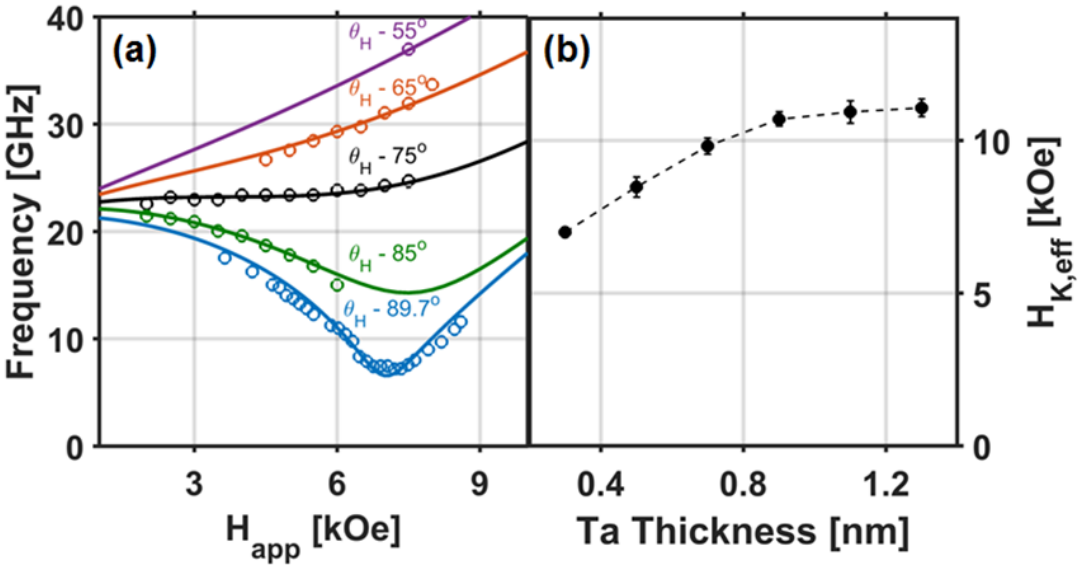

Fig. 4.3. (a) Resonance frequencies extracted from TR-MOKE DFT spectra (dots) and fit to eq. (1) for 0.3 nm Ta layer. (b) Summarized results of Kittel fitting procedure (eg. shown in (a)) for multiple Ta thicknesses. Taken from **[96]**.

We now turn our attention to the damping behavior of the system by evaluating the lifetime, τ_{eff}, of the magnetic precession for each measurement which is done by fitting the adjusted signal with a damped sinusoid (Fig. 4.4). The fitted lifetime directly determines the effective damping and is inversely proportional to the effective Lorentzian resonance, $\Delta\omega_{eff}$, via the relation

$$\Delta\omega_{eff} = \frac{2}{\tau_{eff}} = 2\omega\alpha_{eff} \qquad (4.3.1)$$

The term "effective" is used because the observed value is a sum of both intrinsic and extrinsic contributions [48, 50]. The intrinsic relaxation lifetime is determined directly by the Gilbert damping parameter, α_G, via the Smit-Suhl formula [97]

$$\frac{1}{\tau_G} = \frac{\Delta\omega_G}{2} = \frac{\alpha_G \gamma (H_1 + H_2)}{2} \tag{4.3.2}$$

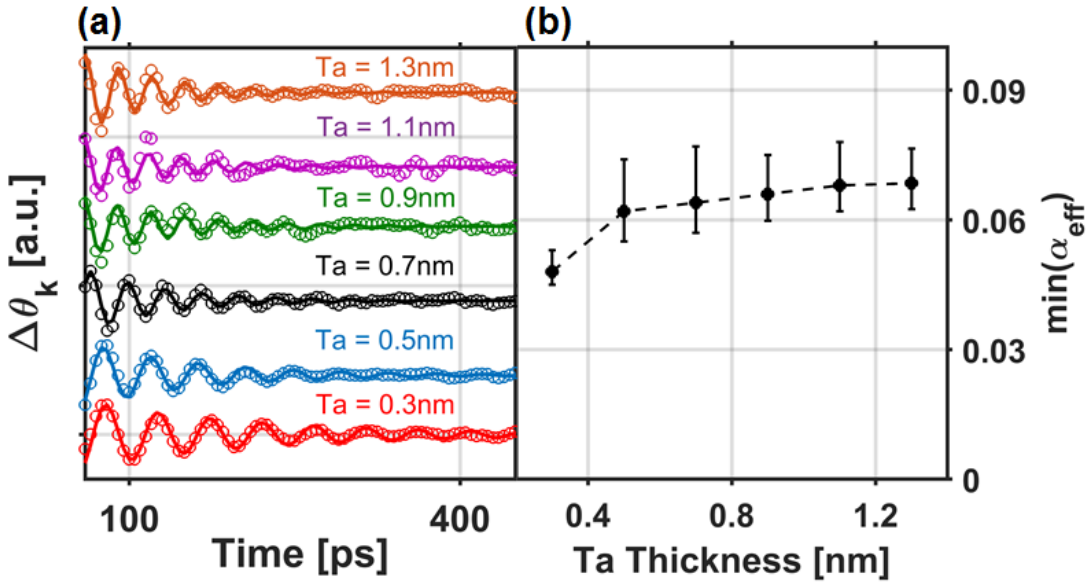

Fig. 4.4. (a) TR-MOKE data (circles) for each Ta thickness after omitting initial demagnetization and subtracting bi-exponential background, lines are the results of a least squares fitting to a damped sinusoid (line) (Data has been offset and normalized for visualization). (b) Minimum α_{eff} measured at a bias field angle $\theta_H = 85^o$ for each of the Ta thicknesses studied.

where H_1 and H_2 are calculated using equations (2.3.22) and (2.3.23). It is well known that when the applied field is sufficiently large, the extrinsic contributions become negligible and α_{eff} converges to the intrinsic α_G. However, because the convergence of α_{eff} is proportional to both $H_{K,eff}$ and $1/\alpha_G$, most experimental setups cannot reach this limit for highly anisotropic materials with low damping, as is the case here. Instead, α_G

can be estimated by evaluating the field dependence to account for the extrinsic contributions.

Previous reports on samples with large interfacial PMA have demonstrated that magnetic inhomogeneities significantly broaden $\Delta\omega_{eff}$ due to a distribution of resonance frequencies in the probe beam cross-section [92, 98, 99]. If the broadening is assumed to be caused primarily by variations of the effective anisotropy field, then it is useful to express this spread as

$$H_{K,eff}(\vec{\boldsymbol{r}}) = H_{K,eff} + \Delta h_{K,eff}(\vec{\boldsymbol{r}}) \tag{4.3.3}$$

where $\Delta h_{K,eff}(\vec{\boldsymbol{r}})$ is the local deviation from the average value, then a spatially dependent precession frequency and its root-mean-square, $\Delta\omega_{rms}$, can be calculated as follows

$$\omega(\vec{\boldsymbol{r}}) = \omega_0 + \frac{d\omega_0}{dH_{K,eff}}\Delta h_{K,eff}(\vec{\boldsymbol{r}}) \tag{4.3.4}$$

$$\Delta\omega_{RMS} = \sqrt{\langle\omega^2\rangle - \langle\omega\rangle^2} = \left|\frac{d\omega_0}{dH_{K,eff}}\right| \sqrt{\langle\Delta h_{K,eff}(\vec{\boldsymbol{r}})^2\rangle} \tag{4.3.5}$$

where ω_o and its derivative with respect to $H_{K,eff}$ is determined by Eq. (2.3.21), and the value in the radical indicates the root-mean-square (RMS) of the anisotropy field. Assuming a normal distribution of $H_{K,eff}$, the RMS value can be converted to the FWHM as follows

$$\Delta H_{K,eff} = \sqrt{2\ln(2)\,\langle\Delta h_{K,eff}(\vec{\boldsymbol{r}})^2\rangle} \tag{4.3.6}$$

It is worth noting that the spatial dependence of $H_{K,eff}$ is not only determined by changes in K_z, but also by changes in M_s which may vary more strongly in regions of thin Ta where N may infiltrate to the top layer of Co. This extrinsic addition to the linewidth can be combined with the intrinsic response in Eq. (4.3.2) to approximate the effective linewidth as

$$\Delta\omega_{eff} = \Delta\omega_G + \Delta\omega_{ext} = 2\omega(\alpha_G + \alpha_{ext}) \approx \alpha_G\gamma(H_1 + H_2) + \left|\frac{d\omega_0}{dH_{K,eff}}\right|\Delta H_{K,eff} \quad (4.3.7)$$

In Fig. 4.5 (a) the field dependence of the effective linewidth taken for $\theta_H \sim 90^o$ is shown for the 1.1 nm Ta sample while Fig. 4.5(b) shows the effective damping α_{eff}. The field dependence of $\Delta\omega_{eff}$ for a single Ta thickness was fit using Eq. (4.3.7) with $\Delta H_{K,eff}$ and α_G as fitting parameters, and was carried out in a similar manner at multiple positions along the wedge to obtain a single $\Delta H_{K,eff}$ and α_G for each Ta thickness. The results are summarized in Fig. 4.6(a) revealing a monotonic increase of $\Delta H_{K,eff}$ with Ta capping layer thickness, which has a pronounced effect on $\Delta\omega_{eff}$. Omission of the extrinsic contribution may have erroneously been interpreted as a large increase of the intrinsic damping of the Co/Ni system due to the capping layer thickness (eg. Fig. 4.4(b)). Instead, we find the data is well matched using a single Gilbert damping of 0.035 for all thicknesses, consistent with recent reports which find no dependence of α_G on the anisotropy [100].

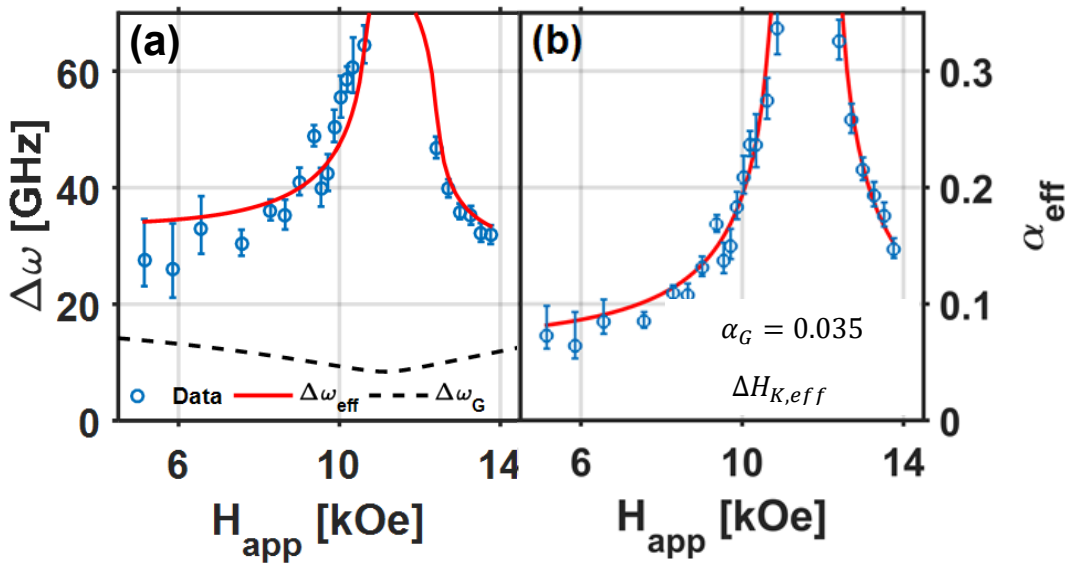

Fig. 4.5. (a) Effective Lorentzian linewidth of the Kittel resonance extracted from TR-MOKE measurements of 1.1 nm Ta cap (dots) and the best fit of $\boldsymbol{\Delta\omega_{eff}}$ using Eq. (4.3.7) (red line), for comparison, the intrinsic linewidth (dashed black line) using $\boldsymbol{\alpha_G = 0.035}$ is plotted to demonstrate the magnitude of IHB; (b) $\boldsymbol{\Delta\omega_{eff}}$ from (a) converted to α_{eff}. Taken from **[96]**.

It is worth discussing other possible mechanisms that can modify the damping when ferromagnetic layers are adjacent to non-magnetic layers (FM and NM, respectively), such as spin-pumping and *d-d* hybridization [101]. Because Ta is a poor spin sink [102] and the thicknesses used in this study are below the spin-diffusion length [103], any influence of spin-pumping on the relaxation behavior is expected to be negligible. Regarding hybridization of *d* orbitals at the FM/NM interfaces, metals with relatively low densities of *d* band electrons at the Fermi energy, such as Au and Ta, are expected to have a minor impact on dynamic relaxation. This claim is supported by a study of Co/Au bilayers which reports little to no dependence of α_{eff} on the Au thickness [104]. However, the Pt layer beneath the Co/Ni does have a high density of *d* band electrons in the conduction band, which can appreciably increase the Gilbert

damping via *d-d* hybridization. From the structural analysis in Fig. 4.2(c) it was determined that the interface roughness of the Pt/Co did not vary, therefore, its influence on α_G is expected to be constant, which is in agreement with our findings.

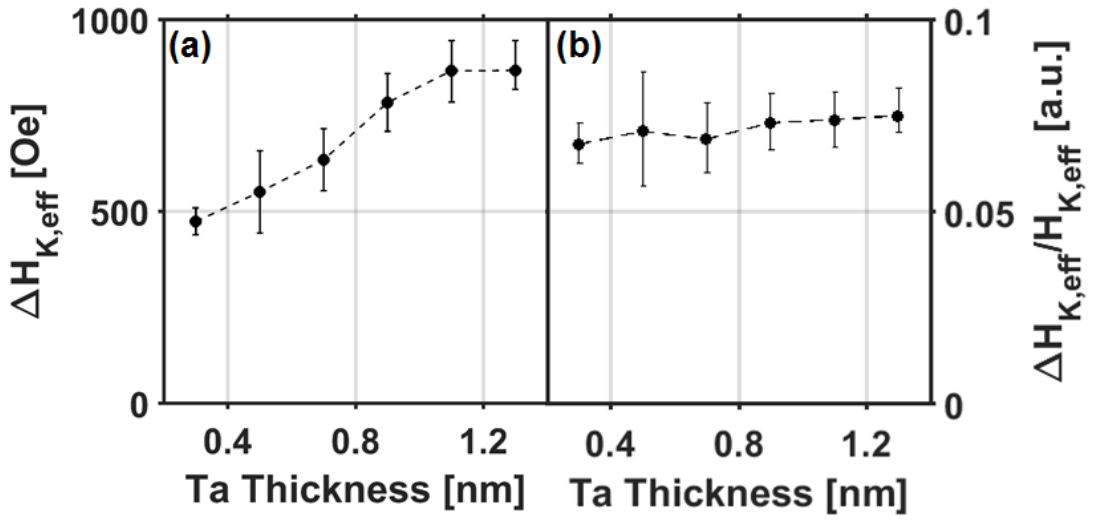

Fig. 4.6. (a) Local anisotropy field distribution as a function of Ta capping layer thickness determined via fitting data to Eq. (4.3.7) as shown in Fig. 4.5 (a). (b) $\Delta H_{K,eff}$ data from (a) normalized by corresponding $H_{K,eff}$ for each Ta thickness reveals a nearly constant ratio for the full range of Ta thicknesses. Taken from **[96]**.

Previous studies employing an inhomogeneous broadening model to explain the damping behavior of samples with large interfacial anisotropy have claimed surface roughness is a likely explanation for the large spread of local anisotropy fields. However, in Fig. 4.6(b) the ratio $\frac{\Delta H_{K,eff}}{H_{K,eff}}$ shows no appreciable change with respect to the Ta thickness, which suggests that the increase of the $\Delta H_{K,eff}$ depends on the magnitude of the anisotropy field instead of increased surface roughness [92, 98]. This interpretation is consistent with the structural analysis shown in Fig. 4.2(c) which also concluded that the surface roughness did not vary along the Ta wedge. These findings demonstrate that although the intrinsic damping is independent of the anisotropy field,

the variations of the local anisotropy field directly depend on $H_{K,eff}$ and act as an extrinsic contribution to the effective damping which may have implications for the rational design of devices.

4.5 Conclusion

In conclusion, TR-MOKE measurements on a Co/Ni sample with a graded Ta capping layer demonstrate a strong dependence of the anisotropy field on the capping layer thickness. Additionally, the observed damping behavior is significantly affected by the Ta layer which can be explained well using a model to account for the local variations of the anisotropy field. Notably, the intrinsic Gilbert damping parameter is independent of the capping layer.

CHAPTER 5
Dual-Purpose Dielectric Coating for SAW Suppression and Cavity Enhancement

5.1 Introduction

In this section, the magnetization dynamics of densely packed arrays of prototypical STT-MRAM devices studied using TR-MOKE will be presented. Because MTJs are vanishingly small, direct far-field MOKE detection of single, isolated nanostructures at technologically relevant dimensions (<100 nm) is not possible. Instead, it is much easier to detect the small-angle precession of dense nanomagnet arrays if each device in the probed area is identical and the ensemble signal reflects the true behavior of individual devices. However, we shall see in this section that imperfections dramatically distort the dynamic behavior and complicate the interpretation of the experimental data. In addition to the ensemble effects, when a dense, periodic array is excited by an ultrafast laser pulse the impulsive thermal expansion of the elements gives rise to surface acoustic waves (SAWs) that propagate along the surface and deform the nanomagnets, which in turn generates a harmonic magneto-elastic field inside the elements. Here, we show that by depositing a dielectric layer on top of the sample, the SAWs can be quenched, which in turn enables us to study the intrinsic magnetization dynamics. Using the nanomagnet profiles obtained from SEM imaging and the IHB theory discussed in chapter 4, the ensemble damping behavior was modelled and found to be in excellent agreement with the experimental

observations.

5.1.1 SAW Excitation in Nanopatterned Arrays

When lithographically defined structures are arranged periodically on a surface they form vibrational modes that are determined by their spacing, or pitch (p), and the speed of sound (v_{sound}) in the substrate via the following relationship [105]

$$f_{SAW} = \frac{v_{sound}}{p} \tag{5.1.1}$$

The speed of sound in most solids ranges between 1-10 km/s, therefore, micron-scale lithography can be used to create SAW devices operating from MHz to GHz frequencies. One of the most common structures for generating SAWs is known as an *interdigital transducer* (IDT), which is shown in Fig. 5.1.

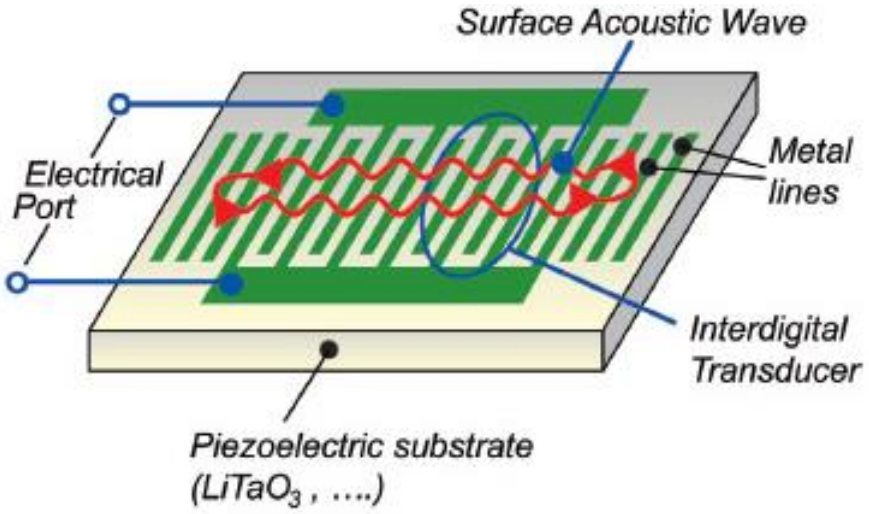

Fig. 5.1. Schematic illustration of a conventional interdigital transducer used to generate SAWs. Taken from ref. **[106]**.

Typically, these devices use piezoelectric substrates that can generate large strains in response to an AC bias tuned to the resonant frequency f_{SAW}. However, it is not

necessary to use a piezoelectric substrate in order to generate SAWs. An alternative approach is to excite the bars using an ultrashort light pulse, which causes rapid thermal expansion of the elements thereby launching SAWs. One advantage of this approach is its simplicity which allows us to freely choose f_{SAW} via the array geometry, whereas a conventional IDT would require an accompanying RF circuit to drive it. Because we are interested in GHz dynamics, circuits in this range can be very complex and expensive. On the other hand, if large strains are required the photoexcitation approach is ultimately limited by the ablation threshold of the elements. This method is also inefficient, because the highly reflective metal used to generate SAWs absorbs only a fraction of the light.

5.1.2 Coupling Between SAWs and Magnetization Dynamics

In 2007, Giannetti et al. published their work in ref. [107] on the ultrafast thermal and mechanical dynamics of a two-dimensional lattice of permalloy nanodisks studied via pump-probe spectroscopy. Their results showed that, to a good approximation, the fundamental mode of the SAWs generated by the absorption of an ultrafast pulse is determined by the relatively simple relationship provided in Eq. (5.1.1). Because there are various periodicities in an array, higher order modes are also supported and are direct multiples of the fundamental frequency governed by the following relationship

$$f_{ij} = \sqrt{i^2 + j^2} f_{SAW} \tag{5.1.2}$$

Here, *ij* denotes the mode order, for example, in a square array there is a diagonal periodicity corresponding to the (1,1) mode which has a frequency of $\sqrt{2}f_{SAW}$. Lastly, in their report the authors also showed that the two-temperature model could be used to estimate the thermal expansion via the lattice temperature. Interestingly, even though the elements in this study were magnetic, the magneto-elastic behavior was not considered, thus, the dynamic coupling between the phonon and spin system remained unexplored.

In 2011, Weiler et al. showed in ref. [108] that SAWs could be used to drive the ferromagnetic resonance of a Ni film placed between a pair of IDTs on a piezoelectric substrate. In this study, the acoustic waves were launched from one of the gratings towards the Ni film and then subsequently detected by another set of transducers on the other side. Using an external magnetic field, they tuned the resonance of the film to the SAW frequency and showed unequivocally that more power was absorbed when the Kittel frequency matched f_{SAW}. Despite the excellent agreement between theory and experiment in their study, a number of questions regarding the dynamic coupling of elastic and magnetic systems remained unanswered.

Because dense nanomagnet arrays are highly regarded for their potential to improve areal storage density in next-generation memory technologies, there was an obvious need to fully characterize their dynamic behavior. However, the novelty of the problem would require innovation in order to capture the complicated physics which underpin the dynamics. Following the approach laid out in ref. [107] to model the acoustic behavior, Yahagi et al. set out to use the elastic deformation obtained via FEM

modelling as an input into a micromagnetic framework to calculate the magneto-elastic field generated by the SAWs via Eq. (2.2.39). After extensive research and development, the OOMMF extension YY-MEL was created to carry out the calculation and was found to be in excellent agreement with the experimentally observed behavior (Fig. 5.2) [18]. Although this approach neglects the effect the spins have on the mechanical system, the superior strength of the SAWs in this case make it an adequate approximation. A direct implication of their results is the need to appropriately choose the array geometry depending on the spin-wave characteristics of the devices. In addition, these results show that SAWs may be used to efficiently drive GHz oscillations at the nanoscale, as opposed to thermal or field-based approaches which each have their respective drawbacks. Finally, the ability to enhance the dynamic MOKE signal without modifying the experimental setup is attractive for the detection of devices which may otherwise be impossible to resolve.

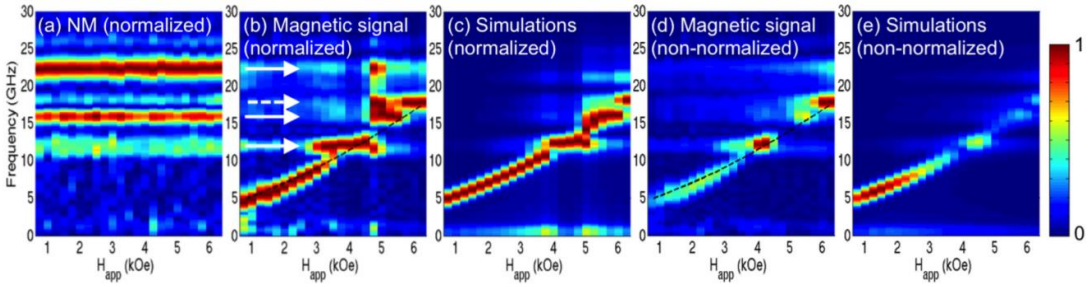

Fig. 5.2. The sample used in this study is an array of 30 nm thick elliptical Ni nanomagnets, with major and minor axes of 140 and 80 nm, respectively, arranged on a pitch of p = 212 nm. The field-dependent DFT of the normalized (a) nonmagnetic signal, (b) the TR-MOKE signal, (c) simulated magnetization dynamics, and (d,e) non-normalized versions of (b,c), respectively. Taken from ref. **[18]**.

5.2 Samples and Experimental Details

While the previous sections explored the generation of SAWs and their dynamic coupling to the magnetization dynamics, we will now turn our attention to the restoration of intrinsic magnetization dynamics in patterned arrays. As can be seen in Fig. 5.2, the presence of mechanical waves dramatically alters the intrinsic spin dynamics, specifically, when the magnetic frequency is near f_{SAW}. In this vicinity, the SAWs – which have a much longer lifetime than the magnetic system – drive the spin dynamics well beyond the lifetime determined by the LLG equation. If we reconsider the damping relationship $\alpha_{eff} = 1/2\pi f \tau_{eff}$, the magneto-elastic coupling results in a significant increase in the effective lifetime and, therefore, a large reduction in the effective damping. This is problematic for the characterization of damping in nanostructured materials because it is virtually impossible to extract the magnetic relaxation rate in this case. Of course, for larger nanostructures one can simply study the device in isolation to avoid generation of SAWs, however, for technologically relevant sample sizes this is not feasible. In this section, the use of a dual-purpose dielectric coating for simultaneous cavity-enhancement (CE) of the MOKE signal and suppression of the acoustic waves will be discussed. This report was published in ref. [109]. In this study, the sample we set out to measure was a pre-commercial, STT-MRAM prototype array of dual magnetic tunnel junction (DMTJ) structures which contained a pair of CoFeB layers (thickness~1.6 nm) sandwiched between MgO tunneling barriers. The sample was provided by our collaborators at Samsung, who could not share the complete stack configuration with us due to company policy.

However, using a nearly identical unpatterned film we confirmed that the TR-MOKE signal could be detected even though the FL is buried beneath multiple metallic layers. Each nanostructure was approximately 70 nm in diameter and the elements were arranged in a square array with a 250 nm pitch (Fig. 5.3 (a)). Unfortunately, the top-most layer of the substrate is a highly reflective TiN film that is critical to the growth of high-quality MTJs. As a result, these devices cannot simply be grown on an antireflection substrate to maximize the MOKE signal as discussed in section 3.1.2. Nonetheless, we performed TR-MOKE experiments

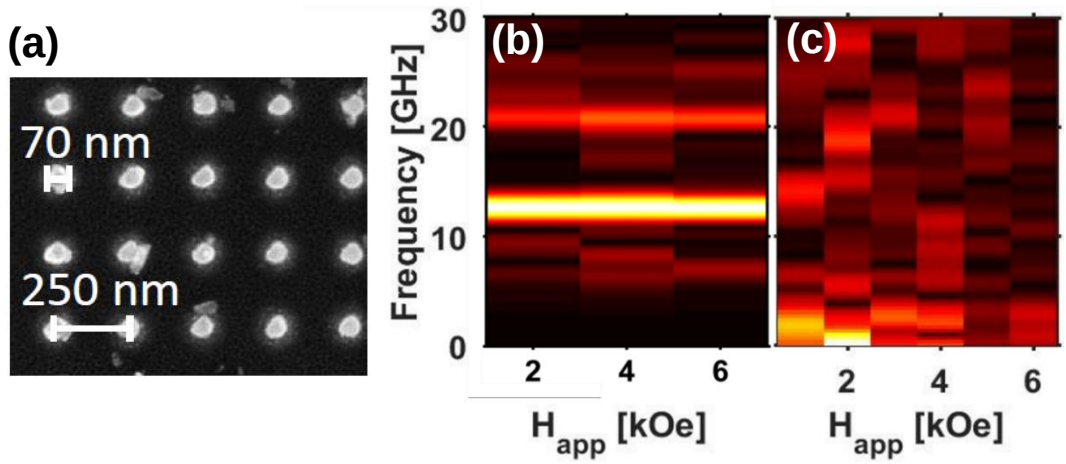

Fig. 5.3. (a) SEM image of the MTJ nanomagnet array revealing slight variations in the shape between devices. Normalized DFT spectra of the TR-MOKE signal taken on the uncoated MTJ array for (b) conventional pump-pulse setup, and (c) two time-delayed pump pulses set to annihilate SAWs. In both cases, no magnetic signal can be observed in the spectra due to the large reflectivity of the TiN surface.

on the as-deposited sample to see if the magnetic signal could be resolved. As discussed in the preceding sections, SAWs are unavoidable in an array geometry. This, coupled with the highly reflective substrate, resulted in a back-reflected probe that was

dominated by the nonmagnetic behavior, as shown in the field-dependent spectra in Fig. 5.3 (b,c).

To improve the optical properties of the surface, we decided that a dielectric layer could be deposited to simultaneously reduce the reflectivity of the TiN surface and improve the Kerr rotation via the CE effect. Per the recommendation of our colleagues at Samsung, we chose SiN as the material to deposit because: (i) it is chemically compatible with the MTJs (compounds with Oxygen could not be used because CoFeB oxidizes easily), (ii) Samsung researchers had well calibrated equipment for this deposition, and (iii) it had previously been used in ref. [62] to study the CE effect. As discussed in section 3.1.2, the most effective way to improve the magneto-optic contrast is to minimize R_{sub}. To this end, we studied the optical response of TiN films coated with varying thicknesses of SiN. To model the reflectivity of the coated samples, the Fresnel coefficient for a bilayer system (SiN/TiN) can be expressed as [110]

$$r = \frac{r_1 + r_2 e^{-2i\delta}}{1 + r_1 r_2 e^{-2i\delta}} \tag{5.2.1}$$

Here, the subscript *1* refers to the Fresnel coefficient at the air/SiN boundary determined as follows

$$r_1 = \frac{1 - n_1}{1 + n_1} \tag{5.2.2}$$

where n_1 = 2.1 is the refractive index of SiN. The second term in Eq. (5.2.1), $r_2 e^{-2i\delta}$, is the Frensel coefficient of the SiN/TiN boundary

$$r_2 = \frac{n_1 - \widetilde{n_2}}{n_1 + \widetilde{n_2}} \tag{5.2.3}$$

Note that because TiN is metallic, the refractive index for this layer is complex ($\widetilde{n_2} = n_2 - ik_2$). The exponential term in Eq. (5.2.1) is the phase picked up as the light travels in the SiN defined as

$$\delta = \frac{2\pi n_1 L}{\lambda} \tag{5.2.4}$$

where L is the SiN thickness. When the partial reflections from the surface destructively interfere the reflectance is minimized. By differentiating the reflectance with respect to the dielectric layer thickness the optimum length can be expressed as

$$L = \frac{(j+1)}{2n_1}\lambda - \frac{\lambda}{4\pi n_1}\arctan\left(-\frac{2n_1 k_2}{n_1^2 - n_2^2 - k_2^2}\right) \tag{5.2.5}$$

where $j \in \mathbb{N}_0$. However, because of the imaginary component of $\widetilde{n_2}$, perfect antireflection occurs when the refractive index of the dielectric layer satisfies

$$n_1 = \sqrt{n_2 + \frac{k_2^2}{n_2 - 1}} \tag{5.2.6}$$

which reduces to the more well-known antireflection condition for two dielectric layers ($n_1 = \sqrt{n_2}$) as the k_2 approaches zero. A series of SiN/TiN films were prepared with SiN thicknesses ranging from 45-75 nm in 10 nm increments, and the reflectivity of

each sample was studied with the probe beam focused onto the sample surface by an f =15 cm lens. The refractive index of the TiN layer and the appropriate SiN thickness were determined by fitting the reflectance according to Eq. (5.2.1) allowing n2 and k2 to vary freely as fitting parameters (shown in Fig. 5.4).

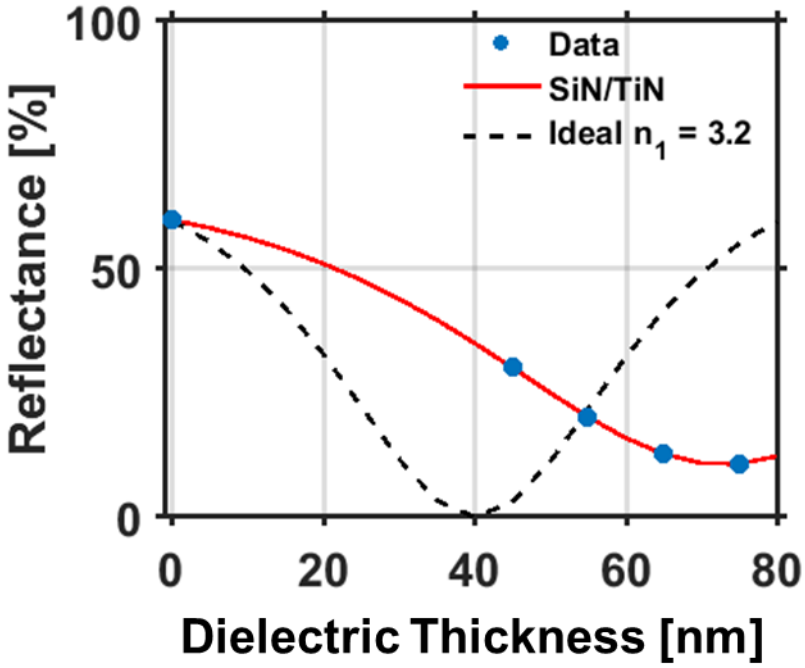

Fig. 5.4. The reflectivity of the SiN/TiN series as a function of the dielectric layer thickness (blue dots) and the calculated response (red line) using an estimated TiN index of $\widetilde{n_2} = 2.83 - 3.68i$. Per Eq. (5.2.6), the ideal dielectric index for perfect antireflection is n_1 = 3.2 (dashed black line).

From the data, we clearly observe the minimum reflectivity for a SiN thickness of 75 nm, however, because we are ultimately interested in the magneto-optic response of the MTJ the CE factor and R_{mag} as a function of SiN thickness must also be considered.

To complete our study, a series of CoFeB MTJ films with a stack structure of Ru(5)/Ta(1.5)/Ru(1.5)/MgO(1)/CoFeB(1.8)/MgO(1)/CoFeB(0.4)/Ta(1)/Ru(5)/Ta(1)/ TiN were coated with SiN films ranging from 55-85 nm. The reflectance and polar Kerr

rotation of each sample was characterized using a "perfectly" crossed polarizer MOKE setup tuned to maximize the *S/N* ratio defined in Eq. (3.3.15) which yields a direct measurement of θ_k. The results are shown in Fig. 5.5 and reveal a solid enhancement of the Kerr rotation for all samples when coated with SiN, however, the sample-to-sample coercivity H_c varies not only between films, but also between different areas on the same film (Fig. 5.5 (a,b))!

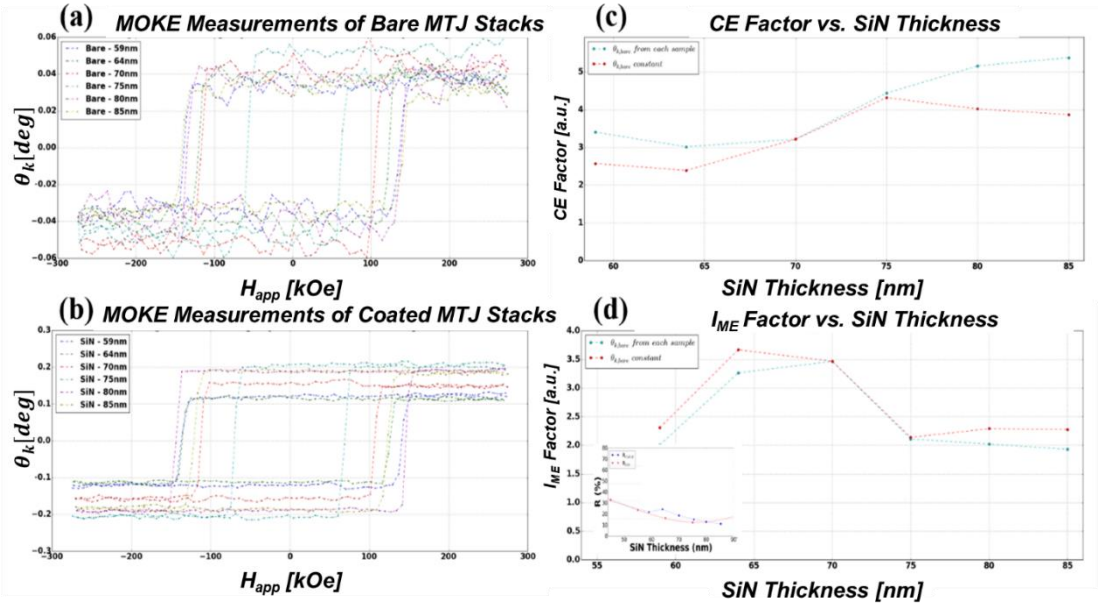

Fig. 5.5. MOKE hysteresis loops of each (a) CoFeB stack without SiN coating and (b) after being coated. The improved signal-to-noise characteristics and Kerr rotation can be seen in the data. (c) The CE factor for each sample using the average Kerr rotation of the entire set (red line) and for each individual sample (blue line), and (d) the corresponding I_{ME} factor; inset: reflectivity of SiN/MTJ stack compared to SiN/TiN.

The discrepancy in H_c and θ_k between samples most likely stems from variations in the interfacial PMA at the CoFeB/MgO boundaries, which is highly sensitive to the layer thicknesses, composition and interface roughness. Furthermore, because the stack structure used for the CE study was not identical to the nanomagnet array that was the

target of our study, the optimum dielectric thickness determined from this study is may not be the same for the array sample. Nonetheless, the *improvement factor* I_{ME}, which is a measure of how much coating improves the detectability of the Kerr rotation, can be determined as follows [61]

$$I_{ME} = \sqrt{CE \frac{R_{mag}}{R_{mag,u}} \frac{R_{sub,u}}{R_{sub}}} \tag{5.2.7}$$

where the subscript *u* denotes the reflectance without a dielectric coating and the CE factor is calculated according to Eq. (3.1.87). Thus, despite the fact that the 75 nm SiN coating produced the smallest substrate reflectivity, per the relationship defined above I_{ME} is largest for SiN thicknesses between 65-70 nm – primarily because the ratio R_{mag}/R_{sub} is largest in this range.

` Based on these results, a 65 nm SiN film was deposited on the nanomagnet array to improve the magneto-optic properties of the surface. Once coated, a field-dependent mode is observed in the TR-MOKE spectra (Fig. 5.6). In addition, the SAWs that previously dominated the dynamic behavior are totally absent from the signal. Again, it bears repeating that the FL thickness of the film is slightly thicker (0.07 nm) which corresponds to a smaller H_K value and smaller precession frequency (for this geometry). Although the magnetization dynamics were now discernible, the large difference in α_eff between the unpatterned film and the array (shown in Fig. 5.6 (c))

was unexpected, because many reports found little or no enhancement of the Gilbert damping due to nanopatterning.

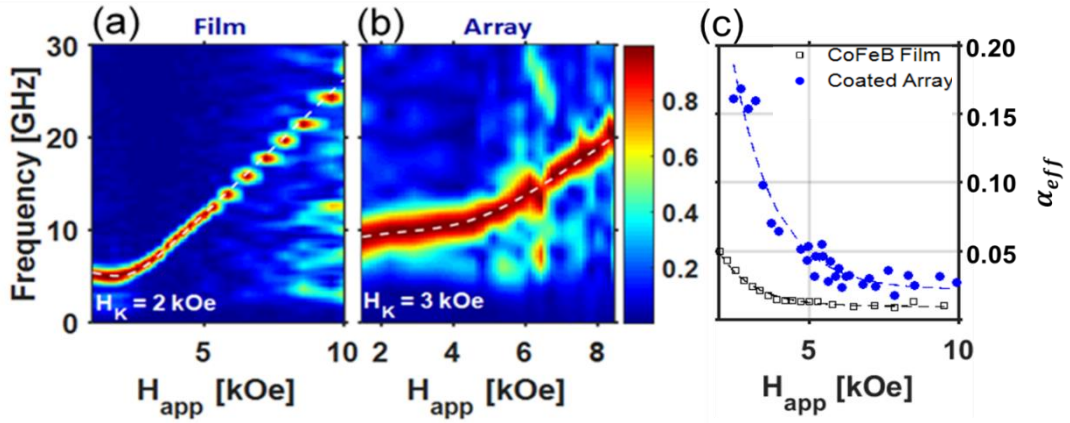

Fig. 5.6. The field-dependent normalized TR-MOKE spectra taken at $\boldsymbol{\theta_H = 75^o}$ of the (a) unpatterned MTJ film and (b) the MTJ nanomagnet array coated with 65 nm of SiN; the dashed lines are the Kittel frequencies (Eq. 2.3.20) corresponding to the H_K values specified in the figures. The higher H_K value of the array is responsible for the slightly higher frequency. In (c), the effective damping of both samples are shown, revealing a large discrepancy in $\boldsymbol{\alpha_{eff}}$ between the film and nanomagnets (the dashed lines here are only a guide to the eye).

One outstanding question that stymied interpretation of the damping behavior was the unknown SAW profile of the coated sample. It was unclear if SAWs were still present, and if so, what effect they may have on the observed damping. The issue was further complicated by our incomplete knowledge of the layer structure, which made it virtually impossible to perform the FEM and micromagnetic modelling that would shed light on the response of the coated sample.

5.3 Suppression of SAWs

In order to determine the efficacy of the SAW suppression, we decided to use a simpler sample architecture that would allow us to accurately model the elastic and

magnetic dynamics according to the procedure described in ref. [18]. To this end, two identical nickel arrays composed of square nanomagnets with nominal dimensions of 125x125x30 nm^3 and pitch of 250 nm were fabricated on an antireflection (AR) coated silicon (100) substrate using an established electron beam lithography and lift-off process [18, 111, 112]. A 65 nm SiN film was then uniformly deposited onto the surface of one sample using plasma-enhanced chemical vapor deposition. The arrays were studied using the TR-MOKE setup described in section 3.4 with the pump and probe pulses (pulse width - 165 fs, repetition rate - 76 MHz) focused onto the sample with $1/e^2$ radii of approximately 5 and 2.5 μm, respectively.

A series of measurements were taken with an externally applied field H_{app} kept at a fixed angle $\theta_H = 30^o$ from the surface normal. In Fig. 5.7 (a), the normalized Fourier spectra of a Ni film evince only the well-defined Kittel mode in stark contrast with measurements of the uncoated Ni nanomagnet array (Fig. 5.7 (b)), which contain several pronounced field independent frequencies. Inspection of the time-dependent reflectivity signal (nonmagnetic, Fig. 5.7 (d,e)) reveals that the pinning occurs at well-defined SAW modes (marked by arrows), known to exist when periodically arranged elements are irradiated with an ultrafast pulse [107, 18]. As the spin waves approach the SAW frequencies the two become magneto-elastically coupled and the magnetic response is pinned at the acoustic eigenmodes over a range of fields; enhancing the oscillation amplitude and lifetime thereby rendering damping analysis impossible.

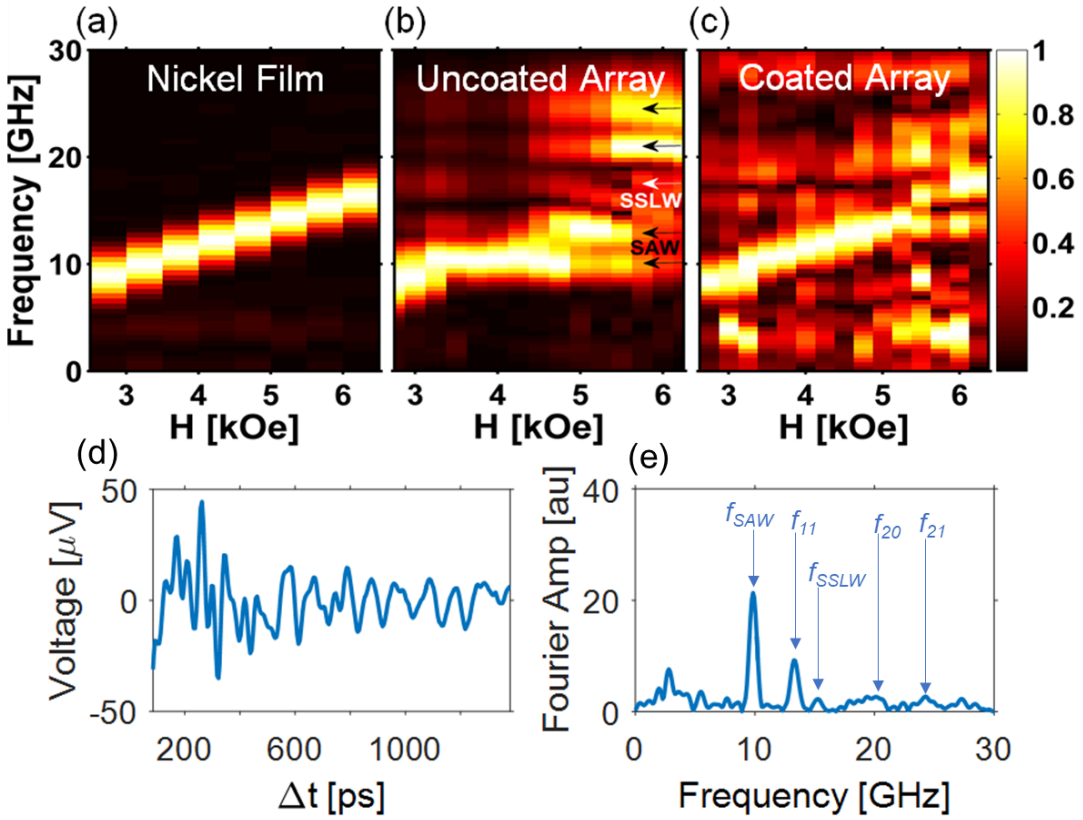

Fig. 5.7. The field-dependent TR-MOKE spectra taken at $\boldsymbol{\theta_H = 30^o}$ for (a) an unpatterned Ni film, (b) the nanomagnet array without coating, and (c) the array coated with 65 nm of SiN. In (d) the time evolution of the lock-in reflectivity is shown, as well as the corresponding DFT in (e) which we use to identify the SAW frequencies, which are accurately predicted by Eq. (5.1.2).

This behavior can be modeled by simulating both elastic motion and the magnetization dynamics. The strain profile obtained from finite element simulations of the optically excited nickel elements creates a magneto-elastic contribution H_{MEL} in the effective applied field entering the Landau-Lifshitz-Gilbert equation in Object-Oriented Micromagnetic Framework (OOMMF) [1]. In order to suppress this coupling, we coated the array with a dielectric silicon nitride (SiN) film (Fig. 5.7 (c)). Qualitatively, the elements' physical motion is restrained which quenches the SAWs, thereby restoring the intrinsic field-dependent TR-MOKE response.

Numerical simulations of the dynamics of the arrays with and without coating are shown in Fig. 5.8. The oscillation amplitude of the H_{MEL} field in the coated sample is reduced by more than a factor of 10, and the field subsides within picoseconds while the MEL response of the bare sample persists for nanoseconds. In Fig. 5.8 (b) the spectra of the time-traces in (a) show that the coating eliminates the Fourier components at the elastic resonances, in agreement with the removal of the pinning of the magnetic response as seen in Fig. 5.7 (c).

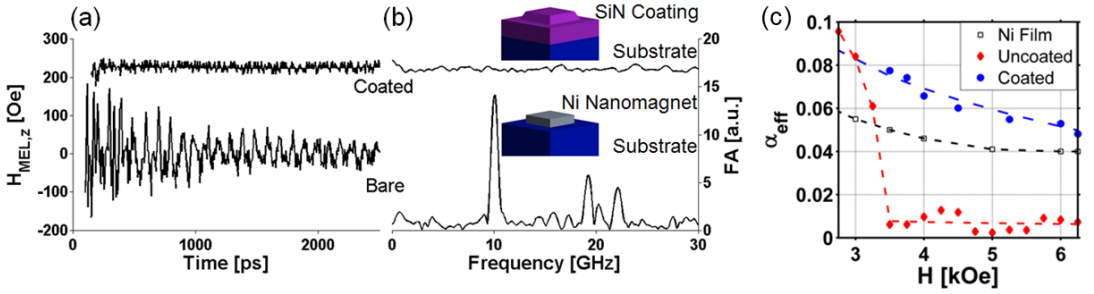

Fig. 5.8. (a) Micromagnetic simulation of magneto-elastic field created by SAWs with and without a dielectric coating; (b) the discrete Fourier transform ($\boldsymbol{H_{app} = 5\ kOe \mid \theta_H = 30^o}$). The coated response is offset for clarity; insets: FEM geometries used for modelling. In (c), the effective damping of the unpatterned film, uncoated and coated arrays are plotted to demonstrate the obscuring of the intrinsic damping behavior (uncoated) and the restoration of the intrinsic response.

Now, the time-domain response at each field can be fit with a damped sinusoid to obtain the oscillation lifetime (τ_{eff}) which is used to determine the effective damping using the relation. First comparing the Ni film and uncoated array in Fig. 5.8 (c), we see that the SAWs extend τ_{eff} and result in much smaller α_{eff} values than the intrinsic α of 0.04 observed in the film. The most extreme instance was observed at H_{app} = 5 kOe, where the decay constant measured for the array ($\tau_{eff} \sim 5\ ns$) is nearly 16 times larger than the purely magnetic response observed in the film

($\tau_{eff} = 300\,ps$) due to driving force of the SAW. In contrast, the SiN coated array (solid circles) shows an increased α_{eff} throughout the entire field range that converges to the film value at large external fields. For this sample, the enhancement of the effective damping is due to fluctuations of key magnetic parameters between devices, and, therefore, a spread in the precession frequencies. As a result, the ensemble relaxation time decreases due to *dynamic dephasing* of the signal, wherein oscillations at distinct frequencies destructively interfere as they become more out of phase with time (Fig 5.9 (a)). Here, the significance of the data lies in the successful restoration of the magnetization dynamics by the dielectric coating which re-opens the door for extraction of pertinent material parameters.

5.4 Damping Behavior of STT-MRAM Devices

For a more quantitative analysis, we focus on the damping behavior of the technologically important CoFeB-based STT-MRAM devices. In Fig. 5.6 (c) we compare the damping behavior of the uncoated film and coated nanomagnet array which exhibits an even larger increase of α_{eff} than for the Ni sample. Here, we conjecture that this increase is primarily due to two extrinsic effects. The first is a contribution from magnetic inhomogeneities (MI), due to variations of the local effective anisotropy field, H_K. The second one is a variation in nanomagnet shapes which broadens the spread of precession frequencies and thus, through dynamic dephasing, increases the apparent damping of the time response [113] – this mechanism applies only to the patterned array. When the applied field cannot reach large enough values to converge to the intrinsic Gilbert damping α, as is the case here, one can relate

the effective lifetime, τ_{eff}, obtained with TR-MOKE to the Lorentzian resonance linewidth, $\Delta\omega_{eff}$, using the relation $\Delta\omega_{eff} = {}^{2}/_{\tau_{eff}}$. The extrinsic contributions to the effective linewidth are given by

$$\Delta\omega_{eff} = \Delta\omega_{int} + \Delta\omega_{ext} \approx \Delta\omega_{int} + \Delta\omega_{MI} + \Delta\omega_{S} \tag{5.4.1}$$

where $\Delta\omega_{int}$ is given by the Smit-Suhl formula, $\Delta\omega_{MI}$ represents the spread in the resonance frequencies due to MI present before patterning, and $\Delta\omega_S$ is the spread due to nanomagnet shape fluctuations. If the distribution of resonant frequencies is assumed to be primarily caused by a distribution of the local anisotropy field with a peak-to-peak width, ΔH_K, then $\Delta\omega_{MI}$ can be approximated as [114]

$$\Delta\omega_{MI} \approx \left|{}^{\partial\omega}/_{\partial H_K}\right| \Delta H_K + \left|{}^{\partial\omega}/_{\partial\theta_H}\right| \Delta\theta_H \tag{5.4.2}$$

where $\Delta\theta_H$ represents a spread due to orientation of grains and can be directly related to ΔH_K in the vicinity of a resonance [115]. However, it can be shown that $\Delta\omega_{MI}$ vanishes when the external field is applied perpendicular to the sample plane. FMR measurements employing this configuration were performed by colleagues at Samsung on the film used in this study as well as the array sample before patterning, and the intrinsic α for the film and array FLs were found to be 0.003 and 0.005, respectively. We reiterate that the two samples are not identical; the FL in the array is approximately 0.7Å thinner than the film shown which is known to correspond to larger H_K and α values [3]. First fitting τ_{eff} for the film using only ΔH_K as a free parameter we find excellent agreement to the data (lines in Fig. 5.9 (b)) using $\Delta H_{K,film} = 280\ Oe$. In

order to quantify $\Delta\omega_s$, we analyzed the SEM image in Fig. 5.3 (a) to extract actual device shapes for 20 elements and used the resulting demagnetization field profiles as input for micromagnetic modelling of the magnetization dynamics. The simulations confirm a significant spread in the precession frequencies due to variations in device shape. For example, at $H_{app} = 4\ kOe$ the resonances of the samples are distributed between 13.4 – 14.5 GHz. To ensure that the spread we extract from the simulations is statistically relevant, we verified that the summed signals were identical when 10 or more devices were considered. The normalized sum (shown in Fig. 5.9 (a)) of the time evolution from each of the 20 elements considered here (shown in Fig. 5.3 (a)) was fitted with a damped harmonic function to estimate the ensemble relaxation rate.

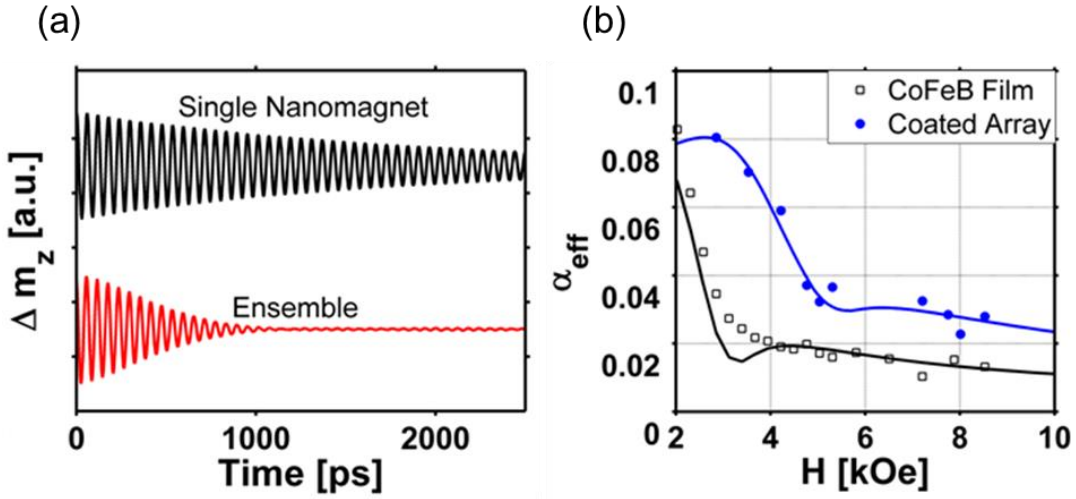

Fig. 5.9. In (a), the normalized time evolution ($\boldsymbol{H_{app} = 5kOe, \theta_H = 80^o}$) of a single device (top, $\boldsymbol{\alpha = 0.005}$) is shown adjacent to the normalized ensemble signal, which is the sum of all 20 elements with slightly different shapes used as inputs for the micromagnetic simulation (Fig. 5.3 (c)). A large reduction in the apparent lifetime of the signal occurs due to dynamic dephasing of the ensemble response. Using Eq. (5.4.2), we estimated the FWHM of the spread in the nanomagnet anisotropy fields caused by shape fluctuations ($\boldsymbol{\Delta H_{K,shape} \approx 150}$ Oe). The experimentally observed, field-dependent ($\boldsymbol{\theta_H = 80^o}$) damping of the film and coated MTJ array are shown in (b) and were also fitted using Eq. (5.4.2) to determine $\boldsymbol{\Delta H_{K,film}}$ and $\boldsymbol{\Delta H_{K,array}}$.

For comparison, the precession of a single device, which represents the intrinsic response of each nanomagnet, is shown in Fig. 5.9 (c). Fitting the ensemble response yields an estimate of the extrinsic shape-induced contribution to the linewidth ($\Delta\omega_s$, defined in Eq. (5.4.1)), which in turn directly corresponds to a spread in anisotropy fields $\Delta H_{K,shape} \approx 150\ Oe$. If $\Delta H_{K,array}$ is a combination of the $\Delta H_{K,film}$ and $\Delta H_{K,shape}$, then $\Delta H_{K,array} = \Delta H_{K,film} + \Delta H_{K,shape}$. Combining the full width at half maximum values of the film measurements and micromagnetic simulations yields an estimate of $430\ Oe$, which is remarkably close to the value extracted from the fit in Fig. 5.9 (b) of $\Delta H_{K,array} = 480\ Oe$. The difference between the predicted value of $\Delta\omega_{ext}$ and the experimental result may be explained by: (i) a slightly larger $\Delta H_{K,film}$ in the patterned sample due to the larger intrinsic H_K of the sample (as shown in Chapter 4), or (ii) error in the simulated responses stemming from oversimplification of the device structure. Because OOMMF uses a finite-difference method (FDM) to solve the LLG equation, surface roughness at the edges of the nanomagnets was not considered in the calculation. Consequently, the spread $\Delta\omega_S$ we determined using OOMMF was likely smaller than in the actual measurement, which is consistent with the experimental result.

5.5 Conclusion

We have demonstrated that the addition of a dielectric smoothing layer to a nanopatterned surface can suppress optically excited SAWs that interfere with the evaluation of the spin dynamics, and, consequently, accurate determination of the

relevant magnetic properties. We successfully used this technique to resolve the spin dynamics of an array of 70 nm STT-MRAM devices. Our findings reveal a significant enhancement of the parameter α_{eff} due to nanopatterning, which is fit remarkably well by a local resonance model using the SEM images of the devices as inputs to the micromagnetic modelling. This, in turn, unambiguously showed that nanomagnet shape variations were the predominant source of enhanced damping of the array signal with respect to the film, as opposed to a change in the intrinsic damping. Because the Gilbert damping is known to directly determine the power threshold required to switch MTJ devices, precise determination of this parameter in nanostructures is crucial to the realization of highly efficient STT-MRAM elements. Lastly, our technique for suppressing SAWs is widely applicable to TR-MOKE studies of densely packed nanomagnet arrays, which are well-known to be the leading candidates for next-generation storage technologies.

CHAPTER 6
Magneto-elastic Excitation of Single Nanomagnets for Optical Measurement of the Intrinsic Gilbert Damping

6.1 Introduction

In the preceding section, we saw that the dynamic coupling between SAWs and magnetization dynamics make it impossible to estimate key magnetic parameters, such as the Gilbert damping. We showed that quenching the mechanical vibrations via deposition of a smoothing layer on to the patterned surface restored the intrinsic magnetization dynamics. However, because the acoustic wave has a well-defined, narrowband frequency, it logically follows that the damping could be estimated from the field-swept linewidth of the MEL resonance akin to microwave cavity based FMR. The prospect of utilizing SAWs instead of quenching them is exciting because the latter requires additional design, fabrication and characterization steps. Sadly, the seminal report of elastically driven ferromagnetic resonance by Weiler et al. [108] found that the damping associated with the FMR of an elastically driven Ni thin film was at least an order of magnitude larger than the intrinsic damping of Ni. The authors conjectured that the inhomogeneity of the MEL field generated by the SAWs as they traverse the Ni film may be responsible for the enhanced damping, nonetheless, their finding discouraged the use of SAWs to the study the damping behavior. In this section, the damping behavior of both isolated and densely packed arrays of nanomagnets driven by SAWs will be presented. This work was reported in ref. [116].

If the damping of elastically driven ferromagnetic resonance in thin films is enhanced solely by the spatial character of the MEL field generated by the SAWs, it follows that nanomagnets sufficiently smaller than λ_{SAW} should not be affected by this issue. Indeed, Yahagi et al. reported in ref. [117] that the SAWs formed by the ultrafast photoexcitation of an array could be used to study the damping behavior of the array. The authors showed the field-dependent TR-MOKE spectra at the driving frequency f_{SAW} could be split into real and imaginary parts, and fit using Lorentzian-like functions to determine the field-swept linewidth of the resonance

$$Im(\mathcal{F}\{\mathrm{m_z}(t)\}) \propto \frac{\Delta H_p^2}{\left(H_{app} - H_{res}\right)^2 + \frac{\Delta H_p^2}{2}} \tag{6.1.1}$$

$$Re(\mathcal{F}\{\mathrm{m_z}(t)\}) \propto \frac{16\Delta H_P\left(H_{app} - H_{res}\right)}{\left(4\left(H_{app} - H_{res}\right)^2 + \Delta H_P^2\right)} \tag{6.1.2}$$

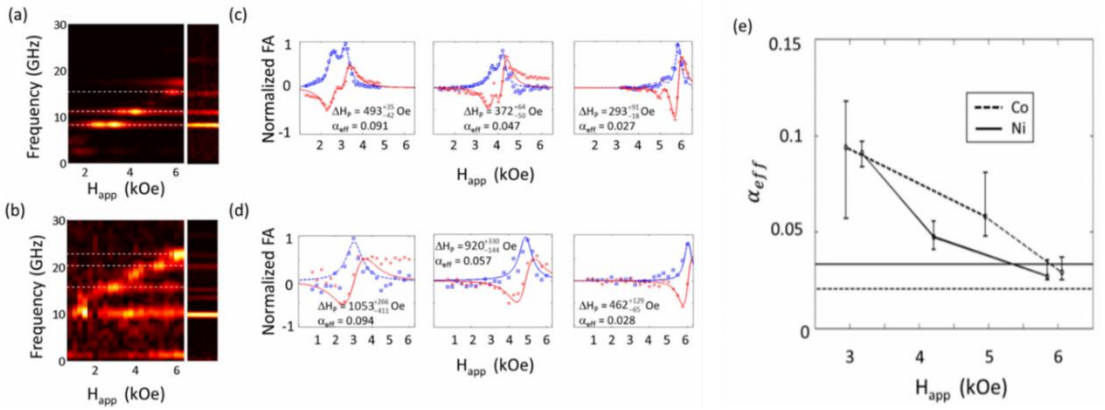

Fig. 6.1. The field-dependent, absolute Fourier spectra of TR-MOKE measurements of (a) Nickel and (b) Cobalt nanomagnet arrays comprised of 160x160x30 nm^3 squares with pitches of 330 and 250 nm, respectively. The cropped plots on the right of (a,b) are the nonmagnetic channels recorded by the sum channel signal which are used to determine the SAW frequencies. The results of fitting Eqs. (6.1.1) and (6.1.2) are shown in (c) for the Ni sample and (d) for the Co sample. For (c), the double resonance in the spectra is caused by the pronounced edge mode being strongly excited in addition

to the center mode. In (e) the effective damping of both arrays was determined via Eq. (6.1.3) and plotted for 3 resonances, while the lines correspond to the well-known intrinsic Gilbert damping of Ni (solid) and Co (dashed). Taken from ref. **[117]**.

where ΔH_P is the field-swept linewidth, or *pinning width*, and H_{res} is the field at which the magnetic frequency is identical to f_{SAW}. In Fig. 6.1 (a-d), the field-dependent spectra of Co and Ni nanomagnet arrays were fit remarkably well using the equations above at three distinct SAW frequencies. As was shown in section 2.4, the linewidth of each resonance can be related to the damping via the following relationship [1]

$$\Delta H_P = \alpha_{eff} \frac{4\pi f_{SAW}}{\gamma} \tag{6.1.3}$$

In Fig. 6.1 (e) this relationship was used to relate the measured linewidth to the damping, which shows that the damping of both samples approaches the film value as the applied field increases. This result is consistent with the behavior caused by dynamic dephasing due to magnetic inhomogeneities between elements, which becomes negligible when the resonance frequency increases. Therefore, this work supports the notion that the large damping observed in Ni films by Weiler et al. was enhanced due to the spatial character of the acoustic wave.

The authors then utilized the same multi-step simulation procedure presented in ref. [117] to model the MEL resonance. By fitting the Fourier spectra of the field-dependent dynamics to determine the pinning width, just as in the experiment, they again found a direct connection between ΔH_p and α (Fig. 6.2). However, unlike the TR-MOKE result, the damping was field-independent in the simulation (i.e. α_{eff} was constant). Indeed, this behavior is common when comparing micromagnetic

simulations to TR-MOKE measurements because extrinsic effects – namely, two magnon scattering (TMS) and inhomogeneous broadening (IHB)– are absent in the calculation.

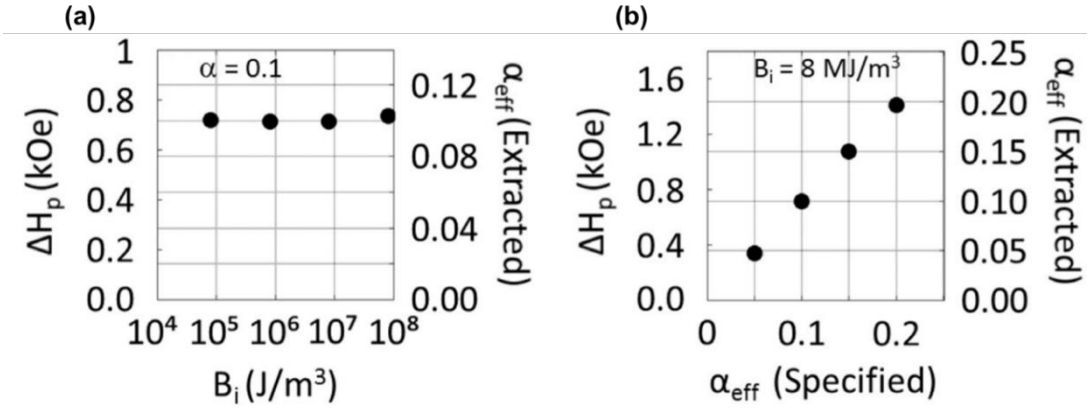

Fig. 6.2. To verify that the pinning width (and α_{eff}) are independent of the strength of the magneto-elastic effect, the field-dependent response was modeled for B_i spanning four orders of magnitude, the result shown in (a) verifies that this method is independent of the magneto-elastic coefficient. In (b), the damping specified in the simulation was varied to test the validity of Eq. (6.1.3) and yielded a direct measurement of the input in each case. Taken from ref**. [117].**

Recall, however, that TMS is the scattering of the uniform precession into degenerate spin waves, which is only possible if and only if the magnon dispersion doesn't increase monotonically. Unlike in a thin film, the spin waves in the nanomagnet are quantized by the relevant lateral dimension (L) of the structure as $k = n\pi/L$. As a result, the spin wave manifold in the nanomagnet increases for all allowed k, and TMS is, therefore, not operative [118]. Hence, the most-likely explanation for the enhanced damping observed in the experiment (Fig. 6.1 (c)) was ensemble broadening of the resonance. This would mean that if a single nanomagnet could be driven by SAWs, one might expect to measure the intrinsic damping of the structure! Such a result would be highly relevant to the study of nanostructured magnetic devices, because conventional TR-

MOKE relies on thermalization to instigate the magnetization precession as well as an anti-reflecting (AR) surface in order to detect the sample. Typically, this isn't an issue when studying unpatterned films with large thermal conductivities (W) (e.g. $W_{Ni} \sim 90\ W/m \cdot K$), because the thermal energy can diffuse laterally. The nanomagnet, however, sits on a dielectric AR surface (HfO_2) that has a relatively low thermal conductivity ($W_{HfO2} \sim 1\ W/m \cdot K$). Thus, the heat is essentially trapped in the nanostructure for the duration of the measurement (~1 ns), which is problematic because the damping depends on T as we saw in section 2.4.1. For this reason, we set out to develop a nonthermal method to excite dynamics in order to study the intrinsic damping behavior.

6.2 Samples and Experimental Details

To study the spin dynamics excited exclusively by SAWs, two novel sample designs were conceived, fabricated and characterized. Because the dynamics are recorded via TR-MOKE, which is a lock-in detection scheme, the excitation needs to be synchronized with the probe pulse. Therefore, the conventional approach of generating SAWs via electrically driven IDTs on a piezoelectric substrate was not compatible with our measurement technique. Instead, we focused on sample designs that would allow us to generate SAWs optically like the previous studies. One critical limitation of optical excitation is the travel time of SAWs, which propagate at a relatively slow speed ($v_s \sim \mu$m/ns) compared to the speed of light, which determines the window of time available in our measurements (~4 ns). This means that it is critical in our study to generate the SAWs as close as possible to the nanomagnet being

measured. However, unlike the arrays where the nanomagnets generate the periodic strain, the sample being measured in this case does not need to generate the vibrations. Furthermore, in order to measure genuine MEL dynamics, it is important that the spins are excited as little as possible by the intense pump pulse.

To minimize the distance between the nanomagnet and the source of the SAWs, we utilized multilevel electron beam lithography, electron beam evaporation and lift-off processes to embed a Ni nanocylinder (D = 200 nm, 30 nm thick) in an array of nominally identical, nonmagnetic Al nanocylinders spaced with a pitch of p = 500 nm (Fig. 6.2 (a)) on top of a commercial AR-coated Si substrate. By using a two-material array we ensure that the signal in the difference channel of our balanced photodiode bridge is solely generated by the singular magnetic surface. To minimize the photoexcitation of the spin system and simultaneously excite more Al nanostructures, the spot size of the pump beam in this experiment was expanded to a FWHM of approximately 10 μm using the scheme discussed in sec. 3.4, while the probe beam was kept at the diffraction-limited size of w_0 = 500 nm.

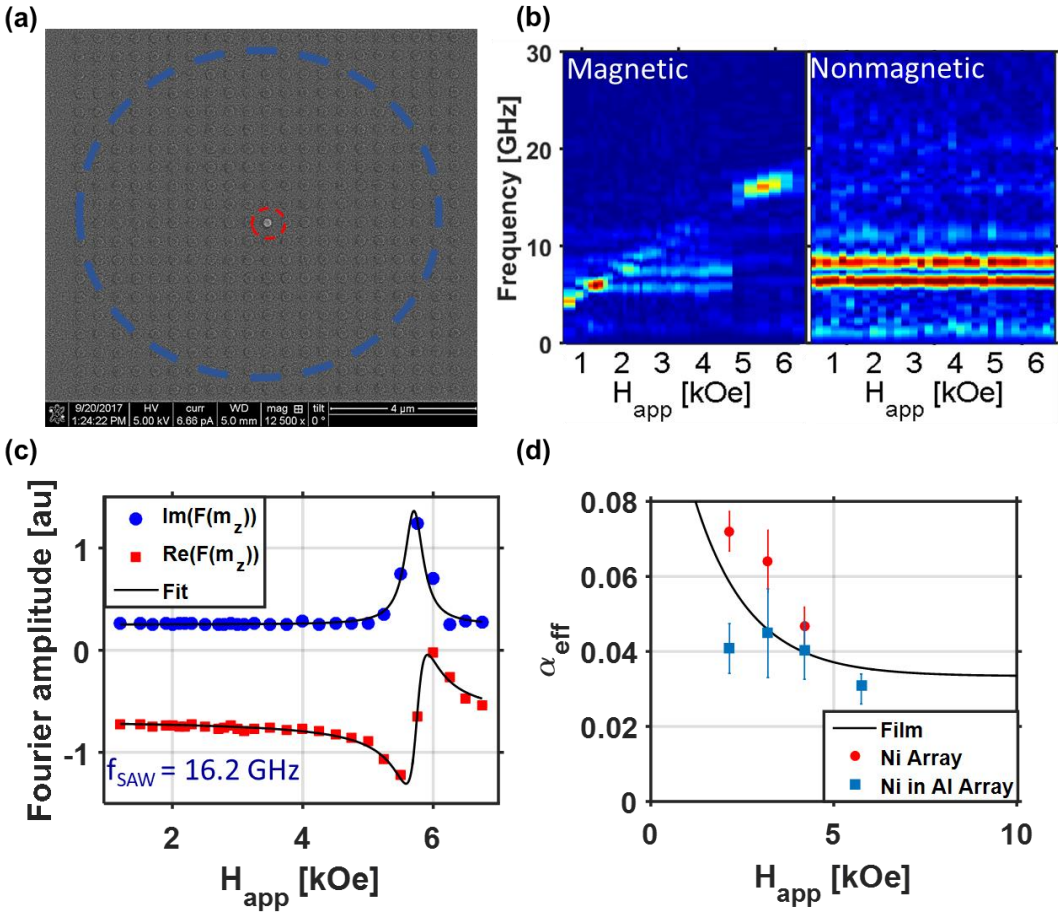

Fig. 6.3. (a) SEM image of the two-material array, the dashes show the dimensions of the pump (blue) and probe (red) beams used in this study. In (b) the field-dependent Fourier spectra of the magnetic and nonmagnetic spectra show the well-defined SAWs frequencies determined by Eq. (5.1.1), and just as before the magnetic signal is enhanced when the spin-wave frequency is in the vicinity of f_{SAW}. The magnetic spectra in the 16.2 GHz bin from (b) is fitted in (c) using the Lorentzian-like functions defined in sec. 6.1 using a singular damping parameter for both functions to improve the accuracy. This procedure was carried out for each of the crossover points which is summarized in (d) alongside the effective damping measured on an unpatterned film with conventional TR-MOKE, as well as the damping estimated from a purely Ni array with identical dimensions.

In Fig. 6.2 (b), the magnetic mode is clearly visible throughout the entire field range and the signal amplitude is enhanced at the 'crossover' points where the frequencies of the magnetic and mechanical oscillations match. The continuous, Kittel-like response of the nanomagnet we observe in the measurement caused by the heat

generated by the pump pulse, which is centered on the nanomagnet. Thus, despite our efforts to minimize the photoexcitation of the spin system there was still a significant amount of optical power delivered to the sample. Nonetheless, at the pinning sites the spectra at the SAW frequencies can be isolated and fit using Eqs. (6.1.1) and (6.1.2) in order to estimate ΔH_p, which is directly proportional to α_{eff} per Eq. (6.1.3). An exemplary fit at the highest frequency (Fig. 6.3 (c)) used in this study ($f_{21} = 2\sqrt{2}f_{SAW} = 16.2$ GHz) shows excellent agreement to the data using a single parameter of $\alpha = 0.03$, which is the intrinsic value for Ni. At the lower frequency crossover points, the linewidths are slightly larger but are all well beneath the values measured on a purely Ni array with identical geometry. In addition, the effective damping of the isolated nanomagnet is equal to or lower than the damping of the unpatterned film measured using conventional TR-MOKE (black line) at each MEL resonance. Therefore, this study unambiguously shows that ensemble effects are partially responsible for the large low-field damping observed by Yahagi et al [117].

A significant issue with the two-material array used in this study was the lack of separation between the acoustic modes, which resulted in overlapping MEL resonances. This, in turn, led to much larger error bars in the estimated damping and may have been responsible for the larger damping at these crossover points as well. The obvious solution to this problem is to increase the separation between the elastic modes, which can be accomplished by either decreasing the pitch or reducing the periodicity down to a single dimension. If the pitch is reduced, a greater portion of the nonmagnetic structures will lie within the probe beam cross section, resulting in a larger

effective R_{sub} value that will reduce the magneto-optic sensitivity. In addition, because the linewidth is proportional to the fundamental frequency ($\Delta f \propto f$) the overlap between resonances will not improve much, if at all. On the other hand, the periodicity can be reduced by simply replacing the nanostructures with equally spaced nanowires which will provide better spacing between the SAWs. In addition, this will also limit the wavevectors to a single direction and increase the fill factor, both of which will result in higher-amplitude SAWs using the same optical power.

To implement these changes, a quasi-one-dimensional sample design (shown in Fig. 6.4 (a,b)) was fabricated using the same multilevel procedure described above for the two-material array. In addition to the advantages discussed above, we'll see later that another positive aspect of this design is the ability to excite SAWs without thermalizing the magnetic sample.

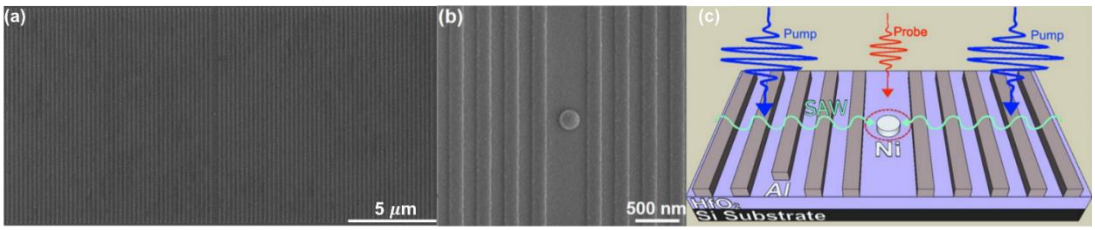

Fig. 6.4. SEM image of (a) a single nanomagnet placed between identical sets of Al bars which are used to generate the SAWs, and (b) a zoomed in version of (a). In (c), the optical geometry of the experiment is illustrated.

The amplitude of SAWs excited by an ultrashort pulse is directly limited by the ablation threshold of the material, which determines the largest fluence that can be used without damaging the phononic structure. One way to increase the overall power delivered to the sample is to increase the spot size, however, as the beam grows it will excite a larger portion of bars that are not in-line with the nanomagnet and the SAWs

generated in these regions will not interact with the sample. Instead, we opted to split the pump into two identical pulses that are focused onto the bars (FWHM ~ 3.5 μm, here) at a distance approximately 3 μm away from the nanomagnet. This approach doubles the optical power delivered to the wire grid that is in-line with the nanomagnet. Although half of the available power is lost by splitting the beams, because we are limited by the ablation threshold of the bars and not the available power this is not an issue here. The geometry of the experiment is sketched in Fig. 6.4 (c), which also shows that the SAWs from each side of the structure propagate in opposite directions. When the two acoustic waves meet at the center, they form a standing wave with an antinode at the middle of the nanomagnet.

We begin by comparing the field-dependent dynamics of optically excited (i.e. conventional TR-MOKE) measurements to the SAW-driven measurements (Fig. 6.5). For the optically excited film and nanomagnet (D = 200 nm), the Kittel mode can be observed throughout the entire field range, whereas for the SAW-driven nanomagnet the resonance is only observed at the crossover point between the magnetic and mechanical resonances. Thus, the bars allow for essentially no photoexcitation of the spins, or 'cold excitation', and provided superior separation between the acoustic modes, which were both issues in the previous two-material structure discussed in this section. Furthermore, from the time traces in Fig. 6.5 (a,b,e) we see that the dynamics of the MEL resonance persist for over 4 ns, whereas the optically excited signal decays within 1 ns. In Fig. 6.5 (f), we see that the nonmagnetic signal is largest at $\Delta t \approx 1$ ns, which indicates that the SAW amplitude is largest. Because the speed of sound in HfO_2

is approximately 3 μ m/ns, this confirms that the pump pulses are focused approximately 3 microns away from the nanomagnet. It is worth noting that the magnetic oscillation slightly lags the strain, which is consistent with the observations reported in ref. [119].

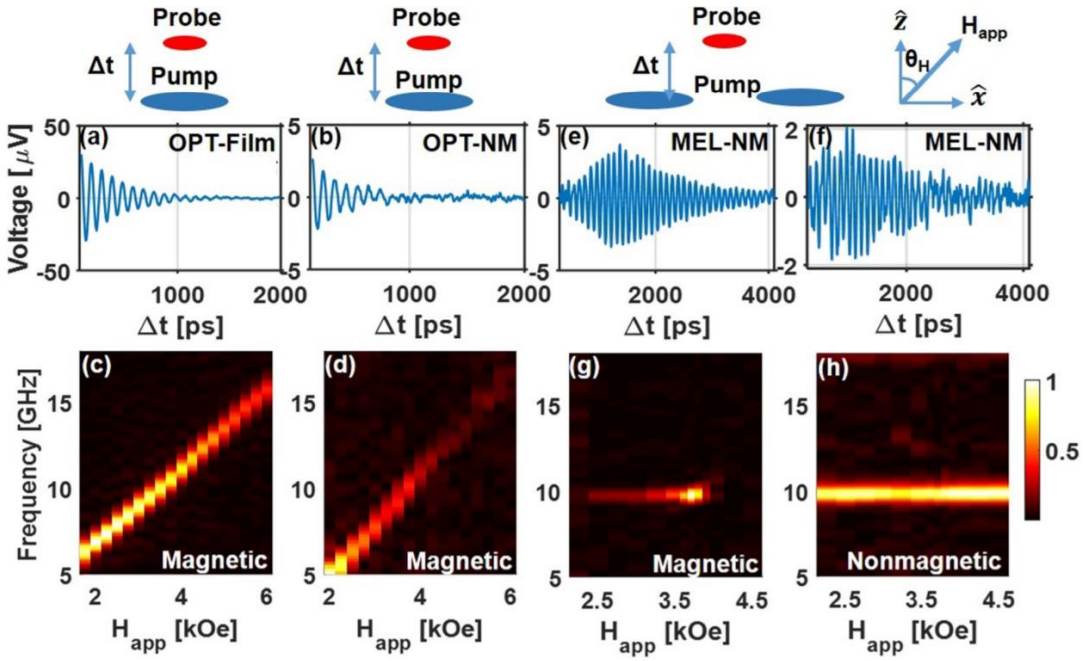

Fig. 6.5. TR-MOKE time traces of the optically (OPT) excited (a) Ni film and (b) isolated nanomagnet (NM), and (c), (d) the corresponding field-dependent Fourier spectra of the film and NM, respectively, measured with a fixed field angle $\boldsymbol{\theta_H}$ = 30°. (e) TR-MOKE trace of the MEL driven nanomagnet (H_{app} = 3.7 kOe), and (f) nonmagnetic signal of the acoustically modulated nanostructure. The illustrations in panels (a), (b) and (e), (f) indicate the pump-probe configurations used and the applied field geometry, respectively. The field-dependent Fourier spectra of the acoustically driven NM shown in (g) reveals strong MEL enhancement when the magnetic and nonmagnetic modes are degenerate. SAWs are identified by monitoring the transient reflectivity, shown in (h), and therefore do not depend on the applied field. Taken from ref. **[116]**.

6.3 Results and Discussion

With the qualitative characteristics of the experiment established we can now turn to the primary focus of this work, which is to study the damping behavior of isolated nanomagnets excited by SAWs. To this end, we fabricated four samples with nominally identical Ni nanomagnets (D = 200 nm) embedded between Al bars with various pitches (p = 250, 300, 350, 400) that correspond to fundamental SAW frequencies of f_{SAW} = 11.45, 9.75, 8.65, 7.75 GHz, respectively. This was done to improve the confidence interval on the estimated damping and to determine whether the damping parameter we extract from the MEL resonance was field- or frequency-dependent. The field dependence of each sample was measured using the experimental configuration above and the spectra were fit using Eqs. (6.1.1) and (6.1.2) to determine ΔH_p.

In addition, the field-swept resonance of the p = 400 nm sample was measured at various applied field angles (θ_H) ranging from 20 to 60o from the surface normal to confirm the absence of extrinsic damping mechanisms, which are known to strongly depend on the magnetization angle (θ_M). The data and fits are plotted in Fig. 6.6 and show excellent agreement between theory and experiment for each of the measurements using a single damping value of $\alpha = 0.034^{+0.04}_{-0.04}$, which is within experimental error of the intrinsic Gilbert damping value (0.03). For comparison, we now compare the MEL damping behavior to the effective damping obtained by fitting the damped precession of conventional TR-MOKE measurements (e.g. Fig. 6.5 (a,b)) of a nominally identical nanomagnet and film in Fig. 6.7.

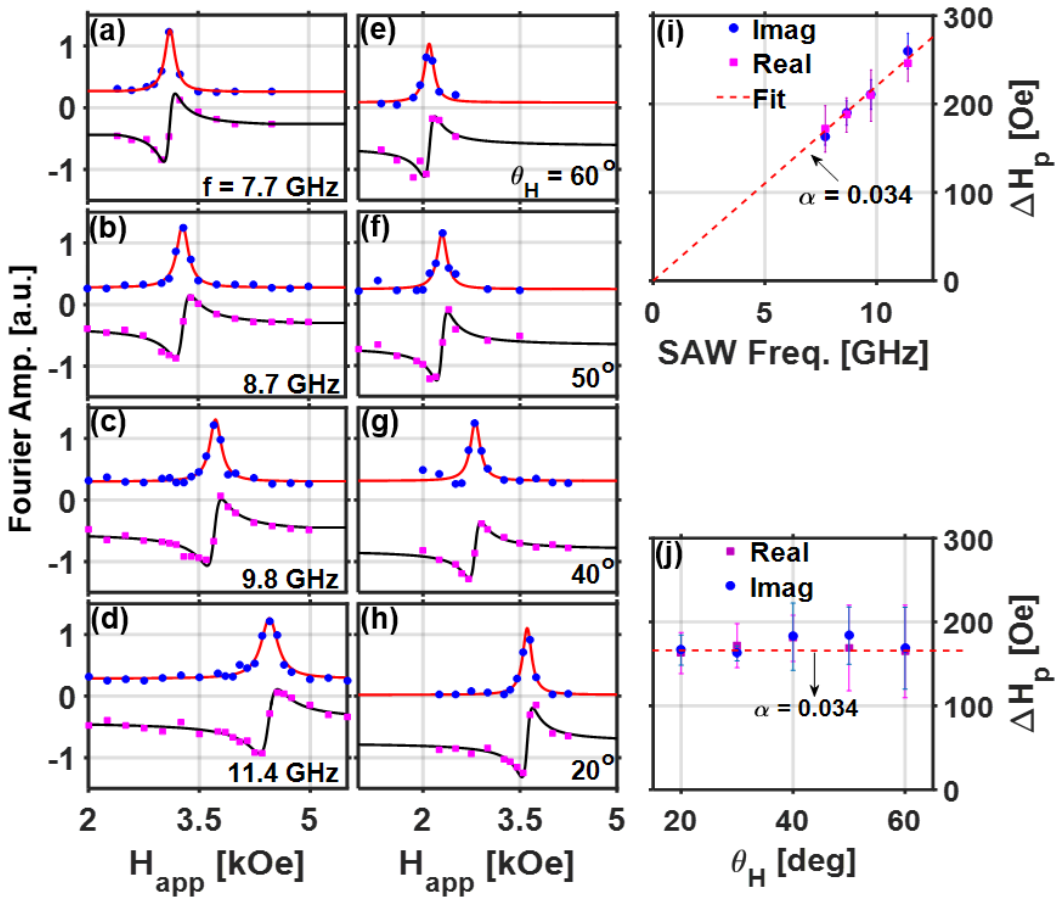

Fig. 6.6. Field dependence of the normalized complex Fourier spectra (imaginary Fourier component – circles, real Fourier component – squares) of the MEL driven dynamics at (a)-(d) four distinct SAW frequencies, and (e)-(h) four distinct applied field geometries using a single sample (pitch = 400 nm). (i) Pinning width determined by fitting both the real and imaginary Fourier spectra from Figs. 4(a-d) plotted against f_{SAW} including the fit to Eq. (3) (red dashed line) used to estimate the damping, and (j) summary of ΔH_p from Figs. 4(a),(e)-(h) plotted against θ_H. The data exhibits no significant variation of the pinning width as a function of the applied field angle, which supports the interpretation that the relationship between α and ΔH_p for the nanomagnet is not complicated by extrinsic mechanisms. Taken from ref. **[116]**.

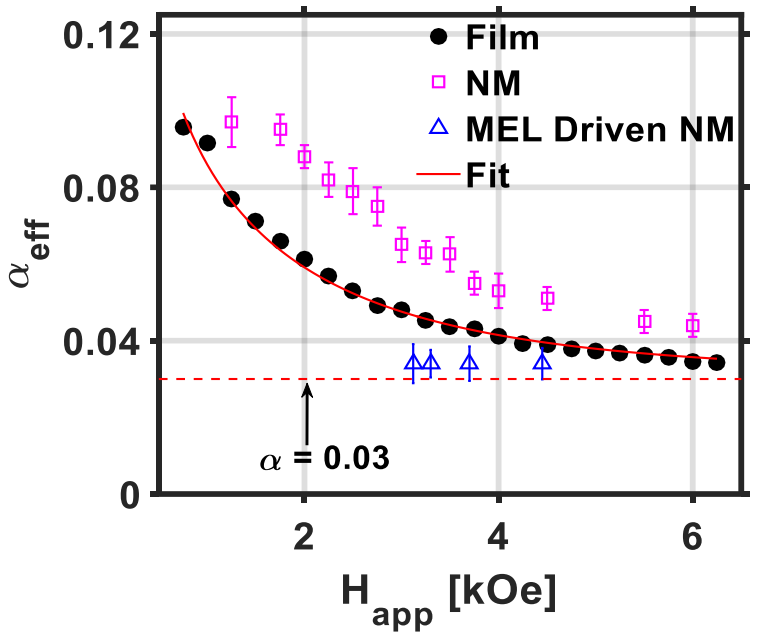

Fig. 6.7. Field dependence of the effective damping of the Ni film and single nanomagnet (NM) measured using conventional TR-MOKE (closed black circles and open pink squares, respectively). For comparison, the damping measured using the MEL approach is included (blue triangles). The effective damping of the film was fit using Eq. (2.x.x) to estimate the intrinsic damping (0.03) (red line), and the dashed red line is a guide to the eye indicating the intrinsic α. Taken from ref. **[116].**

We can clearly see that the impulsive excitation of the nanomagnet leads to an effective damping value that is consistently larger than the film and never converges to the intrinsic value. Using only conventional TR-MOKE, this behavior could easily have been inappropriately identified as an increase in the intrinsic damping due to nanopatterning, however, the results of our SAW-driven experiments show that this is not the case. As was previously discussed, the elevated temperature of the photoexcited nanomagnet is likely the source of the increased damping. An additional complication

of the elevated temperature profile is the formation of oxide on the nanomagnet surface, which was observed when the magnet was illuminated by the intense pump pulse. Although this could be mitigated by using less optical power or coating the surface with a smoothing layer, the signal-to-noise ratio of the experiment is too low to reduce the optical power any further. Thus, our nonlocal, SAW-driven method of determining the damping in magnetic nanostructures is highly advantageous compared to conventional pump-probe magnetic spectroscopy. Since this approach does not require any significant modification to existing TR-MOKE setups, we anticipate that it can be readily implemented by other groups studying magnetic nanostructures.

In addition, our results are also the first to confirm that the coupling efficiency between magnon and phonon systems is ultimately limited by α. The behavior we report is highly attractive for ultralow-power magnetic logic devices, because strains can be generated with relatively small losses thanks to piezoelectrics. In contrast, spintronic approaches (e.g. STT) tend to be much less efficient because the impedances in these devices are typically on the order of kΩ-MΩ, thus, significant Joule heating occurs when current passes through them. Another potential application of acoustically driven nanostructures is in radio-frequency communications, where the operating frequencies of telecommunications transceivers are well into the GHz regime. Our data shows that nanoscale magneto-elastic systems are viable candidates for applications in this space. For example, an acoustically driven MTJ ($\alpha \approx 10^{-4}$) would generate an electrical signal and could, therefore, serve as an extremely efficient oscillator or filter. Lastly, for magnonic applications the additional degrees of freedom provide means of

control and tunability that can be utilized to realize novel designs. This work is highly relevant to the rational design of novel straintronic technologies and provides a critical reference for future studies of magnetic nanostructures.

CHAPTER 7
SAW-Driven Spin Dynamics of Single Nanomagnets with Varying Size and Shape

7.1 Introduction

In the previous chapter, the size and shape of the acoustically driven nanomagnets were kept constant. However, it is well-known that both the strain profile and the demagnetizing field depend directly on the shape of the sample, therefore, the sample geometry could provide another means to improve the operation characteristics. Moreover, we saw in the previous chapter that the damping of the magneto-elastic resonance in nanomagnets is directly related to α, while previous reports have found that in unpatterned films it is an order of magnitude larger [108]. A natural question one must ask is – at what point does the behavior transition? While it makes sense that the FMR mode of a film (k = 0 rad/cm) cannot efficiently couple to an acoustic wave with a finite wavelength, it is nonetheless crucial to determine a relationship between the damping of the magneto-elastic resonance and the size of the nanomagnet. In this section, the dynamic behavior of nanomagnets of different shapes and sizes will be presented. This work was reported in ref. [120].

7.2 Samples and Experimental Details

In this study, we again use the phononic Al wire grids to nonlocally generate SAWs that drive the spin dynamics of isolated magnetic nanostructures embedded between the bars. Two separate, but similar, studies will be presented in this chapter:

(i) selective excitation of nanomagnet modes by exploiting shape anisotropy and (ii) a systematic study of the damping of the magneto-elastic resonance as a function of both nanomagnet size and SAW wavelength. To study the selective excitation of nominally identical nanomagnets (i), 30 nm thick elliptical nanomagnets with major and minor axes of 316 and 160 nm, respectively, were embedded between Al bars spaced on a pitch of 400 nm (f_{SAW} = 7.75 GHz) at orthogonal orientations. Recall that the demagnetization field depends on the direction of the magnetization, hence, the effective field and ferromagnetic resonance frequency depends on the orientation of the sample. Here, we use SAWs to preferentially excite the magnetic resonances in nominally identical samples via control of the externally applied field. Then, to investigate what role the sample geometry has on the efficiency of the MEL resonance (ii), three sets of nominally identical cylindrical nanomagnets with diameters (D) varying from 200 to 700 nm were fabricated between Al bars with pitches of p = 309, 362, 412 nm, which correspond to SAW frequencies of f_{SAW} ~ 9.6, 8.5, 7.75 GHz, respectively. By changing both the relevant lateral dimensions and SAW wavelengths, we hope to find a critical connection between (D) and (λ_{SAW}) that determines the damping behavior of the magneto-elastic resonance.

7.3 Magneto-Mechanical Simulations of Nonlocal SAW Design

Because the TR-MOKE signal is the ensemble response of the structure, it provides no information about the spatial character of the resonance. Hence, to complement our experimental studies we utilized the multi-step approach presented in ref. [18] to model the dynamics. Since we are interested in the interplay between the

sample geometry and the characteristics of the magneto-elastic resonance, we predict that the profiles of the elastic and magnetic dynamics will determine the behavior. This was the primary motivation to carry out accurate micromagnetic simulations, which provide a means to spatially parse the dynamic magnetic behavior. In the seminal work by Yahagi et al. referenced above, they opted to use periodic boundary conditions (PBC) to model the dynamics because it allowed them to use only a single cell (*cell area* = p^2) to simulate the array behavior. One drawback of using PBC, however, is that this approach assumes there are an infinite number of samples that undergo impulsive thermal expansion and subsequently form SAWs. In our experiment, the pump pulses ($FWHM \sim 6\ \mu$m) illuminate a finite number of bars – approximately 15 bars each when p = 400 nm, thus, PBC are not necessarily justified here.

We set out to improve the accuracy of the simulation by considering a realistic number of bars to better match the experiment. Because the wire grid is long (15 μm) compared to the nanomagnets (<1 μm), the sample only needed to be discretized in the *xz* plane (as opposed to all three dimensions) and quasi-PBC were implemented along a the direction parallel to the length of the bars (y-direction). This reduced the complexity of the SAW calculation from N^3 to N^2, where N is the number of cells in the simulation, which allowed us to increase the lateral size of the simulated structure by approximately two orders of magnitude (~400 nm to 40 μm). As a result, we were able to model the thermal expansion of precisely 15 bars on each side of the nanomagnet generate the SAWs, which produces a realistic response with a finite lifetime comparable to the experiment. In Fig. 7.1 (a), a snapshot of the z-displacement

(u_z) 2 ns after the pump excites SAWs is shown. The side profile shows the two-dimensional structure used in the simulation that is repeated an infinite number of times in the direction perpendicular to the page. Because we ultimately need the three-dimensional strain profile of the nanomagnet for the micromagnetic calculations, $u_x(t)$ and $u_z(t)$ of the two-dimensional simulation are then used as inputs for a separate FEM simulation of the nanomagnet strain which is shown (enhanced by 10^3) in the inset of Fig. 7.1 (a). The experimentally observed SAW, via the dynamic reflectance of the 200 nm magnet studied in the previous chapter, is compared to the simulated strain in Fig. 7.1 (b,c), to show that the simulated response qualitatively matches the experiment.

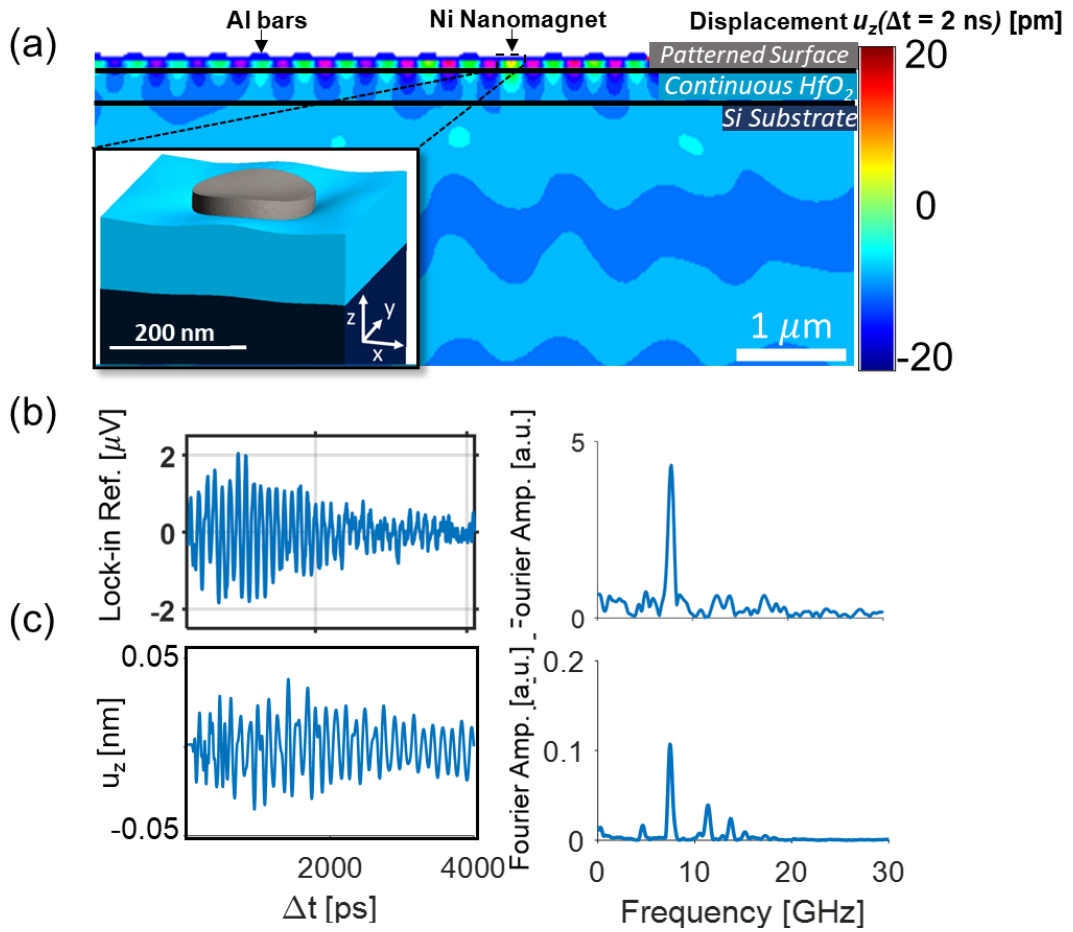

Fig. 7.1. (a) The displacement ($u_z(t)$) at each node in the *xz* plane at the center of the nanomagnet 2 ns after the pump triggers the SAWs; (inset) mesh of the simulated elastic response of a 200x30 nm Ni nanocylinder deformed by SAWs (enhanced by a factor of 1000 for visualization). In (b), the lock-in reflectivity signal and corresponding DFT of a D = 200 nm between Al bars (p = 400 nm) shows a realistic SAW, and in (c) the simulated response exhibits qualitatively similar behavior.

7.4 Role of Nanomagnet Size and Shape on SAW Driven Spin Dynamics

7.4.1 Selective Excitation and Damping Behavior of Orthogonally Oriented Elliptical Nanomagnets

In this section, the magneto-elastic coupling between SAWs and elliptical nanomagnets is utilized to preferentially excite the spin dynamics at distinct applied

fields. It has long been known that that the shape anisotropy plays a crucial role in determining the spin wave dispersion of laterally confined magnetic structures. However, until now there have been no studies that investigated the dynamic characteristics of anisotropic nanomagnets driven by SAWs. Here, the major and minor axes of the ellipses are along the direction of the acoustic wave propagation, and we refer to them as the 'easy-' and 'hard-axis' samples, respectively, because the shape anisotropy is along the major axis of the ellipse. Thus, the easy-axis sample (Fig. 7.2 (a)) is magnetized along its preferred direction whereas the hard-axis sample (Fig. 7.2 (d)) is forced into an energetically unfavorable state by the strong external field.

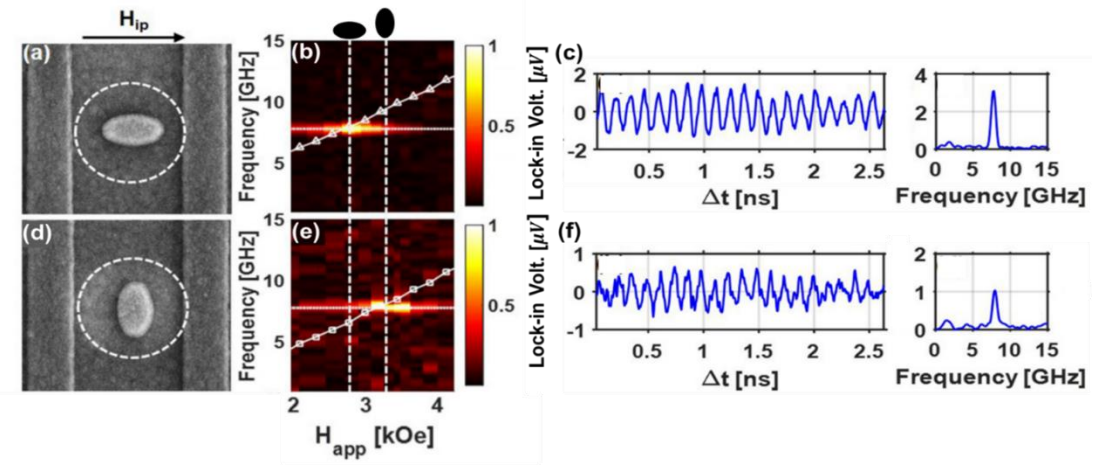

Fig. 7.2. (a) SEM image of the easy-axis ellipse embedded between the Al bars where the dashed line illustrates the FWHM of the probe beam, (b) the TR-MOKE spectra of the SAW driven dynamics, and (c) the time evolution of the Kerr signal on resonance (H_{res} = 2.8 kOe). The same data for the hard-axis ellipse is shown in (d-f), where the resonance in for this sample occurs at H_{res} ~ 3.2 kOe due to the shape anisotropy. The dashed lines in the colormaps (b,e) show the spin wave characteristics of each device measured using conventional TR-MOKE which relies on ultrafast demagnetization to excite the magnetic precession. Taken from **[120]**.

The field-dependent magneto-elastic dynamics of the orthogonally oriented ellipses excited (Fig. 7.2) by SAWs (λ_{SAW} = 400 nm, f_{SAW} ~ 7.8 GHz) were measured using identical optics, spot sizes and fluences described in the previous chapter. We see

from the dynamic Kerr signal of each sample on resonance (i.e. $H_{app} = H_{res}$) that the lock-in voltage of the ellipse driven along its 'easy-axis' (Fig. 7.2 (a-c)) is more than twice as large as the 'hard-axis' ellipse (Fig. 7.2 (d-f)) despite the fact that both samples are excited by the same SAW. The smaller SNR of the hard-axis sample results in precessions that can only be discerned for an exceedingly small ranger of fields close to H_{res}, whereas the precession of the easy-axis ellipse can be detected hundreds of Oe away from H_{res}. Furthermore, from the conventional TR-MOKE measurements (dashed lines) we see that the resonance field in the SAW driven experiment is precisely the same applied field at which the impulsive response oscillates at f_{SAW}, which confirms that the applied strain does not significantly alter the resonance frequency of the nanomagnet.

Once the dynamic behavior of each device had been measured in isolation, we studied the behavior of the two devices simultaneously to determine whether the individual resonance of each could be discerned. In Fig. 7.3 (a), the probe profile is overlaid on the SEM image of the two adjacent devices, and in (b) the colormap of the ensemble response shows two clear peaks in the spectra attributed to the distinct resonance of each device. This data also shows that the magnetostatic interaction between the two devices does not appreciably affect the resonance, which is important for applications that require high areal bit densities (e.g. bit-patterned media).

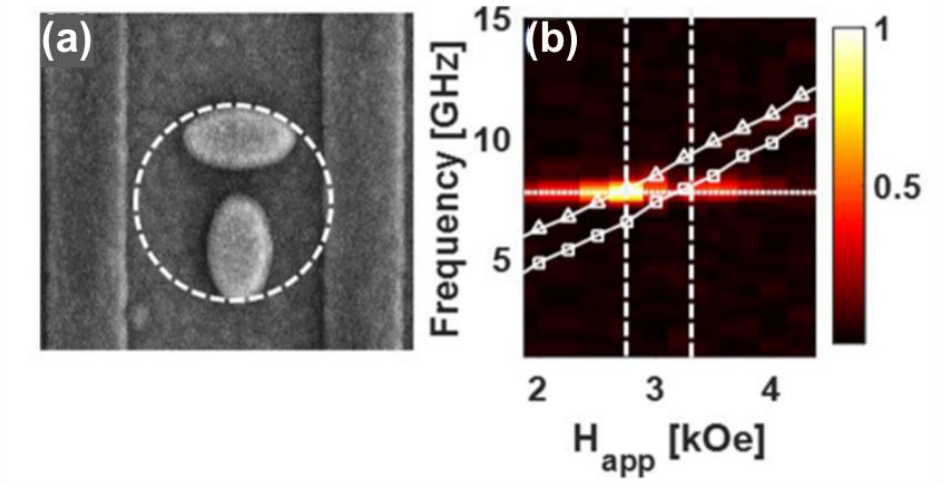

Fig. 7.3. (a) SEM image of the two adjacent, orthogonal ellipses embedded in the bars with the the probe profile (dashed line) overlaid just as before, and (b) the field-dependent spectra of the ensemble response showing that the resonance of both devices can be detected simultaneously. Taken from **[120]**.

To complement the experiment, we carried out micromagnetic simulations of the magneto-elastic devices using the approach described in section 7.3 to calculate the strain. The elastic profile was used as an input for OOMMF to determine the field H_{MEL} formed inside the sample by the induced elastic deformation. In Fig. 7.4 (a,b), the field-dependent spectra of the micromagnetic simulations are essentially identical to the measured response shown in Fig. 7.2 (a,d). The agreement between theory and experiment lends confidence to the accuracy of our novel approach to model the SAWs.

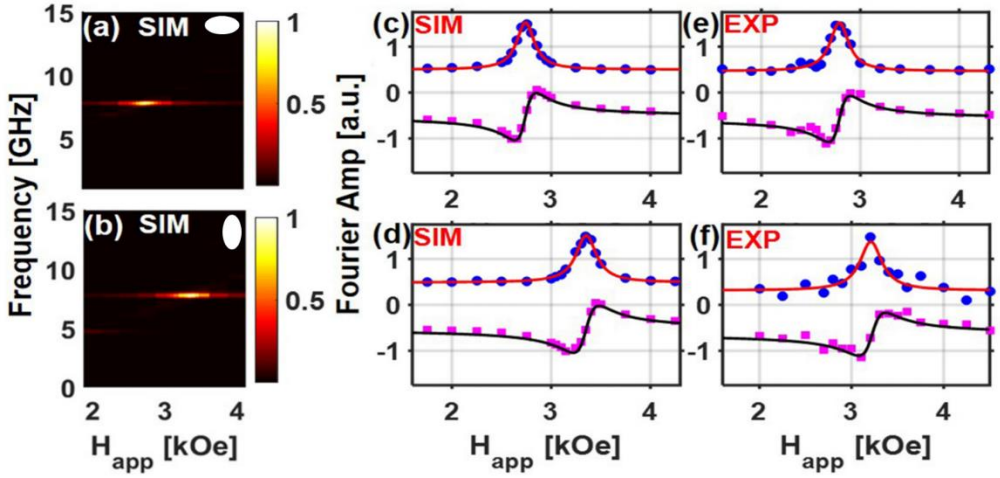

Fig. 7.4. (a,b) Field-dependent spectra of the magneto-elastic simulations of the easy- and hard-axis ellipses, respectively, and in (c,d) the corresponding linewidth analyses of the simulated resonances show enhanced damping for both samples. In (e,f), the experimental linewidths of the data shown in Fig. 7.2 show nearly identical behavior as the simulations. Taken from **[120]**.

We now turn to the damping behavior of these devices, which we know from the previous chapter is ultimately determined by the Gilbert damping. Here, we again performed linewidth analysis by decomposing the field-dependent spectra into real and imaginary parts and fitting the data using the Lorentzian-like functions defined in Eqs. (6.1.1) and (6.1.2) (Fig. 7.4 (c-f)). Fitting the experimentally measured spectra yields the following estimates of the effective damping for both samples, $0.044^{+0.008}_{-0.008}$ and $0.055^{+0.02}_{-0.02}$ for the easy- and hard-axis samples, respectively. Both values are significantly larger than the intrinsic Gilbert damping value of 0.03. We performed the same analysis to the simulated responses which provided the same qualitative result – the sample with the in-plane field component along the easy-axis had much lower damping. It is worth pointing out that in the simulation the Gilbert damping was a fixed

input set to $\alpha = 0.03$, therefore, the enhancement in the simulation is purely caused by the sample geometry just as in the experiment.

To determine the underlying cause of the shape-dependent damping behavior, we first considered what effect the demagnetization field has on the resonance. As described in section 2.3, the ferromagnetic resonance cannot follow a helical trajectory in the presence of a strong anisotropy field. Instead, the magnetic precession about the effective field is squeezed into an elliptical shape, which leads to an observed response with apparently larger damping per Eq. (2.3.21). A similar expression can be determined for the elliptical nanomagnets per ref. [121] as follows

$$\alpha' = \frac{\alpha\left(N_x^d + N_y^d\right)}{2\sqrt{N_x^d N_y^d}} \tag{7.4.1}$$

where α' is the enhanced damping due to the shape anisotropy, $N_{x,y}^d$ are the diagonal components of the demagnetization tensor. For our samples, the in-plane components are approximately 0.09 and 0.15, whereas the out-of-plane component is about 0.76. According to the equation above this effect would yield a 3% increase in the effective damping ($\alpha_{eff} \approx 0.031$), whereas the experimentally determined damping parameter for both samples was more than 50% larger than the intrinsic α. Hence, although shape anisotropy has some effect on the increased damping it is an order of magnitude too small to explain the observed α_{eff}.

In addition to the anisotropy-induced change in the shape of the precession, lateral confinement of the magnetic structure also leads to localization of the

ferromagnetic resonance. Surprisingly, oftentimes the magnetic response to a stimulus is strongest at the edges where the spins are uncompensated, and the exchange field is a fraction of the bulk value. In our experiment, however, because the SAWs form a standing wave with an antinode located at the center of the nanomagnet, the strain and, therefore, H_{MEL} is largest at the center. This means the positions of the driving force and the ferromagnetic resonance could be mismatched, which can also lead to an increase in the damping of the magneto-elastic resonance. To investigate whether this was the case in our study, we utilized the micromagnetic simulations to examine the spatial character of the ferromagnetic resonance. Because OOMMF is a finite-difference method calculation, the LLG equation is solved at each cell in the structure, which means the impulse response of each cell is a damped precession. The spatiotemporal profile of the magnetization is then transformed into the frequency domain using a DFT algorithm so we can analyze the spatial character of the resonance. We first considered the impulse response of the ellipses using a field-like pulse (i.e. ultrafast demagnetization) in order to determine the natural response of the nanomagnets. We then plotted the Fourier amplitude of the spectra at the ensemble resonance frequency (7.8 GHz) to determine where the energy was localized in the structure (Fig. 7.5 (a,b)). We see that for the impulsively excited, hard-axis sample the mode is strongest at the edges of the magnet due to the in-plane applied field along that direction. Conversely, the mode is strongest at the center of the magnet for the easy-axis sample because the stray field at the edge is more uniform.

Now, we turn to the magneto-elastically driven ellipses shown in Fig. 7.5 (c,d) where it is evident that the mode profiles have been changed by the induced strain. For the hard-axis

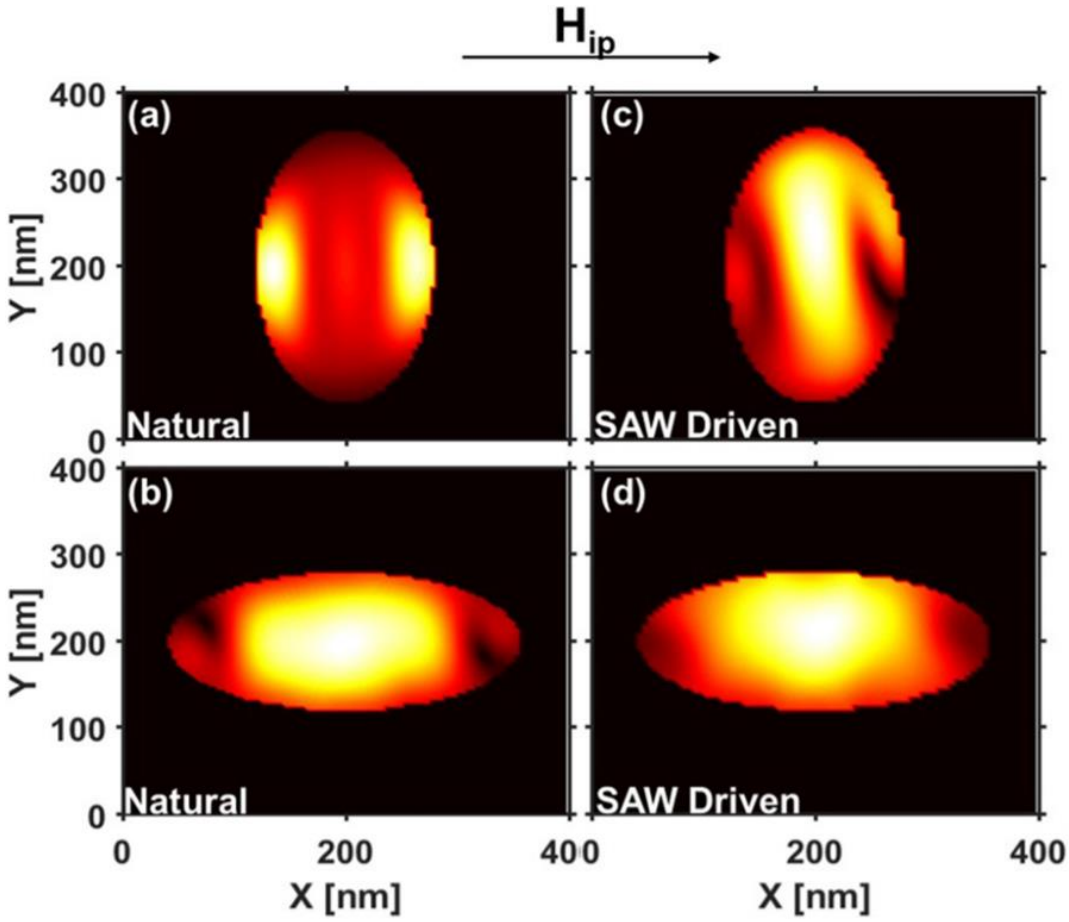

Fig. 7.5. (a,b) Fourier amplitude of the ensemble resonance frequency component (7.8 GHz) for the hard- (H_{app} = 3.2 kOe) and easy-axis (H_{app} = 2.8 kOe) samples, respectively, excited by a small field-like pulse. The same data is plotted in (c,d) for MEL excited nanomagnets where the mode is now at the center of the sample where H_{MEL} is largest. Taken from ref. **[120]**.

sample, the mode has been forced to the center of the magnet which is in stark contrast with the natural response. On the other hand, for the easy-axis sample, the response is still strongest at the center but is now more tightly confined in the x-direction than the

natural response. Based on these results, we conjecture that the damping of the magneto-elastic resonance is primarily enhanced by the spatial mismatch between the the natural and SAW-driven responses.

In conclusion, in this study we have shown that the magnetic precessions of remote nanomagnets can be preferentially excited by nonlocally generated SAWs. Using a pair of identical, but orthogonal, elliptical nanomagnets we show that the signals can be distinguished when recorded simultaneously. We then show that the damping behavior of the magneto-elastic resonance depends on the geometry as well. Using micromagnetic calculations, we find a correlation between the damping and the spatial overlap of the natural and forced responses. This work was reported in ref. [120].

7.4.2 Size-Dependent Damping of Cylindrical Nanomagnets

In the previous section we saw that the damping behavior of the nanomagnets was connected to the sample geometry. However, in that study the focus was on the preferential excitation of magnetic precessions using nonlocally generated SAWs. Here, we investigate the characteristics of the MEL resonance using Ni nanocylinders ranging from 150 to 730 nm in diameter (D) excited by SAWs with three distinct wavelengths (λ_{SAW}= 309, 362, 412 nm).

We first measured the magneto-elastic resonance of each sample which revealed an interesting connection between the amplitude, nanomagnet size and SAW wavelength. From the data we see that the precession amplitude decreases exponentially as D increases, but when the lateral dimension of the nanomagnet is

approximately 50% larger than the SAW wavelength (i.e. $D > 1.5\ \lambda_{SAW}$, Fig. 7.6 (d)) the signal amplitude drops off sharply. This result indicates the magneto-elastic excitation is well-suited for vanishingly small nanomagnets, most likely because the strain profile is more homogenous throughout the structure as D decreases. Because the damping is inversely proportional to the Q-factor of the resonator, the increase in the amplitude for small magnets could also be related to the damping behavior. If the damping is lower, more energy is stored in the magneto-elastic device which could explain the increase in the precession amplitude we have observed.

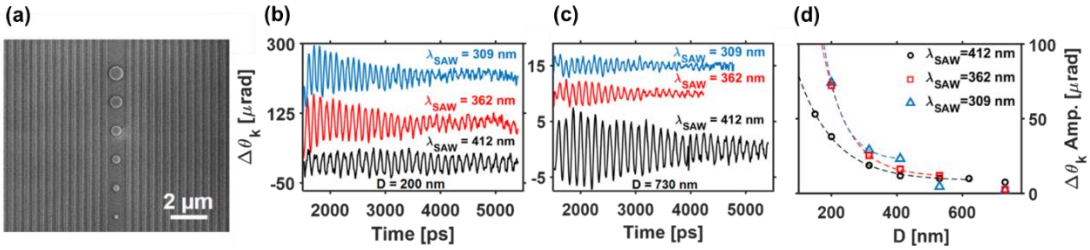

Fig. 7.6. (a) SEM image of the 200 to 700 nm nanomagnets embedded in the Al wire grid. In (b,c) the dynamic Kerr signals of the D = 200 (H_{res} = 3.1 kOe) and D = 700 nm (H_{res} ~ 2.6 kOe) samples shows the large difference in the precession amplitudes as well as the opposite scaling behavior of $\boldsymbol{\Delta\theta_k}$ with $\boldsymbol{\lambda_{SAW}}$. Similar measurements were performed for each sample and the amplitudes are summarized in (d) for the three wavelengths. The dashed lines are exponential fits to the data using the following function $\boldsymbol{\Delta\theta_K \propto Aexp\left(-\frac{D}{B}\right) + C}$ for the samples that satisfy ($D < 1.5\ \boldsymbol{\lambda_{SAW}}$).

To study the damping of the magneto-elastic resonance for the various sizes we again utilize the linewidth analysis method. Because the largest sample in this study contains more than one period of the acoustic wave, we suspect that the mismatch between the sample's natural resonance and H_{MEL} will result in larger damping. In Fig 7.7 (a,b), the resonance and linewidth analysis of the D = 600 nm sample excited by a 412 nm SAW is shown. A clear, single peak in the spectra shows that the sample is

forced to oscillate at the acoustic frequency. However, the linewidth analysis yields a damping estimate of $\alpha_{eff} = 0.05^{+0.0025}_{-0.0025}$ which is again much higher than the intrinsic damping of Ni ($\alpha = 0.03$). In Fig. 7.7 (c), the effective damping is plotted as a function of *D*, which shows that the damping of the magneto-elastic resonance jumps when the sample is larger than the SAW. Moreover, we see that for the smallest sample (*D* = 150 nm), the estimated value is even closer to the intrinsic damping, however, we must note that this change is within the standard error of the measurement which means we cannot be certain the difference is meaningful. Nonetheless, the fact that the damping of the magneto-elastic resonance is lowest for the smallest sample is consistent with our interpretation of the data and the enhancement of $\Delta\theta_k$ seen in Fig. 7.6 (d).

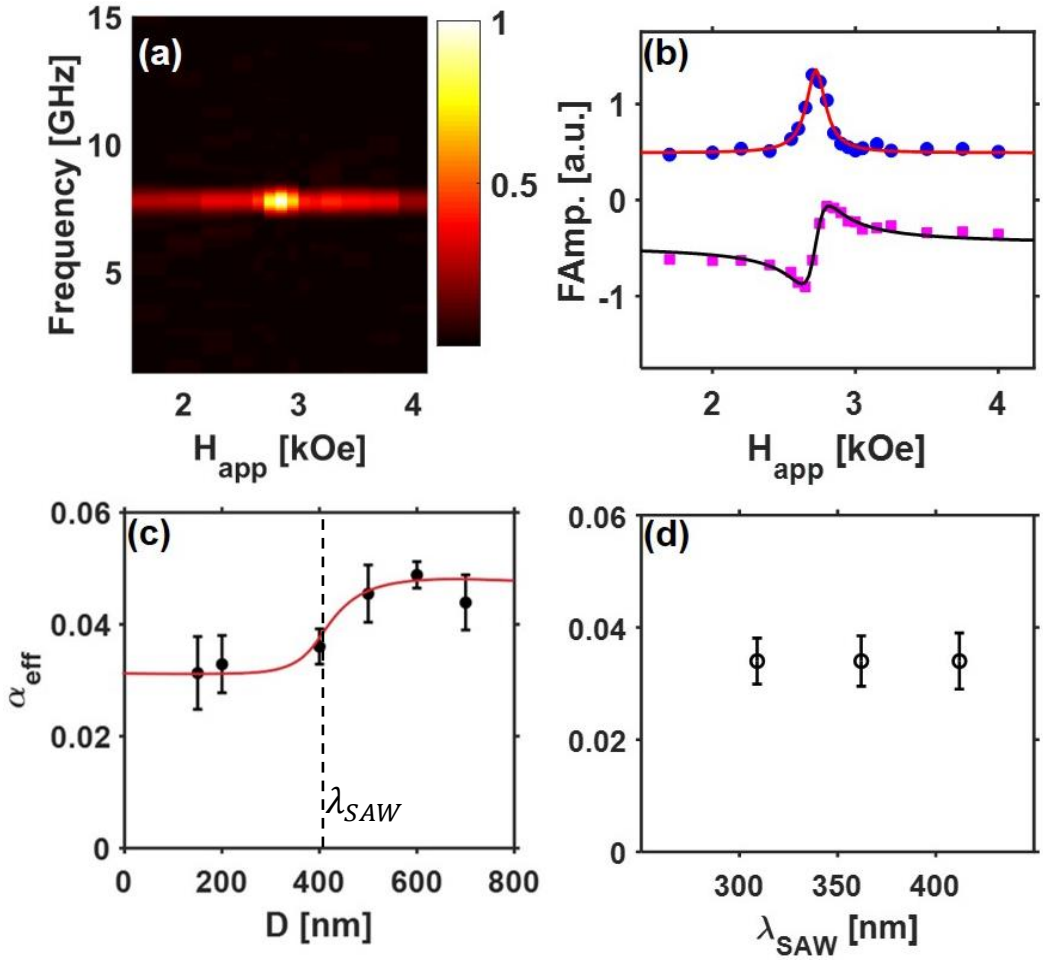

Fig. 7.7. (a) The field-dependent TR-MOKE spectra of the D = 600 nm, p = 412 nm sample, and (b) the corresponding Fourier components used to analyze the damping behavior. The damping for diameters ranging between 150 to 730 nm are summarized in (c), which reveals a critical point near $D = \boldsymbol{\lambda_{SAW}}$ where the damping jumps substantially. Finally, in (d) the effective damping of a D = 200 nm sample driven by various SAWs is (within error) the exact same for all three measurements.

Once again, we turn to micromagnetic simulations of the magneto-elastic behavior to elucidate the origins of the enhanced damping. To ensure that the simulations accurately reproduce the experimentally observed results, we simulated the response of nanomagnets with various diameters and found that the amplitude of the magnetic moment (m_z) increases exponentially with shrinking D just as in the experiment (Fig. 7.7 (a)). However, it should be noted that the increase is not as steep

as in the experiment. It is unclear whether this is caused by a discrepancy between the simulated geometry (ideal cylinder) and the sample geometry (dome-like). Even if this does not affect the magnetization dynamics appreciably, the larger dynamic Kerr rotation of the smaller samples could also be linked to the geometry of the magneto-optic interaction at the surface. Lastly, because we have observed oxide formation on our nanomagnets in the past, we cannot rule out possible changes in the effective magnetic properties of the

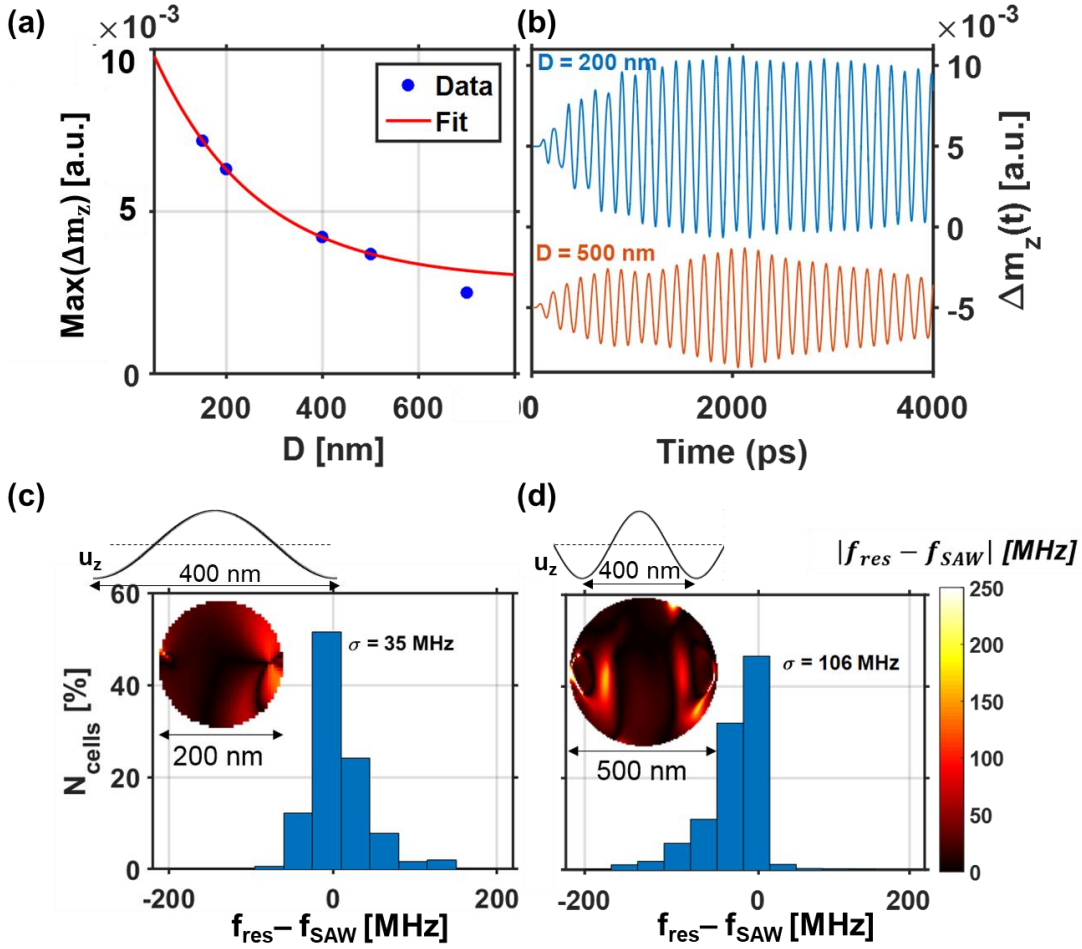

Fig. 7.8. (a) The maximum precession amplitudes of m_z taken from micromagnetic calculations of SAW driven ($\boldsymbol{\lambda_{SAW} = 400\ nm}$) spin dynamics for various nanomagnet diameters reveal an exponential increase with decreasing D, just as was experimentally observed. In (b), the time evolution of m_z is shown for the D = 200 and 500 nm

nanomagnets, respectively, to show the distinct behavior of each sample at H_{res}. In (c) and (d), the difference between f_{SAW} and the local resonance frequency (f_{res}) of each cell in the simulation is plotted as a histogram to show that the resonance frequencies in the small sample are more tightly distributed; inset: spatial distributions of $|\boldsymbol{f_{res} - f_{SAW}}|$ for each sample which show that the magnetic resonance deviates most near the nodes of the standing wave which is shown by the illustration of the fundamental acoustic mode (u_z) above the mode profiles.

nanomagnets as the *S/V* ratio increases with decreasing *D*. Nonetheless, the qualitative agreement between the simulation and experiment suggests that the favorable scaling characteristics are real, which is promising for prospective straintronic devices.

To shed light on the experimentally observed damping behavior, we once again investigate the spatial profile of the magneto-elastic resonance using the micromagnetic calculations to explain the change in α_{eff}. To minimize the computational intensity, we opted to simulate the D = 500 nm device instead of the largest (D = 730 nm) in this study because the latter has substantially more cells to consider (approximately 2-fold more) which makes visualization a challenging process for a desktop PC. In Fig. 7.8 (b), the time evolutions of the nanomagnets are compared side-by-side to show the size-dependent behavior. Using the spatiotemporal magnetic profile of the micromagnetic calculations and applying a DFT algorithm to the data we determine the spatial character of the resonance. Using the highest amplitude Fourier component of each cell we determined the local resonance frequency (f_{res}). Although the devices are being driven at the SAW frequency, regions near the nodes of the standing wave experience little-to-no H_{MEL} field and may be able to oscillate off-resonance. To quantify the extent of this behavior, the difference between the $f_{res}(x,y)$ and f_{SAW} was determined for each cell and then plotted as a histogram for both samples in Fig. 7.8 (c,d). For the 200 nm

sample we see that the distribution is more tightly distributed about the driving frequency, which we quantify using the standard deviation (σ) of the distribution. On the other hand, the same analysis for the D = 500 nm sample yields a much wider distribution of f_{res} in this sample with a nearly 3-fold larger σ than the smaller sample. In the inset of the histograms, the spatial character of $|f_{res} - f_{SAW}|$ is plotted to highlight regions that are significantly off resonance. Just as predicted, the locations that correspond to the SAW nodes are precisely where the difference is largest.

To make use of the spatial profile of f_{res} provided by the micromagnetic calculations, we need a solid framework to explain the enhanced damping. Recall from chapters 2 and 5 that the extrinsic effect known as dynamic dephasing occurs when there is a distribution of frequencies detected by the probe beam. The simulations provide the exact spatial profile of f_{res}, therefore, instead of relying on the relationship between the relaxation lifetime and the linewidth ($\Delta f = 1/\pi\tau$) that was used in chapters 4 & 5, here, we have direct access to Δf. In fact, we can use one of the most fundamental relationships for the damping which is [122]

$$\alpha = \frac{\Delta f}{2f} \tag{7.4.2}$$

where Δf is the frequency-swept linewidth and f is the operating frequency. Here, however, Δf is the sum of both the intrinsic (Gilbert) response as well as the SAW-induced contribution which depends on the interplay between D and λ_{SAW}. If we make use of the following relationship between the FWHM and σ

$$FWHM = 2\sqrt{2\ln(2)}\,\sigma \tag{7.4.3}$$

we can rewrite Eq. (7.4.2) as follows

$$\alpha_{eff} = \frac{\Delta f_{eff}}{2f} = \frac{\left(2\alpha f_{SAW} + 2\sqrt{2\ln(2)}\,\sigma\right)}{2f_{SAW}} \tag{7.4.4}$$

Now, using the standard deviations shown in the inset of the histograms in Fig. 7.7(c,d), we estimate effective damping values of 0.036 and 0.047 for the 200 and 500 nm samples, respectively, which is in excellent agreement with the experimentally observed values of $0.034^{+0.004}_{-0.004}$ and $0.046^{+0.006}_{-0.006}$. Therefore, our simulations support the interpretation that when λ_{SAW} is smaller than *D*, the extent of inhomogeneity in H_{MEL} results in regions that are not on resonance with the SAW. This leads to dynamic dephasing of the signal that is averaged during the measurement and manifests as an increase in the apparent damping.

7.5 Conclusion

In conclusion, we carried out size-and-wavelength-dependent measurements of magnetization dynamics in nanostructures resonantly driven by SAWs. Our findings show that the efficiency of the MEL resonance depends on the Gilbert damping as well as the relative nanomagnet size and acoustic wavelength. Magneto-mechanical simulations show that inhomogeneous broadening of the elastically driven spin dynamics cause the enhanced damping observed for nanomagnets larger than the SAW wavelength. Conversely, our results suggest that the losses associated with acoustically driven spin dynamics scale favorably with nanomagnet dimensions. These findings

provide a critical reference for the rational design of highly efficient nanoscale magneto-elastic devices operating at high frequencies.

CHAPTER 8
SAW-Assisted, Helicity-Dependent All-Optical Switching of FeTb Thin Films

8.1 Introduction

In this section, the development of an all-optical magnetization switching setup and a MOKE imaging system used to monitor the surface magnetization will be presented. Using this system, the applied optics group is working to combine SAWs with the exciting phenomenon known as helicity-dependent all-optical switching (HD-AOS) to lower the amount of optical power needed to switch the magnetization.

HD-AOS of the magnetization was first discovered in 2007 by Stanciu et al. while studying the ferrimagnetic alloy $Gd_{22}Fe_{74.6}Co_{3.4}$ [123]. The authors showed that a circularly polarized, ultrafast pulse (40 fs, $\lambda = 800$ nm, $f_{rep} \sim 1$ kHz) could write magnetic domains, where

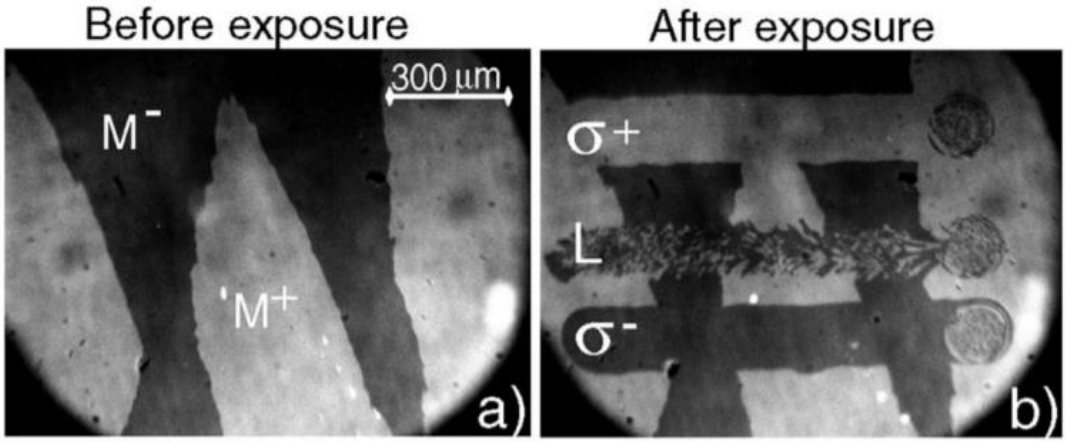

Fig. 8.1. (a) MOKE-microscope image of the GdFeCo sample after it has been demagnetized by an oscillating magnetic field where the light and dark portions of the image correspond to positive and negative magnetic moments, respectively. In (b), the sample has been illuminated by a right-hand ($\boldsymbol{\sigma}^+$) pulse (top) which switches the region

that had previously had a negative magnetic moment to positive while the pulse has no effect on the region that was already positively magnetized. At the bottom of the image, $\boldsymbol{\sigma}^-$ pulse was used and shows that the opposite is true in this case. Between the two opposite helicity CP pulses, the authors used a linearly polarized pulse which resulted in random magnetic domains with no net magnetization. Taken from ref. **[123]**.

the phrase 'helicity-dependent' refers to the fact that the magnetic state is directly determined by the handedness of the CP light.

A few unique characteristics of the optically written domain can be seen in Fig. 8.1. First, when the laser is scanned across the surface a clean, linear magnetic domain is written, but when the laser is stationary the result is a demagnetized circle encapsulated by a homogeneously magnetized perimeter. The authors carried out fluence-dependent measurements and found that the size of the written spot was directly related to the intensity (Fig. 8.2).

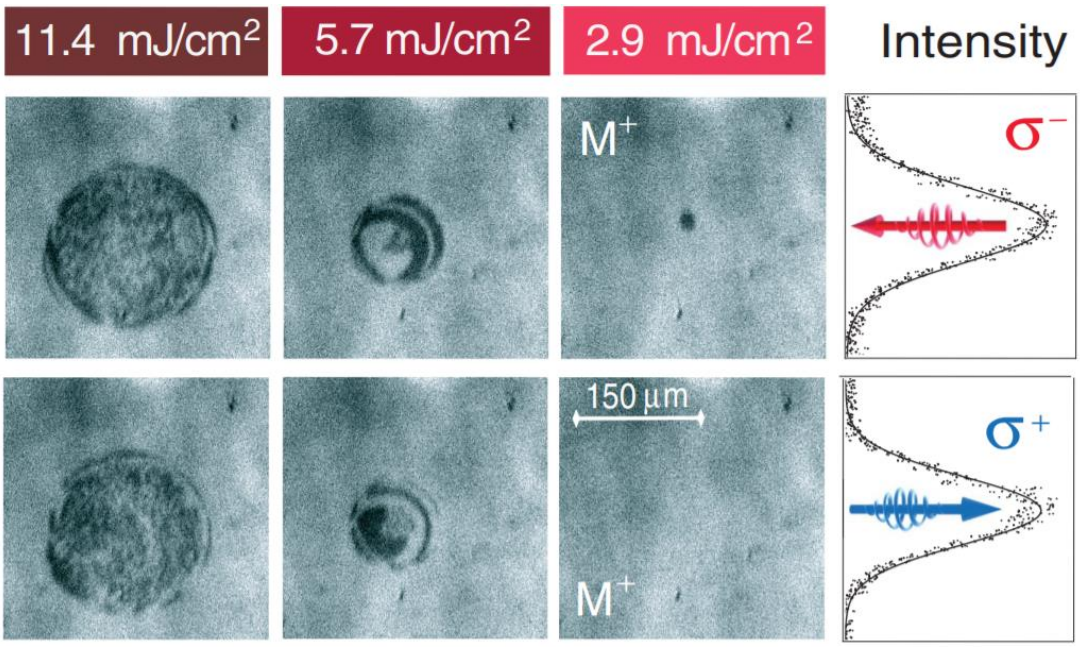

Fig. 8.2. MOKE images of the GdFeCo surface after being subjected to approximately 20 laser fluences using both LHCP and RHCP. The profiles on the right show the

intensity of the pulses used to write the spots. The sample was saturated to the M^+ direction before each measurement. Taken from ref. **[123]**.

The figure above also shows that when the fluence reaches a critical value (F = 2.9 mJ/cm^2), the written domain is a (nearly) perfect circle with no demagnetized region. Although the authors did not directly record the speed of the writing process in this study, they did note that the magnetization reversal must occur on a sub-picosecond timescale because the field induced by the helicity of the light only persists in the sample for a few hundred femtoseconds. Indeed, multiple reports have since confirmed that the magnetization reversal takes place within a picosecond or so, although the exact number does depend on the magnetic properties of the material.

Prior to this report, it was believed that, "the fastest and most efficient recording method involves precessional switching" [124], which would mean that high damping would allow the magnetization to relax more quickly but would also require more power to overcome the inertia of the magnetization in equilibrium. In ref. [124] the authors showed that the magnetization could not be deterministically switched faster than picosecond timescales via precessional switching. For HD-AOS, however, the magnetization does not follow a helical trajectory (i.e. it is not governed by the LLG) which allows for much faster switching speeds than previously than were previously believed to be possible. The finding also raised several questions regarding our understanding of ultrafast magneto-optics, for example, many studies could not agree on the magnitude of the opto-magnetic field in the sample generated by the CP pulse [125] [126]. To this day, the microscopic origins of HD-AOS remain the subject of intense debate. However, this has not hindered experimental progress. Over the past

decade, studies have shown that this phenomenon occurs in multilayer ferromagnetic samples [127] , including magnetic tunnel junctions [128], and it was recently demonstrated that ultrafast electrical pulses can be used to switch the magnetization in a similar way as HD-AOS [129]. Indeed, the prospect of combining the ultrafast switching speeds that HD-AOS offers with other forms of control and detection is highly attractive.

8.2 AOS Setup at UCSC

At a glance it seems that HD-AOS simply requires an ultrafast laser system, but, other properties of the laser system, such as the repetition rate, are also important to consider. In the past our lab has tried to use the Ti:Sapphire oscillator in our TR-MOKE setup to conduct HD-AOS experiments. However, after extensive trial and error our lab found that HD-AOS could not be performed using this system. Recently, a femtosecond laser source with a tunable repetition rate, the Calmar Cazadero, that was used for three-photon microscopy became available. Some relevant properties of the system are summarized in the table below. Most notably, the repetition rate goes as low as 250 kHz with a corresponding pulse energy of approximately 700 nJ. Per Fig. 8.2, the critical fluence required for HD-AOS is approximately 3 mJ/cm^2 for GdFeCo which provides an estimate for us to consider. The largest pulse energy provided by the Cazadero system is 700 nJ, which corresponds to a spot size of 86 μm to reach a fluence of 3 mJ/cm^2. For reference, using the diffraction-limited spot size of this laser we can

estimate the maximum possible fluence as follows: $F_{max} = \frac{E_{pulse}}{\pi * w_{0,min}^2} \approx \frac{E_{pulse}}{\pi * (0.61\lambda)^2} =$ 25,000 mJ/cm^2.

Parameter	*Specification*
Wavelength (nm)	1550
Pulse Width (fs)	<100 @ 250 kHz-1MHz, <350 @ 2 MHz, <500 @ 4,8, 16, 32 MHz
Maximum Average Power (mW)	> 700
Pulse Energy (nJ)	>700 @ 250 kHz-1 MHz, > 350 @ 2 MHz, 175 @ 4 MHz, 87.5 @ 8 MHz, >43 @ 16 MHz, > 22 @ 32 MHz

Table 8.1. List of the relevant properties of the Calmzer Cazadero laser system.

Even though the pulse energy and repetition rate of the laser are compatible with HD-AOS, the operating wavelength is nearly two times larger than the output of a Ti:Sapphire which is almost ubiquitously used for this type of experiment. Before we began building the setup, we could only find a single report where light with a wavelength of 1.55 μm had been used to optically switch the magnetization, and in that experiment the authors studied GdFeCo [130]. Here, we would like to study the all-optical switching of FeTb films grown by our collaborators at the University of Augsburg in Germany who extensively studied these samples using 800 nm light [131]. Specifically, to the best of our knowledge, no report has investigated the interplay between a dynamic elastic wave and all-optical switching. To this end, we hope to combine the nonlocal SAW generation technique utilized in the preceding chapters with HD-AOS. We envision that the magneto-elastic field (H_{MEL}) generated by the

SAW will, hopefully, affect the fluence threshold for helicity-dependent optical switching of the magnetization. In addition, we anticipate that the pattern of the domain will follow the spatial character of the SAW, which could provide an additional means of controlling the spatial character of the magnetization in devices that HD-AOS.

8.3 Experimental Results

8.3.1 HD-AOS of FeTb Films

Our first goal was to determine if the Cazadero system could be used for the study we wished to conduct. Thankfully, only two optical components are necessary for HD-AOS: a quarter-wave plate (QWP) to CP the light pulse, and a focusing element that can tighten the beam to a few tens of microns. However, because micron-sized spot sizes are required to achieve large enough fluences for all-optical switching, a high-resolution MOKE microscope is required to observe the small domains written by the laser. The optical setup that we built to test the Cazadero system is shown below in Fig. 8.3, where in (a) the beam path used for the AOS of the film is shown and all the extra components used for MOKE imaging are removed during the experiment. By flipping the mirror and beamsplitter back into place, the laser pulse is blocked and the light from the monochromatic lamp is focused onto the sample surface via a Kohler illumination setup (Fig. 8.3 (b)). The light collected by the MO and directed towards the analyzer to detect the MOKE signal (crossed-polarizer scheme). Once the system has been carefully aligned, this allows for us to quickly switch between AOS experiments and MOKE imaging in a matter of seconds.

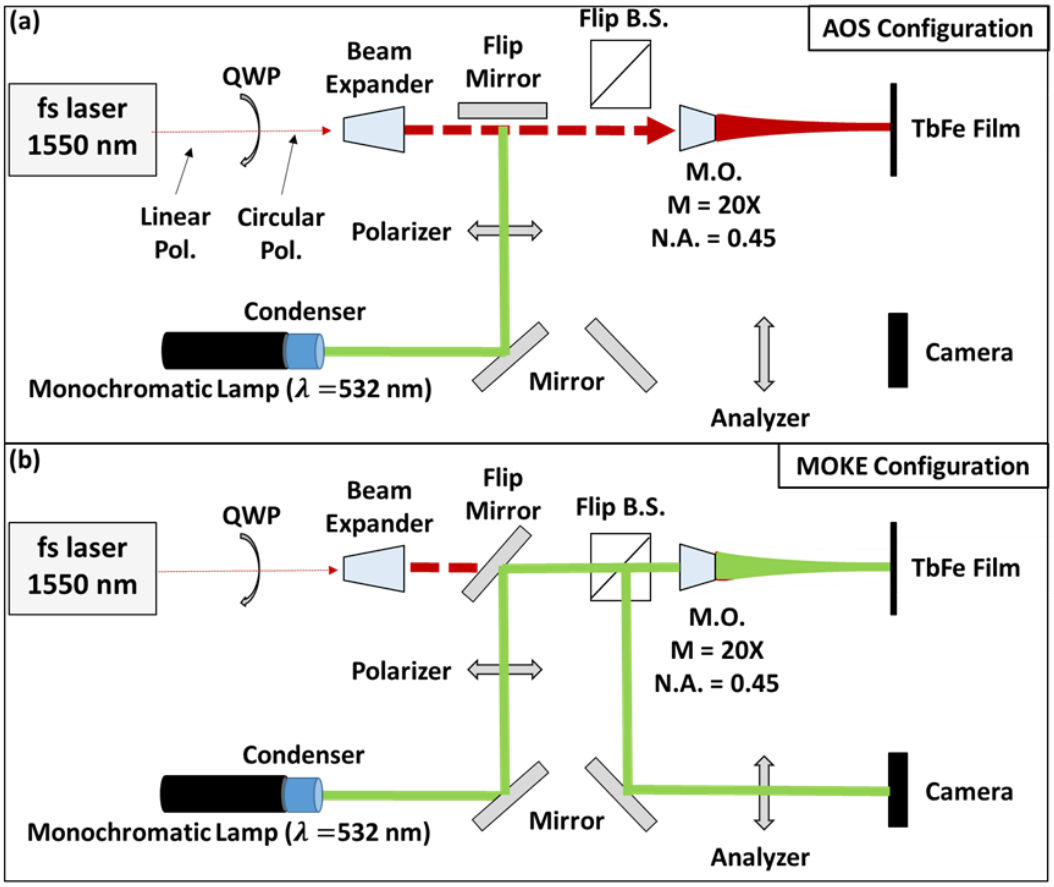

Fig. 8.3. (a) The HD-AOS beam path used to test the FeTb films, and (b) the MOKE imaging path to detect the micron-scale changes in the magnetization. In (c), MOKE image of the FeTb sample surface after AOS beams with opposite helicities and various fluences were scanned across the sample surface. The size of the written domains are directly proportional to the fluence. In the regions surrounding the HD-AOS lines, the sample is demagnetized and forms randomly oriented domains that reduce the magnetostatic energy.

One thing that is not shown is the 3-dimensional micrometer stage the FeTb sample is mounted on which allows us to scan the sample and vary the distance from the objective. The latter part is especially important because the chromatic aberration of the objective (which is not corrected for 1.55 μm light) results in a nearly 0.5 mm difference between the focal distance of the IR light and green light used to monitor the magnetization. Thus, to accurately control the spot size of the AOS beam the

distance between the objective and the sample must be precisely adjusted. Once the system was aligned, the tests quickly revealed that the laser system is suitable for HD-AOS experiments on FeTb films. In Fig. 8.3 (c), the MOKE image shows the results of scanning opposite helicities of CP light across the surface using various fluences to change the size of the optically written domains. One characteristic feature of successful HD-AOS is the ability to overwrite domains which is clearly seen at the point indicated by the arrow.

8.3.2 SAW-Assisted HD-AOS Experiments

In order to synchronize the arrival of the acoustic and optical pulses, we emulated the pump-probe setup of our TR-MOKE experiment. However, because we are not interested in the back-reflected beam in this experiment we do not need to worry about spectral separation of the pump and switching pulses; hence, we do not need to double the frequency of the "pump" beam that will generate the SAWs like in the TR-MOKE setup.

As we saw in the previous chapters, the speed of the SAWs is many orders of magnitude slower than light ($v_s \sim 4$ μm/ns), thus, an appropriate time delay must be built into the two optical paths to allow time for the strain wave to travel from the bars to the location of the HD-AOS pulse. For this reason, the AOS beam path shown in Fig. 8.3 was modified to include a mechanical time delay stage for the switching pulse (Fig. 8.4) that allows the user to set the time delay for the experiment. Because we want to avoid photoexcitation of the spins prior to the arrival of the acoustic wave, we intend

to separate the focused spots by at least 5 microns, which corresponds to a SAW travel time of roughly 1.25 ns that, in turn, requires an OPL difference of at least 40 cm to account for. Note that unlike the TR-MOKE experiment where we use an automated mechanical delay line that can travel up to 1 m with ultrafine resolution (<10 nm),

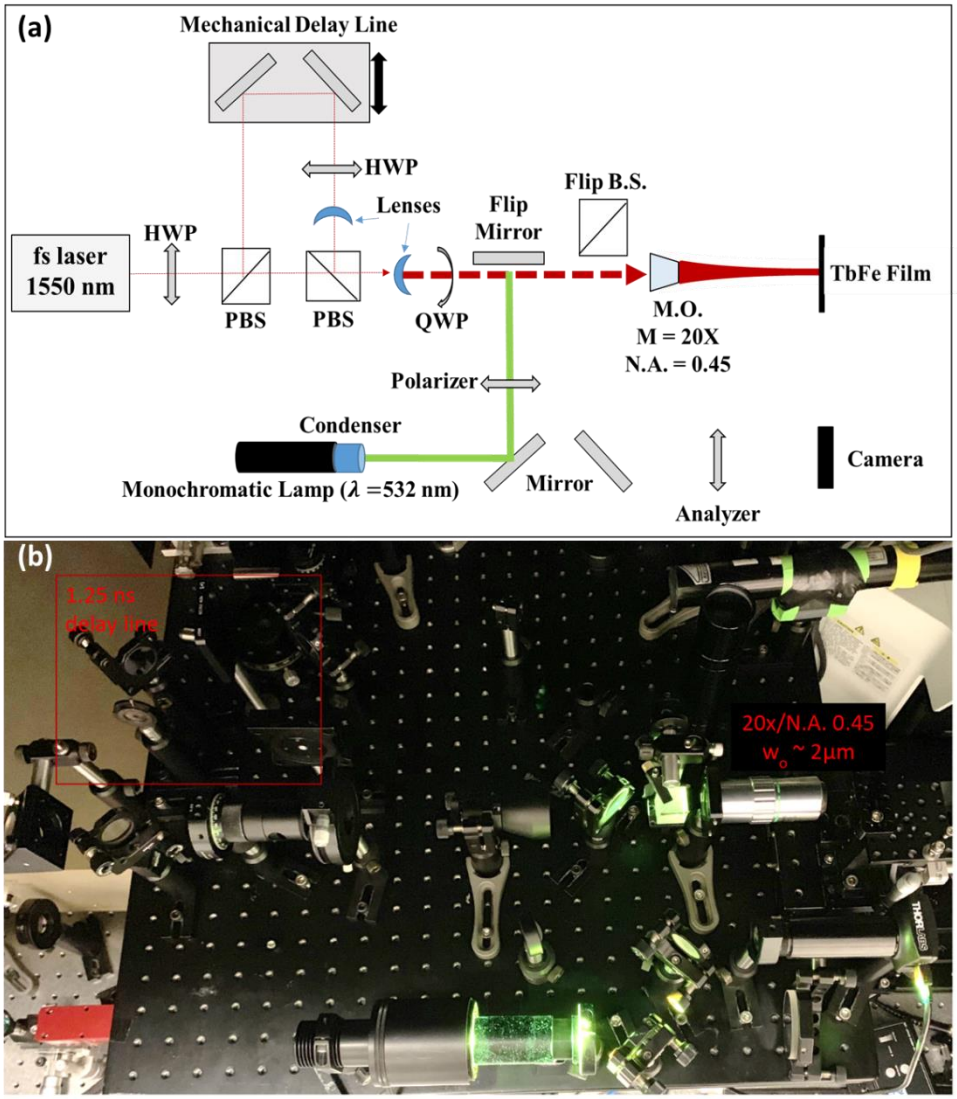

Fig. 8.4. (a) Modified AOS setup that splits the pulse into two beams that have a variable time delay that corresponds to the time required for the SAW to travel from the bars to the AOS pulse. (b) Photograph of the completed HD-AOS setup in the Sinsheimer 111c microscopy lab.

here, the OPL is static except for the pair of retroreflecting mirrors mounted on a micrometer with a 25 mm travel range that corresponds to a delay of approximately 160 ps.

Another difference between the HD-AOS and TR-MOKE experiments is the size of the pump and probe spot sizes, which were approximately 5 μm and 500 nm, respectively, for the TR-MOKE. Here, the pulse energy is over an order of magnitude larger which allows us to use much larger spot sizes to generate stronger SAWs with larger lifetimes. However, because we want to maximize the amplitude of the SAWs and simultaneously use the smallest fluence for AOS, the power and spot size of each beam needs to be varied independently. By inserting half-wave plates (HWP) into two locations in the setup and using polarizing beam splitters (PBS) to separate and recombine the beams, the power of each arm can be controlled precisely. To vary the spot sizes of the beams we utilized a pair of lenses to change the beam properties at the MO. For the AOS beam a lens focuses the light prior to being recombined by the second PBS, after which the beam is collimated by the second lens in the setup with a larger beam waist than it originally har. The pump beam that generates the SAWs, however, only passes through a single lens which focuses the laser into the MO, thereby changing the effective N.A. for this pulse. This optical configuration allows us to separate the focal planes of the two beams in order to control the spot size of each independently in the experiment.

Now that the experimental apparatus was setup, we were ready to attempt combining SAWs and HD-AOS. Because we were working with unpatterned FeTb

films, we initially opted to simply mill bar patterns into the film using a Ga^+ focused ion-beam (FIB) with a resolution of 7nm. However, during our experiment we noticed that the magnetic properties of the film near the FIB-milled regions were directly affected by the Ga^+. Indeed, it is well-known that the Ga^+ ions are implanted into the sample and alter the magnetic order [132]. The extent of the damage is shown in Fig. 8.5, where we see that the magnetic order of the film has been disturbed up to a hundred microns away from the bars. In this region, the film could no longer be deterministically switched using CP light. Interestingly, the region remained magnetic but possessed a much lower coercivity (~1 kOe) than the virgin film (>2T). In addition, once the region was switched by an external field the ultrafast pulse could still switch the magnetization, but the result did not depend on the polarization and could not be overwritten using the laser. This behavior suggests that the switching in this case is due to purely thermal effects. In order to use the FIB-milled bars for our study, the SAWs would need to travel to the unaffected portion of the sample, which is approximately 100 μm (25 ns) from the bars. This is problematic because the optical path length of the AOS beam path would need to be extended by a few meters, and the optically excited SAW would completely dissipate into the substrate by the time it reached the unaffected portion of the film. Thus, the FIB milling of the FeTb film was incompatible with the SAW-assisted HD-AOS study, and we were forced to turn to other fabrication methodologies that do not change the magnetic properties of the sample.

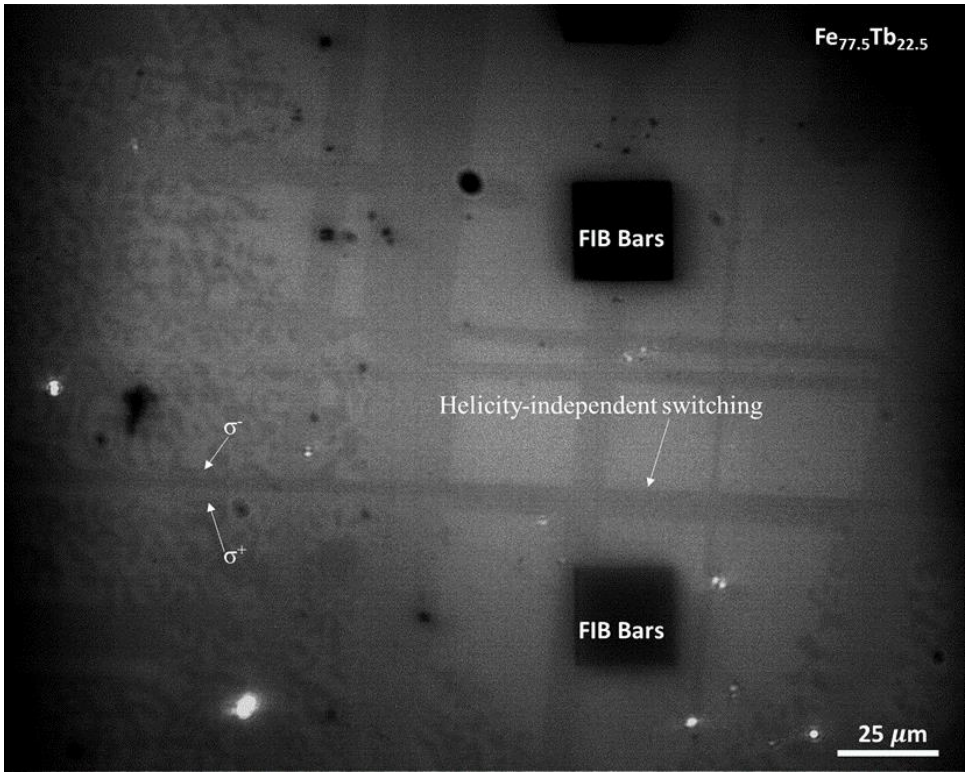

Fig. 8.5. Wide-field MOKE image of the FeTb film near the FIB-milled regions (dark squares). On the perimeter of the image the virgin film is demagnetized and has a large coercivity (~ 2 T) and is compatible with HD-AOS. In stark contrast, the area surrounding the bars are single domain and can be switched by an external field on the order of 1 kOe. When the ultrafast beam is scanned across the area irradiated by Ga^+ ions, a helicity-independent domain is written that can only be reversed by an external field. From left to right, two domains were written side-by-side using two beams with opposite helicities, however, once they enter the perturbed region there is no difference in the domain written by each beam.

Instead of using ion milling to define wire grids to generate SAWs, we instead use the same electron beam lithography and evaporation process used in the previous chapters to deposit Al bars onto the surface of the FeTb. MOKE imaging and HD-AOS experiments confirmed that the Al nanowires have no effect on the magnetic properties of the FeTb film beneath, thus, this sample should be suitable for the experiment. However, during our initial attempts to conduct the experiment we encountered another unexpected issue – when the two beams have even a small amount of overlap, the

switching behavior of the region where the two beams overlap changes significantly (Fig. 8.6).

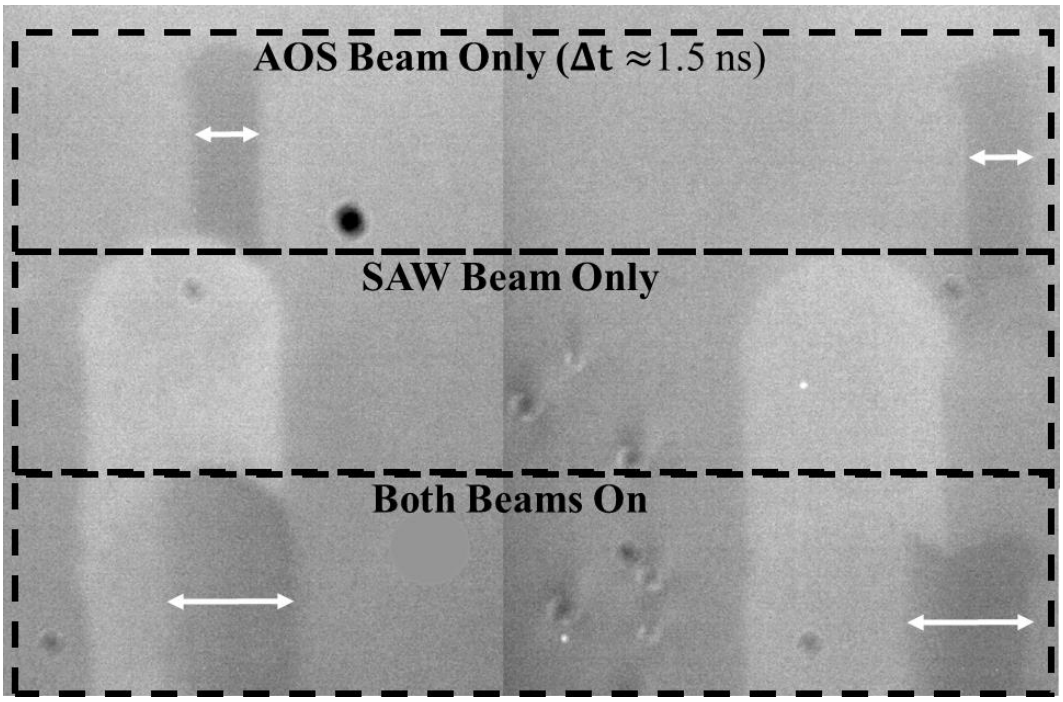

Fig. 8.6. Wide-field MOKE images of the FeTb film surface when illuminated by the AOS beam (top), the SAW beam (middle), and both beams which are separated by a 1.5 ns time delay. On the left-hand side of the figure the larger beam completely encompasses the smaller one, whereas on the right-hand side the domains are completely separated only one beam is on. Note that even though the domains are separated when one beam is on, they overlap when both strike the sample, which is shown in the bottom panel. Here, the domain written by the AOS beam is nearly twice as large despite having the same fluence and spot size. In addition, the domain on the left-hand side of the time-delayed beam in both cases is demagnetized, as opposed to uniformly magnetized.

Recall that the magnetization switches within a few picoseconds for HD-AOS. Thus, it is astounding that the first pulse – which arrives roughly 1.5 ns earlier – has any influence on the magnetic domain written by the second pulse. On the other hand, however, this behavior prevents us from focusing the beams too close to each other because we cannot be certain if any change in the switching behavior is due to overlap between the beams or SAW-assisted HD-AOS. Therefore, the two beams must be separated entirely to avoid the behavior we see in Fig. 8.6. Because the SAWs will have only a fraction of their initial amplitude after traveling such a long distance, we do not expect any significant change in the energy threshold for optical switching. To avoid this issue, we have turned to Al bar designs that focus the strain waves at the spot we intended to perform the SAW-assisted HD-AOS experiment, as shown below.

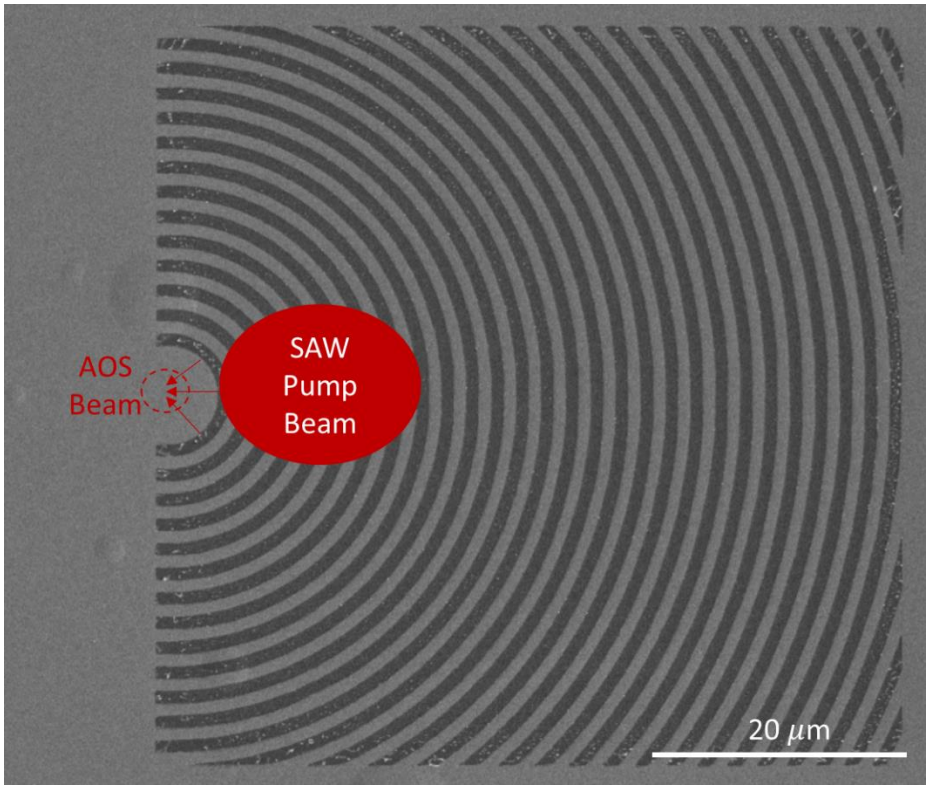

Fig. 8.7. SEM image of circular Al bars deposited on the FeTb film to focus the strain wave at an optimum distance from the SAW pump beam.

8.4 Conclusion

In this section the development of an experimental apparatus that can be used to study the interplay between SAWs and HD-AOS was presented in detail. We showed, for the first time, that FeTb films could be optically switched using light pulses with a central wavelength of 1550 nm. In addition, our observations that the optically written domains are influenced by pulses separated by more than a nanosecond show that the system remains in a highly non-equilibrium state long after the magnetization has switched. Currently, the Applied Optics group is investigating the acoustic behavior of focused-SAW structures that will allow for greater separation of the beams.

[1] A. Gurevich and G. Melkov, Magnetization Oscillations and Waves, New York, New York: CRC Press, 1996.

[2] D. Sander, S. Valenzuela, D. Makarov, C. Marrows, E. Fullerton, P. Fischer, J. McCord, P. Vavassori, S. Magnin, P. Pirro, B. Hillebrands, A. Kent, T. Jungwirth, O. Gutfleisch, C. Kim and A. Berger, "The 2017 Magnetism Roadmap," *J. of Appl. Phys. D: Appl. Phys.,* vol. 50, no. 36, 2017.

[3] A. Khvalkovskiy, D. Apalkov, S. Watts, R. Chepulskii, R. Beach, A. Ong, X. Tang, A. Driskill-Smith, W. Butler, P. Visscher, D. Lottis, E. Chen, V. Nikitin and M. Krounbi, "Basic Principles of STT-MRAM Cell Operation in Memory Arrays," *J. Appl. Phys. D,* vol. 46, no. 7, 2013.

[4] M. Nikitin, A. Orlov, I. Sokolov, A. Minakov, P. Nikitin, J. Ding, S. Bader, E. Rozhkova and V. Novosad, "Ultrasensitive Detection Enabled by Nonlinear Magnetization of Nanomagnetic Labels," *Nanoscale,* vol. 10, 2018.

[5] M. Wang, W. Cai, K. Cao, J. Zhou, J. Wrona, S. Peng, H. Yang, J. Wei, W. Kang, Y. Zhang, J. Langer, B. Ocker, A. Fert and W. Zhao, "Current-Induced Magnetization Switching in Atom-Thick Tungsten Engineering Perpendicular Magnetic Tunnel Junctions with Large Tunnel Magnetoresistance," *Nat. Comm.,* vol. 9, no. 671, 2018.

[6] S. Ikeda, H. Sato, H. Honjo, E. Enobio, S. Ishikawa, M. Yamanouchi, S. Fukami, S. Kanai, F. Matsukura, T. Endoh and H. Ohno, "Perpendicular Anisotropy CoFeB-MgO Based Magnetic Tunnel Junctions Scaling Down to 1X nm," in *IEDM*, San Francisco, 2014.

[7] S. Lequeux, V. Nguyen, N. Perrissin, J. Chatterjee and L. Tille, "Towards High Density STT-MRAM at sub-20nm Nodes," in *TMRC*, Milipitas, 2018.

[8] D. Kang and Y.-B. Kim, "Embedded STT-MRAM Oppurtunities in New System Hierarchies," in *ISOCC*, Gyeongju, 2015.

[9] H. Choi, S. Kang, S. Cho, I.-Y. Oh, M. Shin, H. Park, C. Jang, B.-C. Min, C.-I. Kim, S.-Y. Park and C. Park, "Spin Nano-Oscillator-Based Wireless Communication," *Scientific Reports,* vol. 4, 2014.

[10] H. Fulara, M. Zahedinejad, R. Khymyn, A. A. Awad, S. Muralidhar, M. Dvornik and J. Akerman, "Spin-Orbit- Torque-Driven Propagating Spin Waves," *Sci. Adv.,* vol. 5, no. 9, 2019.

[11] J. Torrejon, M. Riou, F. Abreu Araujo, S. Tsunegi, G. Khalsa, D. Querlioz, P. Bortolotti, V. Cros, K. Yakushiji, A. Fukushima, H. Kubota, S. Yuasa, M. Stiles and J. Grollier,

"Neuromorphic Computing with Nanoscale Spintronic Oscillators," *Nature,* vol. 547, pp. 428-431, 2017.

[12] M. Tarequzzaman, T. Bohnert, M. Decker, J. Costa, J. Borme, B. Lacoste, E. Paz, A. Jenkins, S. Serrano-Guisan, C. Back, R. Ferreira and P. Freitas, "Spin Torque Nano-Oscillator Driven by Combined Spin Injection from Tunneling and Spin Hall Current," *Nat. Comm. Phys.,* vol. 2, no. 20, 2019.

[13] K. Lange, B. Rapp and M. Rapp, "Surface Acoustic Wave Biosensors: A Review," *Anal. Bioanal. Chem.,* vol. 391, pp. 1509-1519, 2008.

[14] K.-Y. Hashimoto, Surface Acoustic Wave Devices in Telecommunications, Berlin: Spinger-Verlag, 2000.

[15] V. Sampath, N. D'Souza, D. Bhattacharya, G. Atkinson, S. Bandyopadhyay and J. Atulasimha, "Acoustic-Wave-Induced Magneitzation Switching of Magnetostrictive Nanomagnets from Single-Domain to Nonvolatile Vortex States," *Nano Lett.,* vol. 16, no. 9, 2016.

[16] N. Roschewsky, S. Schafer, F. Hellman and V. Nikitin, "Perpendicular Magnetic Tunnel Junction Performance Under Mechanical Strain," *Appl. Phys. Lett.,* vol. 112, 2018.

[17] L. Loong, X. Qui, Z. Neo, P. Deorani, Y. Wu, C. Bhatia, M. Saeys and H. Yang, "Strain-Enhanced Tunneling Magnetoresistance in MgO Magnetic Tunnel Junctions," *Sci. Rep.,* vol. 4, 2014.

[18] Y. Yahagi, B. Harteneck, S. Cabrini and H. Schmidt, "Controlling Nanomagnet Magnetization Dynamics via Magnetoelastic Coupling," *Phys. Rev. B,* vol. 90, no. 14, 2014.

[19] R. Skomski, Simple Models of Magnetism, Oxford, UK: Oxford University Press, 2008.

[20] L. Lifshits and E. Landau, "On the Theory of the Dispersion of Magnetic Permeability in Ferromagnetic Bodies," *Phys. Z. Sowjetunion,* vol. 8, no. 135, 1935.

[21] T. L. Gilbert, "A Langrangian Formulation of the Gyromagnetic Equation of Motion of the Magnetization Field," *Phys. Rev.,* vol. 100, no. 1243, 1955.

[22] S. B. Santra, "Thermodynamics and Statistical Mechanics," Indian Institute of Technology Guwahati, Guwahati, Assam, 2014.

[23] W. Pauli, General Principles of Quantum Mechanics, Berlin, Germany: Spinger-Verlag, 1980.

[24] A. Aharoni, Introduction to Theory of Ferromagnetism, Oxford, UK: Clarendon Press, 1996.

[25] B. Kalinikos and A. Slavin, "Theory of dipole-exchange spin wave spectrum for ferromagnetic films with mixed exchange boundary conditions," *Journal of Physics C: Solid State Physics,* vol. 19, no. 35, 1986.

[26] D. J. Griffiths, Introduction to Electrodynamics, London, UK: Pearson, 1989.

[27] Geek3, "Wikimedia Commons," May 2017. [Online]. Available: https://commons.wikimedia.org/wiki/File:VFPt_magnets_BHM.svg. [Accessed July 2019].

[28] G. Wysin, "Demagnetization Fields," April 2012. [Online]. Available: https://www.phys.ksu.edu/personal/wysin/notes/demag.pdf. [Accessed July 2019].

[29] J. Jackson, Classical Electrodynamics, John Wiley & Sons, Inc., 1961.

[30] J. A. Osborn, "Demagnetizing Factors of the General Ellipsoid," *Phys. Rev.,* vol. 67, no. 11, pp. 351-357, 1945.

[31] Ag2gaeh, "Wikimedia Commons," December 2015. [Online]. Available: https://commons.wikimedia.org/wiki/File:Ellipsoide.svg. [Accessed July 2019].

[32] B. D. Cullity, Introduction to Magnetic Materials, Piscataway, NJ: IEEE Press, 1972.

[33] Z. Cao and H. Gu, "Cubic Atom and Crystal Structures," *International Journal of Physics,* vol. 2, no. 6, pp. 277-281, 2014.

[34] J. Bidaux, R. Schaller and W. Benoit, "Study of the H.C.P.-F.C.C. Phase Transition in Cobalt by Acoustic Measurements," *Acta Metallurgica,* vol. 37, no. 3, pp. 803-811, 1989.

[35] A. Hirohata, H. Sukegawa, H. Yanagihara, I. Zutic, T. Seki, S. Mizukami and R. Swaminathan, "Roadmap for Emerging Materials for Spintronic Device Applications," *IEEE Transactions on Magnetics,* vol. 51, no. 10, 2015.

[36] D. Worledge, G. Hu, D. Abraham, J. Sun, P. Trouilloud, J. Nowak, S. Brown, M. Gaidis, E. O'Sullivan and R. Robertazzi, "Spin Torque Switching of Perpendicular Ta|CoFeB|MgO-based Magnetic Tunnel Junctions," *Applied Physics Letters,* vol. 98, no. 2, 2011.

[37] S. Ikeda, K. Miura, H. Yamamoto, K. Mizunuma, H. Gan, M. Endo, S. Kanai, J. Hayakawa, F. Matsukura and H. Ohno, "A Perpendicular Anisotropy CoFeB-MgO Magnetic Tunnel Junction," *Nature Mat.,* vol. 9, pp. 721-724, 2010.

[38] E. Lee, "Magnetostriction and Magnetomechanical Effects," *Reports on Progress in Physics,* vol. 18, no. 184, pp. 185-229, 1955.

[39] E. d. T. d. Lacheisserie, "Definition and Measurement of the Surface Magnetoelastic Coupling Coefficients in Thin Films and Multilayers," *Phys. Rev. B,* vol. 51, no. 22, pp. 925-932, 1995.

[40] C. Kittel, "On the Theory of Ferromagnetic Resonance," *Phys. Rev.,* vol. 73, no. 2, pp. 155-161, 1948.

[41] H. Beljers and J. Smit, "Ferromagnetic Resonance Absorption in BaFe12O19 a Highly Anisotropic Crystal," *Phil. Res. Rep.,* vol. 10, no. 113, 1955.

[42] H. Suhl, "Theory of the Magnetic Damping Constant," *IEEE Transactions on Magnetics,* vol. 34, no. 4, pp. 1834-1838, 1998.

[43] S. Bhagat and P. Lubitz, "Temperature Variation of Ferromagnetic Relaxation in the 3d Transition Metals," *Phys. Rev. B,* vol. 10, no. 179, 1974.

[44] V. Kambersky, "On the Landau-Lifshitz Relaxation in Ferromagnetic Metals," *Can. J. Phys.,* vol. 48, no. 24, 1970.

[45] V. Kambersky, "On Ferromagnetic Resonance Damping in Metals," *Czechoslovak Journal of Physics B,* vol. 26, no. 12, pp. 1366-1383, 1976.

[46] V. Kambersky, "FMR Linewidth and Disorder in Metals," *Czechoslovak Journal of Physics B,* vol. 34, no. 10, pp. 1111-1124, 1984.

[47] K. Gilmore, Y. Idzerda and M. Stiles, "Identification of Dominant Precession-Damping Mechanism in Fe, Co, and Ni by First-Principles Calculations," *Phys. Rev. Lett.,* vol. 99, no. 2, 2007.

[48] M. Farle, T. Silva and G. Woltersdorf, "Spin Dynamics in the Time and Frequency Domain," in *Magnetic Nanostructures*, New York, New York, Springer, 2013, pp. 37-83.

[49] M. Sabino, "Ferromagnetic Resonance Studies of Low Damping Multilayer Films with Perpendicular Magnetic Anisotropy for Memory Applications," 20 August 2014. [Online]. Available: https://scholarbank.nus.edu.sg/handle/10635/118580. [Accessed July 2019].

[50] R. Arias and D. Mills, "Extrinsic Contributions to the Ferromagnetic Resonance Response of Ultrathin Films," *Phys. Rev. B,* vol. 60, no. 10, pp. 7395-7409, 1999.

[51] P. Landeros, R. Arias and D. Mills, "Two Magnon Scattering in Ultrathin Ferromagnets: The Case When the Magnetization is Out of the Plane," *Phys. Rev. B,* vol. 77, no. 21, 2008.

[52] M. Faraday, "On the Magnezation of Light and the Illumination of Magnetic Lines of Force," *Phil. Trans. Royal Soc.,* vol. 136, no. 1, 1846.

[53] J. Kerr, "On Rotation of the Plane of Polarization Upon Reflection From the Pole of a Magnet," *Phil. Mag.,* vol. 3, no. 19, pp. 321-343, 1877.

[54] W. Voigt, "Doppelbrechung von im Magnetfeld befindlichem Natriumdampf in der Richtung normal zu den Kraftlinien (Birefringence of sodium vapour in amagnetic field along a direction perpendicular to the lines of force)," *Nacher. Kgl. Ges. Wiss. Göttingen,* vol. 4, no. 355, 1898.

[55] A. Cotton and H. Mouton, "Sur les propriétés magnéto-optiques des colloides et des liqueurshétérogénes (On magneto-optic properties of colloids and inhomogeneous liquids)," *Ann. Chim. Phys.,* vol. 11, no. 145, 1907.

[56] E. Hecht, Optics, New York: Addison-Wesley, 2002.

[57] W. Kuch, R. Schafer, P. Fischer and F. Hillebrecht, Magnetic Microscopy of Layered Structures, Berlin: Springer, 2015.

[58] H. Lorentz, "The Theory of Electrons and Its Applications to the Phenomena of Light and Radiant Heat," *Science,* vol. 31, no. 789, 1910.

[59] G. FitzGerald, "Note on the Connection between the Faraday Rotation of Plane of Polarisation and the Zeeman Change of Frequency of Light Vibrations in a Magnetic Field," *Proc. of the Royal Soc. of London,* vol. 63, pp. 31-35, 1898.

[60] U. Tiwari, R. Ghosh and P. Sen, "Theory of Magneto-Optic Kerr Effects," *Phys. Rev. B,* vol. 49, no. 3, pp. 2159-2162, 1994.

[61] S. Wang, A. Barman, H. Schmidt, J. Maas, A. Hawkins, S. Kwon, B. Harteneck, S. Cabrini and J. Bokor, "Optimization of Nano-Magneto-Optic Sensitivity Using Dielectric Layer Enhancement," *Appl. Phys. Lett.,* vol. 90, no. 25, 2007.

[62] N. Quereshi, H. Schmidt and A. Hawkins, "Cavity Enhancement of the Magneto-Optic Kerr Effect for Optical Studies of Magnetic Nanostructures," *Appl. Phys. Lett.,* vol. 85, no. 3, 2004.

[63] L. Coldren and A. Corzine, Diode Lasers and Photonic Integrated Circuits, New York: Wiley, 1995.

[64] J. Zak, E. Moog, C. Liu and S. Bader, "Fundamental MagnetoOptics," *Appl. Phys. Lett.,* vol. 68, no. 8, 1990.

[65] P. Yeh, "Optics of Anisotropic Layered Media," *Surface Science,* vol. 96, 1979.

[66] I. Neudecker, G. Woltersdorf, B. Heinrich, T. Okuno, G. Gubbiotti and C. Back, "Comparison of Frequency, Field, and Time Domain Ferromagnetic Resonance Methods," *Journal of Magnetism and Magnetic Materials,* vol. 307, no. 1, pp. 148-156, 2006.

[67] E. Beaurepaire, J. Merle, A. Daunois and A. Bigot, "Ultrafast Spin Dynamics in Ferromagnetic Nickel," *Phys. Rev. Lett.,* vol. 76, no. 22, 1996.

[68] I. Razdolski, A. Alekhin, U. Martens, D. Burstel, D. Diesing, M. Munzenberg, U. Bovensiepen and A. Melnikov, "Analysis of the Time-Resolved Magneto-Optical Kerr Effect for Ultrafast Magnetization Dynamics in Ferromagnetic Thin Films," *Journal of Phys.: Condensed Matter,* vol. 29, no. 17, 2017.

[69] E. Turgut, D. Zusin, D. Legut, K. Carva, R. Knut, J. Shaw, C. Chen, Z. Tao, H. Nembach, T. Silva, S. Mathias, M. Aeschlimann, P. Oppeneer, H. Kapteyn, M. Murnane and P. Grychtol, "Stoner versus Heisenberg: Ultrafast Exchange Reduction and Magnon Generation During Laser-Induced Demagnetization," *Phys. Rev. B,* vol. 94, no. 22, 2016.

[70] N. Bergeard, M. Hehn, S. Mangin, G. Lengaigne, F. Montaigne, M. Lalieu, B. Koopmans and G. Malinowski, "Hot-Electron-Induced Ultrafast Demagnetization in Co/Pt Multilayers," *Phys. Rev. Lett.,* vol. 117, no. 14-30, 2016.

[71] B. Koopmans, M. van Kampen, J. Kohlepp and W. de Jonge, "Ultrafast Magneto-Optics in Nickel: Magnetism or Optics?," *Phys. Rev. Lett.,* vol. 85, no. 4, 2000.

[72] W. You, P. Tengdin, C. Chen, X. Shi, D. Zusin, Y. Zhang, C. Gentry, A. Blosnky, M. Keller, P. Oppeneer, H. Kapteyn, Z. Tao and M. Murnane, "Revealing the Nature of the Ultrafast Magnetic Phase Transition in Ni by Correlating Extreme Ultraviolet Magneto-Optic and Photoemission Spectroscopies," *Phys. Rev. Lett.,* vol. 121, no. 7, 2018.

[73] P. Tengdin, W. You, C. Chen, X. Shi, D. Zusin, Y. Zhang, C. Gentry, A. Blonsky, M. Keller, P. Oppeneer, H. Kapetyn, Z. Tao and M. Murnane, "Critical Behavior within 20fs Drives the Out-of-Equilibrium Laser-Induced Magnetic Phase Transition in Nickel," *Science Advances,* vol. 4, no. 3., 2018.

[74] A. Einstein and W. de Haas, "Experimenteller Nachweis der Ampèreschen Molekularströme," *Verhandl. Deut. Phys. Ges.,* vol. 15, pp. 152-170, 1915.

[75] C. Dornes, Y. Acremann, M. Savoini, M. Kubli, M. Neugebauer, E. Abreu, L. Huber, G. Lantz, C. Vaz, E. Bothschafter, M. Porer, V. Esposito, L. Rettig, M. Buzzi, A. Alberca, Y.

Windsor, P. Beaud, U. Staub, D. Zhu, S. Song, J. Glownia and L. Johnson, "The Ultrafast Einstein de-Haas Effect," *Nature,* vol. 565, 2019.

[76] B. Koopmans, G. Malinowski, D. Longa, D. Steiauf, M. Fahnle, T. Roth, M. Cinchetti and M. Aeschlimann, "Explaining the Paradoxical Diversity of Ultrafast Laser-Induced Demagnetization," *Nature Mater.,* vol. 9, 2009.

[77] C. Jozsa, H. Rietjens, M. van Kampen, E. Smalbrugge, M. Smit, W. de Jonge and B. Koopmans, "Retrieving Pulse Profiles from Pump-Probe Measurements on Magnetization Dynamics," *Journal of Appl. Phys.,* vol. 95, no. 7447, 2004.

[78] B. Koopmans, "Laser-Induced Magnetization Dynamics," in *Spin Dynamics in Confined Magnetic Structures II*, Berlin, Springer, 2003, pp. 253-320.

[79] D. Allwood, G. Xiong, M. Cooke and R. Cowburn, "Magneto-Optical Kerr Effect Analysis of Magnetic Nanostructures," *J. Phys. D: Appl. Phys.,* vol. 36, 2003.

[80] J. Wolberg, Data Analysis Using the Method of Least Squares, Berlin: Springer, 2006.

[81] J. Gallego, D. Lederman, S. Kim and I. Schuller, "Oscillatory Behavior of the Transport Properties in Ni/Co Multilayers: A Superlattice Effect," *Phys. Rev. Lett.,* vol. 74, no. 22, 1995.

[82] B. Gopman, C. Dennis, P. Chen, Y. Iunin, P. Finkel, M. Staruch and R. Shull, "Strain-Assisted Magnetization Reversal in Co/Ni Multilayers with Perpendicular Magnetic Anisotropy," *Sci. Rep.,* vol. 6, no. 27774, 2016.

[83] P. Levy, "Antisymmetric Exchange," *Phys. Rev. Lett.,* vol. 20, no. 1366, 1968.

[84] T. Moriya, "Anisotropic Superexchange Interaction and Weak Ferromagnetism," *Phys. Rev.,* vol. 120, no. 1, 1960.

[85] A. Wachowiak, J. Wiebe, M. Bode, O. Pietzsch, M. Morgenstern and R. Wiesendanger, "Direct Observation of Internal Spin Structure of Magnetic Vortex Cores," *Science,* vol. 298, no. 5593, 2002.

[86] N. Vernier, D. Allwood, D. Atkinson, M. Cooke and R. Cowburn, "Domain Wall Propagation in Magnetic Nanowires by Spin-Polarized Current Injection," *EDP Sciences,* vol. 65, no. 4, 2004.

[87] S. Muhlbauer, B. Binz, F. Jonietz, C. Pfleiderer, A. Rosch, A. Neubauer, R. Georgii and P. Boni, "SKyrmion Lattice in a Chiral Magnet," *Science,* vol. 323, no. 5916, 2009.

[88] R. Conte, G. Karnad, E. Martinez, K. Lee, N.-H. Kim, D.-S. Han, J.-S. Kim, S. Prenzel, T. Schulz, C.-Y. You, H. Swagten and M. Klaui, "Ferromagnetic Layer Thickness

Dependence of the Dyzaloshinskii-Moriya Interaction and Spin-Orbit Torques in Pt\Co\AlO," *AIP Adv.,* vol. 7, no. 6, 2017.

[89] D. Bromberg, M. Moneck, V. Sokalski, J. Zhu, L. Pileggi and J.-G. Zhu, "Experimental Demonstration of Four-Terminal Magnetic Logic Device with Separate Read- and Write-Paths," in *IEEE International Electron Devices Meeting*, San Francisco, 2014.

[90] M. Haertinger, C. Back, S.-H. Yang, S. Parkin and G. Woltersdorf, "Properties of Ni/Co Layers as a Function of the Number of Multilayer Repetitions," *J. Appl. Phys. D,* vol. 46, no. 17, 2013.

[91] J. Beaujour, D. Ravelosona, I. Tudosa, E. Fullerton and A. Kent, "Ferromagnetic Resonance Linewidth in Ultrathin Films with Perpendicular Magnetic Anisotropy," *Phys. Rev. B,* vol. 80, no. 18, 2009.

[92] A. Capua, S. Yang, T. Phung and S. Parkin, "Determination of Intrinsic Damping of Perpendicularly Magnetized Ultrathin Films from Time-Resolved Precessional Magnetization Dynamics," *Phys. Rev. B,* vol. 92, no. 22, 2015.

[93] D. Lau, V. Sundar, J. -G. Zhu and V. Sokalski, "Energetic Molding of Chiral Magnetic Bubbles," *Phys. Rev. B,* vol. 94, no. 6, 2016.

[94] M. Bjorck and G. Andersson, "GenX: An Extensible X-Ray Reflectivity Refinement Program Utilizing Differential Evolution," *J. Appl. Crys.,* vol. 40, no. 6, 2007.

[95] L. Parrat, "Surface Studies of Solids by Total Reflection of X-Rays," *Phys. Rev.,* vol. 95, no. 2, 1954.

[96] M. Jaris, D. Lau, V. Sokalski and S. Schmidt, "Magnetization Dynamics and Damping Behavior of Co/Ni Multilayers with a Graded Ta Capping Layer," *J. Appl. Phys.,* vol. 121, no. 16, 2017.

[97] H. Suhl, "Ferromagnetic Resonance in Nickel Ferrite Between One and Two Kilomegacycles," *Phys. Rev.,* vol. 97, no. 2, 1955.

[98] G. Malinowski, K. Kuiper, R. Lavrijsen, H. Swagten and B. Koopmans, "Magnetization Dynamics and Gilbert Damping in Ultrathin CoFeB Films with Out-of-Plane Anisotropy," *Appl. Phys. Lett.,* vol. 94, no. 10, 2009.

[99] S. Iihama, S. Mizukami, H. Naganuma, M. Oogane, Y. Ando and T. Miyazaki, "Gilbert Damping Constants of Ta/CoFeB/MgO(Ta) Thin Films Measured by Optical Detection of Precessional Magnetization Dynamics," *Phys. Rev. B,* vol. 89, no. 17, 2014.

[100] J. Shaw, H. Nembach and T. Silva, "Resolving the Controversy of a Possible Relationship Between Perpendicular Magnetic Anisotropy and the Magnetic Damping Parameter," *Appl. Phys. Lett.,* vol. 105, no. 6, 2014.

[101] E. Barati, M. Cinal, D. Edwards and A. Umerski, "Gilbert Damping in Magnetic Layered Systems," *Phys. Rev. B,* vol. 90, no. 1, 2014.

[102] Y. Tserkovnyak, A. Brataas and G. Bauer, "Spin Pumping and Magnetization Dynamics in Metallic Multilayers," *Phys. Rev. B,* vol. 66, no. 22, 2002.

[103] O. Boulle, V. Cros, J. Grollier, L. Pereira, C. Deranlot, F. Petroff, G. Faini, J. Barnas and A. Fert, "Shaped Angular Dependence of the Spin Transfer-Torque and Microwave Generation without Magnetic Field," *Nat. Phys.,* vol. 3, pp. 492-497, 2007.

[104] S. Azzawi, A. Ganguly, M. Tokac, R. Rowan-Robinson, J. Sinha, A. Hindmarch, A. Barman and D. Atkinson, "Evolution of Damping in Ferromagnetic/Nonmagnetic Thin Film Bilayers as a Function of Nonmagnetic Layer Thickness," *Phys. Rev. B,* vol. 93, no. 5, 2016.

[105] B. Auld, Acoustic Waves and Fields in Solids, New York: John Wiley and Sons, 1973.

[106] C. Ozbek, "Co Gas Sensor Applications of Fe Doped Calix[4]Arene Molecules," Izmir, 2013.

[107] C. Gianetti, B. Revaz, F. Banfi, M. Montagnese, G. Ferrini, F. Cilento, S. Maccalli, P. Vavassori, G. Oliviero, E. Bontempi, L. Depero, V. Metlushko and F. Parmigiani, "Thermomechanical Behavior of Surface Acoustic Waves in Ordered Arrays of Nanodisks Studied by Near-Infrared Pump-Probe Diffraction Experiments," *Phys. Rev. B,* vol. 76, no. 12, 2007.

[108] M. Weiler, L. Dreher, C. Heeg, H. Huebl, R. Gross, M. Brandt and S. Goennenwein, "Elastically Driven Ferromagnetic Resonance in Ni Thin Films," *Phys. Rev. Lett.,* vol. 106, no. 11, 2011.

[109] M. Jaris, Y. Yahagi, B. Mahato, S. Dhuey, S. Cabrini, V. Nikitin, J. Stout, A. Hawkins and H. Schmidt, "Intrinsic Spin Dynamics in Optically Excited Nanoscale Magnetic Tunnel Junction Arrays Restored by Dielectric Coating," *Appl. Phys. Lett.,* vol. 109, no. 20, 2016.

[110] K. Park, "The Extreme Values of Reflectivity and the Conditions for Zero Reflection from Thin Dielectric Films on Metal," *Appl. Optics,* vol. 3, no. 7, 1964.

[111] A. Barman, S. Wang, J. Maas, A. Hawkins, S. Kwon, A. Liddle, J. Bokor and H. Schmidt, "Magneto-Optical Observation of Picosecond Dynamics of Single Nanomagnets," *Nano Lett.,* vol. 6, no. 12, 2006.

[112] Z. Liu, R. Brandt, Y. Yahagi, B. Hansen, B. Harteneck, J. Bokor and H. Schmidt, "Detecting Single Nanomagnet Dynamics Beyond the Diffraction Limit in Varying Magnetostatic Environments," *Appl. Phys. Lett.,* vol. 98, no. 5, 2011.

[113] H. Nembach, J. Shaw, T. Silva, W. Johnson, S. Kim, R. McMichael and P. Kabos, "Effects of Shape Distortions and Imperfections on Mode Frequencies and Collective Linewidths in Nanomagnets," *Phys. Rev. B,* vol. 83, no. 9, 2011.

[114] J. Linder, I. Barsukov, C. Raeder, C. Hassel, O. Posth and R. Meckenstock, "Two Magnon Damping in Thin Films in Case of Canted Magnetization: Theory vs Experiment," *Phys. Rev. B,* vol. 80, no. 22, 2009.

[115] J. Dubowik, K. Zaleski, H. Glowinski and I. Goscianska, "Angular Dependence of Ferromagnetic Resonance Linewidth in Thin FIlms," *Phys. Rev. B,* vol. 84, no. 18, 2011.

[116] W. Yang, M. Jaris, L. Hibbard-Lubow, C. Berk and H. Schmidt, "Magnetoelastic Excitation of Single Nanomagnets for Optical Measurement of the Intrinsic Damping," *Phys. Rev. B,* vol. 97, no. 22, 2018.

[117] Y. Yahagi, C. Berk, B. Hebler, S. Dhuey, S. Cabrini, M. Albrecht and H. Schmidt, "Optical Measurement of Damping in Nanomagnet Arrays Using Magnetoelastically Driven Resonances," *J. of Phys. D.: Appl. Phys.,* vol. 50, no. 17, 2017.

[118] S. Rezende, F. de Aguiar and A. Azevedo, "Magnon Excitation by Spin-Polarized Currents in Magnetic Nanostructures," *Phys. Rev. B,* vol. 73, no. 9, 2006.

[119] M. Foerester, F. Macia, N. Statuto, S. Finizio, A. Hernandez-Minguez, S. Lendinez, P. Santos, J. Fontcuberta, J. Hernandez, M. Klaui and L. Aballe, "Direct Imaging of Delayed Magneto-Dynamic Modes Induced by Surface Acoustic Waves," *Nat. Comm.,* vol. 8, no. 407, 2017.

[120] W. Yang, M. Jaris, C. Berk and H. Schmidt, "Preferential Excitation of a Single Nanomagnet Using Magnetoelastic Coupling," *Phys. Rev. B,* vol. 99, no. 10, 2019.

[121] M. Beleggia, M. Graef and T. Millev, "The Equivalent Ellipsoid of a Magnetized Body," *J. Appl. Phys. D: Appl. Phys.,* vol. 39, no. 5, 2006.

[122] S. Kalarickal, p. Krivosik, M. Wu and C. Patton, "Ferromagnetic Resonance Linewidth in Metallic Thin Films: Comparison of Measurement Methods," *J. Appl. Phys.,* vol. 99, no. 9.

[123] C. Stanciu, C. Hansteen, A. Kimel, A. Kirilyuk, A. Tsukamoto, A. Itoh and T. Rasing, "All-Optical Magnetic Recording with Circularly Polarized Light," *Phys. Rev. Lett.,* vol. 99, no. 4, 2007.

[124] I. Tudosa, C. Stamm, A. Kashuba, F. King, H. Siegmann, J. Stohr, G. Ju, B. Lu and D. Weller, "The Ultimate Speed of Swtiching in Granular Recording Media," *Nat.,* vol. 428, 2004.

[125] D. Hinzke, M. Berritta, U. Atxitia, R. Mondal, P. Oppeneer and U. Nowak, "Inverse Faraday Effect as Mechanism for Ultrafast All-Optical Magnetic Switching," in *IEEE International Magnetics Conference*, Beijing, 2015.

[126] F. Hoveyda, E. Hohenstein, R. Judge and S. Smadici, "Demagnetizing Fields in All-Optical Switching," *J. of Phys.: Cond. Matt.,* vol. 30, no. 3, 2017.

[127] M. Vomir, M. Albrecht and J. Bigot, "Single Shot All Optical Switching of Intrinisc Micron Size Magnetic Domains in Pt/Co/Pt Ferromagnetic Stack," *Appl. Phys. Lett.,* vol. 111, no. 24, 2017.

[128] J. Chen, L. He, J. Wang and M. Li, "All-Optical Switching of Magnetic Tunnel Junctions with Single Subpicosecond Laser Pulses," *Phys. Rev. Appl.,* vol. 7, no. 2, 2017.

[129] Y. Yang, R. Wilson, J. Gorchon, C. Lambert, s. Salahuddin and J. Bokor, "Ultrafast Magnetization Reversal by Picosecond Electrical Pulses," *Science Adv.,* vol. 3 , no. 11, 2017.

[130] L. He, J. Chen, J. Wang and M. Li, "All-Optical Switching of Magnetoresistive Devices Using Telecom-Band Femtosecond Laser," *Appl. Phys. Lett.,* vol. 107, no. 10, 2015.

[131] A. Hassdentefeufel, B. Hebler, C. Schubert, A. LIebig, M. Teich, M. Helm, M. Aeschlimann, M. Albrecht and R. Bratschitsch, "Thermally Assisted All-Optical Helicity Dependent Magnetic Switching in Amorphous FeTb Alloy Films," *Adv. Mat.,* vol. 25, 2013.

[132] J. Read, P. Braganca, N. Robertson and J. Childress, "Magnetic Degradation of Thin Film Multilayers During Ion Milling," *Appl. Phys. Lett. Mat.,* vol. 2, no. 4, 2014.